applied sciences

Special Issue Reprint

Geomaterials

Latest Advances in Materials for Construction and Engineering Applications (2nd Edition)

Edited by
José Manuel Moreno-Maroto

mdpi.com/journal/applsci

MDPI

Geomaterials: Latest Advances in Materials for Construction and Engineering Applications (2nd Edition)

Geomaterials: Latest Advances in Materials for Construction and Engineering Applications (2nd Edition)

Guest Editor

José Manuel Moreno-Maroto

MDPI

Basel • Beijing • Wuhan • Barcelona • Belgrade • Novi Sad • Cluj • Manchester

Guest Editor
José Manuel Moreno-Maroto
Department of Geology
and Geochemistry
Autonomous University
of Madrid
Madrid
Spain

Editorial Office
MDPI AG
Grosspeteranlage 5
4052 Basel, Switzerland

This is a reprint of the Special Issue, published open access by the journal *Applied Sciences* (ISSN 2076-3417), freely accessible at: https://www.mdpi.com/journal/applsci/special_issues/CW27P59EB3.

For citation purposes, cite each article independently as indicated on the article page online and as indicated below:

Lastname, A.A.; Lastname, B.B. Article Title. *Journal Name* **Year**, *Volume Number*, Page Range.

ISBN 978-3-7258-8627-2 (Hbk)
ISBN 978-3-7258-8628-9 (PDF)
https://doi.org/10.3390/books978-3-7258-8628-9

Cover image courtesy of José Manuel Moreno-Maroto

© 2026 by the authors. Articles in this reprint are Open Access and distributed under the Creative Commons Attribution (CC BY) license. The reprint as a whole is distributed by MDPI under the terms and conditions of the Creative Commons Attribution-NonCommercial-NoDerivs (CC BY-NC-ND) license (https://creativecommons.org/licenses/by-nc-nd/4.0/).

Contents

About the Editor . . . . . **vii**

Preface . . . . . **ix**

José Manuel Moreno-Maroto
Present Insights and Future Prospects on Geomaterials: Introducing the Concept of Technite
Reprinted from: *Appl. Sci.* **2026**, *16*, 172, https://doi.org/10.3390/app16010172 . . . . . **1**

Zilu Xie, Zengzhen Qian, Hao Wang, Yingzhe Qi and Bing Yue
Synergistic Preparation and Mechanistic Investigation of Full Industrial Solid Waste-Based Cementitious Materials for Aeolian Sand Stabilization
Reprinted from: *Appl. Sci.* **2025**, *15*, 3858, https://doi.org/10.3390/app15073858 . . . . . **3**

José Manuel Moreno-Maroto, Julia M. Govea, Pablo Poza, Mercedes Regadío, Jaime Cuevas, Ana Isabel Ruiz, et al.
Hydrothermal Manufacture of Zeolitic Lightweight Aggregates from Clay and Marine Plastic Litter
Reprinted from: *Appl. Sci.* **2024**, *14*, 7674, https://doi.org/10.3390/app14177674 . . . . . **24**

Daniel Ferrández, Alicia Zaragoza-Benzal, Rocío Pastor Lamberto, Paulo Santos and Jacek Michalak
Optimizing Masonry Mortar: Experimental Insights into Physico-Mechanical Properties Using Recycled Aggregates and Natural Fibers
Reprinted from: *Appl. Sci.* **2024**, *14*, 6226, https://doi.org/10.3390/app14146226 . . . . . **40**

Nikki Shaji, Niall Holmes and Mark Tyrer
Early Age Assessment of a New Course of Irish Fly Ash as a Cement Replacement
Reprinted from: *Appl. Sci.* **2024**, *14*, 4128, https://doi.org/10.3390/app14104128 . . . . . **63**

Abel A. Belay, Julita Krassowska and Marta Kosior-Kazberuk
Comparative Performance Analysis of Small Concrete Beams Reinforced with Steel Bars and Non-Metallic Reinforcements
Reprinted from: *Appl. Sci.* **2024**, *14*, 3957, https://doi.org/10.3390/app14103957 . . . . . **78**

Ho Anh Thu Nguyen, Duy Hoang Pham, and Yonghan Ahn
Effect of Data Augmentation Using Deep Learning on Predictive Models for Geopolymer Compressive Strength
Reprinted from: *Appl. Sci.* **2024**, *14*, 3601, https://doi.org/10.3390/app14093601 . . . . . **90**

Carlos Mota-Heredia, Jaime Cuevas and Raúl Fernández
Geochemical Evolution of Mg-Bentonite Affected by the Contact of Carbon Steel and a Hydrothermal Gradient
Reprinted from: *Appl. Sci.* **2024**, *14*, 1259, https://doi.org/10.3390/app14031259 . . . . . **111**

Munder Bilema, Choon Wah Yuen, Mohammad Alharthai, Zaid Hazim Al-Saffar, Salam Ridha Oleiwi Aletba and Nur Izzi Md Yusoff
Influence of Warm Mix Asphalt Additives on the Physical Characteristics of Crumb Rubber Asphalt Binders
Reprinted from: *Appl. Sci.* **2023**, *13*, 10337, https://doi.org/10.3390/app131810337 . . . . . **132**

Hamid Reza Manaviparast, Nuno Cristelo, Eduardo Pereira and Tiago Miranda
A Comprehensive Review on Clay Soil Stabilization Using Rice Husk Ash and Lime Sludge
Reprinted from: *Appl. Sci.* **2025**, *15*, 2376, https://doi.org/10.3390/app15052376 . . . . . **147**

Hamid Reza Manaviparast, Tiago Miranda, Eduardo Pereira and Nuno Cristelo
A Comprehensive Review on Mine Tailings as a Raw Material in the Alkali Activation Process
Reprinted from: *Appl. Sci.* **2024**, *14*, 5127, https://doi.org/10.3390/app14125127 . . . . . **171**

About the Editor

José Manuel Moreno-Maroto

José Manuel Moreno-Maroto is Assistant Professor at the Department of Geology and Geochemistry, Autonomous University of Madrid (Spain). He obtained his PhD from the University of Castilla-La Mancha in 2019, receiving the distinctions Cum Laude and International Doctorate, together with four doctoral thesis awards, including the Extraordinary Doctorate Award from the University of Castilla-La Mancha and the Best Doctoral Thesis Award from the Spanish Ceramic and Glass Society. His research focuses on the development of advanced and sustainable geomaterials for construction and environmental applications, particularly lightweight aggregates, geopolymers, zeolites and hybrid zeopolymeric systems produced from industrial and agricultural residues. Dr. Moreno has published more than 40 papers in JCR-indexed journals, which have received over 1,200 citations. He has participated in numerous competitive research projects funded at the European level, in addition to taking part in and serving as Principal Investigator in research projects at the national and regional levels. He is the inventor of five patents related to sustainable construction materials and has led several industrial R&D transfer projects in collaboration with the industry. In addition, he serves as reviewer and evaluator for scientific journals and research funding agencies, is a member of several international scientific societies and technical committees, and currently serves on the Board of the Spanish Clay Society.

Preface

Welcome to the second edition of the Special Issue on Geomaterials: Latest Advances in Materials for Construction and Engineering Applications. It has been a privilege to once again serve as the Guest Editor for this collection, which confirms the growing scientific and technological interest in geomaterials and their essential role in addressing current societal challenges.

Although often taken for granted, geomaterials underpin modern civilization. They constitute the basis of buildings, transport infrastructure, geotechnical works and environmental engineering systems, while also supporting a wide range of industrial applications. Their importance has become even more evident in recent years, as the transition towards more sustainable construction practices and circular economy strategies has intensified the search for innovative geomaterials with improved technical and environmental performance.

The articles gathered in this Special Issue reflect the diversity and vitality of current research in the field. They explore topics ranging from sustainable cementitious materials and alkali-activated systems to waste valorization, industrial by-products, soil improvement and mineral-based technologies, illustrating how geomaterials continue to evolve in response to the demands of a changing world. Collectively, these contributions reinforce the idea that reducing environmental impacts while maintaining or improving engineering performance is not only possible but increasingly achievable.

I would like to express my sincere gratitude to all the authors who contributed their excellent research, as well as to the reviewers for their valuable time, expertise and constructive comments, which have undoubtedly enhanced the quality of this volume. I also wish to thank the editorial team for their continuous support throughout the publication process.

Finally, I hope this Special Issue provides readers with valuable scientific insights while encouraging further research and innovation in the field of geomaterials. I also hope that the concept of technite, introduced in the accompanying Editorial, stimulates discussion on the long-term geological significance of human-made lithic materials and their potential role within a circular economy. As geomaterials have accompanied the development of humankind throughout history, they will undoubtedly continue to play a fundamental role in building a more sustainable future.

José Manuel Moreno-Maroto
Guest Editor

applied sciences

MDPI

Editorial

Present Insights and Future Prospects on Geomaterials: Introducing the Concept of Technite

José Manuel Moreno-Maroto

Department of Geology and Geochemistry, Faculty of Sciences, Autonomous University of Madrid, Cantoblanco, 28049 Madrid, Spain; josemanuel.moreno@uam.es

Following the success of the first edition of the Special Issue "Geomaterials: Latest Advances in Materials for Construction and Engineering Applications", this second edition has followed the same course, confirming that research on geomaterials is more active than ever. In fact, Tyrer and Moreno-Maroto [1] introduced the relevance that geomaterials have had throughout history (even prehistory) showing that their development is inseparable from that of humankind; one cannot be understood without the other.

The truth is that while geomaterials have demonstrated functionality and high performance over the centuries, at times in a remarkably persistent manner, society at large has adopted them so naturally that the science and technology underpinning them is often forgotten, or rather unknown. In this sense, geomaterials sometimes seem to be relegated to the background in comparison to other types of materials which, due to their perceived "exoticism" or apparent "sophistication," may appear more attractive, even when their functionality, cost-effectiveness, applicability and future industrial scalability are not entirely evident.

Despite this, research aimed at developing improved geomaterials continues to grow, aligning perfectly with global strategies for sustainable development, climate change mitigation and circular economy. This is entirely reasonable, considering that activities associated with the production and application of geomaterials, generally linked to the construction and civil engineering sectors, are among those generating the greatest environmental impacts [2–4]. However, it must also be acknowledged that their socio-economic impact is highly positive, generating for instance a large number of jobs and a robust industrial network, among other benefits. In this regard, reducing environmental impacts while increasing socio-economic benefits can be complementary goals. In fact, although this approach has been pursued for decades, the paradigm shift towards more sustainable geomaterial production is increasingly demanded, for example, through energy optimization or the use of waste as a raw material, which in turn offers direct economic benefits to industries [2,4].

Therefore, everything points toward a promising future for geomaterials, with a trajectory of success that will continue to grow in parallel with the development of society itself.

As a final reflection, considering the mineral nature and long-term stability of many existing geomaterials, such as concrete, cement, ceramics and others, their persistence in the environment at the end of their service life may be extremely long. In this regard, and acknowledging their stone-like character, the term *technite* (technological rock) is proposed here to refer to this new class of human-made rocks that may emerge in the environment. The intention is not to replace or exclude the existing terms *artifact* or *technofossil*, which carry broader and, to some extent, controversial connotations by encompassing all kinds

of human-derived remnants within the geological record [5–8], but rather to propose a more specific concept that highlights their lithic nature and their potential to be reused as secondary inputs in the production of new geomaterials.

Conflicts of Interest: The author declares no conflict of interest.

References

1. Tyrer, M.; Moreno-Maroto, J.M. Geomaterials: Latest advances in materials for construction and engineering applications. *Appl. Sci.* **2023**, *13*, 9129. [CrossRef]
2. AMI2030. Materials 2030 Roadmap. Advanced Materials Initiative 2030. December 2022. Available online: https://prod5.assets-cdn.io/event/7788/assets/8344028155-dea5c531da.pdf (accessed on 10 December 2025).
3. European Commission. Internal Market, Industry, Entrepreneurship and SMEs. Construction Sector. 2023. Available online: https://single-market-economy.ec.europa.eu/sectors/construction_en (accessed on 10 December 2025).
4. European Commission. A New Circular Economy Action Plan for a Cleaner and More Competitive Europe (COM(2020) 98 Final). 2020. Available online: https://eur-lex.europa.eu/resource.html?uri=cellar:9903b325-6388-11ea-b735-01aa75ed71a1.0017.02/DOC_1&format=PDF (accessed on 10 December 2025).
5. Zalasiewicz, J.; Williams, M.; Waters, C.N.; Barnosky, A.D.; Haff, P. The technofossil record of humans. *Anthr. Rev.* **2014**, *1*, 34–43. [CrossRef]
6. Zalasiewicz, J.; Waters, C.N.; Ivar do Sul, J.A.; Corcoran, P.L.; Barnosky, A.D.; Cearreta, A.; Edgeworth, M.; Gałuszka, A.; Jeandel, C.; Leinfelder, R.; et al. The geological cycle of plastics and their use as a stratigraphic indicator of the Anthropocene. *Anthropocene* **2016**, *13*, 4–17. [CrossRef]
7. Chen, H.; Zou, X.; Ding, Y.; Wang, Y.; Fu, G.; Yuan, F. Are microplastics the 'technofossils' of the Anthropocene? *Anthr. Coasts* **2022**, *5*, 8. [CrossRef]
8. Gabbott, S.; Zalasiewicz, J. *Discarded: How Technofossils Will Be Our Ultimate Legacy*; Oxford University Press: New York, NY, USA, 2025; ISBN 978-0-19-286933-3.

Disclaimer/Publisher's Note: The statements, opinions and data contained in all publications are solely those of the individual author(s) and contributor(s) and not of MDPI and/or the editor(s). MDPI and/or the editor(s) disclaim responsibility for any injury to people or property resulting from any ideas, methods, instructions or products referred to in the content.

https://doi.org/10.3390/app16010172

applied sciences

MDPI

Article

Synergistic Preparation and Mechanistic Investigation of Full Industrial Solid Waste-Based Cementitious Materials for Aeolian Sand Stabilization

Zilu Xie, Zengzhen Qian *, Hao Wang, Yingzhe Qi and Bing Yue

School of Engineering and Technology, China University of Geosciences, Beijing 100080, China; 3002220008@email.cugb.edu.cn (Z.X.); 2102230104@email.cugb.edu.cn (H.W.); 2102230102@email.cugb.edu.cn (Y.Q.); yue@email.cugb.edu.cn (B.Y.)
* Correspondence: 2005011930@cugb.edu.cn

Abstract: Aeolian sand serves as the principal foundation material for construction in desert regions, yet its stabilization predominantly relies on cement, presenting critical carbon emission challenges. This study developed a cementitious material utilizing complementary industrial solid wastes (ISWs)—steel slag (SS), ground granulated blast-furnace slag (GGBFS), phosphorus slag (PS), and carbide slag (CS)—based on clinker three chemical moduli (TCM) and simplex lattice design, aiming to replace cement for aeolian sand stabilization. ISW dosage effects on stabilized sand strength and mechanical properties were investigated, with stabilization mechanisms studied via phase and microstructural analysis. Results demonstrated that GGBFS exerted the most significant positive influence on the strength of stabilized sand. The optimal proportion was determined as SS:GGBFS:PS:CS = 5:35:20:40, achieving strength comparable to cement-stabilized aeolian sand in the literature. The elastic modulus and ductility of stabilized sand exhibited linear positive and exponential negative correlation with uniaxial compressive strength. The hydration products of ISWs, including C(-A)-S-H gel and ettringite similar to clinker, effectively enhanced interparticle bonding strength and pore-filling capacity. ISW proportions governed the composition and distribution of hydration products, thereby modulating microstructural density and strength, ultimately dictating macroscopic performance variations. The conclusions provide an environmentally friendly solution for aeolian sand stabilization in desert regions.

Keywords: synergistic preparation; mechanistic investigation; cementitious materials; industrial solid wastes; aeolian sand

1. Introduction

In recent years, the intensification of desertification due to global climate change coupled with the increasing level of urbanization has necessitated the construction of numerous buildings on aeolian sand foundations [1–5]. In regions with extensive desert areas such as Northwest China, the Middle East and North Africa, the majority of new construction projects must address the geotechnical challenges posed by aeolian sand foundations [6–13]. However, aeolian sand is a special type of material characterized by excessive fluidity (angle of repose < 28°), negligible cohesion (<1 kPa in natural state), and a loose granular structure (void ratio > 0.65) [14–18]. These properties result in critically low bearing capacities and pronounced susceptibility to differential settlement under load, which significantly increase the difficulty of foundation construction and severely restrict engineering development in desert regions [19–22].

The traditional method for aeolian sand foundation treatment involves complete excavation and replacement with imported clay or crushed stone [23–25]. Unfortunately, although it can significantly enhance the bearing capacity of the foundation, the scarcity of replacement materials and the limited transportation conditions in remote deserts render this method costly [26]. By contrast, the in situ improvement of aeolian sand using cementitious materials to enhance its bearing capacity represents a more economical treatment method. Ordinary Portland Cement (OPC), as the most widely used inorganic cementitious material globally, has been a common curing stabilizer in past research and applications of aeolian sand stabilization. Previous studies demonstrate that the unconfined compressive strength (*UCS*) and shear strength of cement-stabilized aeolian sand exhibit positive correlations with cement content and curing age [20,27–29]. At an optimal water–cement ratio with 8–10% cement dosage, the 28-day *UCS* of stabilized aeolian sand exceeds 1.5 MPa [30], accompanied by a cohesive strength surpassing 90 kPa [26]. However, the decarbonization of limestone during OPC clinker production, coupled with fossil fuel combustion in kilns, results in substantial carbon emissions, which renders the application of OPC in the stabilization of aeolian sand increasingly incompatible with the carbon peaking and carbon neutrality goals.

Utilization of industrial solid wastes (ISWs) to develop cementitious materials as alternatives to OPC has been recognized as an environmentally sustainable soil stabilization strategy that effectively enhances soil bearing capacity while mitigating the challenges of ISW stockpiling, therefore garnering significant attention [31]. Similar to the OPC clinker, ISWs containing reactive calcium silicates (C_2S/C_3S) and calcium aluminates (C_3A) generate calcium (aluminate) silicate hydrate [C-(A)-S-H] gels under alkaline conditions, strengthening interparticle bonding to achieve stabilization performance comparable to or superior to OPC [32–35]. Current research has extensively investigated partial OPC replacement with fly ash (FA) [36–39] and ground granulated blast-furnace slag [40–43], accompanied by the progressive establishment of relevant standards. On the other hand, studies exploring the use of solid wastes such as steel slag [44–46], red mud (RM) [47–49], and desulfurized gypsum (DG) [50–52] to develop fully industrial solid waste-based cementitious materials (ISW-CMs) as complete replacements for OPC have also been reported. It is noteworthy that the oxide content and reactivity vary significantly among different ISWs, making it crucial to determine their proportions according to specific principles in order to optimize the strength and workability of ISW-CMs. However, current studies predominantly rely on empirical data and trial-and-error experiments, resulting in inefficiency and inconsistent performance.

In the production of the OPC clinker, to obtain the desired oxide proportions and subsequently achieve the targeted clinker properties, the admixture ratio of raw materials is adjusted through the use of the three chemical moduli (TCM), which encompass the silicon modulus (SM), iron modulus (IM), and lime saturation coefficient (KH) [53]. Nowadays, TCM have been extensively utilized in the quality control of the OPC clinker and also provide a design framework for the proportioning of raw materials in ISW-CMs. Studies have shown that the soft soil stabilized using ISW-CMs developed with TCM achieve comparable or even higher strength than that stabilized with OPC [53,54]. In addition, mixture experimental design based on the simplex lattice/centroid method is another approach to determine proportion, with advantages including a reduced number of experimental points, high prediction accuracy, and the ability to swiftly identify optimal proportion. This approach involves strategically designing a few experiments with varying proportions in a simplex of two or more dimensions to obtain a regression equation between the response values and raw material percentages. Consequently, the optimal proportion can be determined, and further investigation into the inherent relationship

between proportions and response values can be conducted. Currently, studies employing this method to develop ISW-CMs that simultaneously meet multiple property requirements have been reported [55,56].

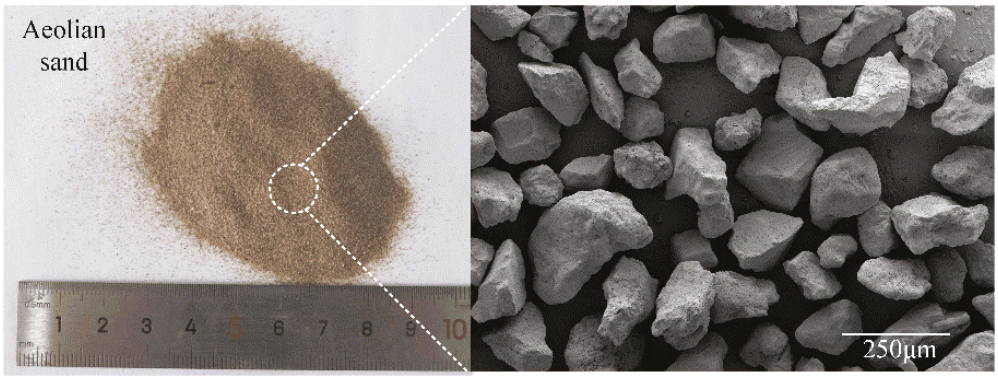
Despite numerous practical applications of ISW-CMs as an alternative to OPC for soil stabilization, the current literature primarily focuses on the stabilizing of clays with certain bearing capacity in their natural state. Research on aeolian sand, which exhibits inferior engineering properties and necessitates higher solidification demands, remains limited. Furthermore, trial-and-error-based development approaches for ISW-CMs frequently exhibit inefficiency and theoretical deficiencies, often yielding materials that fail to concurrently satisfy strength and workability requirements, thereby imposing significant barriers to their widespread implementation.

This study prepared a fully ISW-based cementitious material for stabilizing aeolian sand in desert regions using four complementary industrial solid wastes—blast-furnace slag (GGBFS), steel slag (SS), phosphorous slag (PS), and carbide slag (CS)—as raw materials. The TCM theory of the cement clinker and the simplex lattice design were used to systematically investigate the influence of ISW dosages on the *UCS* of stabilized aeolian sand and determine the optimal proportion of ISWs. Phase and microstructural analyses were employed to investigate the content of hydration products and their cementitious effects on particle bonding in aeolian sand stabilized with varying proportions of the cementitious materials. The findings provide novel insights and references for the development of ISW-based cementitious material for aeolian sand stabilization.

2. Materials and Methods

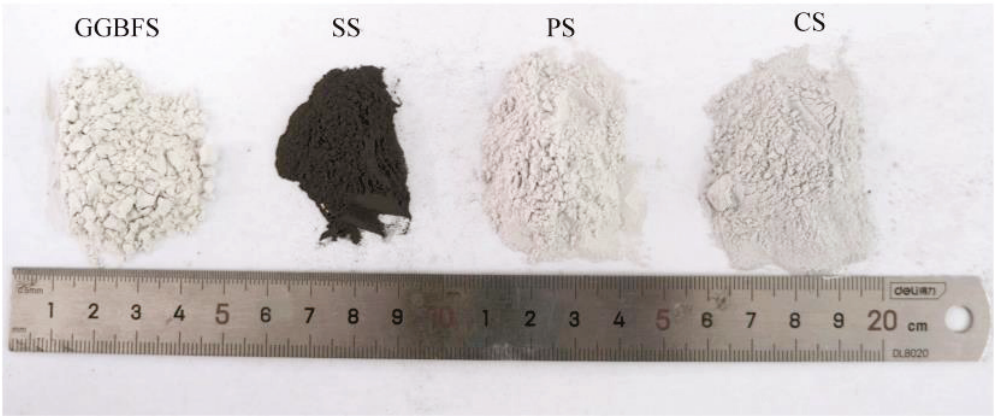
2.1. Materials

The aeolian sand utilized in this study was sourced from the Taklamakan Desert in Xinjiang, China. Sand samples were excavated from a depth of 1.5 m below the surface, immediately packed in sealed bags, and transported to the laboratory. Natural moisture content, bulk density, and porosity were measured in the laboratory, with these parameters detailed in our previously published work [30]. Figure 1a illustrates the natural morphology and microstructural characteristics of the untreated aeolian sand particles. Observations reveal that the aeolian sand particles exhibited angular to sub-rounded shapes with smooth surfaces and minimal fines content, indicating limited interparticle cohesion and weak natural cementation. Results of laser particle size analysis (LPSA, as shown in Figure 2) indicate that the limiting particle size d_{60} of aeolian sand was 345 μm, with uniformity coefficient C_u of 2.62 and curvature coefficient C_c of 0.88.



(**a**)

Figure 1. *Cont.*



(**b**)

Figure 1. Materials used in this study: (**a**) macro/microscopic morphologies of aeolian sand; (**b**) ISWs.

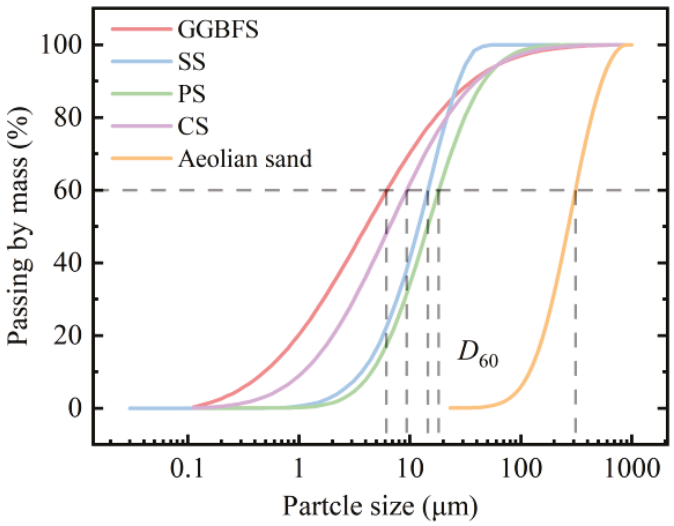


Figure 2. Particle size distribution of materials.

GGBFS employed in this study was provided by a mineral powder plant in Hebei, China. As shown in Figure 1b, the GGBFS appears as a pale powder with a specific surface area of approximately 0.43 m^2/g, produced by crushing and grinding waste slag generated during blast-furnace iron smelting. The d_{60}, C_u, and C_c of GGBFS were measured as 6.31 μm, 12.6, and 1.0, respectively. X-ray fluorescence (XRF) spectroscopy results (Table 1) reveal that the primary oxides in GGBFS are SiO_2 and CaO (30% and 40%, respectively), along with minor Al_2O_3 (14%) and MgO (8%). These oxides predominantly exist as amorphous glassy phases with weak intermolecular bonding due to the rapid cooling rate during discharge, thereby endowing the material with high pozzolanic reactivity.

Table 1. Chemical composition of materials.

Material	SiO_2	CaO	Fe_2O_3	Al_2O_3	MgO	SO_3	Na_2O	K_2O
OPC	20.24	60.93	3.58	5.26	3.66	2.68	1.19	1.13
SS	17.18	30.01	29.1	8.43	4.41	0.62	0	0.01
GGBFS	30.07	38.22	0.88	16.50	8.33	2.08	0.51	0.86
PS	44.89	43.97	0.01	3.88	3.72	0	0.05	0.84
CS	2.72	70.35	1.03	0.89	0.62	0	0	0

SS and PS are two additional ISWs employed to provide reactants for pozzolanic reactions. Coarse SS and coarse PS were collected from a steel plant and a phosphate chemical plant in Henan, China, respectively. In the laboratory, the coarse slags were milled into black and white powder, respectively, via high-energy ball milling and fully passed through a 150-mesh sieve (aperture size: 106 μm). The elevated temperature generated during this process evaporated residual moisture in the raw materials. The d_{60}, C_u, and C_c of SS were 15.1 μm, 4.08, and 1.0, respectively, while those of PS were 17.9 μm, 3.9, and 1.13, respectively. XRF results revealed that SS contains 30% CaO and 30% Fe_2O_3, along with 17% SiO_2, while PS is composed of 40% SiO_2 and 40% CaO, with minor contributions from other oxides. These compositions enabled precise modulation of the oxide ratios within the binder system.

CS was a by-product generated during acetylene production via calcium carbide hydrolysis. The employed CS in this study was collected from an acetylene chemical plant in Hebei, China, presented as white powder. Results of LPSA indicated that d_{60}, C_u and C_c of CS were 10.0 μm, 9.1, and 0.87, respectively. Chemical composition analysis identified it as comprising 70% CaO with trace impurities of silicon- and iron-phase compounds. In the binder system, CS primarily functions as a CaO supplement to enhance alkalinity due to its high CaO content.

2.2. Specimen Design

The proportioning design of ISWs in stabilized aeolian sand specimens was programmed according to the following steps: (a) determination of a basic dosage based on TCM of OPC; (b) establishment of the ISW dosage range using the basal dosage as a reference point; and (c) configuration of experimental points by defining the dosage range's supper and lower limits within the simplex lattice design framework.

The reference OPC, compliant with Chinese Portland cement standards [57] and supplied by China United Cement Corporation, was used to determine the basic proportion of ISWs through TCM methodology. Based on the oxide composition of the clinker (SiO_2, Al_2O_3, Fe_2O_3, and CaO as listed in Table 1), its TCM were calculated using Equations (1)–(3), yielding values of SM = 2.29, IM = 1.47, and KH = 0.91. By integrating the oxide compositions of ISWs, a quaternary linear equation system (Equation (4)) was formulated. In Equation (4), rows of the coefficient matrix represent oxide contents within ISWs, while columns correspond to distinct oxide components. The right-hand vector denotes the required oxide quantities to achieve TCM equivalence with the reference OPC. As a result, the basic proportion of ISWs was determined as SS:GGBFS:PS:CS = 10.0:18.1:26.8:57.1.

$$SM = \frac{SiO_2}{Al_2O_3 + Fe_2O_3}, \tag{1}$$

$$IM = \frac{Al_2O_3}{Fe_2O_3}, \tag{2}$$

$$KH = \frac{CaO - 1.65Al_2O_3 - 0.35Fe_2O_3}{2.8SiO_2}, \tag{3}$$

$$\begin{cases} 17.18m_{SS} + 31.07m_{GGBFS} + 44.89m_{PS} + 2.31m_{CS} = 20.24 \\ 30.01m_{SS} + 38.22m_{GGBFS} + 43.97m_{PS} + 70.35m_{CS} = 60.93 \\ 29.1m_{SS} + 0.88m_{GGBFS} + 0.01m_{PS} + 1.03m_{CS} = 3.58 \\ 8.43m_{SS} + 16.5m_{GGBFS} + 3.88m_{PS} + 0.89m_{CS} = 5.26 \end{cases} \tag{4}$$

where m_i stand for dosages of ISWs i.

The experimental determination of cementitious material for aeolian sand stabilization constitutes a typical mixture design with specific constraints requiring the summation

of all component dosages to equal 100%. The simplex lattice method (SLM) serves as a conventional framework for such experimental configurations. Given that the binder developed in this study comprises four types of ISWs, the experimental points were distributed within a regular tetrahedron, as illustrated in Figure 3, where each axis represents a distinct ISW component and each vertex corresponds to a specific proportion. The lattice degree of SLM was specified as three, establishing three compositional levels for each ISW, and the design was augmented with axial points and centroid point. A total of 26 test specimens were designed, comprising 25 SLM-designed proportions and one basic proportion. Additionally, the binder content was set at 11% of the aeolian sand mass, while water content was set at 9%, which has the maximum stabilization aeolian sand strength according to previous study [30]. The proportion of experiment points is listed in Table 2. Additionally, to compare the effectiveness of ISW-CMs and cement in stabilizing aeolian sand, a control group utilizing cement with an equivalent dosage was established.

Table 2. Proportion of ISWs in design experiment points.

No.	Proportion of ISWs (%)			
	SS	GGBFS	PS	CS
1	30.0	10.0	20.0	40.0
2	21.7	18.3	20.0	40.0
3	21.7	10.0	28.3	40.0
4	21.7	10.0	20.0	48.3
5	13.3	26.7	20.0	40.0
6	13.3	18.3	28.3	40.0
7	13.3	18.3	20.0	48.3
8	13.3	10.0	36.7	40.0
9	13.3	10.0	28.3	48.3
10	13.3	10.0	20.0	56.7
11	5.0	35.0	20.0	40.0
12	5.0	26.7	28.3	40.0
13	5.0	26.7	20.0	48.3
14	5.0	18.3	36.7	40.0
15	5.0	18.3	28.3	48.3
16	5.0	18.3	20.0	56.7
17	5.0	10.0	45.0	40.0
18	5.0	10.0	36.7	48.3
19	5.0	10.0	28.3	56.7
20	5.0	10.0	20.0	65.0
21	11.3	16.3	26.3	46.3
22	20.6	13.1	23.1	43.1
23	8.1	25.6	23.1	43.1
24	8.1	13.1	35.6	43.1
25	8.1	13.1	23.1	55.6
26	10.0	18.1	26.8	57.1
CE	-	-	-	-

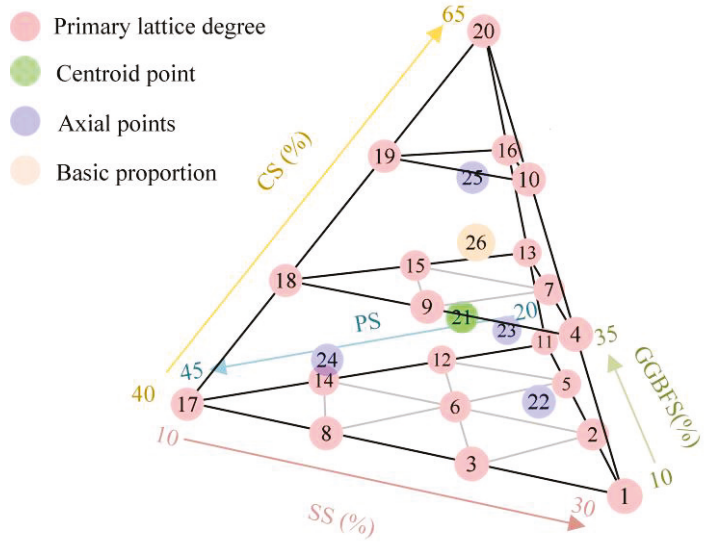


Figure 3. Distribution of experiment points.

2.3. Specimen Preparation

The specimens of stabilized aeolian sand were prepared in accordance with American standards [58]. ISWs and aeolian sand were oven-dried at 105 °C for 6 h to eliminate absorbed moisture, followed by precise weighing according to the designed proportion. The blended ISWs were initially homogenized using a planetary mixer, until uniform coloration was achieved. Subsequently, the aeolian sand was incrementally introduced into the mixture until visual homogeneity was re-established. Distilled water was then added in a controlled stream, followed by high-speed mixing for an additional 5 min.

The homogenized mixture was transferred via funnel into stainless-steel cylindrical molds (50 mm in diameter × 100 mm height) and compacted in three successive layers. Each layer underwent 15 compactive blows using a stainless-steel tamper, applied radially from the periphery inward, with interlayer surface scarification to enhance bonding. Then, the top surfaces were immediately sealed with laboratory-grade polyethylene sealing film to prevent moisture dissipation. After 3 days of in-mold curing, the specimens were demolded and transferred to a humidity-controlled curing chamber maintained at 23 °C for continued curing over 25 days, achieving a total curing time of 28 days. Three parallel samples were prepared for each experiment points.

2.4. UCS Test

UCS of stabilized aeolian sand specimens was evaluated using an electronically universal compression testing machine. This apparatus employs a hydraulic jack-driven link rod to vertically displace specimens against pressure sensor (10 kN capacity, ±0.001 kN accuracy). A displacement sensor integrated with the link rod recorded real-time specimen deformation. The load was applied under displacement control, commencing at 0.1 mm/min until the sensor registered 0.5 kN, confirming proper specimen–sensor contact. The loading rate was then reduced to 0.08 mm/min for the formal test phase. Specimen failure was defined as a post-peak force reduction exceeding 30% of the maximum recorded load, at which point testing was terminated. Failed specimens were subsequently milled, oven-dried, and stored in sealed bags for subsequent analysis.

2.5. X-ray Diffraction Analysis

X-ray diffraction (XRD) was employed to analyze the phase composition of solidified aeolian sand, utilizing a D8 Advance X-ray diffractometer (Bruker, Hongkong) with Cu Kα

radiation generated at 60 kV and 80 mA. The scanning range was set from 15° to 80°, with a step size of 0.02°/step and a scanning speed of 30 steps/s.

2.6. Scanning Electron Microscope

The microstructure of stabilized eolian sand was observed using an SU8220 field emission scanning electron microscope (SEM, HITACHI High-tech Co., Tokyo, Japan) with the voltage set at 5 kV. Due to the poor electrical conductivity of both eolian sand and ISWs (immobilized sand–water mixtures, presumably), gold sputtering was performed on the sample surfaces for 2 min with a current of 10 mA using an ion sputter coater prior to observation. Additionally, energy dispersive spectroscopy (EDS) mapping was employed to determine the elemental composition of the observed materials.

2.7. Thermogravimetric Analysis and Differential Scanning Calorimetry

The hydrated products and thermal stability of stabilized aeolian sand samples were analyzed using Thermogravimetric Analysis/Differential Scanning Calorimetry (TG/DSC) with an SDT Q600 synchronous thermal analyzer (TA Instruments Inc., New Castle, DE, USA). A 10 mg powder sample was first stabilized at room temperature for 30 min and then heated to 800 °C at a rate of 10 °C/min under a nitrogen atmosphere. During the heating process, the curves of sample weight and heat flow as a function of temperature were recorded.

3. Results and Analysis

3.1. Stress–Strain Response

Figure 4a–e present the stress (σ)–strain (ε) curves for all specimens, and Figure 4f demonstrates a typical characteristic of the σ–ε curve. It can be observed that, at the initial stage of loading, the curves undergo a relatively short phase with increasing slope, reflecting the gradual enhancement of the specimen resistance to deformation due to being progressively compressed and densified. The slope of the curves gradually stabilizes as the load increases, representing the elastic phase of the specimens. Subsequently, the curves become nonlinear again and reach a peak. Finally, the curves begin to decline, indicating that the specimens have lost their load-bearing capacity, which is accompanied by the appearance of obvious shear cracks on specimens. Based on these characteristics, the *UCS* of the specimens was determined as the stress corresponding to the peak of the curve; the elastic modulus E was calculated as the ratio of the change in stress ($\Delta\sigma$) to the change in strain ($\Delta\varepsilon$) during the stable slope phase; and the ductility *DI* was taken as the ratio of the strain at failure (ε_f) to the peak strain (ε_u). The *UCS*, E, and *DI* of test specimens are summarized in Table 3.

Table 3. *UCS*, E and *DI* of test specimens.

No.	*UCS* (MPa)	E (MPa)	*DI*
1	0.45	63	1.26
2	0.97	114	1.08
3	0.43	76	1.28
4	0.34	44	1.16
5	1.14	127	1.09
6	0.90	114	1.12
7	0.85	89	1.09
8	0.64	76	1.22
9	0.43	50	1.23
10	0.33	39.7	1.24

Table 3. *Cont.*

No.	*UCS* (MPa)	*E* (MPa)	*DI*
11	1.55	127	1.09
12	1.51	147	1.10
13	1.23	114	1.09
14	1.19	133	1.12
15	0.81	116	1.19
16	0.82	135	1.23
17	1.06	122	1.09
18	0.51	55	1.14
19	0.43	74	1.20
20	0.27	41	1.31
21	0.95	122	1.19
22	0.51	76	1.26
23	1.34	159	1.08
24	0.71	94	1.27
25	0.53	58	1.44
26	0.82	106	1.10
CE	1.50	139	1.03

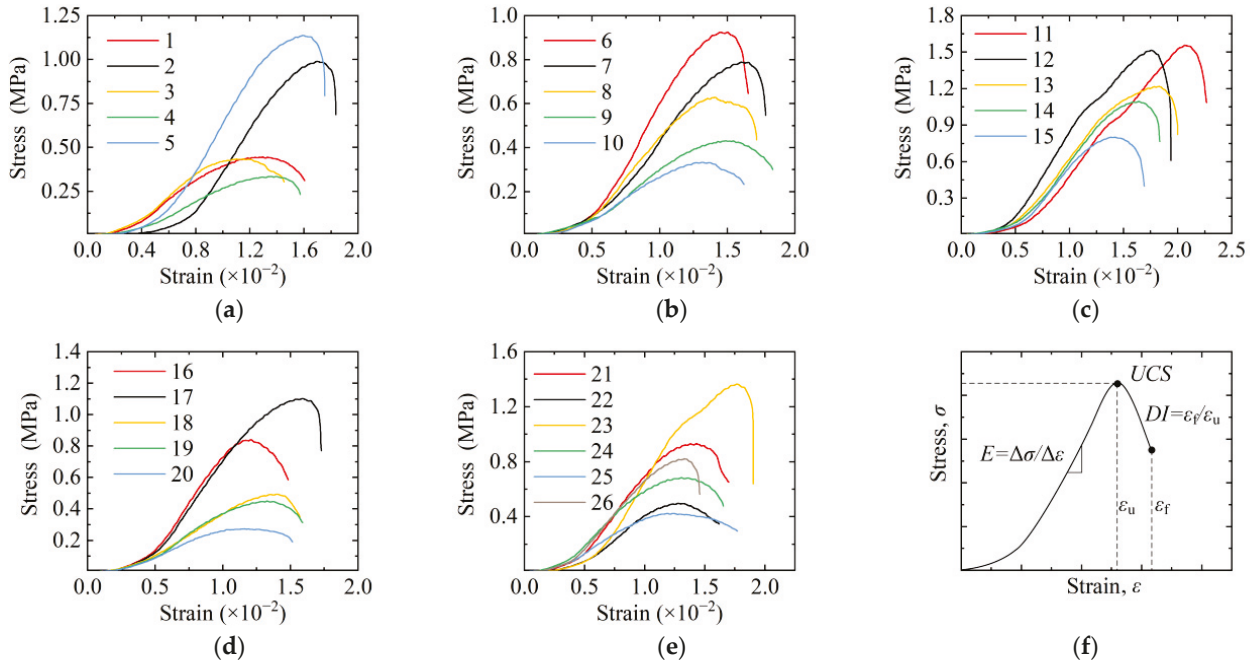


Figure 4. Stress–strain curves of test specimens: (**a**) 1–5, (**b**) 6–10, (**c**) 11–15, (**d**) 16–20, (**e**) 21–26, and (**f**) typical characteristic of σ–ε curve.

3.2. Effect of Proportion of ISWs on UCS and the Optimal Proportion

The ternary plot in Figure 5 illustrates the variation in the *UCS* of stabilized aeolian sand with the proportions of ISWs, where the name of ISWs represents their dosages. Since four types of ISWs were utilized as raw materials in this study and a single ternary plot can only accommodate three variables, to depict their synergistic effects and mutual influences, each ternary plot fixes one variable at a specific level. Subsequently, the changes in *UCS* with respect to the other three variables are investigated for different levels of the fixed variable.

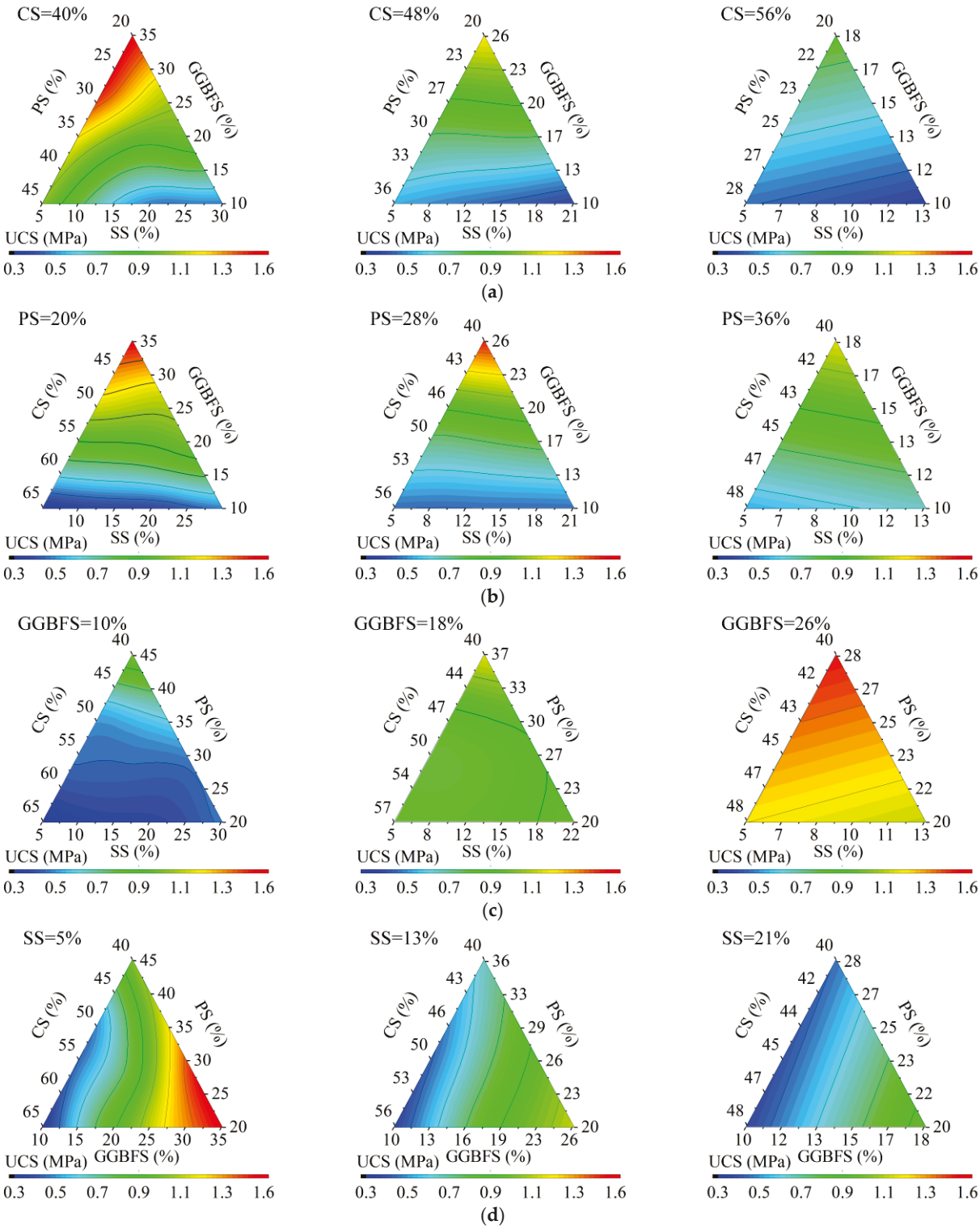


Figure 5. Effect of proportion of ISWs on *UCS* of stabilized aeolian sand, where fixed factor is (**a**) CS, (**b**) PS, (**c**) GGBFS, and (**d**) SS.

The fixed factor of Figure 5a is CS. It can be observed that, regardless of the CS dosages, the *UCS* of stabilized aeolian sand increases with the increment in the GGBFS dosage but decreases with the increase in PS and SS dosages. When the CS dosage is 40%, the *UCS* of stabilized aeolian sand reaches its maximum value at a PS dosage below 30% and GGBFS dosage above 32%, while the SS dosage above 17% leads to a significant decrease in *UCS*. When the CS content is increased to 48.3% and 56.7%, the changes in *UCS* become more

pronounced, and the contour lines gradually become perpendicular to the GGBFS axis, indicating that the influence of the GGBFS dosage on *UCS* is most significant at these levels. The main chemical component of CS is CaO, and changes in its dosage can alter the alkalinity of the system. The increase in alkalinity caused by an increase in CS dosage may be the reason why the influence of GGBFS becomes more significant.

In Figure 5b, with PS serving as the fixed factor, the variation trend of *UCS* of stabilized aeolian sand is similar to that observed when the dosage of is fixed. However, it exhibits a slight increase with the elevation of SS dosage. This trend becomes more pronounced when the PS dosage reaches 21.6%. This can be explained by the fact that a higher PS dosage limits the incorporation of GGBFS with the highest reactivity. At this point, increasing the SS dosage can, to a certain extent, supplement the reactants for the pozzolanic reaction. Nevertheless, due to the inherently low reactivity of SS, it fails to elicit particularly significant changes in strength. Meanwhile, an increase in CS leads to a notable decrease in *UCS*, indicating that excessively high alkalinity is detrimental to the strength of stabilized aeolian sand.

The fixed factor of Figure 5c is GGBFS. It can be indicated that the *UCS* of stabilized aeolian sand increases with the elevation of PS dosage. Notably, when the GGBFS dosage reaches 18%, a CS content higher than 47% (with SS dosage less than 12% and PS dosage less than 30%) results in a rapid decline in *UCS*. This is attributed to the fact that both PS and GGBFS, which serve as reactants for the pozzolanic reaction, are present at relatively low levels at this point, and CaO constitutes the majority of CS, with its hydration product almost exclusively $Ca(OH)_2$, which leads to an excessively high alkalinity in the system and a relative scarcity of hydration products with a gelling effect.

SS serves as the fixed factor in Figure 5d. It can be observed that, regardless of the level of SS, the influence pattern of the proportion of the other three ISWs on the strength of stabilized aeolian sand remains consistent. Specifically, the *UCS* increases with the increase in GGBFS dosage but decreases with the increase in PS and CS dosages. This is because the primary role of SS in the system is to provide Fe_2O_3, which is one of the precursors of C_4AF and mainly affects the working properties of the cementitious material rather than its strength.

The analysis above elucidates a prevailing pattern in experiment results: the incremental dosage of GGBFS substantially enhances the strength of stabilized aeolian sand. This phenomenon primarily stems from GGBFS's superior pozzolanic reactivity compared to other investigated ISWs, attributable to its vitreous microstructure containing reactive compounds that readily participate in hydration processes. PS demonstrates comparatively lower reactivity, while SS exhibits the least reactive characteristics. These observations suggest that the exclusive utilization of GGBFS could theoretically yield cementitious materials with maximum compressive strength. However, practical engineering considerations regarding the workability of cementitious composites and long-term stability of stabilized aeolian sand necessitate maintaining oxide proportions within reasonable ranges. Therefore, through dual optimization employing TCM theory and SLM, the optimal proportion of ISWs used to stabilize aeolian sand was determined as 5:35:20:40, which corresponds to the specimen exhibiting the highest *UCS* in SLM experiments. Furthermore, comparative analysis with the cement-stabilized aeolian sand control group (CE) revealed that the *UCS* of aeolian sand that stabilized ISW-CMs with the basic proportion was 45% lower than that of CE, whereas the ISW-CMs with optimal proportion stabilized specimen exhibited a 3% strength enhancement over CE. This demonstrates the following: (a) the proportion determined by the dual optimization strategy incorporating TCM and the SLM was superior than that determined solely by TCM; (b) synergistically prepared ISW-CMs achieve comparable effectiveness to cement in aeolian sand stabilization.

3.3. Mechanical Properties of Stabilized Aeolian Sand

The elastic modulus *E* and ductility coefficient *DI*, derived from stress–strain curves, were employed to quantify the specimen's deformation resistance during the elastic phase and post-failure ductility. Figure 6 illustrates the variations in E and *DI* with *UCS* for specimens in SLM experiments. The results reveal a positive correlation between the strength of stabilized aeolian sand and its elastic modulus. Specimens with higher *UCS* values exhibited a rapid increase in deformation resistance following the compaction phase, typically accompanied by pronounced shear-induced cracks at failure. This enhancement is attributable to two synergistic mechanisms: (1) the abundance of cementitious compounds reinforcing interparticle bonds and (2) the presence of high-hardness crystalline phases (e.g., ettringite), which fill intergranular voids and inhibit particle displacement. These microstructural features collectively improve the cohesion and friction angle along shear planes.

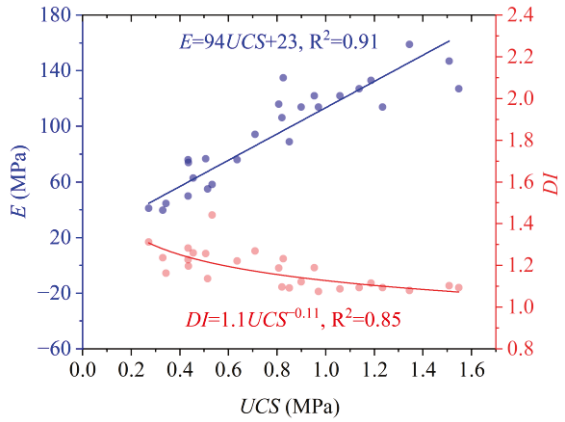


Figure 6. Variations in E and *DI* with *UCS* for specimens.

Conversely, ductility inversely correlated with strength. Specimens with lower *UCS* displayed broader stress–strain curve peaks, characterized predominantly by axial splitting fractures parallel to the specimen axis. This behavior arises from two factors: (1) reduced cumulative strain energy under lower loads, resulting in gradual post-peak stress dissipation and (2) diminished hydration products, leading to weaker particle bonding and more micropores (a critical contributor to splitting failure modes). After specimen failure, the partial closure of these micropores generates residual strength, thereby decelerating the descending phase of stress–strain curves.

The quantitative relationships between *UCS* and the mechanical parameters can be mathematically expressed by linear and exponential functions, respectively, as shown in Figure 6.

3.4. Phase Composition and Microstructure

Figure 7 presents the XRD patterns of selected specimens from the SLM experiments along with their corresponding *UCS* values and ISW proportions (SS:GGBFS:PS:CS). Significant variations in phase composition were observed among specimens with different ISW proportions. The characteristic diffraction peak around $2\theta = 29.5°$, attributed to C(-A)-S-H gel formation, is recognized as the primary contributor to the strength development of aeolian sand consolidation. Specimens NO. 4 and NO. 8 with low *UCS* demonstrated attenuated C(-A)-S-H gel diffraction intensities. In contrast, specimens NO. 12 and NO. 11 with higher mechanical performance displayed enhanced peak intensities at this position, with specimen NO. 11 manifesting an additional characteristic peak, which indicates the increased gel formation—a phenomenon consistent with its elevated GGBFS content.

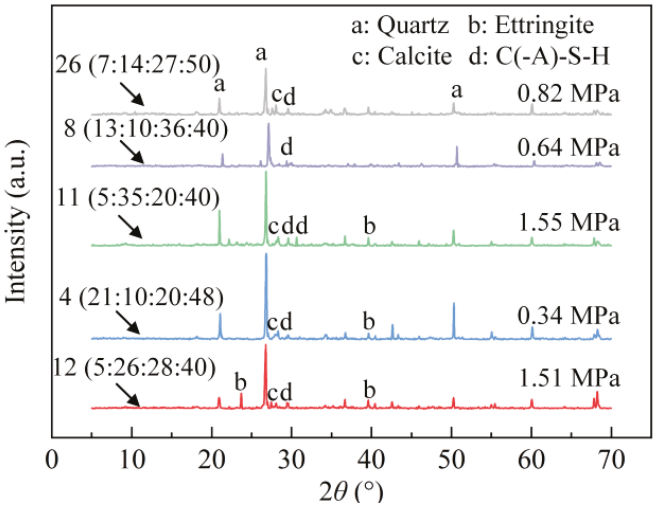


Figure 7. XRD patterns of specimens in SLM experiment.

Ettringite diffraction peaks at 2θ = 40° were detected in all specimens except specimen NO. 8, with specimen NO. 12 exhibiting supplementary ettringite-related peaks. This absence in specimen NO. 8 may be attributed to its higher SS content and reduced CS proportion, resulting in excessive Fe-phase oxides and diminished alkalinity within the system. These conditions potentially inhibited the synthesis of ettringite through the reaction pathway described in Equation (5):

$$C_3A + 3(CaSO_4 \bullet 2H_2O) + 2Ca(OH)_2 + 24H_2O \rightarrow 3CaO \bullet Al_2O_3 \bullet 3CaSO_4 \bullet 32H_2O \quad (5)$$

Additionally, characteristic peaks of calcite ($CaCO_3$) were identified, with their formation attributed to the carbonation of $Ca(OH)_2$ during the curing process. Similar to ettringite, calcite contributes to strength enhancement by filling the pores between particles and increasing the density of stabilized aeolian sand. The highest calcite peak intensities were observed in Specimens NO. 4, 11, and 26, while its diminished presence in Specimen NO. 8 correlates with the absence of CS. However, despite their pronounced calcite content, Specimens NO. 4 and 26 exhibited suboptimal mechanical performance. This phenomenon may stem from the formation of weaker particle connections by the limited amount of C(-A)-S-H gel, which could be disrupted by the volumetric expansion caused by excessive calcite crystal generation.

Figure 8 displays the TG and DSC curves of selected specimens in the SLM experiment. The TG curve quantifies mass loss during heating, enabling the clear comparison of hydrated phase contents across specimens due to distinct decomposition temperatures of different hydration products. Concurrently, the DSC curve monitors the heat flux differential between the sample and reference, providing insights into endothermic and exothermic events within the material. The combined analysis of TG-DSC data enhances the characterization of ISW hydration products in stabilized aeolian sand. Three prominent thermal mass loss stages can be observed in Figure 8: (a) 60–120 °C: Attributed to the loss of bound water from hydration products such as C(-A)-S-H gel and ettringite, corresponding to the P1 endothermic peak in the DSC curve; (b) 380–500 °C: Associated with hydroxyl group removal from $Ca(OH)_2$ in the matrix, marked by the P2 endothermic peak; and (c) 600–720 °C: Corresponding to the decomposition of carbonate phases (e.g., calcite). Specimens with lower *UCS* such as specimens NO. 4 and 8 exhibited reduced mass loss and diminished peak areas in the first stage, indicative of limited gel and ettringite formation. Notably, Specimen NO. 4 demonstrated significantly higher mass loss in the second stage, consistent with its elevated CS content, which also contributed to enhanced thermal decomposition

(third-stage mass loss and peak area). Conversely, Specimen NO. 4 displayed minimal third-stage mass loss, likely due to suppressed carbonation during curing, resulting in diminished calcite production.

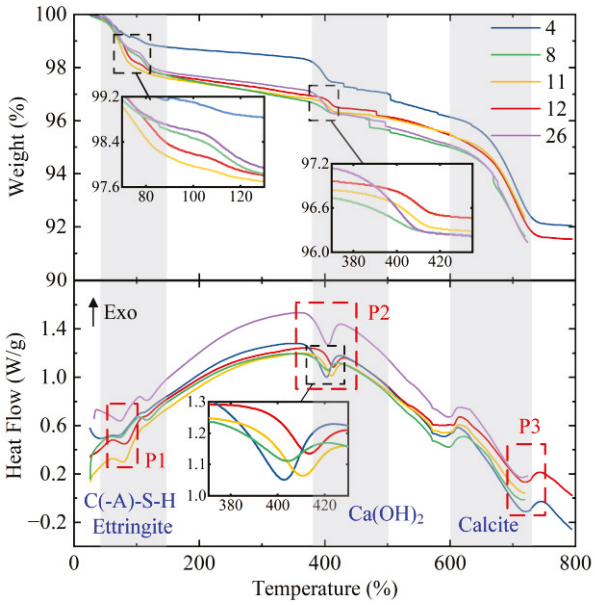


Figure 8. TG and DSC curve of specimens in SLM experiment.

The TG/DSC results, corroborated by XRD analysis, collectively demonstrate that Specimen No. 11 achieved superior mechanical performance through optimized hydration product, validating its ISW proportion as the most effective composition.

Figure 9 presents the particle morphology of Sample No. 11 observed using SEM. Figure 9a demonstrates a typical characteristic of aeolian sand particles encapsulated by cementitious materials. Through comparative analysis with untreated aeolian sand particles shown in Figure 1, it can be observed that a dense layer of hydration products composed of gel and ettringite thoroughly coats the particle surface. At 500× magnification, neither distinct pores nor the original surface texture of soil particles can be clearly discerned; however, small and shallow pores became discernible upon magnification to 5000×. This observation corresponds to the higher gel production detected in the phase analysis of this specimen, as well as the elevated GGBFS dosage and enhanced *UCS* observed at macroscopic scale. Figure 9b illustrates the interconnections formed between multiple soil particles through hydration products. As previously discussed, the natural aeolian sand exhibits a loose microstructure with minimal interparticle bonding under untreated conditions, resulting in load-bearing capacity that relies solely on mechanical interlocking. After stabilization using ISW-based cementitious materials, multiple particles encapsulated by gel and other hydration products gradually establish stable connections during compaction and curing processes. The matrix of these connections primarily consists of C(-A)-S-H gel, internally reinforced by crystalline phases including ettringite, $Ca(OH)_2$, and calcite, which collectively provide robust structural support. However, a limited quantity of unhydrated ISW particles can still be detected under high magnification, which may be attributed to the weak hydration activity of specific ISW components. These findings exhibit similarities with previously reported microstructures of cement-stabilized aeolian sand. Nevertheless, compared to the porous interparticle connections observed in cement-treated specimens, the ISW-stabilized aeolian sand demonstrates significantly denser and more compact bonding configurations. This evidence confirms that ISW cementitious materials can establish a more reliable and higher-strength microstructure at the microscopic scale.

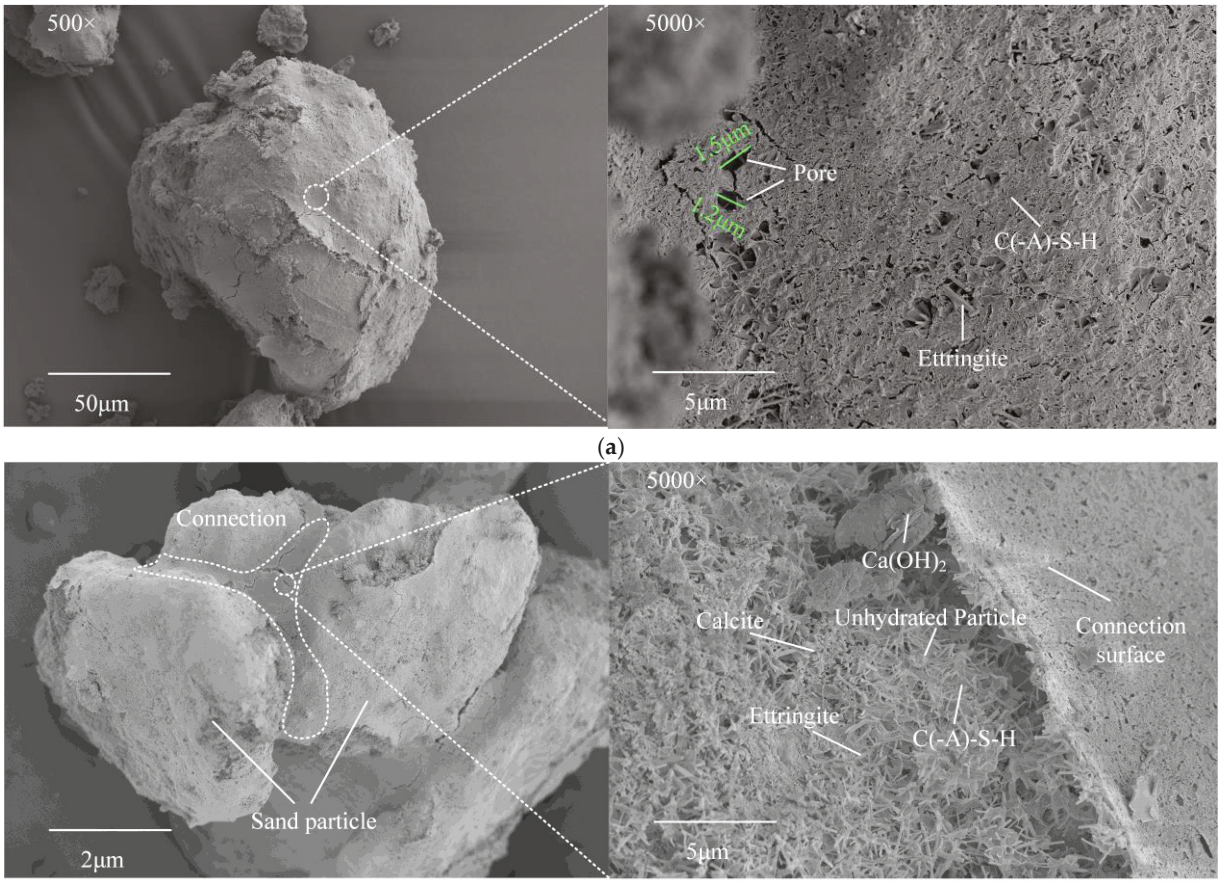


Figure 9. Particle morphology of Sample No. 11. (**a**) aeolian sand particles encapsulated by cementitious materials; (**b**) connection between sand particles.

For comparative analysis, Figure 10 exhibits the microstructural morphologies of lower-strength specimens No. 4, 8, and 26, through which the influence of ISW proportions on the microstructure of stabilized aeolian sand can be systematically elucidated. In Figure 10a, depicting the particle encapsulation status of Specimen No. 4, it is evident that, although hydration products such as gel and ettringite were generated, the particle surfaces were merely covered by an exceedingly thin layer, leaving the significant exposure of sand particle surfaces. Upon further magnification to 10,000×, the C(-A)-S-H gel predominantly exhibited flocculent structures with limited spatial coverage and short filament lengths, cementing sparse ettringite and $Ca(OH)_2$ crystals. Unlike the integrated matrix observed in Specimen No. 13, these hydration products failed to form a continuous network, while unhydrated ISW particles were ubiquitously distributed. Such microstructural configurations resulted in feeble interparticle connections prone to external load-induced damage, ultimately manifesting as substantially reduced bearing capacity at the microscopic scale.

Figure 10b illustrates the particle surface morphology of Specimen No. 8. Although the hydration product layer appeared thicker compared to Specimen No. 4, the residual exposure of sand particle surfaces was still detected. At higher magnification, localized interconnected systems of gel–ettringite–calcium hydroxide were partially observable; however, the scarcity of the gel matrix rendered such systems spatially limited, with unbonded ettringite crystals persisting. This trend correlates with the increased hydration reaction products induced by reduced SS and elevated GGBFS and PS dosages, corresponding macroscopically to a marginal increase in *UCS*. Furthermore, this progressive trend persists in the microstructural morphology of Specimen No. 26 shown in Figure 10c. A substantial

interconnected network of hydration products was observed, with minimal independent ettringite or $Ca(OH)_2$ crystals detectable even under high magnification. Nevertheless, excessive CS dosage in this specimen constrained gel production, resulting in comparatively porous and sparse particle encapsulation relative to Specimen No. 11. Trace amounts of unhydrated ISW particles were also identified, collectively contributing to its inferior mechanical performance.

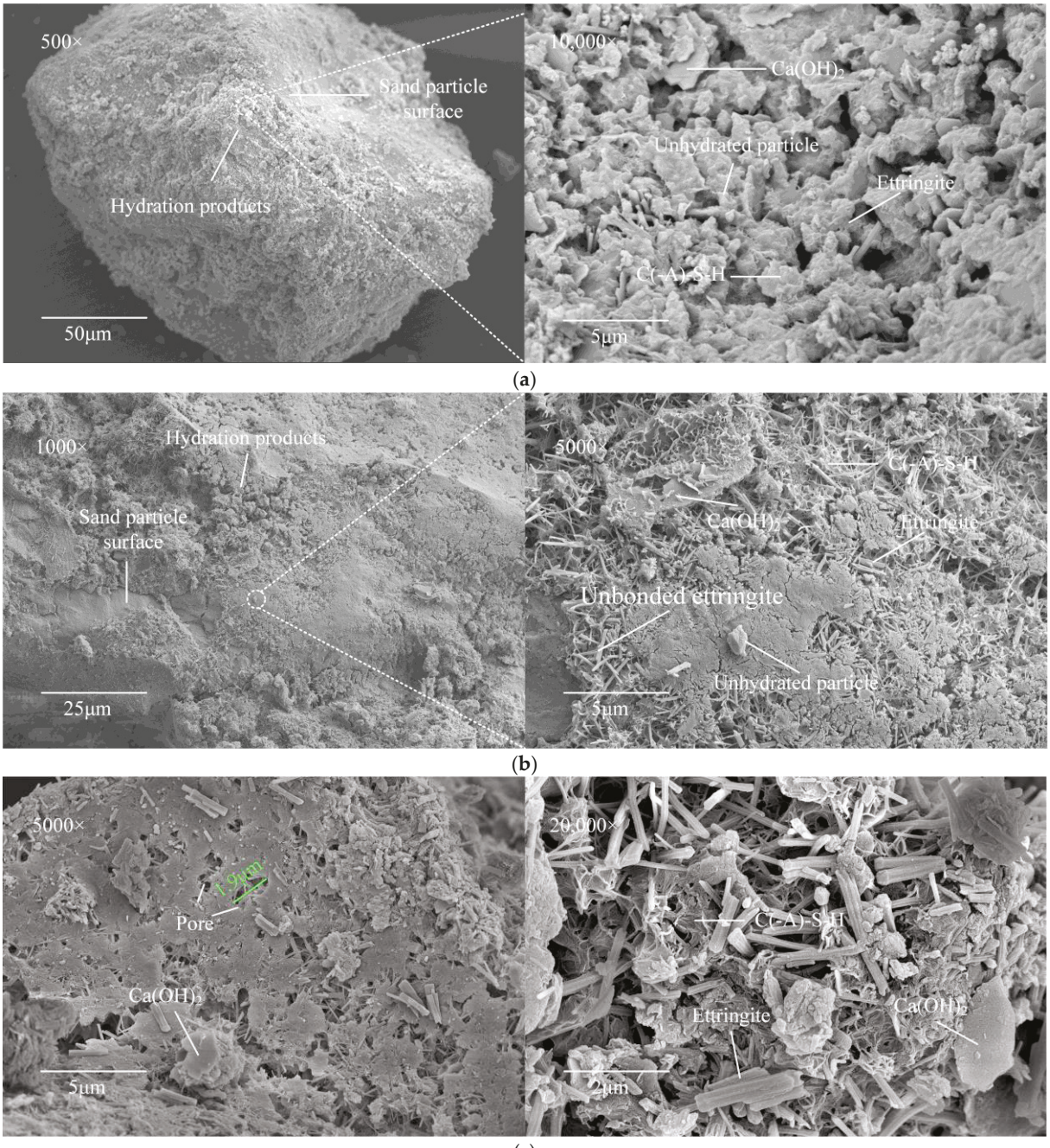


Figure 10. Particle morphology of sample with low strength: (**a**) specimen No. 4; (**b**) specimen No. 8 and (**c**) specimen No. 26.

4. Discussion

4.1. Analysis of ISW Interactions and Hydration Phase Quantification

The synergistic interplay between SS, GGBFS, PS, and CS in hydration reactions critically governs the mechanical performance of stabilized aeolian sand. As evidenced by

the chemical compositions in Table 1, GGBFS contributes high SiO_2 (30.07%) and CaO (38.22%), serving as the primary source of reactive silicates for C-(A)-S-H gel formation. PS, with its elevated SiO_2 (44.89%) and CaO (43.97%), complements GGBFS by supplying additional amorphous silica, while CS (70.35% CaO) acts as a pH regulator to sustain alkaline conditions for sustained pozzolanic activity. SS, despite its lower reactivity, introduces Fe_2O_3 (29.1%), which facilitates the formation of ferrite phases (e.g., C_4AF) that enhance microstructural strength.

Quantitative TG/DSC analysis (Figure 8) and XRD results (Figure 7) highlight distinct hydration behaviors across ISW proportions. Specimens with optimal ISW proportions (No. 11) exhibited markedly higher mass loss in the 60–120 °C range compared to suboptimal mixtures (e.g., No. 4), correlating with enhanced C-(A)-S-H and ettringite formation. The stoichiometric synergy between GGBFS-derived silicates and CS-provided Ca^{2+} ensures balanced C/S ratios in hydration products, maximizing gel polymerization and pore-filling efficiency. Conversely, excessive CS disrupts this equilibrium, promoting $Ca(OH)_2$ precipitation and calcite overgrowth, as observed in SEM micrographs (Figure 10c), which weaken interparticle bonding through crystalline expansion.

4.2. Long-Term Durability and Field Application Prospects

The hyper-arid desert environment imposes multifactorial challenges to the long-term stability of stabilized aeolian sand, including diurnal thermal cycling, UV radiation, and salt-laden winds particularly regarding potential degradation mechanisms induced by salt crystallization (e.g., sulfate-chloride interactions), acid attacks from pH fluctuations in contaminated soils, and ion-exchange reactions with heavy metal pollutants that may alter the pozzolanic reaction kinetics. The chemical compatibility between ISW-derived alkaline components (e.g., free CaO) and acidic contaminants ($H^+/SO_4{}^{2-}$) could critically influence the stability of hydration products like C-(A)-S-H gels, while chloride infiltration might accelerate matrix deterioration through Friedel's salt formation-disintegration cycles under thermal stresses. Such physicochemical interactions necessitate the systematic evaluation of long-term phase evolution using accelerated aging protocols simulating multi-factor desert environmental conditions. While the current study focuses on 28-day mechanical properties, the intrinsic characteristics of ISW-CM hydration products suggest potential durability advantages over conventional cement-based systems. The dense C-(A)-S-H gel matrix observed in SEM micrographs (Figure 9a,b) and the absence of large ettringite clusters (compared to OPC systems) may mitigate crack propagation under thermal stresses. Additionally, the high calcite content detected in XRD patterns (Figure 7) could enhance carbonation resistance, though excessive crystallization risks interfacial debonding as evidenced in low-strength specimens (Figure 10c).

In field applications, the workability (e.g., fluidity, setting time), volume stability of the cementitious materials, and their applicability to other specialty soils represent pivotal determinants for large-scale implementation, warranting systematic exploration to validate technological scalability. Additionally, both current and previous studies reveal that cement and ISW-based cementitious materials stabilized aeolian sand typically exhibit limited ductility, posing reliability risks in engineering applications through sudden load-bearing capacity loss upon reaching critical stress thresholds—a phenomenon detrimental to life and property protection under extreme conditions. While geosynthetics (geomembranes, geotextiles) or reinforcement techniques may partially mitigate this issue, enhancing intrinsic ductility through fiber incorporation into stabilized sand matrices presents a promising research direction.

4.3. Limits and Future Perspectives

The primary objective of this study is to develop cementitious materials using four types of ISWs for aeolian sand stabilization. Although the prepared materials achieved compressive strength comparable to cement-stabilized sand reported in the literature, limited research outcomes are available for direct comparison. This scarcity arises from the historical predominance of transportation infrastructure (e.g., roads, railways) in desert construction projects, with existing cement stabilization studies predominantly focusing on subgrade filler performance. Notably, fundamental disparities exist between subgrade and building foundation requirements regarding cement dosage, service environments, and loading patterns, rendering direct strength comparisons between these distinct applications scientifically invalid. Consequently, while preliminary strength comparisons were made between ISW-based materials and cement-stabilized sand, comprehensive evaluations of stabilization efficacy, including compressive, shear, and tensile strengths, should be further investigated.

Among the ISWs employed, GGBFS demonstrated substantial pozzolanic reactivity, accounting for its dominant influence on *UCS* variations in stabilized sand. A widely accepted paradigm suggests that alkaline activation can enhance the reactivity of most ISWs, with various alkali excitation techniques having been extensively applied in soft soil and sludge stabilization. However, the inherent low moisture content of aeolian sand in desert environments raises critical questions regarding the efficacy of alkali activation for ISW-based stabilization systems, necessitating dedicated investigation.

5. Conclusions

This study developed a quaternary industrial solid waste (ISW)-based cementitious material composed of steel slag (SS), granulated blast-furnace slag (GGBFS), phosphorus slag (PS), and carbide slag (CS) for the stabilization of aeolian sand in desert regions using a four-factor simplex lattice experiment (SLM) based on the three chemical moduli (TCM) theory referenced standard cement. The optimal proportion of ISWs is determined, and the solidification effects are evaluated in terms of mechanical properties, hydration product levels, and microstructure. The main conclusions obtained are as follows:

(1) The results of the simplex lattice point experiment indicate that an increase in the dosage of GGBFS has a significant positive effect on the *UCS* of stabilized aeolian sand due to its highest pozzolanic reactivity. Conversely, higher SS incorporation reduced *UCS*. Considering the workability of the cementitious material in conjunction with the TCM theory, the optimal proportion of ISWs was determined to be 5:35:20:40, and the *UCS* of aeolian sand stabilized using ISWs with optimal proportion was comparable with that stabilized by OPC.

(2) The *UCS* of stabilized aeolian sand exhibited a linear positive correlation with its elastic modulus but a negative correlation with ductility. The failure mode of stabilized aeolian sand specimens was related to their strength: specimens with higher strength exhibited pronounced inclined shear cracks upon failure, while specimens with lower strength mostly displayed splitting cracks.

(3) The abundance of hydration products such as C(-A)-S-H gel and ettringite was the primary reason for the high strength of stabilized aeolian sand with the optimal proportion. A higher content of CS can increase the level of $Ca(OH)_2$ in the system, leading to an increase in calcite formed through carbonation. However, an unreasonable proportion results in insufficient gel in the system, causing an incomplete particle encapsulation and weak connections between particles, which can be disrupted by the expansion of crystals such as ettringite and calcite, leading to a porous and loose microstructure and thus reducing the strength of stabilized aeolian sand.

Author Contributions: Conceptualization, Z.X., B.Y. and Z.Q.; methodology, Z.X. and Z.Q.; software, Z.Q.; validation, H.W. and Y.Q.; formal analysis, Z.X.; investigation, Z.X., H.W. and Y.Q.; resources, Z.Q.; data curation, B.Y.; writing—original draft preparation, Z.X.; writing—review and editing, Z.Q. and B.Y.; visualization, Z.X.; supervision, Z.Q. and H.W.; project administration, Y.Q.; funding acquisition, Z.Q. All authors have read and agreed to the published version of the manuscript.

Funding: This research was funded by the National Natural Science Foundation of China (Grant No. 42372318).

Data Availability Statement: The raw data supporting the conclusions of this article will be made available by the authors upon request.

Conflicts of Interest: The authors declare no conflicts of interest.

References

1. Akin, I.D.; Tirkes, S.; Collins, C.E. Geotechnical insights of mammal burrows in loose desert sand. *Acta Geotech.* **2024**, *19*, 1449–1459. [CrossRef]
2. Chen, J.Y.; Qiao, G.F.; Wang, R. Turning desert sand into building material products: An ambitious attempt of solar 3D printing. *J. Clean. Prod.* **2022**, *380*, 134790. [CrossRef]
3. Lopez-Ordoñez, C.; Crespo-Cabillo, I.; Calzada, J.R.; Garcia-Nevado, E.; Coch, H. Reducing residential cooling demand in a sprawling desert city through vertical urban densification. *J. Build. Eng.* **2024**, *95*, 110089. [CrossRef]
4. Ma, Z.G.; Li, X.F. Experiments on the State Boundary Surface of Aeolian Sand for Road Building in the Tengger Desert. *Appl. Sci.* **2023**, *13*, 879. [CrossRef]
5. Sherzad, M.F.; Goossens, D. Wind Tunnel Experiments and Field Observations of Aeolian Sand Encroachment around Vernacular Settlements in the Saharan and Arabian Deserts. *Buildings* **2022**, *12*, 2006. [CrossRef]
6. Dammala, P.K.; Kolli, S.; Garaga, R.; Reddy, K.R.; Kumar, P. Aeolian sand dune fixation—Critical review of measures, challenges and future perspectives with a case study on Thar Desert. *Catena* **2025**, *250*, 108786. [CrossRef]
7. Fathali, M.; Nasrabad, M.M.K.; Abbasi, H.R.; Amrollahi, A.; Soleymani, M. Aeolian sand challenges in desert rail infrastructures, overview of Iran's experience and advancement. *Constr. Build. Mater.* **2024**, *438*, 136953. [CrossRef]
8. Feng, L.Q.; Liu, W.B.; Jiang, W.J.; Wang, G.Z. Mechanics and road performance of mudstone modified stabilized gravel subgrade in arid desert areas. *Case Stud. Constr. Mater.* **2024**, *20*, e02799. [CrossRef]
9. Shu, K.; Zani, N.; Ghidini, L.; Petrogalli, C.; Yu, L.; Mazzù, A.; Ding, H.; Wang, W. Wear and damage behaviors of wheel-rail with different material matchings under various sand deposition densities of rail top in desert environments. *Wear* **2025**, *560–561*, 205622. [CrossRef]
10. Su, X.J.; Li, Z.H.; Wang, Q.; Li, J.X.; Xie, X.Y.; Mao, X.; Ren, Z.F.; Liu, J.K. Comparison and Optimization of Bearing Capacity of Three Kinds of Photovoltaic Support Piles in Desert Sand and Gravel Areas. *Buildings* **2024**, *14*, 2559. [CrossRef]
11. Wang, F.; Liu, S.X.; Sun, L.Y.; Huang, S.P.; Zhu, H.; Zou, H.H.; Li, G.R. Analysis of significant risk factors for sand accumulation on desert expressways. *Meas. Sci. Technol.* **2024**, *35*, 095802. [CrossRef]
12. Yang, S.H.; Zhang, L.; Xu, Z.F. Effect of high temperature on residual splitting strength of desert sand concrete. *Struct. Concr.* **2023**, *24*, 3208–3219. [CrossRef]
13. Zuo, L.; Dai, P.Z.; Yan, H.M.; Zhou, L. Effect of sand and crosswind on the performance of solar chimney power plant. *Energy Sci. Eng.* **2023**, *11*, 1294–1310. [CrossRef]
14. Al-Sanad, H.; Ismael, N.; Nayfeh, A. Geotechnical properties of dune sands in Kuwait. *Eng. Geol.* **1993**, *34*, 45–52.
15. Al-Taie, A.J.; Al-Shakarchi, Y.J.; Mohammed, A.A. Investigation of geotechnical specifications of sand dune soil: A case study around Baiji in Iraq. *IIUM Eng. J.* **2013**, *14*. [CrossRef]
16. Cui, Q.; Liu, G.; Zhang, Z.H.; Fang, Y.Q.; Gu, X.D. Experimental Investigation on the Strength and Microscopic Properties of Cement-Stabilized Aeolian Sand. *Buildings* **2023**, *13*, 395. [CrossRef]
17. Padmakumar, G.P.; Srinivas, K.; Uday, K.V.; Iyer, K.R.; Pathak, P.; Keshava, S.M.; Singh, D.N. Characterization of aeolian sands from Indian desert. *Eng. Geol.* **2012**, *139*, 38–49. [CrossRef]
18. Xu, J.; Li, X.H.; Liu, Y.H.; Li, Z.H.; Wang, S.H. Evaluation of wind erosion resistance of EICP solidified desert sand based on response surface methodology. *Constr. Build. Mater.* **2024**, *447*, 138119. [CrossRef]
19. Cheng, Y.; Ding, S. Prototype tests of assembly foundation of transmission line in aeolian sand area. *Rock Soil Mech.* **2012**, *33*, 3230–3236.
20. Lu, X.; Qian, Z.; Yang, W.; Zheng, W. Cement-stabilization of aeolian sand foundation and performance test. *Ind. Constr.* **2018**, *48*, 103–108.

21. Sheng, M.; Zou, C.; Qian, Z.; Lu, X. Experiments on the bearing capacity of aeolian sand stabilized by cement stabilizers. *Bull. Geol. Sci. Technol.* **2022**, *41*, 147–153.
22. Xia, H.; Zhang, J.; Cai, J.; Pan, H.; She, X. Study on the bearing capacity and engineering performance of aeolian sand. *Adv. Mater. Sci. Eng.* **2020**, *2020*, 3426280.
23. Jing, P.; Song, X.T.; Shen, Y.P.; Zhang, L.; Zhang, Y.Q.; Wang, P.C. Hydraulic behavior of sandy subgrade under extreme rainfall in Alashan, China. *Transp. Geotech.* **2023**, *42*, 101049. [CrossRef]
24. Qian, Z.Z.; Sheng, M.Q.; Huang, F.M.; Lu, X.L. Uplift Performance of Plate Anchors in Cement-Stabilised Aeolian Sand. *Front. Earth Sci.* **2021**, *9*, 783148. [CrossRef]
25. Qian, Z.Z.; Lu, X.L.; Shijun, D. Experimental study of assembly foundation for transmission line tower in Taklimakan desert. *Rock Soil Mech.* **2011**, *32*, 2359–2364.
26. Liu, W.Z.; Huang, X.J.; Yin, W.H.; Liu, G.Y. Static and dynamic characteristics of cement-treated and untreated aeolian sand from the Tengger desert hinterland: Laboratory tests and prediction models. *Constr. Build. Mater.* **2025**, *458*, 139733. [CrossRef]
27. Ruan, B.; Yuan, Z.; Zheng, S.; Zhang, J. Experiment on the splitting tensile strength of cemented aeolian sand reinforced with different kinds of fibers. *J. Rail Way Sci. Eng.* **2022**, *19*, 2240–2248.
28. Yang, X.; Hu, Z.Q.; Wang, Y.; Wang, X.L. Aeolian sand stabilized by using fiber- and silt-reinforced cement: Mechanical properties, microstructure evolution, and reinforcement mechanism. *Constr. Build. Mater.* **2024**, *411*, 134750. [CrossRef]
29. Zhang, X.D.; Geng, J.; Pang, S.; Su, L.J.; Cai, G.J.; Zhou, Z.C. Microscopic Properties and Splitting Tensile Strength of Fiber-Modified Cement-Stabilized Aeolian Sand. *J. Mater. Civ. Eng.* **2023**, *35*, 04023128. [CrossRef]
30. Yang, H.; Qian, Z.Z.; Yue, B.; Xie, Z.L. Effects of Cement Dosage, Curing Time, and Water Dosage on the Strength of Cement-Stabilized Aeolian Sand Based on Macroscopic and Microscopic Tests. *Materials* **2024**, *17*, 3946. [CrossRef]
31. Wang, Y.G.; Liu, X.M.; Zhu, X.; Zhu, W.X.; Yue, J.W. Synergistic effect of red mud, desulfurized gypsum and fly ash in cementitious materials: Mechanical performances and microstructure. *Constr. Build. Mater.* **2023**, *404*, 133302. [CrossRef]
32. Bulinska, S.; Sujak, A.; Pyzalski, M. Sustainable Management of Photovoltaic Waste Through Recycling and Material Use in the Construction Industry. *Materials* **2025**, *18*, 284. [CrossRef]
33. de Paiva, F.F.G.; Tamashiro, J.R.; Silva, L.H.P.; Kinoshita, A. Utilization of inorganic solid wastes in cementitious materials—A systematic literature review. *Constr. Build. Mater.* **2021**, *285*, 122833. [CrossRef]
34. Feng, W.L.; Yu, Z.H.; Bao, R.; Xiong, J.; Yan, K.; Liu, R.Y.; Zhang, R.; Lu, X.B. Manufacture of tailings-based cementitious materials: Insights into tailings activation strategies. *Constr. Build. Mater.* **2024**, *439*, 137194. [CrossRef]
35. Vashistha, P.; Park, S.; Pyo, S. A Review on Sustainable Fabrication of Futuristic Cementitious Binders Based on Application of Waste Concrete Powder, Steel Slags, and Coal Bottom Ash. *Int. J. Concr. Struct. Mater.* **2022**, *16*, 51. [CrossRef]
36. Jiao, D.W.; Shi, C.J.; De Schutter, G. Estimation of Magnetic Force between Micrometer-Sized Fly-Ash Particles in Cementitious Suspensions. *J. Mater. Civ. Eng.* **2023**, *35*, 04022421. [CrossRef]
37. Jones, C.; Ramanathan, S.; Suraneni, P.; Hale, W.M. Mitigating calcium oxychloride formation in cementitious paste using alternative supplementary cementitious materials. *Constr. Build. Mater.* **2023**, *377*, 130756. [CrossRef]
38. Liu, L.; Tan, J.J.; Qiu, H.F.; Zhang, J.B.; Guo, Y. Study on microstructural and mechanical properties of cementitious materials composed of fly ash and dacite powder. *Front. Mater.* **2024**, *11*, 1267197. [CrossRef]
39. Xu, H.C.; Yin, H.; Ge, P. Design and microstructural analysis of the mixture proportion of alkali-activated fly ash-slag composite cementitious material. *Mater. Res. Express* **2024**, *11*, 115303. [CrossRef]
40. Bui, P.T.; Ho, L.S.; Shi, J.Y.; Huynh, T.P. Effect of low-calcium fly ash inclusion on long-term mechanical properties and durability of ground granulated blast furnace slag-based cement-free mortars. *Proc. Inst. Mech. Eng. Part L-J. Mater.-Des. Appl.* **2024**, *238*, 723–738. [CrossRef]
41. Huo, Y.L.; Huang, J.G.; Han, X.Y.; Sun, H.Y.; Liu, T.A.; Zhou, J.Y.; Yang, Y.Z. Mass GGBFS Concrete Mixed with Recycled Aggregates as Alkali-Active Substances: Workability, Temperature History and Strength. *Materials* **2023**, *16*, 5632. [CrossRef]
42. Luo, Y.P.; Yang, L.B.; Wang, D.F.; Zhang, Q.Z.; Wang, Z.Y.; Xing, M.G.; Xue, G.B.; Zhang, J.; Liu, Z. Effect of GGBFS on the mechanical properties of metakaolin-based self-compacting geopolymer concrete. *J. Build. Eng.* **2024**, *96*, 110501. [CrossRef]
43. Pejic, J.S.; Basic, A.D.; Grubor, M.; Serdar, M. Link between the Reactivity of Slag and the Strength Development of Calcium Aluminate Cement. *Materials* **2024**, *17*, 3551. [CrossRef] [PubMed]
44. Baalamurugan, J.; Kumar, V.G.; Padmapriya, R.; Raja, V.K.B. Recent applications of steel slag in construction industry. *Environ. Dev. Sustain.* **2024**, *26*, 2865–2896. [CrossRef]
45. Gao, W.H.; Zhou, W.T.; Lyu, X.; Liu, X.; Su, H.L.; Li, C.M.; Wang, H. Comprehensive utilization of steel slag: A review. *Powder Technol.* **2023**, *422*, 118449. [CrossRef]
46. Yuan, B.; Zhao, D.N.; Lei, J.L.; Song, S.Q. Preparation and Performance Testing of Steel Slag Concrete from Steel Solid Waste. *Buildings* **2024**, *14*, 2437. [CrossRef]
47. Cen, X.Q.; Zhang, Y.Q.; Zhang, H.G. Investigation on the mechanical and microstructure properties of masonry cement-red mud-carbide slag-based paste. *Case Stud. Constr. Mater.* **2024**, *21*, e03979. [CrossRef]

48. Ding, Z.Y.; Cheng, Y.; Jin, L.; Wang, W.T.; Yan, S.Y. Study on the strength characteristics and micro-mechanism of modified solidified red mud. *Front. Mater.* **2024**, *11*, 1461198. [CrossRef]
49. Wu, G.; Chen, T.; Zhang, G. Deformation characteristics of red-mud embankment under monotonic and cyclic loads. In Proceedings of the 5th GeoShanghai International Conference, Shanghai, China, 26–29 May 2024.
50. Chen, T.Z.; Dong, X.; Chen, H.X.; Zhou, F.; Liu, G.; Chang, W.; Zhu, R. Study on the Improvement Performance of Different Clay Components with Desulfurization Gypsum-Containing Cementitious Material. *Buildings* **2024**, *14*, 3274. [CrossRef]
51. Feng, S.Y.; Zhang, G.F.; Ren, Y.L. Properties and microstructure of soil solidified by titanium slag-flue gas desulfurized gypsum-Portland cement composites as solidifiers. *Constr. Build. Mater.* **2024**, *438*, 137061. [CrossRef]
52. Hu, T.; Hao, J.Y.; Cheng, G.J.; Guo, B.; Li, X.J. Preparation and Hardening Performance of Lightweight Gypsum Mortar Based on Desulfurization Gypsum. *Iran. J. Sci. Technol.-Trans. Civ. Eng.* **2023**, *47*, 2717–2730. [CrossRef]
53. Wu, J.; Liu, Q.W.; Deng, Y.F.; Yu, X.B.; Feng, Q.; Yan, C. Expansive soil modified by waste steel slag and its application in subbase layer of highways. *Soils Found.* **2019**, *59*, 955–965. [CrossRef]
54. Wu, J.; Deng, Y.F.; Zhang, G.P.; Zhou, A.N.; Tan, Y.Z.; Xiao, H.L.; Zheng, Q.S. A Generic Framework of Unifying Industrial By-products for Soil Stabilization. *J. Clean. Prod.* **2021**, *321*, 128920. [CrossRef]
55. Hurtado-Figueroa, O.; Escamilla, A.C.; Varum, H.; Amaya, R.J.G. Effect of cassava starch, hydrated lime, and carboxymethylcellulose on the physicomechanical behavior of mixtures with clay matrix. *Case Stud. Constr. Mater.* **2024**, *20*, e03022. [CrossRef]
56. Zhang, Y.F.; Wang, R.X.; Ni, J.J. Study on the preparation, performance, and mechanism for solid waste cementitious materials. *Case Stud. Constr. Mater.* **2024**, *20*, e03408. [CrossRef]
57. *GB 175-2023*; Common Portland Cement. State Administration for Market Regulation: Beijing, China, 2023.
58. *ASTM D5102-2017*; Standard Test Method for Unconfined Compressive Strength of Compacted Soil-Lime Mixtures. ASTM International: West Conshohocken, PA, USA, 2017.

Disclaimer/Publisher's Note: The statements, opinions and data contained in all publications are solely those of the individual author(s) and contributor(s) and not of MDPI and/or the editor(s). MDPI and/or the editor(s) disclaim responsibility for any injury to people or property resulting from any ideas, methods, instructions or products referred to in the content.

applied sciences

MDPI

Article

Hydrothermal Manufacture of Zeolitic Lightweight Aggregates from Clay and Marine Plastic Litter

José Manuel Moreno-Maroto [1,*], Julia M. Govea [1], Pablo Poza [1], Mercedes Regadío [1], Jaime Cuevas [1], Ana Isabel Ruiz [1], Raúl Fernández [1] and Jacinto Alonso-Azcárate [2]

[1] Department of Geology and Geochemistry, Autonomous University of Madrid, 28049 Madrid, Spain; julia.govea@estudiante.uam.es (J.M.G.); pablo.pozar@estudiante.uam.es (P.P.); mercedes.regadio@uam.es (M.R.); jaime.cuevas@uam.es (J.C.); anai.ruiz@uam.es (A.I.R.); raul.fernandez@uam.es (R.F.)

[2] Department of Physical Chemistry, Faculty of Environmental Sciences and Biochemistry, University of Castilla-La Mancha, Avenida Carlos III, s/n, 45071 Toledo, Spain; jacinto.alonso@uclm.es

* Correspondence: josemanuel.moreno@uam.es

Abstract: Mixed plastic fraction (MPF) from marine litter was investigated as a pore-forming agent in formulations with kaolin and a rejected Mg-clay (rich in smectite and sepiolite) to obtain innovative zeolitic lightweight aggregates. Round granules of ~10 mm in diameter were shaped and fired at 600 °C (mixtures of kaolin with 0, 5, 10, and 20 wt.% MPF) and 900 °C (mixtures of rejected Mg-clay:kaolin (1:0, 2:1, 1:2; 0:1) with 10 wt.% MPF). The fired specimens were hydrothermally treated in a 3M NaOH solution at 150 °C for 24 h. Mixtures containing 20 wt.% MPF led to specimen crumbling, while those with 5 and, especially, 10 wt.% MPF favored a significant crystallization of zeolites and feldspathoids (50–80%), highlighting cancrinite, nepheline, zeolite A, and analcime. The resulting materials were lightweight (1.5–1.8 g/cm^3) and their crushing strength increased substantially with the hydrothermal treatment, from 0.04–0.5 MPa to 2.3–5.5 MPa after zeolitization. High content of rejected Mg-clay in the mixture (>67%) negatively affected the zeolitization and the properties of the final aggregate, while 33 wt.% was adequate, increasing slightly the crushing strength (3.4 vs. 3.1 MPa). These findings contribute to plastic waste circularity and sustainability/technological progress in materials production.

Keywords: hydrothermal treatment; zeolitic construction materials; lightweight aggregates; marine plastic litter; clay

1. Introduction

Annually, 10 million tons of waste reach the seas and oceans, a problem of global magnitude [1,2]. Despite the heterogeneous nature of marine litter, plastic is the most predominant fraction [3]. Its presence can amount to several kg per km^2 (millions of fragments) in various oceanic areas, including the Mediterranean Sea [4], which directly affects marine organisms that ingest them [5]. Therefore, it is necessary to look for alternatives to reduce the impact of plastic waste.

Regarding plastic application as a pore-forming agent in ceramic materials, this type of research has been usually restricted mainly to biomedical ceramics [6,7]. The addition of plastic to produce materials for construction has hardly been studied. Some of the first contributions in this sense were associated with the manufacture of lightweight aggregates (porous granular ceramic materials) in the patents by Kirschner [8] and Malloy et al. [9]. However, this research line remained dormant for years, and it was not until years later that plastic residues were studied again in ceramic formulations. Some works published by Moreno-Maroto et al. [10,11] stand out, in which the role of household plastic waste as a porogenic additive in expanded lightweight aggregates was studied, also using other mineral wastes in the mixtures (e.g., mine tailings).

It is worth noting that the manufacture of lightweight aggregates can be carried out through four routes: (i) cold bonding: combining raw materials with pozzolanic capacity, such as fly ash, calcium hydroxide, and Portland cement, to obtain hardened aggregates after mixing with water [12,13]; (ii) autoclaving: starting from raw materials that are also binders, the shaped granules undergo an autoclave curing process at temperatures > 100 °C to promote hardening [12,14]; (iii) geopolymerization: mineral precursors rich in aluminosilicates are mixed with an alkaline activator solution until a paste is obtained, which hardens under suitable curing conditions [15]. Foaming agents, such as silica fume, can be added to develop a lighter structure [16]; and (iv) firing or sintering: this is the most common method to obtain lightweight aggregates, as with suitable raw materials and manufacturing conditions (generally using rotary kilns), it can lead to very light and porous materials.

From an environmental standpoint, the above processes present aspects for improvement: in the case of cold bonding and autoclaving, the starting raw materials are generally obtained at high temperatures to be activated (for example, Portland cement is manufactured at about 1500 °C). Likewise, the rotary kiln firing method involves temperatures that in most cases are between 1050 and 1250 °C [17]. Regarding geopolymerization, although it is not very popular in the manufacture of lightweight aggregates, it is attracting a lot of attention in recent years as a more sustainable method of obtaining alternative binders to Portland cement. Although geopolymerization is usually considered environmentally friendly, the strong impact in the manufacture of its most common activators is usually ignored, such as sodium silicate, which is usually synthesized at 1200–1400 °C [18].

Against this backdrop, it is essential to develop more sustainable manufacturing methods, especially from an energy efficiency perspective. To this must be added the new objectives of the European Union, which aim to promote the development of advanced properties in materials [19,20].

Moreno-Maroto and Alonso-Azcárate [21] have recently developed a new manufacturing method based on alkaline hydrothermal treatment of macroscopic specimens fired at relatively low temperatures (600 and 900 °C). This new approach has been proved satisfactory in kaolin mixtures with 10 wt.% of rubber and polyethylene microplastics. The authors investigated different manufacturing conditions in terms of hydrothermal temperatures (80 and 140 °C), times (24 y 72 h), and NaOH concentrations (1, 3, and 5 M), highlighting the development of highly zeolitized structures (15–74%) and a very noticeable increase in mechanical strength, registering increases of up to 37 times with respect to the material only fired.

In view of this, the work presented here aims to deepen the knowledge of this new technique through the application of different conditions of synthesis and raw materials. On the one hand, the mixed plastic fraction (MPF) from marine litter has been studied as a pore-forming agent, which, as explained above, is a very harmful residue in the environment when released into the sea. On the other hand, in addition to kaolin, a rejected Mg-clay with different physicochemical and mineralogical characteristics has been investigated to find out if it is also a suitable component for this new method.

2. Materials and Methods

2.1. Raw Materials

Two types of clay were studied as mineral precursors: (i) a white kaolin, provided by the company Caobar S.A. (Taracena, Spain); and (ii) a material rejected in a special clay production plant (hereafter rejected Mg-clay) due to its grain size being too small for the market. Table 1 shows the main properties of the two clays, as well as the characterization methods at the foot of the table. The white kaolin under study is very rich in kaolinite (85%) with moderate plasticity and toughness: liquid limit (LL) of 42.1 and plastic limit (PL) equal to 27, so that LL-PL results in a plasticity index (PI) of 15.1 and, therefore, PI/LL = 0.36. This kaolin contains no carbon and a very low iron percentage (0.4%). In the case of the

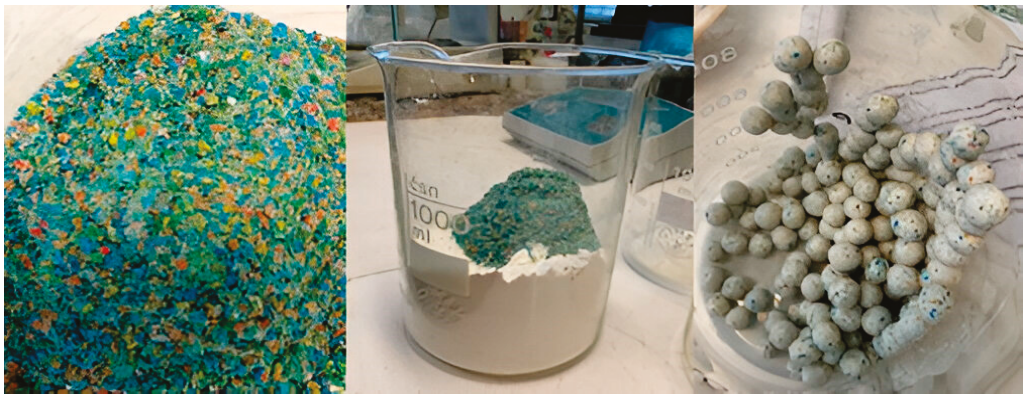
waste material, it is a magnesian clay (MgO = 22%) of very high plasticity and toughness (LL = 171.1; PI/LL = 0.56), rich in smectite (38%) and sepiolite (30%).

Table 1. Characteristics of the clays under study.

Clay	Particle Size (μm) [a]		Atterberg Limits [b]		Carbon (%) [c]	Chemical Composition (%) [d]								Mineralogy (%) [e]								
	d50	Mean	LL	PL	Total (Org.)	SiO_2	Al_2O_3	Fe_2O_3	K_2O	CaO	MgO	Others	LOI	Kao	Sm	Sp	Il	Q	Pg	Fp	Cal	Dol
Kaolin	4.6	8.3	42.1	27.0	–	50.9	35	0.4	0.4	0.1	0.1	0.5	12.6	84.9	–	–	2.5	12.6	–	–	–	–
Rejected Mg-clay	18.5	16.4	171.1	74.8	0.85 (0.44)	54.2	7.2	2.0	1.6	2.0	21.9	1.3	9.8	–	37.8	30	3.9	11.1	4.3	7.9	2.6	2.4

METHODS: [a]: Laser diffraction: Beckman Coulter® LSTM 230 (Nyon, Switzerland); [b]: Casagrande cup for LL and rolling test for PL [22]; [c]: TOC-analyzer Shimadzu® TOC-VCSH (Duisburg, Germany); [d]: X-ray fluorescence: Thermo ARL ADVANT'XP Sequential XRF (Thermo Fisher Scientific, Waltham, MA, USA); [e]: X-ray diffraction (XRD) with Rietveld refinement (see test conditions in Section 2.5), where: Kao = kaolinite; Q = quartz; Pg = plagioclase; Fp = alkali feldspar; Il = Illite; Sm = smectite; Sp = sepiolite; Cal = calcite; Dol = dolomite.

Mixed plastic fraction (MPF) of marine litter has been investigated as a pore-generating additive. The supplier of this MPF was Mares Circulares through the Asociación Vertidos Cero (Madrid, Spain). This material was previously ground at the AIMPLAS Technological Institute (Valencia, Spain) to the desired particle size. First, the MPF plastics were cut with a guillotine to reduce their size to fragments of approximately 5–10 cm. Next, they were passed through a rotary mill with two movable blades and two fixed blades, using a 5 mm mesh, obtaining short plastic filaments (noodle shape). Finally, it was ground by another knife mill, but in this case with the application of nitrogen to avoid melting the plastic. It was passed through a 1 mm mesh to obtain the final powdered plastic used in the study (Figure 1a). The equipment used was a CRS5 cutter mill and an MT15 grinder mill, both from LIDEM (Ontinyent, Spain). The obtained MPF powder had a chemical composition (LECO CHNS-932 elemental analyzer; St. Joseph, MI, USA) of: C = 84.50 ± 0.33%, H = 13.93 ± 0.12%, N = 0.12 ± 0.03%, and S = 0.04 ± 0.02%. The fundamental parameters of its particle size distribution by dry sieving were average particle size of 0.97 mm; d10 = 0.48 mm; d50 =0.86 mm; and d90 = 1.71 mm. The particles were generally flake-shaped.



(**a**) (**b**) (**c**)

Figure 1. (**a**) MPF powder used in the research; (**b**) MPF on kaolin before mixing; (**c**) wet pellets obtained by manual granulation.

2.2. Preparation of Mixtures

This work has two stages:

1. As it has already been proven that the kaolin has zeolitization capacity [21], it has been used as a main component in mixtures with different proportions of plastic, namely 0, 5, 10, and 20 wt.% of powdered MPF (Figure 1b), in order to check how it affects the manufacturing process of zeolitic lightweight aggregates (ZLAs).

2. Secondly, knowing the results obtained in the first stage, the kaolin was mixed with the rejected Mg-clay in proportions 1:0, 2:1, 1:2, and 0:1, thus covering 100%, 33%, 67%, and 0% of each clay in the mixture. A fixed percentage of MPF (in this case 10 wt.%) was added to the resulting clay mixture based on the results of the first stage of the investigation, something that will be discussed later.

The mixing process began with dry homogenization of each of the mixtures for several minutes by vigorous shaking inside a bag. A portion of each mixture was taken and the PL [22] was determined, from which the optimal moisture content (W_{OP}) for subsequent granulation was determined as W_{OP} = PL × 1.234 [21,23]. Based on the W_{OP} results, the different percentages of MPF in the mixtures with kaolin did not significantly affect the amount of water to be added, which in this case ranged between 31 and 36%. On the contrary, the increase in the rejected Mg-clay compared to kaolin in the second stage did lead to a very noticeable increase in the water added to the mixtures, giving the following values: 34, 40, 54, and 100%. This is because the rejected Mg-clay has a very high PL due to its sepiolite content (Table 1). The homogeneous dough obtained after mixing with water passed to the granulation stage.

2.3. Granulation and Firing

Round granules of ~10 mm in diameter were manually formed from the wet dough (Figure 1c). They were oven-dried for 24 h at 105 °C and then fired in a muffle. Simultaneous differential scanning calorimetry-thermogravimetric analysis tests (DSC-TGA) were used as a basis for determining the heating conditions in the muffle (Figure 2).

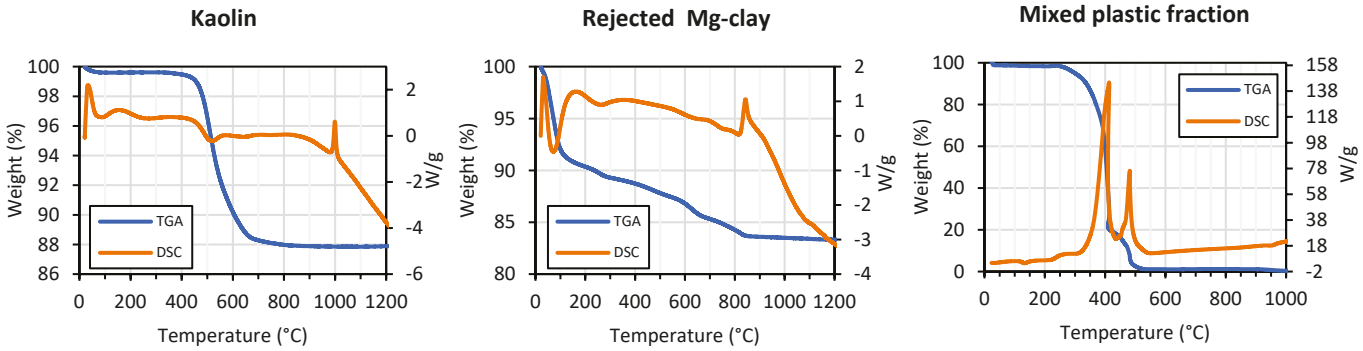


Figure 2. DSC-TGA plots of the raw materials used in this study. Heating ramp: 25 °C/min; atmosphere: air (clays). Equipment: SDT Q600 of TA Instruments (New Castle, DE, USA).

In the case of the mixtures from the first part of the study, the firing temperature was 600 °C. According to Figure 2, this temperature is sufficient for the total thermal decomposition of the MPF and for kaolinite to be activated in the form of amorphous meta-kaolinite by dehydroxylation [24]. However, regarding the addition of the rejected Mg-clay, the temperature was raised to 900 °C since preliminary tests showed that it did not have zeolitization capacity if fired at 600 °C. Thus, the application of 900 °C would ensure the complete destruction of sepiolite and smectite structures, although with a possible minor crystallization of other phases [24], as pointed out by the endothermic–exothermic peak system between 820 and 850 °C (Figure 2). In both cases, the muffle temperature was maintained for 1 h, previously applying a heating ramp of 30 °C/min. The resulting material was cooled by natural radiation inside the muffle.

2.4. Hydrothermal Treatment

For each formulation, about 20 g of the fired granules were weighed and placed into a steel reactor with a Teflon vessel. Approx. 160 mL of 3M NaOH solution was added, corresponding to a liquid/solid ratio of exactly 8 mL/g. The reactor was properly closed and placed in an oven at 150 °C for 24 h. After taking it off the oven and once the temperature of the reactor dropped sufficiently for handling, the supernatant was removed,

and the resulting material was washed with water until neutral pH. Finally, the resulting ZLA was dried in an oven at 105 °C for 24 h.

2.5. Characterization of the Aggregates

According to the characterization tests followed by Moreno-Maroto and Alonso-Azcárate [21], the size of the specimens before and after hydrothermal treatment was determined using a caliper. The volumetric variation was then determined. The crushing strength was tested individually [25,26] in 10 specimens using a Nannetti® FM 96 press (Faenza, Italy), and the final result was calculated as the average of the ten data points.

Part of the fragments resulting from the crushing test were ground to <53 μm with an agate mill. The resulting powder was used to determine the real density (ρ_R) with an AccuPyc 1330 helium pycnometer (Micromeritics, Norcross, GA, USA). This powder material was also used to quantify the mineralogical composition by X-ray diffraction (XRD) with Rietveld refinement. NIST® SRM® 676a alumina standard (Gaithersburg, MD, USA) was used to quantify the amorphous phase. The equipment and conditions used were: PANalytical® diffractometer X'Pert Pro model (Malvern, UK); 45 kV, 40 mA, CuKα radiation, and a system of slits (soller–mask–divergence–antiscatter) of 0.04 rad–10 mm–1/8°–1/2°, with an X'celerator detector and Bragg–Brentano HD module. Water absorption for 24 h (WA_{24}) and particle density (ρ_{rd}) were determined with a water pycnometer according to the EN-1097-6 standard [27]. Based on the data obtained through this test and the ρ_R results, the total, open, and closed porosity (P_T, P_O, and P_C) were calculated through the equations described by Moreno-Maroto and Alonso-Azcárate [21]. The interior of some selected ZLA samples was coated with Au using a Quorum Q150T S sputtering metallizer (Laughton, East Sussex, UK). Then, the ZLA microstructure was observed by scanning electron microscopy (SEM) with a Hitachi S-3000N instrument (Hitachinaka, Japan). The microscope operated under high vacuum conditions with an accelerating voltage of 20 keV, a lifetime of 40 s, a working distance of 14.7 to 17.4 mm, and a beam current of 300 mA. Secondary electrons were detected to accurately visualize surface and crystal morphology.

3. Results and Discussion

3.1. Zeolitic Lightweight Aggregates Obtained from Kaolin and Different Proportions of Marine Plastic

3.1.1. Mineralogical Changes and Zeolitization

The aggregates obtained for each formulation have been designated by the following code: K-xP-600, where K means kaolin, x is the % of MPF added, and 600 is the muffle firing temperature (in this case 600 °C). For hydrothermally treated samples (see specimens in Figure 3), the term H has been added to the end of the name (K-xP-600-H). It is worth noting that the high plastic content of the specimens containing 20 wt.% MPF led to the crumbling of the specimens after firing in the muffle, so that only the formulations with 0, 5, and 10 wt.% MPF could be studied.

The mineralogical changes that occurred during firing and hydrothermal treatment can be seen in Table 2 and Figure 4. The diffractograms are shown in Figure S1 in Supplementary Material. Firing at 600 °C affected the three formulations in a similar way, irrespective of the added MPF content. A very noticeable increase in the amorphization of the sample (82–87%) stands out, mainly associated with the dehydroxylation of kaolinite (endothermic peak with mass loss at ∼525 °C for kaolin in Figure 2), which was reduced from 85% to 2–6%.

However, the hydrothermal treatment of the fired samples has affected the mineralogy in the opposite direction, highlighting a very notable decrease in such an amorphous phase in favor of the crystallization of minerals of the zeolite group (zeolite A, zeolite P1, and analcime) and feldspathoids (cancrinite, hydrosodalite, and nepheline). In the case of the feldspathoids detected, the International Zeolite Association integrates them into its zeolite database as they present a zeolite-type framework [28], so they will be considered as such in this study (Table 2).



(**a**) 0 wt.% MPF (**b**) 5 wt.% MPF (**c**) 10 wt.% MPF

Figure 3. Zeolitic lightweight aggregates obtained from kaolin and (**a**) 0 wt.%, (**b**) 5 wt.%, and (**c**) 10 wt.% of mixed plastic fraction from marine litter. The prints left by the burned plastic can be seen in (**b**) and especially in (**c**).

Table 2. Mineralogical composition of the kaolin and the lightweight aggregates obtained from it and different proportions of MPF (0P, 5P, and 10P mean 0, 5, and 10 wt.% of MPF added). Letter H = hydrothermally treated.

Sample	Mineralogical Composition (%)											
	Kao	**Ill**	**Q**	**Zeo A** [a]	**Can** [ab]	**Hysod** [ab]	**Zeo P1** [a]	**Neph** [ab]	**Ana** [a]	**Am**	**Σ Zeolite** [ab]	**Σ Other Minerals**
Kaolin (unfired)	84.9	2.5	12.6									100
K-0P-600	6.0	2.6	9.2							82.2		17.8
K-5P-600	2.2	1.9	9.2							86.7		13.3
K-10P-600	2.1	1.9	9.8							86.2		13.8
K-0P-600-H		0.7	5.0	9.6	20.1	3.9	0.2	16.9	1.0	42.6	51.7	5.7
K-5P-600-H		0.4	3.1	20.5	5.9	8.4	5.2	16.8	1.5	38.3	58.3	3.5
K-10P-600-H					33.5	2.3	0.8	33.2	10.1	20.2	79.9	

Kao = kaolinite; Ill = illite; Q = quartz; Zeo A = zeolite A; Can = cancrinite; Hysod = hydrosodalite; Zeo P1 = zeolite P; Neph = nepheline; Ana = analcime; Am = amorphous phase. [a] Minerals registered as zeolites in the database of the International Zeolite Association [28]. [b] Feldspathoid with zeolitic framework type [28].

The percentage of plastic added to the starting mixture is a variable that has significantly affected the mineralogy. From a general point of view, the overall zeolite content increases with the MPF content, going from 51.7% zeolite in the sample without plastic, to 58.3% in the sample with 5% MPF, and almost 80% in the materials with 10% plastic added initially (Table 2, Figure 4b). This would be because the pores left by the plastic particles when burning in the muffle would allow (1) a better permeation of the NaOH solution through the whole body of the specimen, and (2) more space for the nucleation and crystallization of the zeolites, both aspects leading to a more effective zeolitization [21]. Zeolite crystallization occurs mainly from the amorphous phase, whose content decreases proportionally with the increase in zeolite, although it is also nourished to a lesser extent by the remnants of kaolinite, illite, and quartz that had not amorphized during firing.

Regarding the mineral species neoformed in each sample during the hydrothermal treatment, according to Table 2 and Figure 4a, the presence of cancrinite and nepheline stands out (20 and 17%, respectively) in the sample without MPF, followed by zeolite A (∼10%), with the rest of the zeolites presenting lower proportions. However, zeolite A (∼20%) is the major mineral in the material to which 5 wt.% plastic was added, followed closely by nepheline (∼17%), and to a lesser extent by hydrosodalite (∼8%), cancrinite, and zeolite P1 (5–6%). However, in the material with 10 wt.% of MPF, no zeolite A has been detected, and as with the sample without plastic, its dominant mineral phases are cancrinite

and nepheline (33% each), highlighting also in this case an abundant crystallization of analcime (10%).

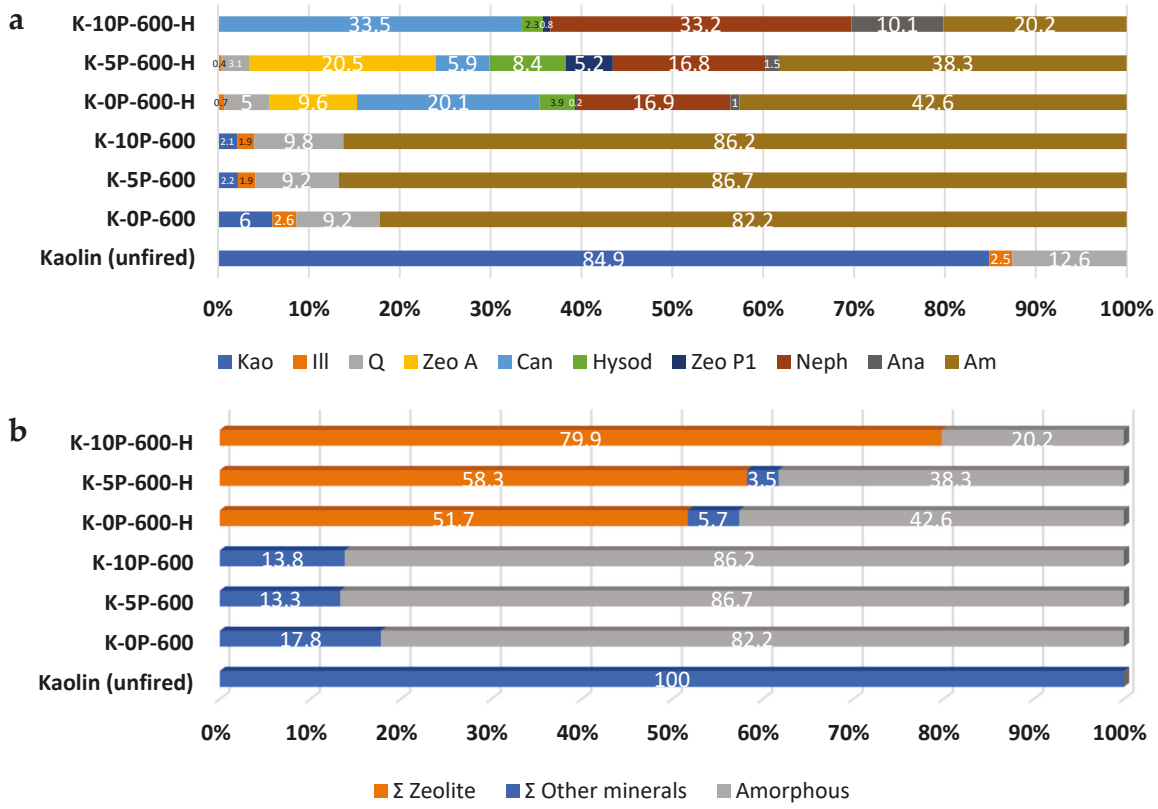


Figure 4. Mineralogical composition of the kaolin and the lightweight aggregates obtained from it and different proportions of MPF (0P, 5P and 10P mean 0, 5, and 10 wt.% of MPF added): (**a**) Kao = kaolinite; Ill = illite; Q = quartz; Zeo A = zeolite A; Can = cancrinite; Hysod = hydrosodalite; Zeo P1 = zeolite P; Neph = nepheline; Ana = analcime; Am = amorphous phase. (**b**) Differentiation between zeolites, other minerals and amorphous phase.

Images taken by SEM have revealed that although crystal growth can occur throughout the body of the material (especially in the sample with 10% plastic, Figure 5a), it is most noticeable inside the pores (Figure 5b), which would be aligned with a higher zeolitization in the samples manufactured with MPF. Regarding the morphology of the neoformed minerals, aggregates of elongated crystals stand out in the three materials (Figure 5a–c). Most of them are flattened (Figure 5a–e), dominated by tabular and columnar habits and, to a lesser extent, acicular ones, characterized by a wedge-shaped end at {201} (Figure 5d), which is typical of nepheline [29,30]. Depending on the observed zones, these crystals can be found together with others of cancrinite, which can exhibit a needle habit with hexagonal prism geometry [31,32] (Figure 5b,c) or with rounded aggregate architecture [31] (Figure 5a). It is also remarkable the presence of analcime crystals with isometric trapezohedral morphology, namely of deltoidal icositetrahedron habit [33,34], especially in the samples to which plastic was added (Figure 5e,f). A common aspect between the sample without plastic and the one synthesized with 5 wt.% MPF is the appearance of cubic crystals (Figure 5g,h) of zeolite A [35,36] not present in the sample with 10 wt.% MPF, thus endorsing the XRD results (Table 2). These cubic crystals may be accompanied by other crystalline aggregates, such as the lepispheres (desert rose shape) shown in Figure 5h, which would be of hydrosodalite [37], although some authors have also reported them for the P1 zeolite [38,39]. Regarding the latter, the crystalline aggregates called by some authors as pinecone type or cactus type shown in Figure 5h,i, correspond to zeolite P1 [38–40], being most likely of the NaP1 type [38].

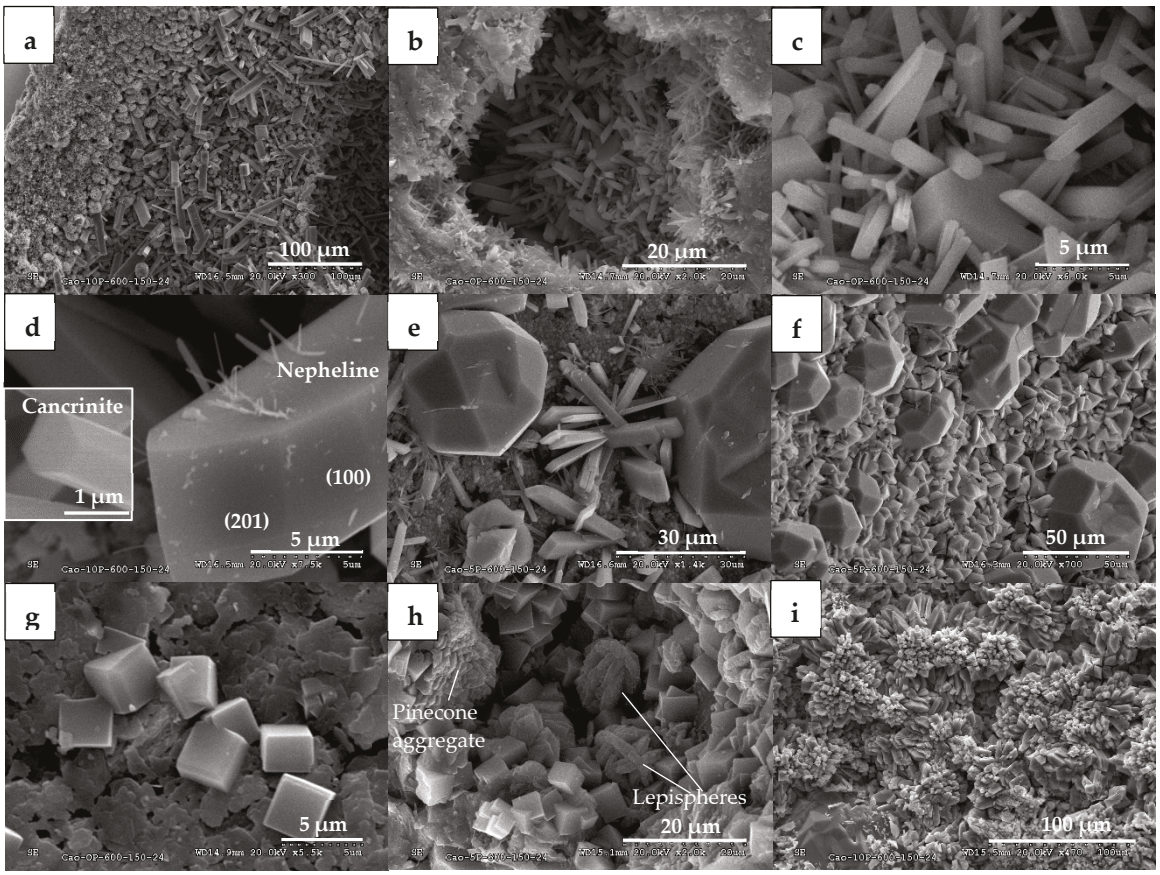


Figure 5. Images taken by SEM of zeolitized samples: (**a**) zeolite crystals along the entire section of sample K-10P-600-H, with rounded crystalline aggregates of cancrinite on the left and aggregates of elongated crystals of nepheline and cancrinite on the right; (**b**) elongated crystals of nepheline and cancrinite within a pore and (**c**) detail view of these in K-0P-600-H; (**d**) tip of an acicular crystal of cancrinite with hexagonal cross-section and tip of a nepheline crystal showing characteristic Miller indices according to Hansen and Fälth [29]; (**e**,**f**) analcime crystals with trapezohedral habit and, in (**e**) together with other nepheline tabular/columnars in K-5P-600-H; (**g**) cubic crystals of zeolite A in K-0P-600-H; (**h**) crystalline aggregate with cubic crystals zeolite A, pinecone aggregate of zeolite P1, and lepispheres of hydrosadalite or zeolite P1 in K-5P-600-H; (**i**) pinecone-like crystalline aggregate typical of zeolite P1 in K-10P-600-H.

3.1.2. Technological Properties of the ZLAs

The main characteristics of the materials obtained are shown in Table 3. First, it can be seen that the average size of the fired aggregates is between 10.5 and 10.7 mm. The alkaline treatment did not result in a substantial change in the diameter of the specimens without MPF; however, it favored an increase of approx. 5% in the two samples with the additive. This could mean that the zeolite neoformation has meant a certain volumetric expansion in these samples (crystal growth in small pores and fissures may have "pushed" the internal structure), also promoted by the growth of microcrystalline crystals on the surface of the material.

As explained in the previous section, zeolitization has occurred most intensely inside the pores (Figure 5b). This has led to a drastic decrease in total porosity (Table 3 and Figure 6a), a phenomenon that has been more pronounced in the sample with 0 and 5 wt.% MPF, dropping from P_T = 45 and 49% to P_T = 24 and 26%, implying a decrease of 20–23 points, i.e., 45–47%, respectively. In the case of the sample with 10 wt.% added plastic, the addition of higher plastic content has helped cushion porosity depletion, so the total porosity has decreased 24.5%, from 48.6% to 36.7%. The open porosity is dominant in the fired samples, with values between 32% (sample with 10 wt.% MPF) and 37% (the other two), while the closed

porosity increased 7, 12, and 16% with the addition of the plastic. Due to this dominance of open porosity over closed porosity, the former has been more affected by zeolitization, being reduced to values between 21 and 25%, while the closed pores represent between 3 and 12% after treatment, being the sample with 10 wt.% of MPF less affected (Table 3). The clogging of the open pores is reasonable since the alkaline solution would penetrate through it without difficulty, and the zeolites can crystallize on the walls of these pores and open fractures (Figure 5b). However, the decrease in the closed porosity is counter-intuitive, and could indicate that the alkaline treatment is capable of permeating a large part of the structure through the different physicochemical and mineralogical transformations that have taken place, even altering the walls of the closed pores, in which crystals could also have grown.

Table 3. Properties of the lightweight aggregates obtained from kaolin and different proportions of MPF (0P, 5P, and 10P mean 0, 5, and 10 wt.% of MPF added). The letter H at the end of the name indicates that the fired aggregates have also undergone hydrothermal treatment.

Aggregate	Diameter (mm)			Crushing Strength (MPa)			Density (g/cm^3)			Water Absorption (%)		Porosity (%)			
	Mean	St. Dv.	Δ (%) [a]	Mean	St. Dv.	Δ Ratio [a]	ρ_{rd}	ρ_R	Δ ρ_{rd} (%) [a]	WA_{24}	Δ (%) [a]	P_T	Δ P_T (%) [a]	P_O	P_C
K-0P-600	10.6	0.7		0.45	0.07		1.49	2.695		25.1		44.6		37.6	7.0
K-5P-600	10.7	0.7		0.13	0.03		1.34	2.635		27.8		49.3		37.2	12.2
K-10P-600	10.5	0.6		0.04	0.02		1.36	2.641		23.7		48.6		32.2	16.4
K-0P-600-H	10.7	0.6	0.9	5.5	1.0	12.3	1.79	2.365	19.7	12.2	−51.4	24.4	−45.2	21.9	2.6
K-5P-600-H	11.2	0.8	4.7	4.4	0.7	33.8	1.66	2.249	24.3	12.5	−54.9	26.2	−46.9	20.8	5.4
K-10P-600-H	11.0	0.6	4.8	2.3	0.6	57.5	1.49	2.348	9.5	16.6	−29.8	36.7	−24.5	24.8	11.9

[a] Variation in hydrothermal treatment over the same material only fired.

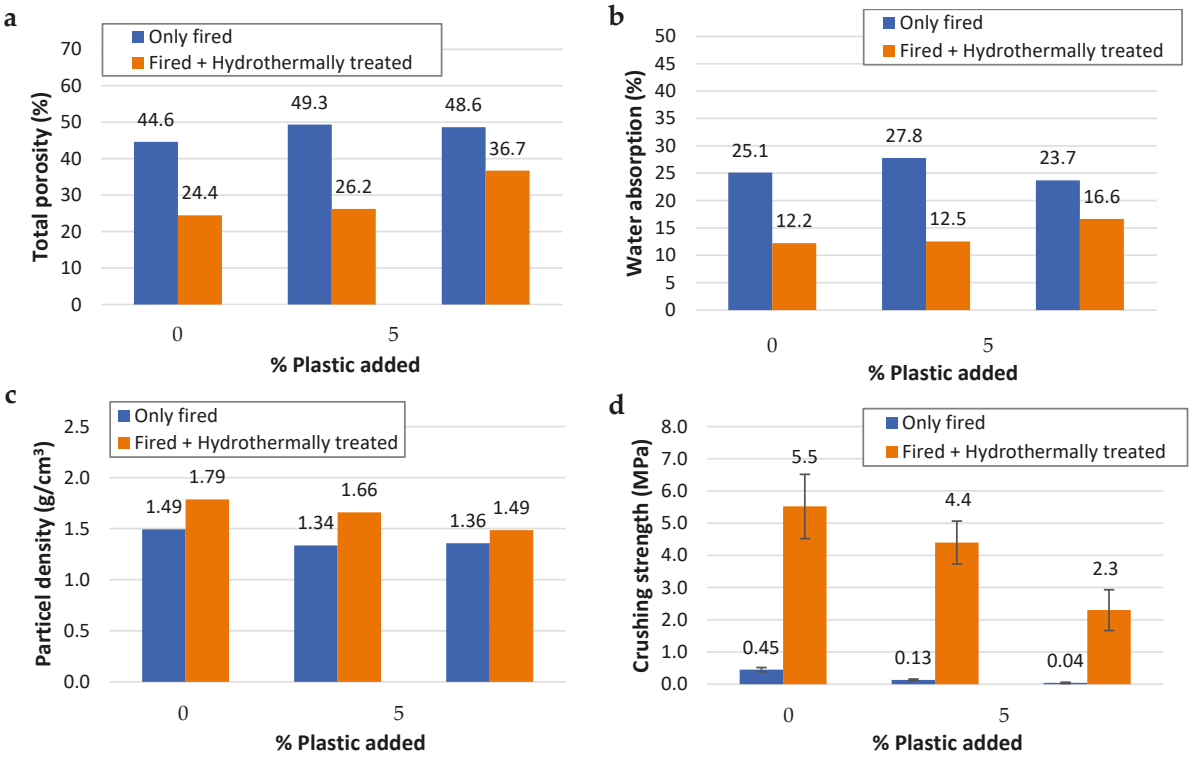


Figure 6. Technological characteristics of the zeolitic lightweight aggregates obtained from kaolin and different proportions of MPF: (**a**) total porosity; (**b**) water absorption; (**c**) particle density; (**d**) crushing strength.

This decrease in porosity is critical, as it has affected the technological properties of the material. Thus, while the water absorption in the samples only fired was around 23–27%, this figure has been reduced after zeolitization to 12% and 17% in the samples with 0 and 5% MPF and 10% MPF, respectively, representing a variation over the non-treated specimens of more than −50% in the former two and almost −30% in the latter (Table 3, Figure 6b).

Regarding the density of the materials obtained, the decrease in porosity of the material has led to the ρ_{rd} values increasing between 10% and 24% compared to the fired material from which they come. Thus, in the sample without added plastic, the starting density was 1.49 g/cm^3, which after the hydrothermal treatment rose to 1.79 g/cm^3. In the case of samples with MPF, the density before zeolitization was ∼1.35 g/cm^3, increasing after it to 1.66 g/cm^3 in materials with 5 wt.% of plastic added and somewhat less (1.49 g/cm^3) in those with 10 wt.% MPF (Figure 6c). It is important to highlight that all values are below the limit of 2.00 g/cm^3 established by the EN 13055-1 [41] standard, which means that the materials obtained could be used as lightweight aggregates.

Finally, an essential parameter is the mechanical strength, in this case measured as the crushing strength of single specimens. According to Figure 6d, several interpretations can be made. Firstly, the only-fired materials have a very low strength, between 0.04 and 0.45 MPa, and the addition of plastic tends to reduce it. However, this is corrected with a significant increase in the crushing strength after zeolitization, presenting values of 5.5, 4.4, and 2.3 MPa in the samples with 0, 5, and 10 wt.% MPF, respectively. This represents an increase ratio of 12, 34, and almost 58 times the strength of the starting fired material (Table 3), which allows lightweight materials with improved mechanical strength to be obtained, in this case zeolitic lightweight aggregates.

Beyond these technological improvements, the environmental impact generated by the burning of plastic waste is an aspect that will be evaluated in a future study. In the fight against plastic landfilling, the most widely used way to dispose of plastic waste in Europe is energy recovery (over recycling). This means that most of the plastic waste is already incinerated to obtain heat, electricity, or fuel, so there is a suitable and safe technology for this [42], which could be adapted to the manufacturing method presented in this work.

3.2. Effect of the Addition of the Rejected Mg-Clay (Rich in Smectite and Sepiolite) on the Zeolitization of Lightweight Aggregates

3.2.1. Mineralogical Changes and Zeolitization

The results of mineralogical composition corresponding to the materials obtained in the mixtures of rejected Mg-clay and kaolin are shown in Table 4. The diffractograms are shown in Figure S1 in Supplementary Material. Based on the findings of the first part of the study, it was decided to add an amount of 10 wt.% MPF to maximize the zeolitization of the samples. The formulations containing 67% and 100% rejected Mg-clay do not appear in Table 4, because the specimens obtained after the hydrothermal treatment tended to crumble in aqueous medium, so they were discarded.

Firing at 900 °C did not lead to significant changes in the mineralogy of the sample with 100% kaolin with respect to its counterpart fired at 600 °C, beyond the complete amorphization of the little kaolinite that remained (Tables 2 and 4). In the case of the granules with 33% rejected Mg-clay, firing has led to the thermal decomposition of the calcite and dolomite of the starting mixture, as well as the destruction of all the phyllosilicates, with the exception of illite, although its content is very low (∼2%). The initial feldspar and plagioclase content (4 and 8%, respectively) has also been reduced to ∼1%. The decomposition of the original phases has led to a significant amorphization of the material (70%), as well as the neoformation of two new phases: pigeonite (4%) and mullite (13%). The DSC-TGA graphs in Figure 2 reveal that these new minerals would not come from kaolin since the peak of mullite formation is located at 1000 °C, which is higher than that applied. However, the endothermic–exothermic peak system between 800 and 850 °C in the rejected Mg-clay

indicates, first, the structural decomposition of smectite and sepiolite and, subsequently, the crystallization of these two new phases [24].

Table 4. Mineralogical composition of the kaolin, the rejected Mg-clay and the lightweight aggregates obtained at 900 °C from kaolin and its mixture 1:2 with rejected Mg-clay (term S because of its high content in smectite and sepiolite) and 10 wt.% MPF (10P). Letter H = material hydrothermally treated after firing.

Sample	Mineralogical Composition (%)																		
	Kao	**Ill**	**Sm**	**Sp**	**Q**	**Plag**	**Fp**	**Cal**	**Dol**	**Pig**	**Mu**	**Zeo A** [a]	**Can** [ab]	**Sod** [ab]	**Phi** [a]	**Neph** [ab]	**Am**	**Σ Zeolite**	**Σ Other Minerals**
Kaolin (unfired)	84.9	2.5			12.6														100
Rejected Mg-clay (unfired)		3.9	37.8	30	11.1	4.3	7.9	2.6	2.4										100
S0K1-10P-900 [c]		3.2			12.2												84.7		15.4
S1K2-10P-900 [c]		1.7			9.1	1.4	0.7			3.8	13						70.3		29.7
S0K1-10P-900-H [c]					0.1							1.7	45.4	5	13.1	11.8	22.8	77	0.1
S1K2-10P-900-H [c]					0.2							1.5	40.9		1.4	4.2	51.8	48	0.2

Kao = kaolinite; Ill = illite; Sm = smectite; Sp = sepiolite; Q = quartz; Plag = plagioclase; Fp = alkali feldspar; Cal = calcite; Dol = dolomite; Pig = pigeonite; Mu = mullite; Zeo A = zeolite A; Can = cancrinite; Sod = sodalite; Phi = phillipsite; Neph = nepheline; Am = amorphous phase. [a] Minerals registered as zeolites in the database of the International Zeolite Association [28]. [b] Feldspathoid with zeolitic framework type [28]. [c] The naming of the samples follows the same rule as that in Table 3, but in this case the proportion of rejected Mg-clay versus kaolin is distinguished with the term S for the former, which refers to its high content of smectite and sepiolite. Therefore, S0K1 indicates a 0:1 ratio (i.e., 100% kaolin) and S1:K2 a 1:2 ratio (33% rejected Mg-clay and 67% kaolin).

Regarding the hydrothermal treatment, it has eliminated all the mineral species from the fired specimens, leaving only a few traces of quartz. The amorphous phase content was also reduced, more markedly in the sample with only kaolin (23% amorphous) than in the one containing 33% rejected Mg-clay (52%). This entails a different degree of zeolitization, being much more noticeable in the former (77% zeolite) than in the latter (48%). This suggests that the addition of the rejected Mg-clay (rich in magnesium smectite and sepiolite) could inhibit the zeolitization process under the conditions studied, which could explain why the formulations with 67% and 100% of this clay did not present structural stability. One possible reason for this is such a high Mg content (Table 1), so that for future research, an acid pretreatment could be considered to reduce its concentration.

Regarding the developed zeolite species, with respect to the sample with only kaolin, it can be seen that firing at 900 °C has led to slight changes, compared to the same formulation fired at 600 °C and then hydrothermally treated (Table 2 vs. Table 4). It stands out that cancrinite continues to be the dominant phase in the material fired at 900 °C (45.4% compared to 33.5% at 600 °C), followed by nepheline (11.8% compared to 33.2%). Likewise, no nepheline or hydrosodalite appears, but phillipsite (13%) and, to a lesser extent, sodalite (5%) and zeolite A (1.7%), which were not detected in the aggregate fired at 600 °C. This would indicate that the firing temperature could be a variable that can greatly affect the mineralogical changes during hydrothermal synthesis.

With regard to the zeolitic content of the material with rejected Mg-clay, the data in Table 4 reveal that, although the contents of cancrinite and zeolite A are very similar to those of the sample with only kaolin, sodalite would not have been formed. In the case of phillipsite and nepheline, their content would be lower than that of the aggregate with 100% kaolin (1.4% and 4.2%, respectively). Therefore, the addition of the rejected Mg-clay does not seem to have inhibited the crystallization of cancrinite (and to a certain extent neither of zeolite A), but it did so for the rest of the phases mentioned above.

The habit of the crystals presents parallels with several of those indicated previously in Figure 5. According to the SEM images in Figure 7, in many areas the only elongated crystals that can be observed are flattened, typical of nepheline (Figure 7), which contrasts with the fact that cancrinite is the dominant mineral in the two zeolitized samples (Table 4). This should be because cancrinite aggregates can also take other morphologies, such as the rounded ones [31] shown in Figure 7. Regarding nepheline crystals, some Y-shaped crystal associations have been observed (Figure 7b), something that also appears in the study of Lin et al. [30]. This type of structure is actually formed by the epitaxial growth of a butterfly twin, typical of nepheline [29], on another crystal of the same mineral.

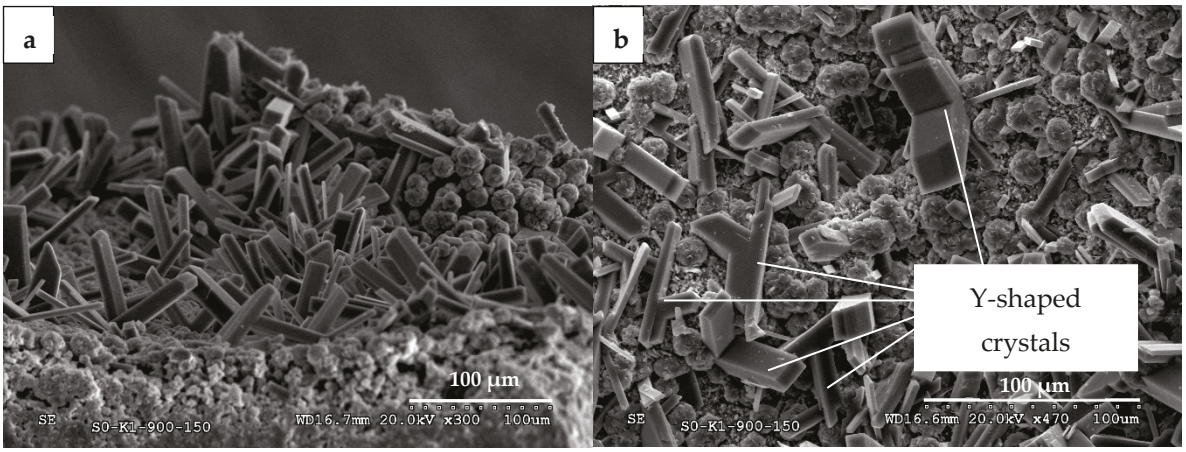


Figure 7. Images taken by SEM of zeolitized samples: (**a**,**b**) tabular and columnar crystals of nepheline and rounded aggregates of cancrinite in S0K1-10P-900-H and, including a detail view in (**b**) of Y-shaped nepheline crystals by epitaxial growth of a butterfly twin on another crystal of the same mineral.

3.2.2. Impact of the Rejected Mg-Clay on the Technological Properties of the ZLAs

The results in Table 5 show that the hydrothermal treatment has favored a slight increase in aggregate size (1–5%), agreeing with the results in Table 4 discussed above. In general terms, the sample containing only kaolin has very similar characteristics to those previously discussed for its counterpart fired at 600 °C, both for the fired sample and the hydrothermally treated sample. Therefore, the differences will not be discussed in detail. It simply needs to be noted that firing at 900 °C would have led to a higher degree of zeolitization of the sample, which has resulted in slightly less porosity and water absorption, as well as a slightly higher density and thus a strength also somewhat higher than those of the samples fired at 600 °C. Such differences could be explained by those shown above for the mineralogy of these samples.

Regarding the addition of 33 wt.% of rejected Mg-clay, the characteristics of the material obtained are very similar to those of the material produced with kaolin alone. In terms of density, the rejected Mg-clay has favored a slight increase in density (1.74 g/cm^3 vs. 1.65 g/cm^3). Despite this, it complies with the EN 13055-1 [41] standard for use as lightweight aggregate. For the rest of the properties, there are hardly any notable differences compared to its counterpart with only kaolin: water absorption of 11.5% compared to 11.8%; crushing strength slightly higher (3.4 MPa vs. 3.1 MPa); and total porosity of 27.4% versus 28.8%, representing a decrease in the porosity of the fired material of 45 and 41%, respectively. This decrease in porosity would affect both the open type (having a value of 20% with rejected Mg-clay and 19.5% without it) and the closed type (9.2% vs. 7.4%).

These results indicate that, although hydrothermal treatment in aggregates shaped with a high content of smectitic-sepiolitic magnesium clays would not lead to suitable zeolitic materials (at least with the conditions studied in this research), its addition in

moderate proportions is promising, since materials with technological properties similar to those obtained only with kaolin could be produced.

Table 5. Properties of the lightweight aggregates obtained from kaolin and its mixture 1:2 with rejected Mg-clay (term S because of its high content in smectite and sepiolite) and 10 wt.% MPF fired at 900 °C. The letter H at the end of the name indicates that the fired aggregates have also undergone hydrothermal treatment.

Aggregate	Diameter (mm)			Crushing Strength (MPa)			Density (g/cm^3)			Water Absorption (%)		Porosity (%)			
	Mean	St. Dv.	Δ (%) [a]	Mean	St. Dv.	Δ Ratio [a]	ρ_{rd}	ρ_R	Δ ρ_{rd} (%) [a]	WA_{24}	Δ (%) [a]	P_T	Δ P_T (%) [a]	P_O	P_C
S0K1-10P-900	10.0	0.9		0.2	0.1		1.39	2.722		25.8		48.8		36.0	12.7
S1K2-10P-900	9.5	0.6		1.7	0.4		1.44	2.859		24.1		49.7		34.8	15.0
S0K1-10P-900-H	10.5	0.7	5.0	3.1	0.6	20.7	1.65	2.312	18.1	11.8	−54.1	28.8	−41.0	19.5	9.2
S1K2-10P-900-H	9.6	0.6	1.1	3.4	0.8	2.0	1.74	2.395	21.1	11.5	−52.4	27.4	−45.0	20.0	7.4

[a] Variation in hydrothermal treatment over the same material only fired.

4. Conclusions

A study is presented to sustainably develop innovative zeolitic lightweight aggregates (ZLAs), based on the protocol recently published by Moreno-Maroto and Alonso-Azcárate [21]. The main conclusions that can be drawn can be summarized as follows:

- The incorporation of MPF in proportions not exceeding 10 wt.% would be positive since its combustion during firing favors the formation of open porosity, which makes the subsequent alkaline hydrothermal treatment more effective. Therefore, adjusting the percentage of MPF in the mixture could help control the final properties of the material obtained. Thus, although the mechanical strength decreases with the MPF, the lightness and degree of zeolitization improve.
- The type of clay used in manufacturing is a critical aspect. Kaolin is very prone to zeolitization, being a suitable raw material for the manufacture of ZLAs. On the contrary, the rejected Mg-clay investigated (rich in magnesium smectite and sepiolite) seems to negatively affect zeolitization when it is added in high proportions. However, in a moderate content (33% rejected Mg-clay over 67% kaolin), it can give rise to materials with properties similar, or even superior (e.g., mechanical strength), to those obtained with kaolin alone. This invites further research into this clay with different formulation and manufacturing conditions, including the application of acid pretreatments for Mg removal.
- The hydrothermal zeolitization method allows working at significantly lower firing temperatures (600–900 °C in this work) than those usual for lightweight aggregates (>1000 °C). This can provide an important economic and environmental advantage by reducing energy consumption during manufacturing. In any case, it will be necessary to investigate these aspects in more detail in the future (for example, through life cycle assessment), especially to check if the emissions linked to the combustion of the MPF are compensated by the energy savings during hydrothermal manufacturing.
- The high zeolite content in the new lightweight aggregates could give them advanced properties compared to conventional ones. In addition to a significant increase in mechanical strength (even >50 fold compared to the starting fired material), it is well known the adsorbent capacity of zeolites, thus paving the way to investigate the decontamination capacity of the new ZLAs.
- Despite the potential environmental advantages indicated above, the impact generated by the burning of plastic waste in the manufacturing process is an aspect to be evaluated (pending for another study). However, it should be noted that the most widely used way of disposing of plastic waste in Europe is energy recovery by incin-

eration [42], which indicates that a viable and safe technology already exists, which could be adapted to the manufacturing method presented in this work.

Considering all of the above, the general conclusion is that the work presented here adapts to: (1) the concept of circularity, by incorporating waste in the manufacture, thus proposing new solutions to waste as problematic as plastics from marine litter; (2) sustainability and energy efficiency, by working at lower temperatures than usual; and (3) technological development, by obtaining zeolitic lightweight aggregates with promising properties compared to their conventional counterparts.

Supplementary Materials: The following are available online at https://www.mdpi.com/article/10.3390/app14177674/s1.

Author Contributions: J.M.M.-M. conceptualization, investigation, methodology, visualization, writing—original draft, writing—review and editing, funding acquisition, project administration, resources, supervision; J.M.G. and P.P. investigation; M.R., J.C., A.I.R. and R.F. writing—review and editing; J.A.-A. investigation, writing—review and editing. All authors have read and agreed to the published version of the manuscript.

Funding: This research was conducted as a part the project "Aplicación de residuos plásticos marinos como componentes tecnológicos en la fabricación de cerámicas zeolitizadas (OZEONIC)" framed within the 6th Edition of the Premios Mares Circulares (Circular Seas Awards) in its Research Projects 2023 modality, funded by Asociación Chelonia and promoted by Coca-Cola Europacific Partners.

Institutional Review Board Statement: Not applicable.

Informed Consent Statement: Not applicable.

Data Availability Statement: The data presented in this study are available on request from the corresponding author. The data are not publicly available due to privacy.

Acknowledgments: This research was conducted as a part the project "Aplicación de residuos plásticos marinos como componentes tecnológicos en la fabricación de cerámicas zeolitizadas (OZEONIC)" framed within the 6th Edition of the Premios Mares Circulares (Circular Seas Awards) in its Research Projects 2023 modality, funded by Asociación Chelonia and promoted by Coca-Cola Europacific Partners. Special thanks to Mares Circulares, Asociación Vertidos Cero and Centro Tecnológico AIMPLAS for providing the ground sample of marine plastic debris.

Conflicts of Interest: The authors declare no conflicts of interest.

References

1. Fundación Conama. *Decálogo Ciudadano Contra las Basuras Marinas*; Ministerio para la Transición Ecológica, Ed.; Centro de Publicaciones: Madrid, Spain, 2016; Catálogo de Publicaciones de la Administración General del Estado, NIPO: 638-18-002-8.
2. Zhang, Y.; Wu, P.; Xu, R.; Wang, X.; Lei, L.; Schartup, A.T.; Peng, Y.; Pang, Q.; Wang, X.; Mai, L.; et al. Plastic waste discharge to the global ocean constrained by seawater observations. *Nat. Commun.* **2023**, *14*, 1372. [CrossRef]
3. Ministerio para la Transición Ecológica y el Reto Demográfico. Basuras Marinas. 2023. Available online: https://www.miteco.gob.es/es/costas/temas/proteccion-medio-marino/basuras-marinas.html (accessed on 11 October 2023).
4. Cózar, A.; Sanz-Martín, M.; Martí, E.; González-Gordillo, J.I.; Ubeda, B.; Gálvez, J.A.; Irigoien, X.; Duarte, M. Plastic Accumulation in the Mediterranean Sea. *PLoS ONE* **2015**, *10*, e0121762. [CrossRef]
5. Ministerio para la Transición Ecológica. *Basuras Marinas*; Catálogo Publicaciones de la Administración General de Estado: Madrid, Spain, 2016; NIPO: 013-18-097-2.
6. Fu, Y.C.; Ho, M.L.; Wu, S.C.; Hsieh, H.S.; Wang, C.K. Porous bioceramic bead prepared by calcium phosphate with sodium alginate gel and PE powder. *Mater. Sci. Eng. C* **2008**, *28*, 1149–1158. [CrossRef]
7. Vitale-Brovarone, C.; Verné, E.; Robiglio, L.; Martinasso, G.; Canuto, R.A.; Muzio, G. Biocompatible glass–ceramic materials for bone substitution. *J. Mater. Sci. Mater. Med.* **2008**, *19*, 471–478. [CrossRef]
8. Kirschner, L.I. Lightweight Aggregate for Concrete and Method for Making Same. United States Patent No. 3992216, 16 November 1976.
9. Malloy, R.; Kashi, M.G.; Swan, C.W. Fly Ash/Mixed Plastic Aggregate and Products Made Therefrom. United States Patent No. US6669773B2, 30 December 2003.
10. Moreno-Maroto, J.M.; González-Corrochano, B.; Alonso-Azcárate, J.; Martínez García, C. A study on the valorization of a metallic ore mining tailing and its combination with polymeric wastes for lightweight aggregates production. *J. Clean. Prod.* **2019**, *212*, 997–1007. [CrossRef]

11. Moreno-Maroto, J.M.; González-Corrochano, B.; Alonso-Azcárate, J.; Martínez García, C. Sintering of sepiolite-rich by-products for the manufacture of lightweight aggregates: Technological properties, thermal behavior and mineralogical changes. *Mater. Construcción* **2021**, *71*, e241. [CrossRef]
12. Ramamurthy, K.; Harikrishnan, K.I. Influence of binders on properties of sintered fly ash aggregate. *Cem. Concr. Compos.* **2006**, *28*, 33–38. [CrossRef]
13. Güneyisi, E.; Gesoglu, M.; Altan, I.; Öz, H.O. Utilization of cold bonded fly ash lightweight fine aggregates as a partial substitution of natural fine aggregate in self-compacting mortars. *Constr. Build. Mater.* **2015**, *74*, 9–16. [CrossRef]
14. Nor, A.M.; Yahya, Z.; Abdullah, M.M.A.B.; Razak, R.A.; Ekaputri, J.J.; Faris, M.A.; Hamzah, H.N. A Review on the Manufacturing of Lightweight Aggregates Using Industrial By-Product. In Proceedings of the 2nd International Conference on Green Design and Manufacture 2016 (IConGDM 2016) MATEC Web of Conferences, Phuket, Thailand, 1–2 May 2016; Volume 78, p. 01067. [CrossRef]
15. Mackenzie, K.J.; Welter, M. Geopolymer (aluminosilicate) composites: Synthesis, properties and applications. In *Advances in Ceramic Matrix Composites*; Woodhead Publishing: Cambridge, UK, 2014; pp. 445–470. [CrossRef]
16. Peyne, J.; Gautron, J.; Doudeau, J.; Rossignol, S. Development of low temperature lightweight geopolymer aggregate, from industrial Waste, in comparison with high temperature processed aggregates. *J. Clean. Prod.* **2018**, *189*, 47–58. [CrossRef]
17. Ayati, B.; Ferrándiz-Mas, V.; Newport, D.; Cheeseman, C. Use of clay in the manufacture of lightweight aggregate. *Constr. Build. Mater.* **2018**, *162*, 124–131. [CrossRef]
18. Fawer, M.; Concannon, M.; Rieber, W. Life cycle inventories for the production of sodium silicates. *Int. J. Life Cycle Assess.* **1999**, *4*, 207–212. [CrossRef]
19. AMI2030. Materials 2030 Manifesto: Systemic Approach of Advanced Materials for Prosperity—A 2030 Perspective. Advanced Materials Initiative 2030. 2022. Available online: https://www.ami2030.eu/wp-content/uploads/2022/06/advanced-materials-2030-manifesto-Published-on-7-Feb-2022.pdf (accessed on 7 February 2022).
20. AMI2030. Materials 2030 Roadmap. Advanced Materials Initiative 2030. 2022. Available online: https://www.ami2030.eu/wp-content/uploads/2022/12/2022-12-09_Materials_2030_RoadMap_VF4.pdf (accessed on 7 February 2022).
21. Moreno-Maroto, J.M.; Alonso-Azcárate, J. Hydrothermal zeolitization: Towards a paradigm shift for producing stronger and more sustainable construction materials. *Constr. Build. Mater.* **2024**, *427*, 136269. [CrossRef]
22. *ASTM D4318-10e1*; Standard Test Methods for Liquid Limit, Plastic Limit, and Plasticity Index of Soils. Annual Book of ASTM Standards. ASTM International: West Conshohocken, PA, USA, 2017.
23. Moreno-Maroto, J.M.; González-Corrochano, B.; Alonso-Azcárate, J.; Rodríguez, L.; Acosta, A. Development of lightweight aggregates from stone cutting sludge, plastic wastes and sepiolite rejections for agricultural and environmental purposes. *J. Environ. Manag.* **2017**, *200*, 229–242. [CrossRef] [PubMed]
24. Földvári, M. *Handbook of Thermogravimetric System of Minerals and Its Use in Geological Practice*; Occasional Papers of the Geological Institute of Hungary; Geological Institute of Hungary: Budapest, Hungary, 2011; Volume 213, ISBN 978-963-671-288-4.
25. Yashima, S.; Kanda, Y.; Sano, S. Relationship between particle size and fracture energy or impact velocity required to fracture as estimated from single particle crushing. *Powder Technol.* **1987**, *51*, 277–282. [CrossRef]
26. Li, Y.; Wu, D.; Zhang, J.; Chang, L.; Fang, Z.; Shi, Y. Measurement and statistics of single pellet mechanical strength of differently shaped catalysts. *Powder Technol.* **2000**, *113*, 176–184. [CrossRef]
27. *EN 1097-6*; Tests for Mechanical and Physical Properties of Aggregates—Part 6: Determination of Particle Density and Water Absorption. European Committee for Standardization: Brussels, Belgium, 2013.
28. IZA. Database of Zeolite Structures. International Zeolite Association. 2024. Available online: https://europe.iza-structure.org/IZA-SC/ftc_table.php (accessed on 1 July 2024).
29. Hansen, S.; Fälth, L. X-ray study of the nepheline hydrate I structure. *Zeolites* **1982**, *2*, 162–166. [CrossRef]
30. Lin, D.-C.; Xu, X.-W.; Zuo, F.; Long, Y.-C. Crystallization of JBW, CAN, SOD and ABW type zeolite from transformation of meta-kaolin. *Microporous Mesoporous Mater.* **2004**, *70*, 63–70. [CrossRef]
31. Deng, Y.; Flury, M.; Harsh, J.B.; Felmy, A.R.; Qafoku, O. Cancrinite and sodalite formation in the presence of cesium, potassium, magnesium, calcium and strontium in Hanford tank waste simulants. *Appl. Geochem.* **2006**, *21*, 2049–2063. [CrossRef]
32. Selim, A.Q.; Mohamed, E.A.; Seliem, M.K.; Zayed, A.M. Synthesis of sole cancrinite phase from raw muscovite: Characterization and optimization. *J. Alloys Compd.* **2018**, *762*, 653–667. [CrossRef]
33. Chen, X.; Qiao, M.; Xie, S.; Fan, K.; Zhou, W.; He, H. Self-Construction of Core−Shell and Hollow Zeolite Analcime Icositetrahedra: A Reversed Crystal Growth Process via Oriented Aggregation of Nanocrystallites and Recrystallization from Surface to Core. *J. Am. Chem. Soc.* **2007**, *129*, 13305–13312. [CrossRef]
34. Ma, X.; Yang, J.; Ma, H.; Liu, C.; Zhang, P. Synthesis and characterization of analcime using quartz syenite powder by alkali-hydrothermal treatment. *Microporous Mesoporous Mater.* **2015**, *201*, 134–140. [CrossRef]
35. Jacas-Rodríguez, A.; Rodríguez-Pascual, P.; Franco-Manzano, D.; Contreras, L.; Polop, C.; Rodriguez, M.A. Mixed Matrix Membranes prepared from polysulfone and Linde Type A zeolite. *Sci. Eng. Compos. Mater.* **2020**, *27*, 236–244. [CrossRef]
36. Campoverde, J.; Guaya, D. From Waste to Added-Value Product: Synthesis of Highly Crystalline LTA Zeolite from Ore Mining Tailings. *Nanomaterials* **2023**, *13*, 1295. [CrossRef]
37. Zgureva, D.; Boycheva, S. Synthetic Zeolitic Ion-Exchangers from Coal Ash for Decontamination of Nuclear Wastewaters. *Bulg. Nucl. Soc. Trans.* **2015**, *20*, 132–136.

38. Tang, Q.; Ge, Y.Y.; Wang, K.T.; He, Y.; Cui, X.M. Preparation of porous P-type zeolite spheres with suspension solidification method. *Mater. Lett.* **2015**, *161*, 558–560. [CrossRef]
39. Zhou, Q.; Jiang, X.; Qiu, Q.; Zhao, Y.; Long, L. Synthesis of high-quality NaP1 zeolite from municipal solid waste incineration fly ash by microwave-assisted hydrothermal method and its adsorption capacity. *Sci. Total Environ.* **2023**, *855*, 158741. [CrossRef] [PubMed]
40. Khodabandeh, S.; Davis, M.E. Zeolites P1 and L as precursors for the preparation of alkaline-earth zeolites. *Microporous Mater.* **1997**, *12*, 347–359. [CrossRef]
41. *EN 13055-1*; Lightweight Aggregates. Part 1: Lightweight Aggregates for Concrete, Mortar and Grout. European Committee for Standardization: Brussels, Belgium, 2002.
42. European Parliament. Plastic Waste and Recycling in the EU: Facts and Figures. 2024. Available online: https://www.europarl.europa.eu/topics/en/article/20181212STO21610/plastic-waste-and-recycling-in-the-eu-facts-and-figures (accessed on 11 August 2024).

Disclaimer/Publisher's Note: The statements, opinions and data contained in all publications are solely those of the individual author(s) and contributor(s) and not of MDPI and/or the editor(s). MDPI and/or the editor(s) disclaim responsibility for any injury to people or property resulting from any ideas, methods, instructions or products referred to in the content.

applied sciences

MDPI

Article

Optimizing Masonry Mortar: Experimental Insights into Physico-Mechanical Properties Using Recycled Aggregates and Natural Fibers

Daniel Ferrández [1,*,†], Alicia Zaragoza-Benzal [1,†], Rocío Pastor Lamberto [2], Paulo Santos [3] and Jacek Michalak [4]

[1] Departamento de Tecnología de la Edificación, Escuela Técnica Superior de Edificación, Universidad Politécnica de Madrid, Avda. Juan de Herrera, 6, 28040 Madrid, Spain; alicia.zaragoza@upm.es
[2] Departamento de Arquitectura y Tecnologías de la Edificación, Escuela Técnica Superior de Arquitectura y Edificación, Universidad Politécnica de Cartagena, C/Real, 3, 30201 Cartagena, Spain; rocio.pastor@upct.es
[3] University of Coimbra, ISISE, ARISE, Department of Civil Engineering, 3030-788 Coimbra, Portugal; pfsantos@dec.uc.pt
[4] Research and Development Center, Atlas sp. z o.o., 2, Kilinskiego St., 91-421 Lodz, Poland; jmichalak@atlas.com.pl
* Correspondence: daniel.fvega@upm.es
† These authors contributed equally to this work.

Abstract: The European Green Deal establishes the efficient management of construction resources as one of its main lines of action. In this sense, the recovery of construction and demolition waste for its reincorporation into the manufacturing process of new sustainable materials has become necessary for the industry. This work deals with the physical and mechanical characterization of cement mortars made with recycled concrete aggregates and reinforced with natural fibers. The reinforcement fibers used (abaca, coconut, and toquilla) are more environmentally friendly compared to traditional synthetic reinforcements. The aim of this research is to analyze the main physico-mechanical properties of these sustainable cement mortars. The results show that mortars made with recycled sand have a lower density and better thermal performance than traditional mortars. In addition, with the incorporation of these natural fibers, the flexural strength of the mortars with recycled aggregate increased by up to 37.6%. Another advantage obtained from the incorporation of these natural fibers is the reduction in shrinkage in the masonry mortars during the drying process, giving them greater dimensional stability and making their behavior similar to that of traditional mortars. Thus, this work shows the potential application of masonry mortars produced under circular economy criteria and their application in the building sector.

Keywords: circular economy; recycled aggregates; natural fibers; cement-based mortars; materials characterization

1. Introduction

According to the latest estimations, the building materials market will reach USD 1.5 trillion by 2027, a consequence, among other factors, of the accelerated growth of infrastructure in emerging economies [1]. Thus, this increase in market share linked to construction's intensive nature will be related to an increase in the consumption of natural resources and energy, leading to a strong environmental impact in terms of greenhouse gas emissions and waste generation [2]. Construction and demolition waste (CDW) is produced in the process of construction, maintenance, demolition and deconstruction of infrastructure and buildings [3]. This waste, mainly solid, has a very heterogeneous and generally inert nature [4]. According to the latest UN figures, each citizen in an economically developed region contributes approximately two tons of CDW per year, which implies more than 500 million tons of CDW per year [5].

Unfortunately, the vast majority of these CDW are disposed of in landfills in large cities, posing a risk to health, the environment and wasting resources [6]. The European Union, aware of this global problem, has promoted the efficient use of resources in construction for responsible economic growth through the European Green Deal [7]. For this reason, in recent decades, several lines of research have emerged that are committed to the incorporation of circular economy criteria and the redesign of traditional construction products. In this work, the study of the physical and mechanical properties of masonry mortars made with recycled concrete aggregate and natural fibers is addressed, thus seeking to promote the application of eco-friendly materials in the construction sector.

Concrete is the most consumed building material on the planet, generating a strong environmental impact due to the high energy consumption required for its production [8], while at the same time it is responsible for most CDW (between $100 \cdot 10^9$ and $340 \cdot 10^9$ kg in the EU alone [9]). The use of recycled concrete aggregates (RCA) is essential for CDW recovery and revalorization, as it allows the production of sustainable mortars and concretes with a lower demand for original raw materials [10]. In general terms, the physical and mechanical characteristics of RCA, such as their high content of surface impurities as a result of the cementitious layer adhered to the aggregate during the crushing and grinding of these wastes [11], make it difficult to use them in structural elements. This mortar layer that covers the RCA decreases its mechanical strength the lower the quality of the old mortar adhered and can also compromise the durability of the composites made with these secondary raw materials as a result of their higher porosity and water absorption capacity compared to natural aggregate [12].

On the other hand, these RCA have a higher content of fine particles, which means that it is necessary to use a higher content of mixing water or to use chemical superplasticizing agents in the dosing of mortars [13]. This aggregate particle size can be corrected to some extent by introducing washing and sieving stages prior to the use of the aggregate, although it is true that qualitatively its physical properties do not usually improve with respect to natural aggregate [14]. Another consequence of the use of these aggregates in the manufacture of masonry mortars is the increase in shrinkage during the setting process, which causes surface cracks that can compromise their durability [15].

For this reason, reinforcement fibers have become a technically and economically viable alternative to improve the properties of mortars and concrete made with these recycled aggregates.

Literature Review on Mortars with Natural Fibers: Coconut, Abaca and Toquilla

For centuries, natural fibers have been present in the execution of construction works, extending their application as reinforcement in the elaboration of materials [16]. So much so that, thanks to their low cost and local availability, they have been frequently used in housing and rural structures, contributing to improve the thermal resistance of the base material and being a light and easy to repair addition [17]. Research has also shown how replacing synthetic fiber reinforcement with natural fibers can help mitigate adverse air pollution effects [18]. The high carbon footprint and a large amount of energy required to produce commercial synthetic fibers are some of the reasons that have driven research to look for alternative and eco-friendly solutions for the reinforcement of composite materials [19]. The use of natural fibers still needs to be improved, but thanks to continuous research, the development of new methods, and the growing awareness that they are a sustainable alternative to conventional materials, their use is increasing in various industries [20].

The origin of these natural fibers is very diverse, e.g., hemp, bamboo, sisal, wheat straw, date palm, rice husk, pineapple, jute or banana, and many research have been carried out in this area [21]. In this research, three natural fibers have been used as reinforcement material for mortars: coconut, abaca and toquilla straw.

First, a review of the most recent studies on coconut fiber reinforced cement mortars is presented in Table 1.

Table 1. Coconut fiber-reinforced cement mortar studies.

Ref.	Fiber Addition	Fiber Length [mm]	Main Results
[22]	0, 4, 6, and 8% by weight of cement	16.7	In all cases the flexural strength was increased, however, for the compressive strength a decrease was observed from 4% added fiber. Capillary water absorption in the mortars is increased. Energy consumption and CO_2 emissions during production decreased by more than 11% compared to the control mortar without coconut fiber.
[23]	0, 0.2, 0.4, and 0.6% mass fractions of cement and soil mix	24.0	The coconut fiber reinforcement increased mortar blocks' residual strength under compression, as well as their ductility and energy absorption. In addition, a significant improvement in mortar durability against freeze–thaw and moisture–dryness cycles was obtained.
[24]	0.5, 1.0, 1.5, and 2.0% relative to the weight of cement	30.0	Properties of cement mortars with coconut fiber in masonry walls were evaluated. The best results were obtained for addition of 0.5% fiber, significantly improving flexural strength and slightly increasing diagonal compression in walls.
[25]	0, 0.25, 0.5, 0.75, 1.0, 1.25 and 1.5% by volume	Less than 3.0	As the interface between added fibers and mortar matrix weakened, there was an improvement in the mortars' cushioning properties. However, there was a compressive strength loss and an increase in porosity.
[26]	0.125, 0.25, 0.5 and 0.75 by weight of mortar mix	24.0	While there was no significant improvement in flexural and compressive mechanical strengths, post-cracking properties such as ductility, residual strength and toughness increased with a higher fraction of coconut fiber in the mortar matrix.
[27]	0, 1, 2.5, and 4% by volume	17.0	Coconut fiber addition positively influenced the first crack deflection, improving the toughness indices, plastic cracking and impact strength of the produced cementitious mortars.
[28]	0, 1, 2 and 3% by volume of mortar	10.0–20.0	The best results were obtained with additions of coconut fiber at 2% by volume of mortar, significantly increasing flexural strength compared to the reference, improving toughness, and preventing cracking.
[29]	0, 1, 2 and 3% by volume of mortar	16.0–18.0	The mortars were subjected to moisture–dryness cycles and an increase in wetting was observed in coconut fiber samples. Natural degradation of the fibers in the mortar matrix occurred, which decreased the mechanical strengths.
[30]	1.5% by volume of mortar	15.0	Higher flexural strengths, increased fracture energy and increased capillary water absorption were obtained compared to traditional mortar.
[31]	0, 5, 10, 15, and 20% by weight of cement	60.0	The potential use of coconut fiber reinforced mortars as a façade cladding material was analyzed. It was found that these mortars with plant fibers could reduce dwelling interior temperatures by 0.5–1.5 °C.
[32]	0.25 and 0.5% by weight of cement	More than 10	The coconut fiber reinforced mortars significantly improved flexural and compressive mechanical strengths, satisfying the criteria for application as mortar in masonry walls according to Colombian standards.
[33]	0, 3, 6, 9, 12, and 15% by weight of cement	10.0–30.0	Composite with a combination of 10% silica fume, 10% metakaolin and 6% coconut fibers showed superior mechanical and physical properties to the reference mortar, with a compact microstructure, making it a sustainable and environmentally friendly alternative.

Note: Search in Web of Science with the keywords: ((“Coco” OR “Coconut”) AND (“Fiber*” OR “Fiber*”) AND (“Mortar*”)).

Firstly, there is a discrepancy in the ideal percentage of fiber to add, as well as in the optimum fiber length. While it is true that additions in mortar volume between 1 and 2% and lengths between 15 and 20 mm provided in all cases improvements in mechanical flexural strengths [28,30]. In addition, it has been observed that the addition of these fibers improved the toughness and prevented mortars cracking [26], while increasing

their thermal resistance [31] and the durability of these cement composites [23]. Negative effects include the possible degradation of the fibers when subjected to moisture–dryness cycles [29].

Similarly, a brief review of the most recent research findings on abaca fiber reinforced mortars is shown in Table 2.

Table 2. Studies on abaca fiber-reinforced cement mortar.

Ref.	Fiber Addition	Fiber Length [mm]	Main Results
[34]	0.2, 0.3 and 0.4% over the total solid weight	20.0, 25.0, 30.0 and 35.0	The best results were obtained in mortars made with treated fibers with a 3% NaOH solution, with a length of 30 mm and incorporated at 0.2% of the mortar weight. With this composition, it was possible to improve the mechanical resistance to bending and compression, with a good fiber integration in the matrix.
[35]	0.2% over the total solid weight	30.0	Flexural strength was improved by 20%, compressive strength by 28% and tensile strength by 26% compared to the reference mortars. In addition, the abaca fiber mortars improved their dimensional stability by reducing shrinkage.
[36]	0, 0.25, 0.5, 1 and 2% of the weight of cement	4.5	The good hygroscopic properties of abaca fibers reduce the autogenous shrinkage of mortars, improving their mechanical performance and mitigating cracking risk. In addition, the presence of these fibers delays mortar setting time.
[37]	1% over the total solid weight	10.0, 30.0, 80.0, 100.0 and 300.0	Abaca fibers showed great potential for application in rehabilitation mortars for masonry houses. The optimum fiber length for improving flexural strength and wall ductility was found to be 80 mm.

Note: Search in Web of Science with the keywords: ((“Abacá” OR “Abaca”) AND (“Fiber*” OR “Fiber*”) AND (“Mortar*”)).

In view of the obtained results by other researchers shown in Table 2, it can be seen that abaca fibers also allow to improve the mechanical behavior to bending in masonry mortars [37]. Additionally, the good hygroscopic properties of these fibers and their potential application to reduce shrinkage are highlighted [35,36]. Finally, the importance of pre-treatment of natural fibers is emphasized, with the aim of increasing their durability and favoring the integration of the fiber into the mortar matrix [34].

No research has been found on the use of toquilla straw fibers in the manufacture of cement mortars, however, the potential applications of toquilla straw as a thermoplastic reinforcement for composite materials were reported [38]. Toquilla straw or *Carludovica palmata* has been commonly used in hot and humid regions of South America for the manufacture of hats and handicrafts. Although its application in construction has not yet been widely exploited, other similar natural fibers such as wheat straw [39], kenaf straw [40], rice straw [41] or cotton straw [42] have been widely used. In general terms, these fibers have been used as structural reinforcement material in mortar and concrete, with the aim of improving the mechanical strength, toughness and deformation capacity of cement-based composite materials, as well as obtaining improved thermal properties [43].

Moreover, there are constantly new reports about the possibility of using new natural fibers, such as guaruma (Ischinosiphon koern) of Amazonian origin—natural fibers still unexplored with great potential for use in cementitious systems [44]. Many review articles, often critical ones, have examined the potential use of natural fibers to reinforce cementitious systems [45–47]. In recent years, the need to reconcile technological development in the cement industry with the preservation of the environment has led to the use of silica-rich ash residues, from the calcination of plant fibers such as corn straw, sugar cane straw or rice straw [48]. This novel application has become a promising alternative for the partial substitution of cement in the development of new eco-friendly mortars, which in turn have physical-mechanical properties that make them competitive in the market [49]. However, although the use of natural fiber has gained prominence in the area of materials engineering due to the versatility of the use of natural fibers in cementitious composites.

There are also some disadvantages of using these fibers in the matrix of mortars. As demonstrated in some research [44], the incorporation of these reinforcing materials can result in a loss of workability of the mix or wettability, as well as the difficulty to distribute the fiber homogeneously or the need for prior treatments that improve the behavior and durability of the fiber for application in matrices.

In short, based on the current state of knowledge, the objective of this research is to analyze the physical and mechanical properties of masonry mortars made with recycled concrete sand and reinforced with natural fibers. For this purpose, a characterization of the developed cement materials, to which coconut, abaca, and toquilla straw fibers have been added, will be carried out. To date, no research work has been found that comparatively analyzes the effect of these three types of reinforcement on cement mortars made with RCA. This may be of particular interest for the development of sustainable mortars in South American countries where these three types of natural fibers are highly abundant. The aim is to contribute to the development of eco-friendly mortars and to promote their application in the building sector. The research thus falls within the framework of the Sustainable Development Goals (SDGs) included in the 2030 Agenda, and more specifically, SDG 9, "Industry, Innovation and Infrastructure" [50]. Moreover, this work is also essential in terms of the contemporary perception of the environmental impact of construction products, namely that using natural materials of plant origin is crucial [51], Any positive example of using recycled materials in construction is additionally significant because demolition/recycled materials are perceived as less valuable in construction for fear that they will not meet specific requirements in terms of mechanical strength [52]. Moreover, the innovative simultaneous use of RCA and natural fibers in masonry mortars is crucial for this research.

2. Materials and Methods

This section describes the raw materials used to make the cement mortars studied in this research, as well as their dosage and manufacturing process. Subsequently, the experimental campaign conducted is described, indicating the equipment and methods applied.

2.1. Materials

The materials used to make the masonry mortars were cement, water, natural aggregate, recycled concrete aggregate, and natural coconut, abaca, and toquilla straw fibers.

2.1.1. Cement

The binder used for the mortars' preparation was CEM II/B-L 32.5 N cement. This material commonly used in building construction, is made up of Portland clinker, limestone, and up to 5% additions [53]. Table 3 shows the elemental composition of this raw material obtained by X-ray fluorescence.

Table 3. Elemental composition of cement type CEM II/B-L 32.5 N. Results in percentage by mass.

CaO	SiO_2	SO_3	Al_2O_3	Fe_2O_3	K_2O	TiO_2	MgO	SrO	BaO	MnO	P_2O_5	I. Loss
67.11	16.98	4.56	4.38	3.56	0.71	0.23	0.25	0.09	0.07	0.09	0.04	1.93

As shown in Table 3, different oxides constitute the cement used in this research, with CaO, SiO_2, SO_3, Al_2O_3, and Fe_2O_3 being the majority. These oxides are essential for the formation of the potential compounds of cementitious materials: tricalcium silicate (SC_3), dicalcium silicate (SC_2), tricalcium aluminate (AC_3), and tetracyclic aluminoferrite (AFC_4) [54]. Finally, it should be noted that the appearance of sulfur oxide in the cement composition is linked to the use of gypsum compounds during the manufacturing process, which are added to mitigate setting time [55].

2.1.2. Water

In the development of the different samples elaborated in this work, drinking water from the Canal de Isabel II of the Community of Madrid has been used. This tap water has been successfully used in previous research [56], according to Council Directive 98/83/EC [57]. Its main characteristics are its combined Cl content of 1.13 mg/L, pH 7.8, and conductivity of 116.7 μS/cm [58].

2.1.3. Aggregates

Two different types of aggregates have been used for the development of this research: natural sand (NA) standardized for reference tests distributed by the Eduardo Torroja Institute of Construction Sciences (Madrid, Spain), and recycled sand from concrete waste (RCA) supplied by the TEC-REC plant (Madrid, Spain). First, the physical properties of these raw materials were analyzed in Table 4, following the recommendations of the reference standards.

Table 4. Aggregates' physical characterization.

Properties	NA	RCA	Normative
Fine Content (%)	1.23 ± 0.06	3.87 ± 0.10	UNE–EN 933-1 [59]
Particle Form	Not relevant	Not relevant	UNE–EN 13139 [60]
Fineness Modulus (%)	2.56 ± 0.14	4.11 ± 0.08	UNE–EN 13139 [60]
Friability Coefficient (%)	14.11 ± 0.25	24.15 ± 0.23	UNE–EN 146404 [61]
Bulk Density (kg/m^3)	1560 ± 17	1387 ± 14	UNE–EN 1097-3 [62]
Dry Density (kg/m^3)	2569 ± 3	2398 ± 16	UNE–EN 1097-6 [63]
Water Absorption (%)	0.54 ± 0.04	5.87 ± 0.09	UNE–EN 1097-6 [63]

As can be seen in Table 4, the fine particle content of the recycled aggregates was higher than that obtained for the standard sand. This is due to the process of crushing and obtaining these secondary raw materials, and if their particle size is not controlled by sieving before use, they can cause a decrease in the mechanical strength of masonry mortars [64]. Furthermore, these recycled sands have a higher friability coefficient and a lower density, which implies a decrease in the mechanical properties of the mortars, as has been demonstrated in another research [65]. It should also be noted that these RCA had a higher water absorption coefficient, which results in a higher water demand during mortar mixing [66].

Figure 1 shows the granulometric curve obtained for applying these aggregates in the manufacture of cement mortar. The aim was to obtain a continuous particle size that favors mixture workability, using a back-and-forth sieve shaker and a series of standardized sieves according to UNE-EN 933-2 [67].

Finally, an elemental analysis was carried out to determine the chemical composition of the recycled concrete aggregates. The results obtained using the X-ray fluorescence technique are shown in Table 5.

Table 5. Elemental composition of recycled concrete aggregates. Results in percentage by mass.

Aggregate	Al_2O_3	CaO	Fe_2O_3	K_2O	MgO	SiO_2	MnO	TiO_2	SO_3	P_2O_5	NaO_2	I. Loss
RCA	10.81	12.03	1.56	2.41	0.98	57.92	0.43	0.65	1.03	0.09	0.41	11.68

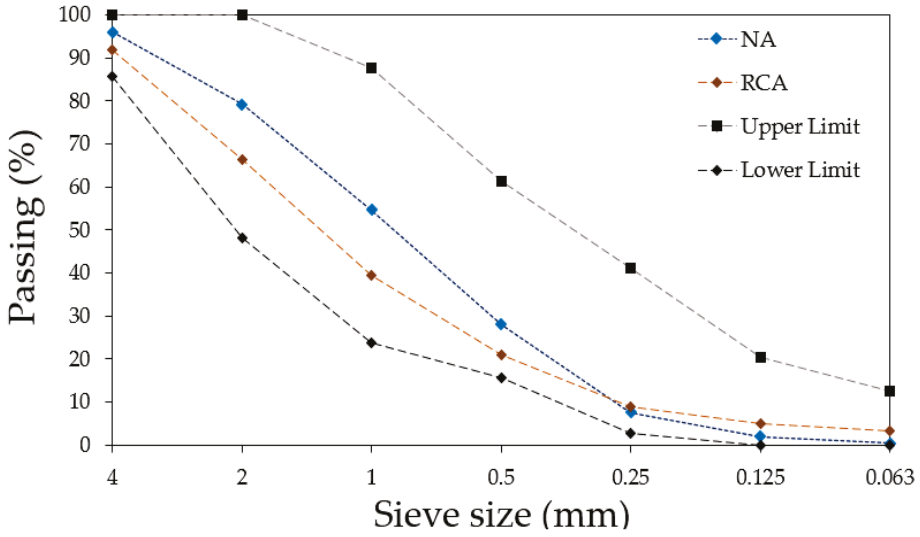


Figure 1. Aggregate particle size curves compared with limits set out in NBE FL-90 standard [67] and adapted to sieves series indicated in UNE-EN 933-2 [68].

As can be seen in Table 5, RCA used have a majority composition of SiO_2 (57.92%) as a consequence of the natural aggregate used in the manufacture of concrete. In addition, CaO and SO_3 impurities are observed, generally coming from gypsum waste mixed in the building demolition process [69]. High content of sulfur impurities can be detrimental to the durability of reinforcement or other steel elements that come into direct contact with these mortars. Therefore, it is important to insist on the need for selective demolition processes at the end of the life of the building [70]. Finally, ignition losses (11.68%) are a consequence of the organic matter content of these secondary raw materials.

2.1.4. Natural Fibers

Three natural fibers have been used as reinforcement material: coconut, abaca and toquilla straw. These fibers are shown in Figure 2.

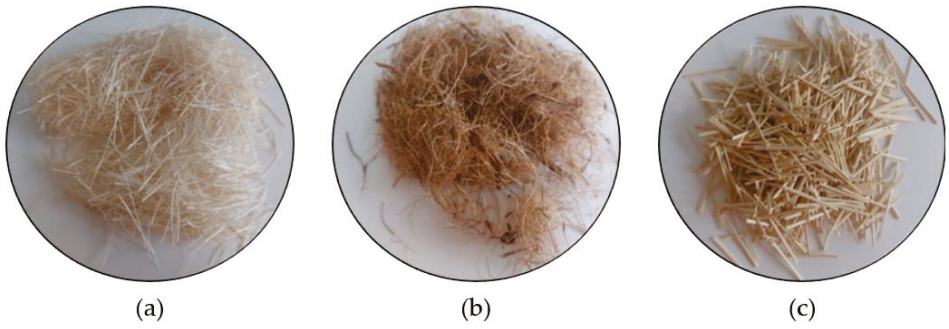


Figure 2. Natural fibers used: (**a**) abaca fiber; (**b**) coconut fiber; (**c**) toquilla straw fiber.

All fibers used and shown in Figure 2 were manually cut to a length of 20 ± 1 mm. In addition, these fibers have the properties shown in Table 6.

Table 6. Properties of the natural fibers used in this research.

Fiber	Bulk Density (kg/m^3)	Young's Modulus (GPa)	Diameter (mm)
Abaca	1230 ± 8	22.7 ± 1.3	0.1–0.4
Coconut	1340 ± 15	16.4 ± 0.9	0.1–1.2
Toquilla straw	670 ± 12	11.5 ± 0.7	0.7–1.1

Regarding the natural fiber treatment, the vast majority of studies have opted for using NaOH solutions in the range of 1–15% [71]. According to a review of the current literature [72,73], this type of pre-treatment improves durability, tensile strength, and Young's modulus compared to untreated natural fibers. Thus, in this research, the three types of fibers used were pre-treated by soaking the fibers in a 5% NaOH solution by mass for 2 days, washing them with water and manually separating the fibers, drying the fibers for 24 h at a temperature of 45 ± 5 °C, and finally, they were stored in airtight containers until their use.

2.2. Production Process

For the preparation of the different types of mortar used in this research, the recommendations of the UNE-EN 196-1 standard [74] were followed. The same techniques and methods outlined in Figure 3 have always been used, using an IBERTEST planetary mixer model IB32-040V01 (Madrid, Spain).

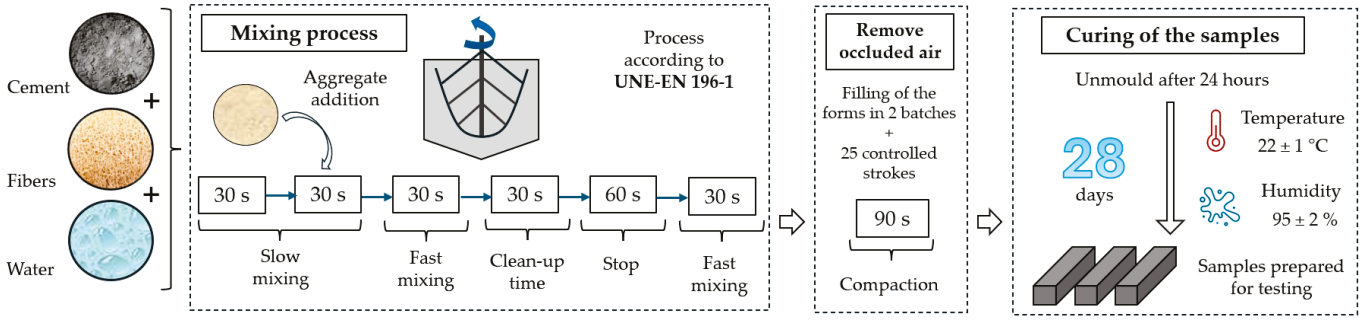


Figure 3. Manufacturing process diagram of the mortar samples used in this research.

As can be seen in Figure 3, all the samples were cured under the same conditions prior to the tests (temperature 22 ± 1 °C and ambient humidity 95 ± 2%) and for a period of 28 days.

Regarding dosages used for the preparation of the samples, Table 7 shows the mass proportions used for each type of mortar.

Table 7. Mass dosages used for the manufacture of mortars.

Type	Cement [g]	Sand [g]	Water [g]	Water/Cement Ratio	Natural Fiber Reinforcement [g]		
					Abaca	Coconut	Toquilla Straw
NA–1:3	450.0	1350	234.0	0.52	—	—	—
RCA–1:3	450.0	1350	328.5	0.73	—	—	—
RCA–1:3–1.5%(A)	450.0	1350	328.5	0.73	6.75	—	—
RCA–1:3–1.5%(C)	450.0	1350	328.5	0.73	—	6.75	—
RCA–1:3–1.5%(T)	450.0	1350	328.5	0.73	—	—	6.75
NA–1:4	337.5	1350	183.0	0.54	—	—	—
RCA–1:4	337.5	1350	283.5	0.84	—	—	—
RCA–1:4–1.5%(A)	337.5	1350	283.5	0.84	6.75	—	—
RCA–1:4–1.5%(C)	337.5	1350	283.5	0.84	—	6.75	—
RCA–1:4–1.5%(T)	337.5	1350	283.5	0.84	—	—	6.75

As seen in Table 7, two proportions of cement/aggregate by mass (1:3 and 1:4) commonly used for manufacturing of mortars have been used. A percentage of natural fiber addition corresponding to 1.5% by weight of cement has been selected, based on the results obtained by other researchers and analyzed in the literature review.

Additionally, with this added fiber proportion it was possible to obtain a plastic and workable consistency corresponding to a mortar diameter of 175 ± 10 mm in the shaking table test, following the UNE-EN 1015-3 standard [75]. It should be noted that in no case

superplasticizers were used, to eliminate environmentally harmful chemical compounds and taking into consideration that the main application of these mortars would be as a non-structural lining or bonding material [14]. Consequently, the water/cement ratio had to be increased compared to mortars made with natural aggregate, since otherwise, as highlighted in the research by Marvila et al. there is a significant difficulty to obtain an adequate workability of the mixture [76]. Finally, it should be noted that two reference mixes were prepared with standardized sand for both cement/aggregate ratios used in this research.

2.3. Experimental Programme

A schematic representation of the experimental programme developed is shown in Figure 4.

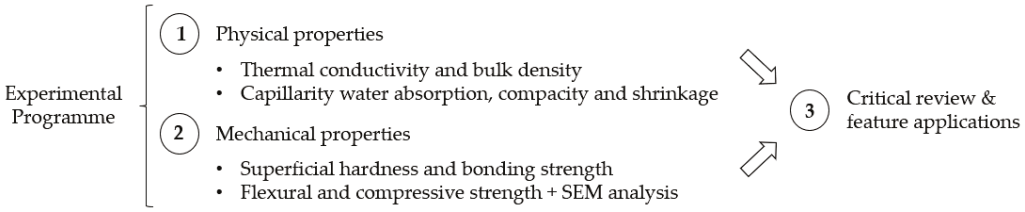


Figure 4. Experimental programme scheme.

In this way, in the first phase, a study of the masonry mortar's physical properties has been conducted through the following tests:

- Bulk density of mortars according to UNE-EN 1015-10 [77]. To determine this value, the average of three measurements taken on samples of dimension $4 \times 4 \times 16$ cm^3 is used. The bulk density is obtained by dividing the mass of the specimen previously dried in an oven for 24 h (65 ± 5 °C) by the apparent volume of the hardened mortar sample.
- Mortar thermal conductivity was determined according to the UNE-EN ISO 8990:1997 standard [78]. For this purpose, a mini thermal hot-box equipped with thermocouples and a datalogger for accumulating temperature data was used. A total of three samples were tested for each type of mortar, with dimensions of $24 \times 24 \times 3$ cm^3. The measurements were taken 24 h after the start of the test to obtain a stationary heat flux.
- Water absorption coefficient by capillarity according to UNE-EN 1015-18 [79]. In this way, six half-samples are obtained from $4 \times 4 \times 16$ cm^3 samples so that the fractured face with the open matrix is the one in contact with the water. Thus, these half-samples, previously dried for 24 h in an oven (65 ± 5 °C), are immersed vertically in water to a depth of 10 ± 1 mm. The capillary absorption coefficient is determined with the help of Equation (1):

$$C = 0.1 \cdot (M_{90} - M_{10}) \quad (1)$$

where C is the capillary absorption coefficient, and M_{10} and M_{90} correspond to the mass of the sample at 10 and 90 min of testing.

- Open porosity determined according to UNE-EN 1396 [80]. It is defined as the ratio between the accessible pore volume and mortar apparent volume. To determine this index, a total of three samples of each type were used and Equation (2):

$$Open_{Por} = \left(\frac{W_{sat} - W_0}{W_{sat} - W_{imm}} \right) \times 100 \quad (2)$$

where $Open_{Por}$ shows the open porosity index in percentage, W_{sat} is mass of water saturated sample, W_{imm} immersed weight of the water-saturated sample determined by hydrostatic balance, and W_0 is the weight of the dried sample.

- Mortar shrinkage over time according to the recommendations of the UNE 80-112-89 standard [81]. For this test, three samples of each type of mortar of dimension $2.5 \times 2.5 \times 28.7$ cm^3 were used. This test allows the determination of the dimensional stability of the mortars over time and is expressed as the longitudinal variation in mm/m experienced by the samples over 120 days.

On the other hand, the mechanical properties of these eco-friendly cement mortars have been studied. The tests carried out in this second phase include:

- Mortar bonding strength according to UNE-EN 1015-12 [82]. For this purpose, a layer of each mortar type of approximately one centimeter thickness is applied to a previously moistened ceramic block. The ceramic piece is moistened immersed in water for 24 h, in such a way that the suction of the water from the mortar mixing by the ceramic piece is avoided. Subsequently, with the help of adhesion equipment, metal discs with a diameter of 50 mm are glued with epoxy resin on the hardened sample. The tensile test determines the adhesion strength between the mortar and the application surface. A total of five samples were tested for each mortar type.
- Mortar surface hardness, determined by using a Shore D durometer (Smooth-On, Inc., Macungie, PA, USA), following the recommendations of UNE-EN-ISO 868 standard [83]. A total of three $4 \times 4 \times 16$ cm^3 samples were analyzed for each dosage, taking five measurements on the two plane-parallel faces that were in contact with the mold and separating each measurement by a minimum distance of 2 cm from each other.
- Mechanical resistance to bending and compression in standardized samples of $4 \times 4 \times 16$ cm^3 according to UNE-EN 196-1 [74]. The flexural strength test consists of a three-point breakage test, where the vertical load is applied perpendicular to the longitudinal axis of the sample and at the center of the span. Subsequently, each of the two pieces generated in this bending test is subjected to a compression breaking test using a uniform load on a surface of 4×4 cm^2. For this test, an IBERTEST hydraulic press model AUTETEST 200-10SW has been used (Madrid, Spain).
- Interior microstructure analysis of the different mortars developed in the research using scanning electron microscopy (SEM). A Jeol JSM-820 (Mitaka, Tokyo) operating at 20 kV and equipped with Oxford EDX analysis was used to carry out this analysis. The test samples were extracted from the inner matrix of the $4 \times 4 \times 16$ cm^3 mortar samples. Additionally, to ensure a good surface conductivity of electrons, the test samples were coated with a thin gold foil using a Cressington 108 model metallizer (Watford, UK).

Finally, at the end of the presentation and discussion of the results, a last subsection has been included where a critical review of the results obtained for the different properties analyzed is addressed. In this way, the application possibilities of the masonry mortars produced under the circular economy criteria studied in this research are explored.

3. Results

This section presents the results obtained after carrying out the planned experimental campaign, as well as a discussion of these results.

3.1. Physical Properties

This section presents the physical properties analyzed for the different mortar types. Firstly, Figure 5 shows the results obtained for bulk density and thermal conductivity.

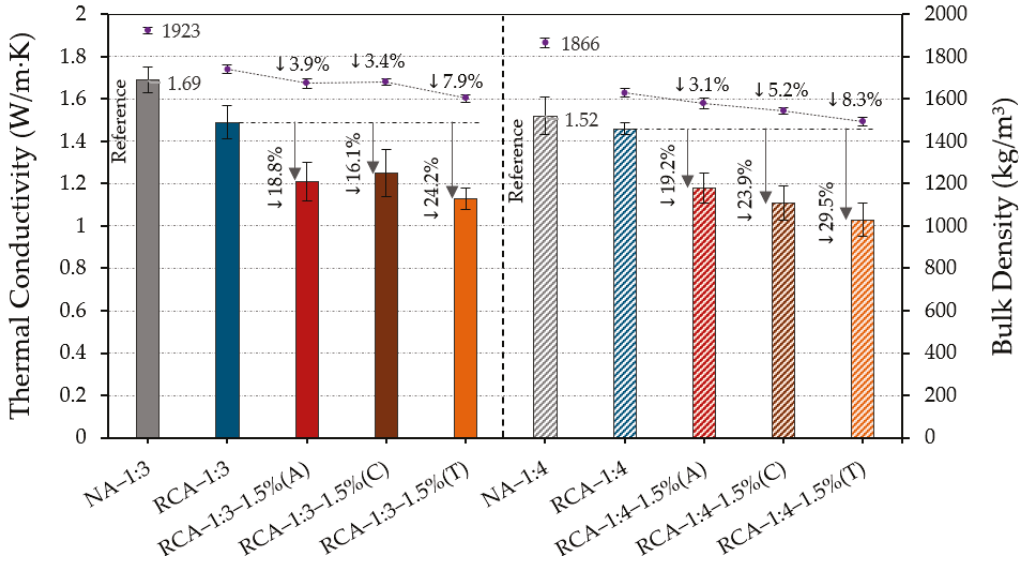


Figure 5. Thermal conductivity (bars) and bulk density (points) of the analyzed mortars.

As can be seen in Figure 5, mortars made with recycled concrete aggregate had a lower bulk density compared to traditional mortars made with natural sand. Additionally, incorporating natural fibers in these recycled mortars causes a slight reduction in density. This trend is observed for both cement/aggregate ratios, where it should be noted that mortars with a 1:4 ratio have a lower bulk density. This slight decrease in density has already been observed in other studies [84]. However, in the case of this research, it was not very significant since the natural fibers are incorporated as an addition and not as a replacement for the aggregate.

On the other hand, it is observed that the bulk density decreases experienced by mortars made with RCA translates into a decrease in their thermal conductivity. This improvement in thermal resistance has become crucial to the application of these products made with secondary raw materials in the construction sector [85]. Furthermore, no significant differences in terms of thermal conductivity were observed between samples made with cement/aggregate ratios of 1:3 and 1:4 by weight, except for the reference sample of conventional mortar. Benmansour et al. also corroborate how the addition of natural fibers reduces the thermal conductivity of masonry mortars [86]. In this sense, the addition of toquilla straw fiber produced the most significant improvements, decreasing the thermal conductivity of the recycled mortars by 24.2% and 29.5% for dosages with cement/aggregate ratios of 1:3 and 1:4, respectively. This decrease in thermal conductivity was expected because the fibers used have a lower thermal conductivity compared to the mortar matrix. In addition, the incorporation of fibers in the matrix tends to generate porosity and air in the matrix, improving the thermal resistance of the composite.

On the other hand, the behavior of the different mortar types produced against the action of water has been analyzed. Table 8 shows the results of the capillary water absorption and open porosity tests.

Table 8. Capillary water absorption and open porosity test results.

Sample	Capillarity Water Absorption ($kg/m^2 \cdot min^{0.5}$)	Open Porosity (%)	Sample	Capillarity Water Absorption ($kg/m^2 \cdot min^{0.5}$)	Open Porosity (%)
NA–1:3	0.41 ± 0.03	67.3 ± 0.9	NA–1:4	0.39 ± 0.01	70.1 ± 0.3
RCA–1:3	0.63 ± 0.01	82.4 ± 1.2	RCA–1:4	0.57 ± 0.03	83.3 ± 0.3
RCA–1:3–1.5%(A)	0.50 ± 0.03	76.5 ± 0.7	RCA–1:4–1.5%(A)	0.44 ± 0.01	76.4 ± 1.3
RCA–1:3–1.5%(C)	0.55 ± 0.02	77.1 ± 0.9	RCA–1:4–1.5%(C)	0.46 ± 0.03	78.8 ± 0.5
RCA–1:3–1.5%(T)	0.57 ± 0.02	76.8 ± 0.4	RCA–1:4–1.5%(T)	0.50 ± 0.02	78.5 ± 0.5

As seen in Table 8, the capillary water absorption coefficient of mortars made with recycled sand is much higher than that of traditional mortars made with natural sand. This phenomenon, attributed to the type of aggregate, has already been observed in previous research, where it was related to the higher water absorption capacity of recycled aggregates [87]. In addition, capillary absorption is inversely proportional to pore size, so mortars made with a cement/aggregate mass ratio of 1:4 have a lower absorption, although they would have a higher water vapor permeability [88]. Finally, as Santo de Lima et al. point out, capillarity is linked to the internal communication between the pores, so the incorporation of natural fibers causes a reduction in the capillarity coefficient that can be attributed to the clogging of the pores by these reinforcing materials [44]. For the three types of natural fibers studied, the addition of abaca fiber was the one that achieved the greatest reduction in capillarity in mortars with RCA.

On the other hand, the open porosity of the mortars with a cement/aggregate ratio of 1:4 by mass was higher than that obtained for the samples made with a 1:3 ratio. It can also be seen that this volume of accessible pores is higher in the mortars made with RCA and increases with the incorporation of natural fibers.

Figure 6 shows shrinkage evolution during the hardening process of the different mortars designed for this research.

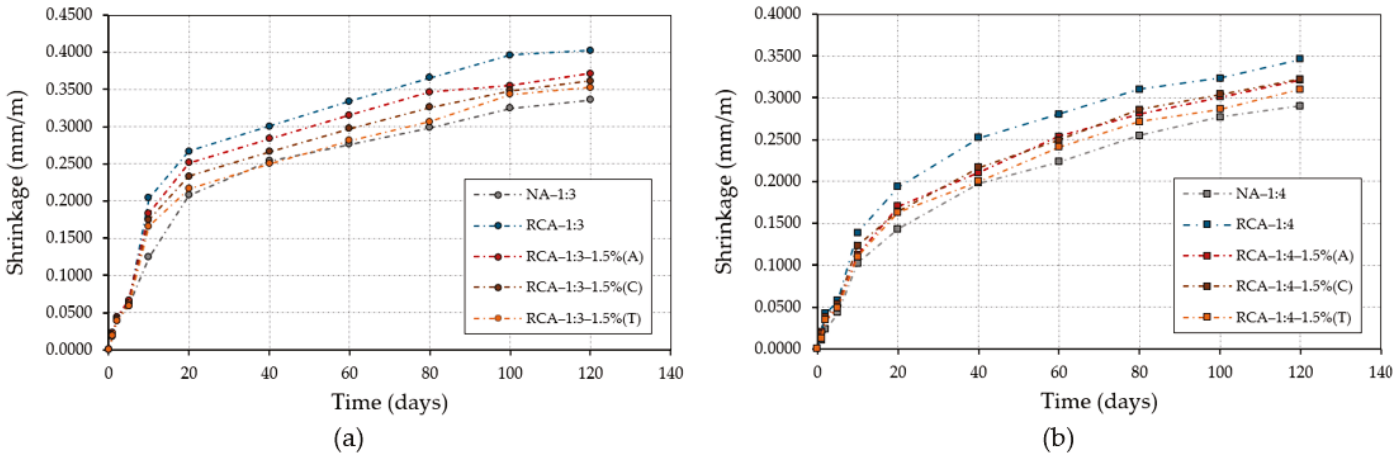


Figure 6. Shrinkage experienced by mortars over time. (**a**) Samples with cement/aggregate mass ratio 1:3. (**b**) Samples with cement/aggregate mass ratio 1:4.

The cement paste shrinks over time and causes surface cracks that contribute to a decrease in the mechanical strength and durability of the mortars [89]. Mainly, shrinkage in masonry mortars made with RCA occurs as a consequence of the higher porosity and water absorption capacity of these sands [90]. Thus, in Figure 6a,b, it can be seen how traditional mortars made with natural sand have a lower shrinkage over time. However, in agreement with previous research [65], the beneficial effect of incorporating fibers into the mortar matrix to improve its dimensional stability and reduce shrinkage is confirmed. In this sense, it was the abaca fibers that reduced the shrinkage of the mortars made with RCA to the greatest extent, approaching the values experienced by the reference mortar with natural aggregate. It can also be seen that shrinkage is higher in mortars with a 1:3 cement/aggregate ratio than in those with a 1:4 cement/aggregate mass ratio. Thus, according to Miah et al., a good distribution of natural fibers during the manufacture of cement mortars would reduce shrinkage during drying and increase the application potential of these sustainable construction materials [91].

3.2. Mechanical Properties

In this section, the mechanical properties obtained during the characterization of the developed mortars are presented. Firstly, Table 9 shows the results for surface hardness and bond strength.

Table 9. Results obtained for surface hardness and adhesion strength tests.

Sample	Superficial Hardness (Shore D Units)	Bonding Strength (MPa)	Sample	Superficial Hardness (Shore D Units)	Bonding Strength (MPa)
NA–1:3	84.1 ± 0.7	0.53 ± 0.05	NA–1:4	83.7 ± 0.6	0.42 ± 0.02
RCA–1:3	83.8 ± 0.4	0.41 ± 0.02	RCA–1:4	83.9 ± 0.5	0.35 ± 0.01
RCA–1:3–1.5%(A)	78.9 ± 0.4	0.35 ± 0.04	RCA–1:4–1.5%(A)	79.2 ± 0.8	0.29 ± 0.03
RCA–1:3–1.5%(C)	78.1 ± 1.1	0.38 ± 0.01	RCA–1:4–1.5%(C)	78.5 ± 0.7	0.30 ± 0.03
RCA–1:3–1.5%(T)	79.3 ± 0.6	0.30 ± 0.02	RCA–1:4–1.5%(T)	78.1 ± 0.4	0.26 ± 0.02

As can be seen in Table 9, there are no significant differences between the surface hardness of mortars made with natural sand and mortars made with RCA. Likewise, the cement/aggregate ratio used is not a discriminating factor for this property. However, a slight decrease in Shore D hardness is observed in those mortars that incorporate natural fibers in their composition (approximately 6–7% on average). A similar behavior was experienced by Piña et al., in their research with mortar made with the addition of recycled mineral wool fibers [57].

On the other hand, in terms of bond strength, greater differences were observed between the reference mortar and the mortar made with RCA. For both cement/aggregate ratios, the adhesion of the traditional mortars was superior to that of the RCA samples, with better adhesion for the samples with higher cement content (1:3 cement/aggregate ratio). This effect was already observed by García López de la Osa in his doctoral thesis, which showed a non-linear relationship between the increase in adhesion and the cement content of the mortars [92]. On the other hand, a slight decrease in the adhesion of mortar on ceramic walls is observed when natural reinforcement fibers are incorporated. This effect may be due to the water retention capacity of these natural fibers, as well as to the weakening of the mortar's internal microstructure at the cement-aggregate interface. Of all the mortar types analyzed, those with the incorporation of toquilla straw fiber were the least resistant to adhesion. In any case, it is worth noting that, during the test, the breakage of the samples with fibers occurred in all cases at the mortar-ceramic piece interface.

Figures 7 and 8 show the results obtained for the flexural and compressive strength tests of the mortars.

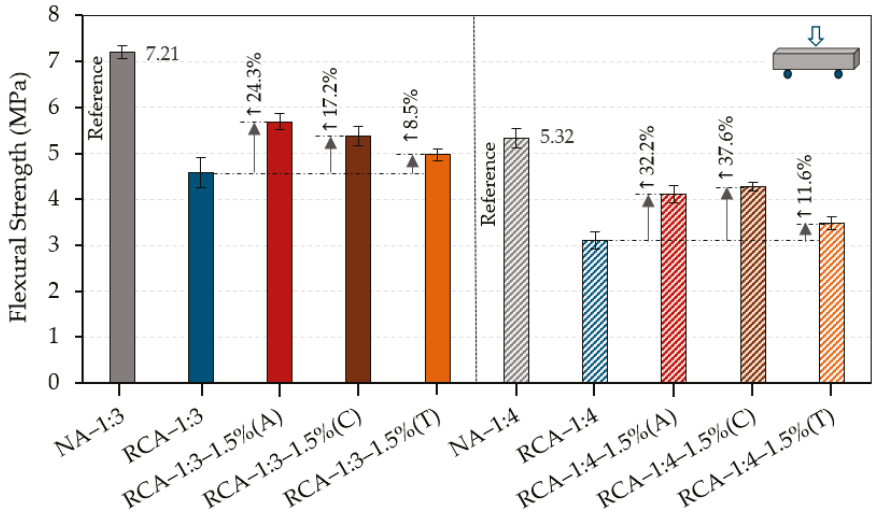


Figure 7. Flexural strength test results.

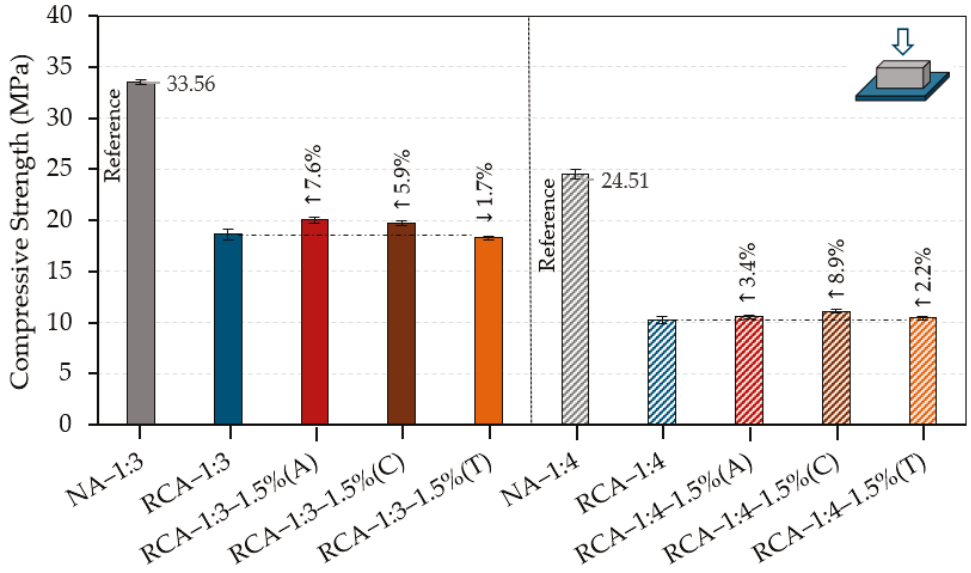


Figure 8. Compressive strength results.

Figure 7 shows that mortars with a higher cement content (1:3 cement/aggregate mass ratio) have a higher flexural strength. Also, in accordance with the results obtained in other investigations, the total substitution of the natural aggregate by RCA results in a decrease in the mechanical flexural strength [93]. For this reason, the incorporation of reinforcement fibers has become a recurrent solution to improve the mechanical strength of these construction materials produced under circular economy criteria. Thus, it is observed that in all cases, the addition of natural fibers led to an improvement with respect to the flexural strength values obtained for recycled mortars without fibers. In addition, it can be seen that coconut and abaca fibers showed a similar behavior, being the ones that increased the flexural strength to the greatest extent. These results are in agreement with others analyzed in the literature review, where natural fibers increased the deformation capacity and reduced cracking in cement mortars [27,33].

Regarding to mortar compressive strength, shown in Figure 8, it is also observed that the traditional mortars surpassed the mortars made with recycled aggregate. In this sense, the dosages with a 1:4 cement/aggregate mass ratio show a lower strength compared to their counterparts with a higher amount of cement. This effect on the compressive strength of recycled aggregates has already been observed by other researchers [94], who highlight this characteristic as one of the main limitations to their widespread use in the construction sector. In addition, it can be observed that for this property, the incorporation of reinforcement fibers does not result in an improvement in strength. In other studies, improvements were only obtained for flexural strength, even reducing the compressive strength as a consequence of the addition of fibers [95].

In view of the results obtained, a potential application of these cement mortars would be in masonry works where the mechanical requirements need not be very high [96]. However, it is important to take into consideration the compatibility between the mortar and the ceramic pieces in order to avoid excessively stiffening the wall [97]. In this sense, other potential applications for this type of mortar according to the literature are the production of prefabricated elements, floor slabs or urban furniture, among others [98,99]. Finally, to complete the discussion of the mechanical results, SEM images have been included to show the microstructure of the mortars produced in this research. The results are presented in Figure 9. It should be noted that these images were obtained with the aim of capturing as much information as possible and thus providing a complementary discussion of the mechanical properties analyzed. For this reason, the magnifications were selected for each mortar according to the diameter of the natural fiber added and the characteristics of the mortars studied.

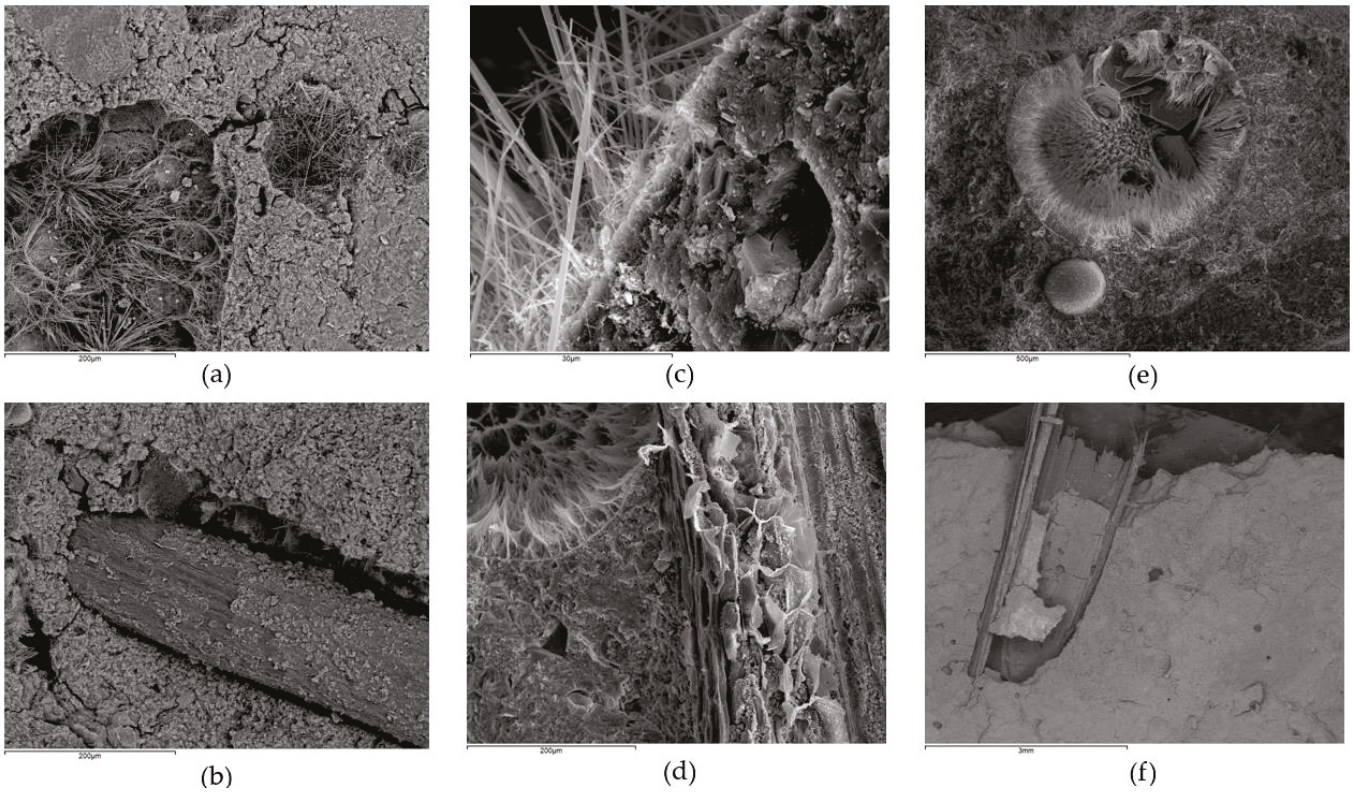


Figure 9. SEM analysis: (**a**,**b**) RCA–1:3–1.5%(C); (**c**,**d**) RCA–1:3–1.5%(A); (**e**,**f**) RCA–1:3–1.5%(T).

Regarding mortars made with coconut fiber, a slight cracking of the matrix around the fibers can be observed in Figure 9a. This weakening may be due to the absorption of hydration water from the cement by the fiber during the hardening process. Also, although fiber dispersion was good, there are preferential points of fiber accumulation. Figure 9b shows in detail the interface between coconut fiber and the cementitious matrix, where the good adhesion between the two and the formation of compounds derived from the hydration of the cement on its surface can be seen. It is well known that the arrangement of strong, stiff, and brittle fibers, as well as a higher strength of the fiber–matrix bond, results in better mechanical properties and reduced ductility [25].

Figure 9c shows the integration of abaca fiber into the cement mortar matrix. As highlighted by some authors [100], the bonding between added fibers and mortar matrix is directly linked to the lignin and cellulose content of these natural reinforcement materials. These biopolymers are shown in Figure 9d, showing one of these fibers in detail. In general, natural fibers exhibit a bridging effect similar to that of existing synthetic fibers, which can reduce autogenous shrinkage by connecting the micro-cracks in the matrix and inhibiting the propagation of cracks at an early stage [36].

Finally, Figure 9e shows in detail the interior of the toquilla straw fiber where its composition can be seen. These larger diameter fibers were the ones that, to a lesser extent increased the flexural strength of the mortars made with RCA. Although it is true that, as seen in Figure 9f, there is a good integration between the reinforcement and the matrix. However, it can be seen how toquilla straw fiber broke after the flexural test, as illustrated in the SEM image obtained.

3.3. Critical Discussion of the Potential Application of the Developed Mortars

In this section, a critical discussion of the results obtained is carried out in order to explore the application potential of the developed cementitious materials. Thus, Figures 10 and 11 show a classification of the mortars developed based on the different properties studied.

The values presented in Figures 10 and 11 are expressed in terms of the increase or reduction experienced concerning traditional mortar in each of the properties determined.

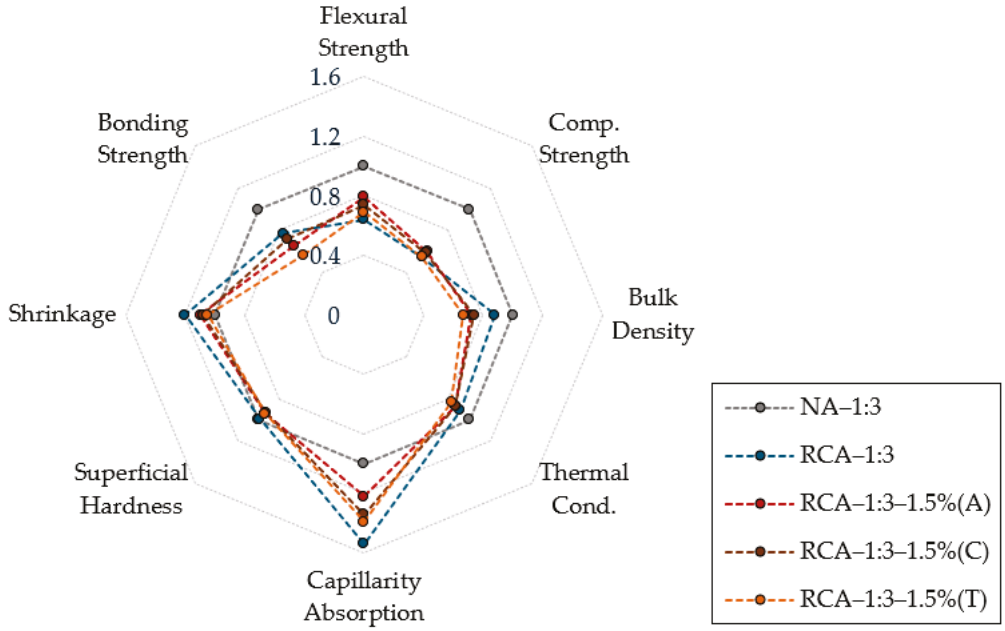


Figure 10. A comparison between the different mortar typologies studied according to the cement/aggregate ratio used, 1:3 ratio by mass.

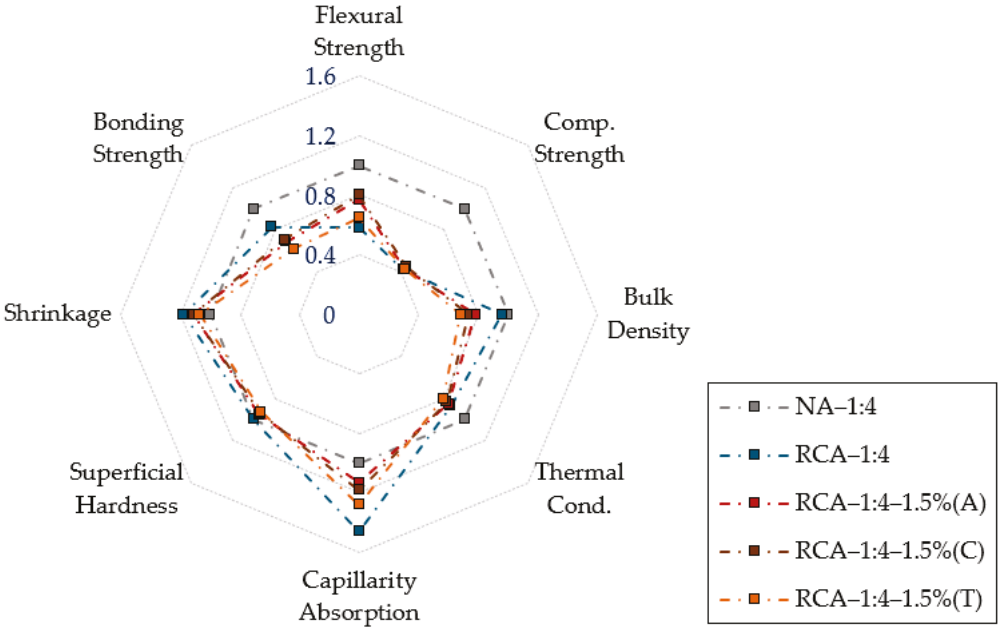


Figure 11. A comparison between the different mortar typologies studied according to the cement/aggregate ratio used, 1:4 ratio by mass.

Comparatively, Figures 10 and 11 show how the decrease in bulk density and thermal conductivity are one of the main advantages of mortars made with recycled aggregates and natural fibers. Thus, a potential application of these composite materials would be the development of prefabricated elements for modular construction with improved thermal performance. These lighter and more thermally resistant parts would reduce material execution times, transport costs, and improve the energy rating of the building [101]. Another key factor to consider is the shrinkage experienced during setting, which, although it is true

that it increases when using recycled sands, the incorporation of natural fibers becomes an economically viable alternative that would improve the dimensional stability of the mortars. In this sense, it would be interesting to analyze the durability of these cementitious materials, since, due to their greater porosity and water absorption by capillarity, they could be difficult to apply in climates where they could be exposed to freeze–thaw cycles.

Regarding mechanical properties, a decrease in flexural and compressive strength is observed with respect to traditional mortar. However, the incorporation of natural fibers significantly improves the flexural strength and avoids brittle fracture of the mortar pieces. In any case, these properties may not be discriminating in terms of the final application of the mortars, since they would be suitable for use in non-structural walls. Finally, the decrease in adhesion on ceramic walls suggests the application of these mortars as reinforcement materials. In this regard, recent research has suggested the use of these materials as cladding materials in traditional adobe houses to improve their performance in earthquakes [17].

Figure 12 shows the process for possibly manufacturing mortar blocks made with the dosages proposed in this research.

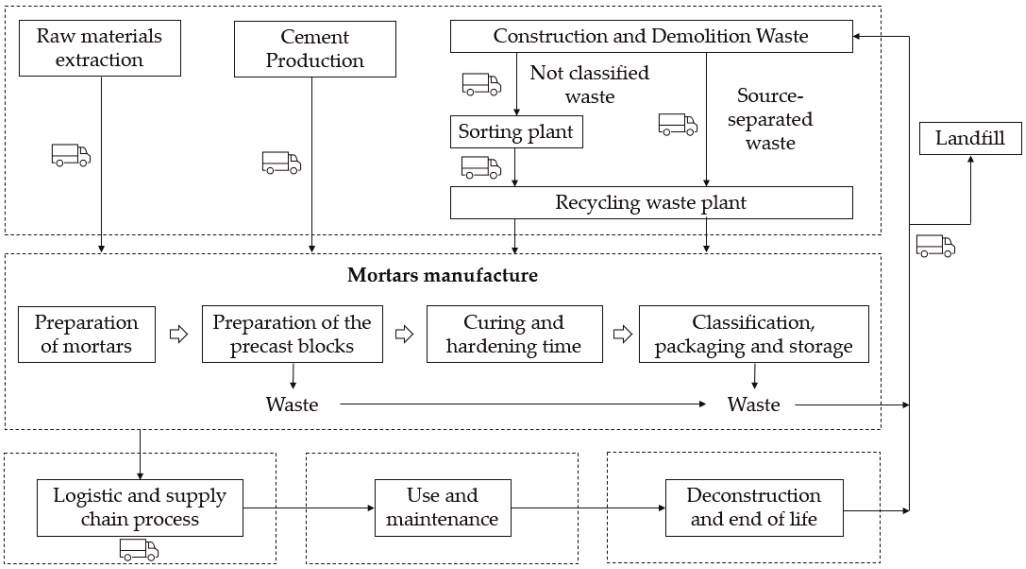


Figure 12. Product system for the manufacture of mortar blocks.

First, it should be noted that the mortars produced in this research did not use a superplasticizer. This chemical agent, which improves the workability of the mixture without impairing its mechanical properties, becomes one of the environmentally harmful agents during the production of mortars with recycled aggregates [14]. In this sense, it is crucial to approach the final application of these materials with the aim of reducing the consumption of these chemical compounds, as they can sometimes be dispensable for non-structural applications.

From the point of view of the process presented in Figure 12, the transport of the raw materials and the final distribution of the prefabricated parts to the point of service are understood as critical phases. This effect has been observed previously by other researchers [102], where it was noted that the most significant environmental impact was derived from the distribution of the product, sometimes offsetting the beneficial effect obtained by using secondary raw materials. Likewise, the design and packaging of the products also become a key factor in optimizing their distribution, a key factor here being the decrease in density experienced by mortars made with recycled aggregate [103]. Thus, a greater lightening of the precast products thanks to the use of these RCA would lead to a reduction in logistics costs and a lower environmental impact associated with this distribution. In addition, this lower density, and consequently better thermal behavior,

would have a positive impact on the improvement of energy efficiency during the use phase. Finally, it is worth highlighting the need to address a waste management plan and carry out careful deconstruction processes, as this would allow CDW to be classified at source and enhance its subsequent recovery, recycling, and revaluation [104].

4. Conclusions

This research has addressed the development and physico-mechanical characterization of cement mortars made with RCA and reinforced with three types of natural fibers. Thus, this research contributes to progress towards the circularity of construction products and the characterization of new materials produced under circular economy criteria. The main conclusions of this study are:

- Mortars made with RCA have a lower bulk density than those made with natural aggregate. This decrease in density of close to 10% is even greater for those samples made with natural fibers. Thus, this lower density and the incorporation of fibers of vegetable origin have a positive effect on the thermal conductivity of the mortars. For the best case, with the incorporation of toquilla straw fibers, the RCA–1:3–1.5%(T) dosage obtained a thermal conductivity 37% lower than that of the reference mortar (NA–1:3).
- Capillary water absorption was much higher in those mortars made with RCA due to the nature of these sands. However, the incorporation of natural fibers managed to reduce the capillary water absorption, although without reaching the values obtained for the traditional mortar made with natural sand.
- The incorporation of natural fibers reduces shrinkage during the drying of mortars made with RCA, thus approaching the behavior experienced by traditional mortars. It has been observed that the mortars made with abaca fiber showed greater dimensional stability.
- Surface hardness was not affected by the type of aggregate used in the manufacture of the mortars, although it was slightly reduced by the incorporation of natural fibers.
- The production of mortars with RCA has a negative impact on bond strength. Thus, the adhesion of traditional mortar is superior to mortar with RCA and, in turn, the incorporation of natural fibers has an impact on the decrease in this mechanical property. Mortars with higher cement content showed higher bond strength.
- Flexural strength of mortars made with recycled aggregate is lower than that of traditional mortar and is reduced as the cement content in the mix decreases. Despite this, the incorporation of natural fibers has a positive impact on the improvement of the flexural strength of mortars made with RCA, with coconut and abaca fibers showing the best performance.
- The incorporation of fibers did not significantly improve the compressive strength of the mortars, the type of aggregate being the determining factor for this property. Thus, the traditional mortars showed a higher compressive strength than their counterparts made with RCA.

This study's limitations and future lines of research include the need to carry out accelerated ageing tests, which would make it possible to estimate the durability of these mortars. In the same way, for its use as a facing material, it would be convenient to analyze the optimum fiber length that allows an improvement in the mechanical properties, without excessively reducing the workability of the mortar. Finally, its application in the development of blocks or prefabricated pieces would be interesting for the future industrialization of these products.

Moreover, taking into account the availability of natural fibers whose impact was examined in this study, i.e., abaca, coconut, and toquilla straw, and that the most beneficial use of these natural raw materials in terms of environmental impact will be in their place of origin, the results of this study are also an indication for professionals involved in construction in areas where these natural fibers occur. The research described in this article fits well with the expectation that recycling and reuse of demolition materials and using

renewable raw materials are/will be a traditional and common practice in the construction sector, bringing us closer to sustainable development.

Author Contributions: Conceptualization, D.F. and A.Z.-B.; methodology, A.Z.-B. and D.F.; software, A.Z.-B. and R.P.L.; validation, D.F., P.S. and J.M.; formal analysis, D.F. and R.P.L.; investigation, A.Z.-B., D.F. and R.P.L.; resources, D.F. and P.S.; data curation, D.F. and A.Z.-B.; writing—original draft preparation, D.F. and A.Z.-B.; writing—review and editing, A.Z.-B., P.S., R.P.L. and J.M.; visualization, P.S. and J.M.; supervision, P.S. and J.M.; project administration, D.F. All authors have read and agreed to the published version of the manuscript.

Funding: This research received no external funding.

Institutional Review Board Statement: Not applicable.

Informed Consent Statement: Not applicable.

Data Availability Statement: All data have been included in the research results.

Acknowledgments: The authors would like to thank the kindness and availability shown by the ATLAS® company, as well as the staff of the laboratories involved in carrying out the tests presented in this work.

Conflicts of Interest: Author Jacek Michalak was employed by the company ATLAS. The remaining authors declare that the research was conducted in the absence of any commercial or financial relationships that could be construed as a potential conflict of interest.

References

1. Bhavsar, V.; Sridharan, S.R.; Sudarsan, J.S. Barriers to circular economy practices during construction and demolition waste management in an emerging economy. *Resour. Conserv. Recycl. Adv.* **2023**, *20*, 200198. [CrossRef]
2. Singh, A.K.; Kumar, V.R.P.; Dehdasht, G.; Mohandes, S.R.; Manu, P.; Rahimian, F.P. Investigating the barriers to the adoption of blockchain technology in sustainable construction projects. *J. Clean. Prod.* **2023**, *403*, 136840. [CrossRef]
3. Aslam, M.S.; Huang, B.; Cui, L. Review of construction and demolition waste management in China and USA. *J. Environ. Manag.* **2020**, *264*, 110445. [CrossRef] [PubMed]
4. Aylap, G.G.; Anaç, M. A comprehensive analysis of the barriers to effective construction and demolition waste management: A bibliometric approach. *Clean. Waste Syst.* **2024**, *8*, 100141. [CrossRef]
5. Zhang, K.; Qing, Y.; Umer, Q.; Asmi, F. How construction and demolition waste management has addressed sustainable development goals: Exploring academic and industrial trends. *J. Environ. Manag.* **2023**, *345*, 118823. [CrossRef] [PubMed]
6. Jain, S.; Singhal, S.; Pandey, S. Environmental life cycle assessment of construction and demolition waste recycling: A case of urban India. *Resour. Conserv. Recycl.* **2020**, *155*, 104642. [CrossRef]
7. Caro, D.; Lodato, C.; Damgaard, A.; Cristóbal, J.; Foster, G.; Flachenecker, F.; Tonini, D. Environmental and socio-economic effects of construction and demolition waste recycling in the European Union. *Sci. Total Environ.* **2024**, *908*, 168295. [CrossRef] [PubMed]
8. Xuan, D.; Sun Poon, C.; Zheng, W. Management and sustainable utilization of processing wastes from ready-mixed concrete plants in construction: A review. *Resour. Conserv. Recycl.* **2018**, *136*, 238–247. [CrossRef]
9. Sobotka, A.; Sagan, J. Decision support system in management of concrete demolition waste. *Autom. Constr.* **2021**, *128*, 103734. [CrossRef]
10. Khelafi, A.; Kaid, N.; Soltani, R.; Elddine, D. Elaboration of recycled concrete sand aggregates-based mortars: An alternative recycling process. *Constr. Build. Mater.* **2023**, *398*, 132333. [CrossRef]
11. Liu, H.; Liu, X.; Wang, X.; Zhu, P.; Yang, L.; Yan, X. The impact of original aggregate and attached mortar types of recycled aggregates on the sulfuric acid resistance of geopolymer recycled concrete. *J. Build. Eng.* **2024**, *82*, 108273. [CrossRef]
12. Muhammad, F.; Harun, M.; Ahmed, A.; Kabir, N.; Khalid, H.R.; Hanif, A. Influence of bonded mortar on recycled aggregate concrete properties: A review. *Constr. Demolition Mater.* **2024**, *432*, 136564. [CrossRef]
13. Saiz, P.; González, M.; Fernández, F.; Rodríguez, A. Comparative study of three types of fine recycled aggregates from construction and demolition waste (CDW), and their use in masonry mortar fabrication. *J. Clean. Prod.* **2016**, *118*, 162–169. [CrossRef]
14. Ferrández, D.; Saiz, P.; Zaragoza-Benzal, A.; Zúñiga-Vicente, J.A. Towards a more sustainable environmentally production system for the treatment of recycled aggregates in the construction industry: An experimental study Author links open overlay panel. *Heliyon* **2023**, *9*, e16641. [CrossRef] [PubMed]
15. Wu, H.; Wang, C.; Ma, Z. Drying shrinkage, mechanical and transport properties of sustainable mortar with both recycled aggregate and powder from concrete waste. *J. Build. Eng.* **2022**, *49*, 104048. [CrossRef]
16. Khan, F.; Hossain, N.; Hasan, F.; Maksudur, S.M.; Khan, S.; Saifullah, A.Z.A.; Asaduzzaman, M. Advances of natural fiber composites in diverse engineering applications—A review. *Appl. Eng. Sci.* **2024**, *18*, 100184. [CrossRef]

17. Saini, K.; Matsagar, V.A.; Kodur, V.R. Recent advances in the use of natural fibers in civil engineering structures. *Constr. Build. Mater.* **2024**, *411*, 134364. [CrossRef]
18. Navaratnam, S.; Selvaranjan, K.; Jayasooriya, D.; Rajeev, P.; Sanjayan, J. Applications of natural and synthetic fiber reinforced polymer in infrastructure: A suitability assessment. *J. Build. Eng.* **2023**, *66*, 105835. [CrossRef]
19. Rajeshkumar, L.; Kumar, P.S.; Boonyasopon, P. Flame retardance behaviour and degradation of plant-based natural fiber composites—A comprehensive review. *Constr. Build. Mater.* **2024**, *432*, 136552. [CrossRef]
20. Elfaleh, I.; Abbassi, F.; Habibi, M.; Ahmad, F.; Guedry, M.; Nasri, M.; Garnier, C. A comprehensive review of natural fibers and their composites: An eco-friendly alternative to conventional materials. *Results Eng.* **2023**, *19*, 101271. [CrossRef]
21. Laverde, V.; Marin, A.; Benjumea, J.M.; Rincón, M. Use of vegetable fibers as reinforcements in cement-matrix composite materials: A review. *Constr. Build. Mater.* **2022**, *340*, 127729. [CrossRef]
22. Sathiparan, N.; Anburuvel, A.; Muralitharan, M.; Kothalawala, D.A.I. Sustainable use of coco pith in cement-sand mortar for masonry block production: Mechanical characteristics, durability and environmental benefit. *J. Clenaer Prod.* **2022**, *360*, 132243. [CrossRef]
23. Thanushan, K.; Yogananth, Y.; Sangeeth, P.; Gracian, J.; Sathiparan, N. Strength and Durability Characteristics of Coconut Fibre Reinforced Earth Cement Blocks. *J. Nat. Fibers* **2021**, *18*, 773–778. [CrossRef]
24. Muñoz Pérez, S.P.; Villena Zapata, L.I.; Tesen Muñoz, F.L.; Coronel Sanchez, Y.C.; Garcia, J.; Ramos, C.E.R. Influence of coconut fiber on mortar properties in masonry walls. *Electron. J. Struct. Eng.* **2023**, *23*, 52–58. [CrossRef]
25. Tang, Z.; Li, Z.; Hua, J.; Lu, S.; Chi, L. Enhancing the damping properties of cement mortar by pretreating coconut fibers for weakened interfaces. *J. Clean. Prod.* **2022**, *379*, 134662. [CrossRef]
26. Sathiparan, N.; Nishanthana, M.; Pavithra, B.H.M. Performance of coconut coir reinforced hydraulic cement mortar for surface plastering application. *Constr. Build. Mater.* **2017**, *142*, 23–30. [CrossRef]
27. Hwang, C.L.; Tran, V.A.; Hong, J.W.; Hsieh, Y.C. Effects of short coconut fiber on the mechanical properties, plastic cracking behavior, and impact resistance of cementitious composites. *Constr. Build. Mater.* **2016**, *127*, 984–992. [CrossRef]
28. Bui, H.; Boutouil, M.; Sebaibi, N.; Levacher, D. Hydration characteristics of coconut fibre-reinforced mortars containing CSA and Portland cement. *J. Mater. Cycles Waste Manag.* **2022**, *24*, 1295–1303. [CrossRef]
29. Bui, H.; Levacher, D.; Boutouil, M.; Sebaibi, N. Effects of Wetting and Drying Cycles on Microstructure Change and Mechanical Properties of Coconut Fibre-Reinforced Mortar. *J. Compos. Sci.* **2022**, *6*, 102. [CrossRef]
30. Kesikidou, F.; Stefanidou, M. Natural fiber-reinforced mortars. *J. Build. Eng.* **2019**, *25*, 100786. [CrossRef]
31. Quiñones-Bolaños, E.; Gómez-Oviedo, M.; Mouthon-Bello, J.; Sierra-Vitola, L.; Berardi, U.; Bustillo, C. Potential use of coconut fibre modified mortars to enhance thermal comfort in low-income housing. *J. Environ. Manag.* **2021**, *277*, 111503. [CrossRef]
32. Syamala, L.M.; Vishnudas, S.; Anil, K.R. Effect of Coir Fiber Reinforcement on Flexural and Compressive Strengths of Masonry Mortar. *J. Mater. Civ. Eng.* **2023**, *35*, 04023457. [CrossRef]
33. Nawad, M.S.; Zeeshan, M.; Zaid, O.; Kahla, N.B.; Sun, Y.; Anwar, N.; Ajwad, A. A study on improving the performance of cement-based mortar with silica fume, metakaolin, and coconut fibers. *Case Stud. Constr. Mater.* **2023**, *19*, e02480. [CrossRef]
34. Alcivar-Bastidas, S.; Petroche, D.M.; Martínez-Echevarria, M.J. The effect of different treatments on abaca fibers used in cementitious composites. *J. Nat. Fibers* **2023**, *20*, 2177235. [CrossRef]
35. Alcivar-Bastidas, S.; Petroche, D.M.; Cornejo, M.H.; Martinez-Echevarria, M.J. Effect of aging process on mechanical performance of reinforced mortar with NaOH abaca fibers. *Case Stud. Constr. Mater.* **2024**, *20*, e03122. [CrossRef]
36. Lee, G.W.; Choi, Y.C. Effect of abaca natural fiber on the setting behavior and autogenous shrinkage of cement composite. *J. Build. Eng.* **2022**, *56*, 104719. [CrossRef]
37. Suhelmidawati, E.; Adibroto, F.; Suhendrik, H.; Numada, M.; Kimiro, M. Experimental Test of Masonry Wallets Retrofitted by Abaca Fiber Reinforced Mortar. *Int. J. Adv. Sci. Eng. Inf. Technol.* **2019**, *9*, 929. [CrossRef]
38. Garzón, L.; López, L.M.; Seminario, J.F.; Zuluaga, R.; Betancourt, S.; Gañán, P.; Cruz, L.J. A new natural fiber: Toquilla straw a potential reinforcement in thermoplastic polymer composites. In Proceedings of the 5th International Conference on Advanced Materials and Systems, Bucharest, Romania, 23–25 October 2014; pp. 49–54.
39. Skinner, C.; Baker, P.; Tomkinson, J.; Richards, D.; Charlton, A. Pressurised disc refining of wheat straw as a pre-treatment approach for agricultural residues: A preliminary assessment of energy consumption and fibre composition. *Bioresour. Technol.* **2020**, *204*, 122976. [CrossRef] [PubMed]
40. Wang, H.; Liu, X.; Wang, S.; Zhou, S.; Zang, T.; Dai, L.; Ai, S. Hydrophobic kenaf straw core for biomass-based cement mortar with excellent mechanical properties. *Mater. Chem. Phys.* **2021**, *267*, 124594. [CrossRef]
41. Basta, A.H.; Lotfy, V.F.; Shafik, E.S. Synergistic valorization of rice straw and red brick demolition in development performance of lightweight cement mortars. *J. Build. Eng.* **2024**, *92*, 109769. [CrossRef]
42. Yu, X.; Li, G.; Zhao, H.; Ma, Y.; Li, Q.; Chen, Y.; Li, W. Influence of chemically-modified cotton straw fibers on the properties of asphalt mortar. *Case Stud. Constr. Mater.* **2023**, *18*, e01787. [CrossRef]
43. Awoyera, P.O.; Akinrinade, A.D.; de Sousa Galdino, A.G.; Althoey, F.; Serkan Kirgiz, M.; Tayeh, B.A. Thermal insulation and mechanical characteristics of cement mortar reinforced with mineral wool and rice straw fibers. *J. Build. Eng.* **2022**, *53*, 104568. [CrossRef]

44. Santo de Lima, T.E.; Natalli, J.F.; Marvila, M.T.; Candido, V.S.; da Silva, A.C.R.; de Azevedo, A.R.G. Potentiality of using guarumã natural fiber (*Ischinosiphon koern*) in sustainable coating mortars. *J. Mater. Res. Technol.* **2024**, *30*, 1301–1309. [CrossRef]
45. de Lima, T.E.; de Azevedo, A.R.; Marvila, M.T.; Candido, V.S.; Fediuk, R.; Monteiro, S.N. Potential of using amazon natural fibers to reinforce cementitious composites: A review. *Polymers* **2022**, *14*, 647. [CrossRef]
46. Lilargem Rocha, D.; Tambara Júnior, L.U.D.; Marvila, M.T.; Pereira, E.C.; Souza, D.; de Azevedo, A.R.G. A review of the use of natural fibers in cement composites: Concepts, applications and Brazilian history. *Polymers* **2022**, *14*, 2043. [CrossRef]
47. Hamada, H.M.; Shi, J.; Al Jawahery, M.S.; Majdi, A.; Yousif, S.T.; Kaplan, G. Application of natural fibres in cement concrete: A critical review. *Mater. Today Commun.* **2023**, *35*, 105833. [CrossRef]
48. Ferreira de Lima, C.P.; Chagas Cordeiro, G. Evaluation of corn straw ash as supplementary cementitious material: Effect of acid leaching on its pozzolanic activity. *Cement* **2021**, *4*, 100007. [CrossRef]
49. Aliu, A.O.; Olalusi, O.B.; Aworera, P.O.; Kiliswa, M. Evaluation of pozzolanic reactivity of maize straw ash as a binder supplement in concrete. *Case Stud. Constr. Mater.* **2023**, *18*, e01790. [CrossRef]
50. United Nations. 17 Goals to Transform Our World. Available online: https://www.un.org/sustainabledevelopment/es/ (accessed on 8 June 2024).
51. Amin, M.N.; Ahmad, W.; Khan, K.; Ahmad, A. A Comprehensive Review of Types, Properties, Treatment Methods and Application of Plant Fibers in Construction and Building Materials. *Materials* **2022**, *15*, 4362. [CrossRef]
52. Harasymiuk, J.; Szafranko, E. On the application of sustainable building materials in geodesy and civil engineering. *Mater. Today Proc.* **2022**, *57*, 701–704. [CrossRef]
53. Real Decreto 256/2016. Instrucción Para la Recepción de Cemento (RC-16). Available online: https://www.boe.es/eli/es/rd/2016/06/10/256/con (accessed on 8 June 2024).
54. Arroyo Portero, J.C.; Morán Cabré, F.; García Messeguer, A. *Homigón Armado*, 16th ed.; Cinter Divulgación Técnica, S.L.: Madrid, Spain, 2018; ISBN 9788493930578.
55. Morón, A.; Ferrández, D.; Saiz, P.; Morón, C. Experimental Study with Cement Mortars Made with Recycled Concrete Aggregate and Reinforced with Aramid Fibers. *Appl. Sci.* **2021**, *11*, 7791. [CrossRef]
56. Piña, C.; del Río, M.; Viñas, C.; Vidales, A.; Kosior-Kaberuk, M. Analysis of the mechanical behaviour of the cement mortars with additives of mineral wool fibres from recycling of CDW. *Constr. Build. Mater.* **2019**, *210*, 56–62. [CrossRef]
57. *Council Directive 98/83/EC of 3 November 1998 on the Quality of Water Intended for Human Consumption*; EU: Brussels, Belgium, 1998.
58. Canal de Isabel, II. Calidad del Agua. Available online: www.canaldeisabelsegunda.es/calidad-del-agua (accessed on 9 June 2024).
59. *UNE–EN 933-1:2012*; Tests for Geometrical Properties of Aggregates—Part 1: Determination of Particle Size Distribution—Sieving Method. UNE: Madrid, Spain, 2012.
60. *UNE-EN 13139/AC:2004*; Aggregates for Mortar. UNE: Madrid, Spain, 2004.
61. *UNE 146404:2018*; Aggregates for Concrete. Determination of the Coefficient of Friability of the Sands. UNE: Madrid, Spain, 2018.
62. *UNE-EN 1097-3:1999*; Tests for Mechanical and Physical Properties of Aggregates—Part 3: Determination of Loose Bulk Density and Voids. UNE: Madrid, Spain, 1999.
63. *UNE-EN 1097-6:2014*; Tests for Mechanical and Physical Properties of Aggregates—Part 6: Determination of Particle Density and Water Absorption. UNE: Madrid, Spain, 2014.
64. Saiz Martínez, P. Utilización de Arenas Procedentes de Residuos de Construcción y Demolición, RCD, en la Fabricación de Morteros de Albañilería. Ph.D. Thesis, Universidad Politécnica de Madrid, Madrid, Spain, 2015. [CrossRef]
65. Morón, A.; Ferrández, D.; Saiz, P.; Atanes-Sánchez, E.; Morón, C. Study of the properties of lime and cement mortars made from recycled ceramic aggregate and reinforced with fibers. *J. Build. Eng.* **2021**, *35*, 102097. [CrossRef]
66. Li, H.; Liu, J.; Xiao, J.; Zhong, P. A method to determine water absorption of recycled fine aggregate in paste for design and quality control of fresh mortar. *Constr. Build. Mater.* **2019**, *197*, 30–41. [CrossRef]
67. *UNE-EN 933-2:2022*; Tests for Geometrical Properties of Aggregates—Part 2: Determination of Particle Size Distribution—Test Sieves, Nominal Size of Apertures. UNE: Madrid, Spain, 2022.
68. *NBE FL-90. Norma Básica de Edificación. Muros Resistentes de Fábrica de Ladrillo*; BOE–Agencia Estatal Boletín Oficial del Estado: Madrid, Spain, 1991.
69. Ulsen, C.; Kahn, H.; Hawlitschek, G.; Masini, E.A.; Angulo, S.C.; John, V.M. Production of recycled sand from construction and demolition waste. *Constr. Build. Mater.* **2013**, *40*, 1168–1173. [CrossRef]
70. Andersen, R.; Stokbro Ravn, A.; Walbech Ryberg, M. Environmental benefits of applying selective demolition to buildings: A case study of the reuse of façade steel cladding. *Resour. Conserv. Recycl.* **2022**, *184*, 106430. [CrossRef]
71. Juradin, S.; Boko, I.; Netinger, I.; Jozić, D.; Mrakovčić, S. Influence of different treatment and amount of Spanish broom and hemp fibres on the mechanical properties of reinforced cement mortars. *Constr. Build. Mater.* **2021**, *273*, 121702. [CrossRef]
72. Jiang, D.; An, P.; Cui, S.; Xu, F.; Tuo, T.; Zhang, J.; Jiang, H. Effect of leaf fiber modification methods on mechanical and heat-insulating properties of leaf fiber cement-based composite materials. *J. Build. Eng.* **2018**, *19*, 573–583. [CrossRef]
73. Cai, M.; Takgi, H.; Nakagaito, A.N.; Li, Y.; Waterhouse, G.I.N. Effect of alkali treatment on interfacial bonding in abaca fiber-reinforced composites. *Compos. Part A Appl. Sci. Manuf.* **2016**, *90*, 589–597. [CrossRef]

74. *UNE-EN 196-1:2018*; Methods of Testing Cement—Part 1: Determination of Strength. UNE: Madrid, Spain, 2018.
75. *UNE-EN 1015-3:1999*; Methods of Test for Mortar for Masonry. Part 3: Determination of Consistence of Fresh Mortar (by Flow Table). UNE: Madrid, Spain, 1999.
76. Marvila, M.; de Matos, P.; Rodríguez, E.; Monteiro, S.N.; de Azevedo, A.R.G. Recycled Aggregate: A Viable Solution for Sustainable Concrete Production. *Materials* **2022**, *15*, 5276. [CrossRef]
77. *UNE-EN 1015-10:2000/A1:2007*; Methods of Test for Mortar for Masonry—Part 10: Determination of Dry Bulk Density of Hardened Mortar. UNE: Madrid, Spain, 2007.
78. *UNE-EN ISO 8990:1997*; Thermal Insulation. Determination of Steady-State Thermal Transmission Properties. Calibrated and Guarded Hot-Box. UNE: Madrid, Spain, 1997.
79. *UNE-EN 1015-18:2003*; Methods of Test for Mortar for Masonry—Part 18: Determination of Water Absorption Coefficient due to Capillary Action of Hardened Mortar. UNE: Madrid, Spain, 2003.
80. *UNE-EN 1936:2007*; Natural Stone Test Methods—Determination of Real Density and Apparent Density, and of Total and Open Porosity. UNE: Madrid, Spain, 2007.
81. *UNE 80-112-89*; Test methods for Cements. Physical Tests: Determination of Drying Shrinkage and Swelling in Water. UNE: Madrid, Spain, 1989.
82. *UNE-EN 1015-12:2016*; Methods of Test for Mortar for Masonry—Part 12: Determination of Adhesive Strength of Hardened Rendering and Plastering Mortars on Substrates. UNE: Madrid, Spain, 2016.
83. *UNE-EN ISO 868:2003*; Plastics and Ebonite—Determination of Indentation Hardness by Means of a Durometer (Shore Hardness) (ISO 868:2003). UNE: Madrid, Spain, 2003.
84. Lamichhane, N.; Lamichhane, A.; Gyawali, T.R. Enhancing mechanical properties of mortar with short and thin banana fibers: A sustainable alternative to synthetic fibers. *Heliyon* **2024**, *10*, e30652. [CrossRef] [PubMed]
85. Francioso, V.; Moro, C.; Velay-Lizancos, M. Effect of recycled concrete aggregate (RCA) on mortar's thermal conductivity susceptibility to variations of moisture content and ambient temperature. *J. Clean. Prod.* **2021**, *43*, 103208. [CrossRef]
86. Benmansour, N.; Agoudjil, B.; Gherabli, A.; Kareche, A.; Boudenne, A. Thermal and mechanical performance of natural mortar reinforced with date palm fibers for use as insulating materials in building. *Energy Build.* **2014**, *81*, 98–104. [CrossRef]
87. Yedra, E.; Ferrández, D.; Morón, C.; Saiz, P. New test methods to determine water absorption by capillarity. Experimental study in masonry mortars. *Constr. Build. Mater.* **2022**, *319*, 125988. [CrossRef]
88. García Morales, S. Metodología de Diagnóstico de Humedades de Capilaridad Ascendente y Condensación Higroscópica, en Edificios Históricos. Ph.D. Thesis, Technical University of Madrid, Madrid, Spain, 1995. [CrossRef]
89. Miah, M.J.; Ali, M.K.; Paul, S.C.; John Babafemi, A.; Kong, S.Y.; Šavija, B. Effect of Recycled Iron Powder as Fine Aggregate on the Mechanical, Durability, and High Temperature Behavior of Mortars. *Materials* **2020**, *13*, 1168. [CrossRef]
90. Mesbah, H.A.; Buyle-Bodin, F. Efficiency of polypropylene and metallic fibres on control of shrinkage and cracking of recycled aggregate mortars. *Constr. Build. Mater.* **1999**, *13*, 439–447. [CrossRef]
91. Miah, M.J.; Chandra Paul, S.; John Babafemi, A. Mechanical strength, shrinkage, and porosity of mortar reinforced with areca nut husk fibers. *Constr. Build. Mater.* **2023**, *363*, 129688. [CrossRef]
92. García López de la Osa, G. Análisis de la Adherencia Entre Morteros y Piezas Cerámicas. Ph.D. Thesis, Univeresidad Politécnica de Madrid, Madrid, Spain, 2020. [CrossRef]
93. Samiei, R.R.; Daniotti, B.; Pelosato, R.; Dotelli, G. Properties of cement–lime mortars vs. cement mortars containing recycled concrete aggregates. *Constr. Build. Mater.* **2015**, *84*, 84–94. [CrossRef]
94. Bedoya, M.A.; Tobón, J.I. Incidence of recycled aggregates and ternary cements on the compressive strength and durability of ecological mortars. *Case Stud. Constr. Mater.* **2022**, *17*, e01192. [CrossRef]
95. Chandrasekaran, R.G.; Ramakishna, G. Experimental investigation on mechanical properties of economical local natural fibre reinforced cement mortar. *Mater. Today Proc.* **2021**, *46*, 7633–7638. [CrossRef]
96. Martínez, I.; Etxeberria, M.; Pavón, E.; Díaz, N. A comparative analysis of the properties of recycled and natural aggregate in masonry mortars. *Constr. Build. Mater.* **2013**, *49*, 384–392. [CrossRef]
97. Mohammad Moayedian, S.; Hejazi, M. Estimating the modulus of elasticity and the compressive strength of brick, mortar and masonry at different scales. *Structures* **2024**, *61*, 103116. [CrossRef]
98. Sánchez-Roldán, Z.; Martín-Morales, M.; Valverde-Espinosa, I.; Zamorano, M. Technical feasibility of using recycled aggregates to produce eco-friendly urban furniture. *Constr. Build. Mater.* **2020**, *250*, 118890. [CrossRef]
99. Wang, B.; Yan, L.; Fu, Q.; Kasal, B. A Comprehensive Review on Recycled Aggregate and Recycled Aggregate Concrete. *Resour. Conserv. Recycl.* **2021**, *171*, 105565. [CrossRef]
100. Tolêdo Filho, R.D.; Scrivener, K.; Engrand, G.L.; Ghavami, K. Durability of alkali-sensitive sisal and coconut fibres in cement mortar composites. *Cem. Concr. Compos.* **2000**, *22*, 127–143. [CrossRef]
101. Zaragoza-Benzal, A.; Ferrández, D.; Santos, P.; Morón, C. Recovery of End-of-Life Tyres and Mineral Wool Waste: A Case Study with Gypsum Composite Materials Applying Circular Economy Criteria. *Materials* **2023**, *16*, 243. [CrossRef] [PubMed]

102. Paula Junior, A.C.; Jacinto, C.; Oliveira, T.M.; Polisseni, A.E.; Brum, F.M.; Teixeira, E.R.; Mateus, R. Characterisation and Life Cycle Assessment of Pervious Concrete with Recycled Concrete Aggregates. *Crystals* **2021**, *11*, 209. [CrossRef]
103. Agung Wibowo, M.; Nur Sholeh, E.M.; Seti Adji, H. Supply Chain Management Strategy for Recycled Materials to Support Sustainable Construction. *Procedia Eng.* **2017**, *171*, 185–190. [CrossRef]
104. Villoria, P.; Del Río, M.; San-Antonio, A.; Porrás-Amores, C. Best practice measures assessment for construction and demolition waste management in building constructions. *Resour. Conserv. Recycl.* **2013**, *75*, 52–62. [CrossRef]

Disclaimer/Publisher's Note: The statements, opinions and data contained in all publications are solely those of the individual author(s) and contributor(s) and not of MDPI and/or the editor(s). MDPI and/or the editor(s) disclaim responsibility for any injury to people or property resulting from any ideas, methods, instructions or products referred to in the content.

applied sciences

MDPI

Article

Early Age Assessment of a New Course of Irish Fly Ash as a Cement Replacement

Nikki Shaji [1], Niall Holmes [1,2,*] and Mark Tyrer [3]

[1] School of Transport & Civil Engineering, TU Dublin City Campus, D01 K822 Dublin, Ireland; nikkimaria.shaji@tudublin.ie
[2] Built Environment Research and Innovation Centre, TU Dublin City Campus, D01 K822 Dublin, Ireland
[3] Institute of Advanced Study, Collegium Basilea, 4053 Basel, Switzerland; m.tyrer@mtyrer.net
* Correspondence: niall.holmes@tudublin.ie; Tel.: +353-(0)1-220-6678

Abstract: This paper explores the potential of a new source of fly ash, deposited on the site of a coal-fired power plant in Ireland dating from 1985 to 1995, as a cement replacement material. A series of X-ray diffraction (XRD) analyses on binder samples with cement replacement levels of 0, 10, 25 and 35% was undertaken to determine the fly ash's mineralogical composition and to determine its suitability as a supplemental cementitious material (SCM). The XRD results reveal a unique mineral composition with promising characteristics for enhancing the strength and durability of concrete. The experimental results were used to calibrate a thermodynamic model to predict changing phase assemblage and hydration behaviour over time and per replacement level. Thermodynamic models have been shown to give credible predictions of the long-term performance of cements, including SCMs. The initial experimental results' thermodynamic modelling demonstrates the feasibility of this fly ash source as a sustainable alternative to traditional cement, paving the way for more eco-friendly construction. Ash deposits dating from 1995 to 2005 and from 2005 to the present will be presented in subsequent publications.

Keywords: fly ash; cement binder; hydration; thermodynamics

1. Introduction

Coal-powered electrical energy in Ireland will be phased out entirely by 2025. The only coal-fired power station in Ireland is located at Moneypoint in Co. Clare on the west coast. Coal-burning for electricity generation in Ireland will be phased out by 2025, when the plant was due for decommissioning, but, due to the current energy crisis, it will continue operations as a back-up until 2029. Moneypoint, which generates up to 915 MW and has been operational since 1987, has several million tonnes of unconditioned ("wet") fly ash deposited over a 25-acre ash field. Between now and 2028, when the station is scheduled to be finally decommissioned, a further 800,000 tonnes of fly ash may be deposited, based on projected operation patterns. The ash stored on site has been separated into three deposits from 1985 to 1995, 1995 to 2005 and 2005 to present. This paper presents a characterisation and hydration study of the ash dating from 1985 to 1995. Subsequent publications will present the two other deposits.

Significant reductions in current carbon dioxide (CO_2) levels proposed by the European Union (80% by 2050 [1]) have been adopted by member states, including Ireland. The production of Portland cement (PC) contributes to 8% of worldwide greenhouse gas emissions [2]. Cement production in Ireland is currently at 5 million tonnes annually, which releases circa 4 million tonnes of CO_2 into the atmosphere. Therefore, partially replacing or blending Portland cement with suitable supplementary cementitious materials (SCMs) would yield substantial reductions in CO_2 emissions per tonne of cement. Current cement standards [3] define two types of siliceous fly ash blends that permit cement replacement by fly ash of up to 20% (CEM II/A-V) or 35% (CEM II/B-V). With a 35% replacement

level (CEM II/B-V), typical in the US and UK, an annual reduction of circa 650,000 of CO_2 could be realised, representing 2% of Ireland's total carbon emissions annually. With over 12 million tonnes of concrete produced annually in Ireland, CEM II/B-V cement could utilise up to 750,000 tonnes of Moneypoint fly ash each year.

In order to investigate the suitability of this fly ash as a suitable cement replacement in concrete, building on previous work [4,5], this paper presents the initial findings of its characterisation, including moisture content and the XRF and XRD over time of hydrating samples. To observe how it performed in concrete, the compressive strength of concrete samples was assessed using 100 mm cubes. Fly ash has been used at CEM I replacement levels of 0, 10, 25 and 35% to demonstrate the optimum point of replacement, which is in accordance with EN 197 [3]. In addition, in order to improve thermodynamic predictions, a suite of phase equations to represent the behaviour of the ash amorphous/glass phase during hydration has been developed, taking into account its oxide proportions. These equations are added to the PHREEQC input file for fly ash replacement levels from 5 to 35% in 5% steps and replace the traditional method of adding additional CaO, Al_2O_3, etc. to represent the glass in fly ash. This approach can also be used to represent the glass phase in most SCMs.

2. Materials and Methods

The ash used for the analysis was taken from that stored at the Moneypoint power station situated in Co. Clare, Ireland (Figure 1). The samples for the study were obtained from three different sections within the ash field, reflecting ash deposits from different phases of operation (Figure 2). Four ash samples (each 5 kg) were collected at each of the three sections. The ash was taken from a depth of 1 m from the surface and stored within air tight containers to maintain the moisture content.



(**a**) (**b**)

Figure 1. (**a**) Location of Moneypoint power station in Ireland, (**b**) Moneypoint site layout.

All experiments were carried out using commercially obtained CEM I cement with and without fly ash at various replacement levels, as described in Table 1. The chemical compositions of the materials were determined by X-ray fluorescence (XRF), and X-ray diffraction (XRD) was used to monitor the changing mineralogical composition over time as hydration continued, as described in Tables 2 and 3. As shown in Table 2, most of the fly ash is SiO_2, with high levels of Al_2O_3 and Fe_2O_3. Due to the lower CaO content and alumina content between 15 and 35%, this ash can be classified as Class F [6], as shown in the ternary diagram (Figure 3). A series of cement pastes were prepared at a w/c of 0.5 and cast into 20 × 20 × 20 mm cube moulds (Figure 4) and cured at 20 °C. XRD was carried out at 1, 7, 28 and 100 days, with a 20 mm cement cube being removed, powered down to

10 µm [7] and placed in the diffractometer for pattern acquisition. XRD data were collected using a Rigaku Miniflex600 spectrometer and scanned between 0 and 90° 2θ.

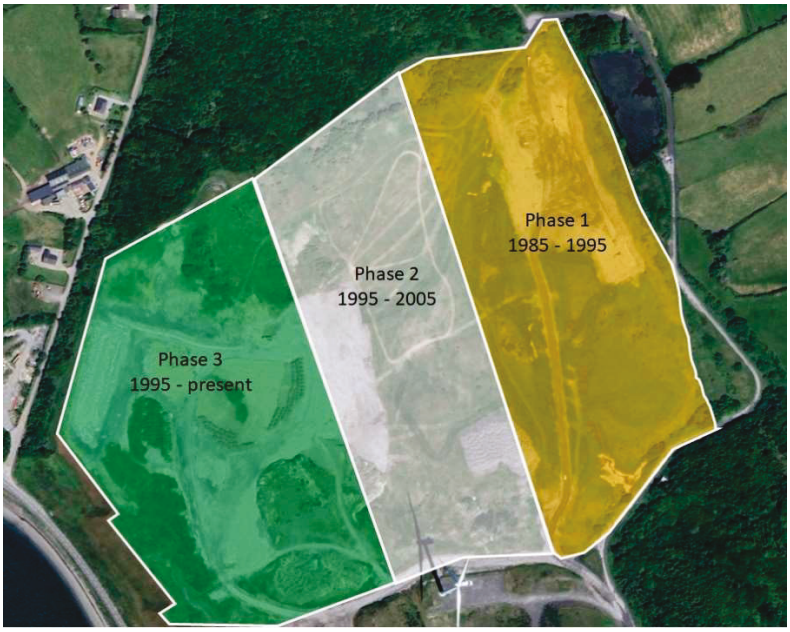


Figure 2. Fly ash storage zones at Moneypoint power station, Co. Clare.

Table 1. Binders studied (wt.%).

CEM I-FA	CEM I	FA
100-0	150	0
90-10	135	15
80-20	120	30
65-35	97.5	52.5

Table 2. Composition of CEM I cement and fly ash.

Oxide (g/100 g)	CEM I [a]	FA
SiO_2	19.04	53.70
Al_2O_3	5.01	16.81
Fe_2O_3	2.83	13.46
CaO	63.4	7.41
MgO	2.31	2.08
K_2O	0.54	2.03
Na_2O	0.28	--
SO_3	2.65	1.11
CaO (free)	1.71	--
CO_2	2.2	--
Periclase	1.0	--
P_2O_5		0.41
TiO_2		1.82
MnO		0.13
LOI	3.20	2.55
Density (g/cm^3)	2.95	2.24
Blaine fineness (m^2/kg)	386	450

[a] XRF data for the CEM I cement were obtained from the manufacturer.

Table 3. Mineralogical composition of CEM I and fly ash used (wt.%).

CEM I [a]		**FA** [b]	
C_3S	55.86	Quartz	1.29
C_2S	10.07	Calcite	1.11
C_3A	8.12	Hematite	4.65
C_4AF	8.24	Mullite	7.95
Lime	1.64	Magnetite	3.37
Calcite	4.79	Amorphous	81.65
Gypsum	4.27		
Periclase	0.96		
K_2SO_4	0.86		
Na_2SO_4	0.28		
K_2O	0.05		
Na_2O	0.15		
MgO	2.21		
SO_3	2.53		

[a] CEM I composition calculated using normalisation [8]. [b] Determined using XRD Rietveld.

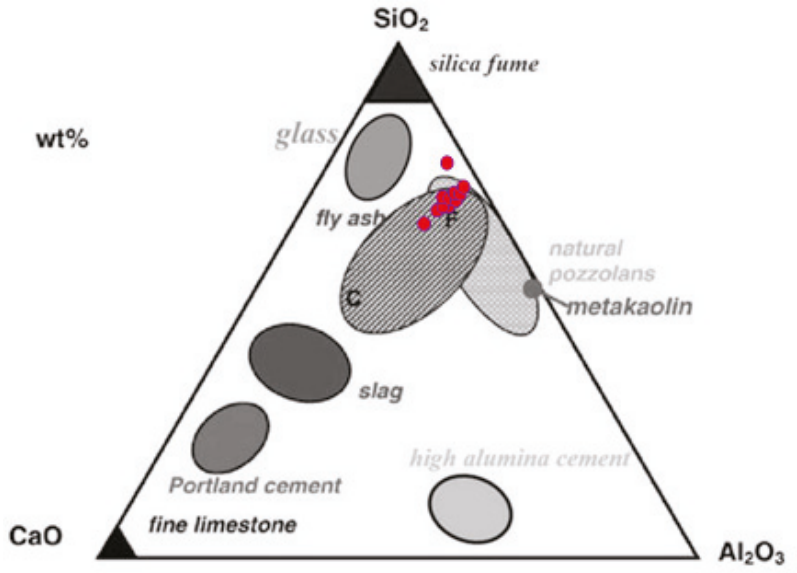


Figure 3. CaO-SiO_2-Al_2O_3 ternary diagram.



Figure 4. mm cement samples.

Particle-size distribution and SEM images of the ash taken from the site are shown in Figures 5 and 6. As may be seen, the ash consists of very fine particles, with circa 99% passing a 0.1 mm sieve. This can also be seen in the SCM images taken at a 50 μm resolution.

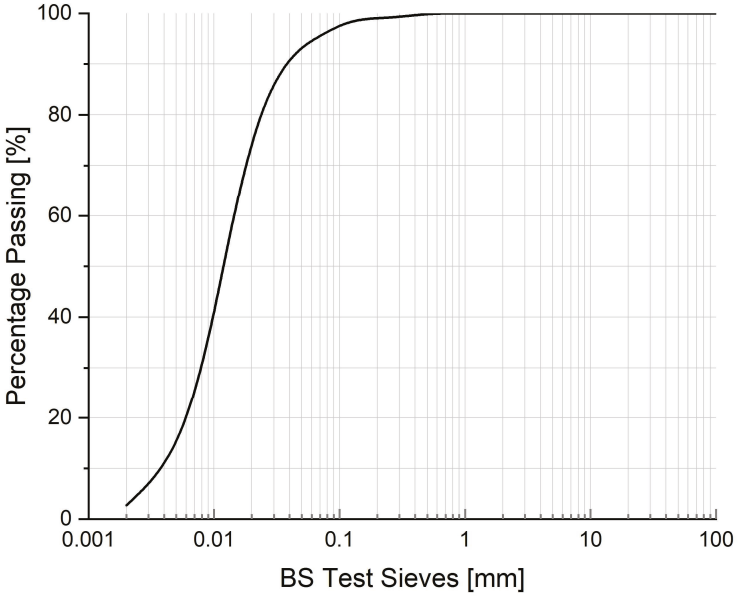


Figure 5. Fly ash particle-size distribution using BS EN 833 [9].

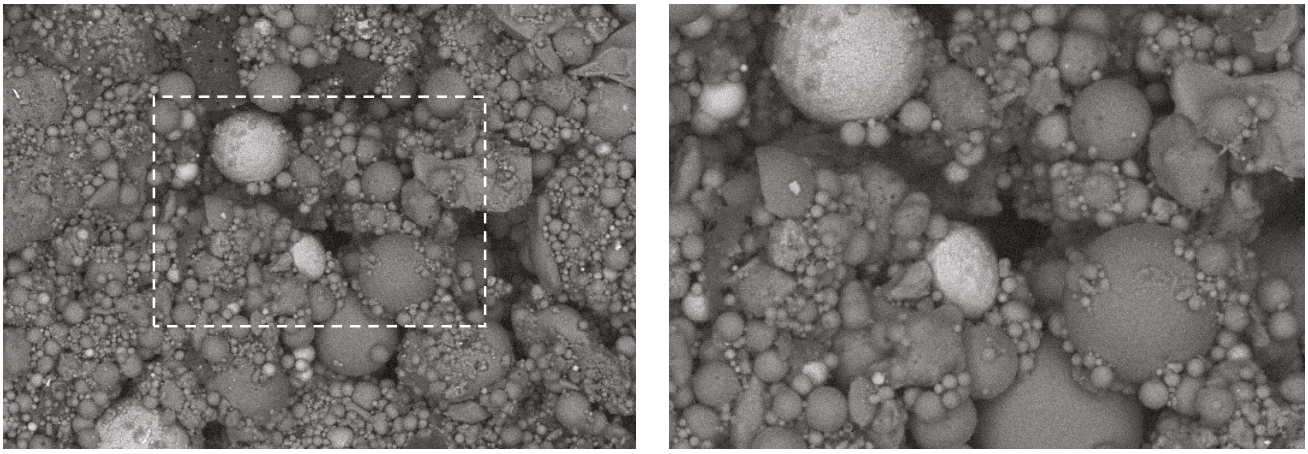


Figure 6. SEM images of unhydrated fly ash.

Figure 7 shows an SCM of the 20% fly ash replacement after 60 days of hydration. The images show the formation of portlandite and ettringite, as highlighted by their expected crystal formation.

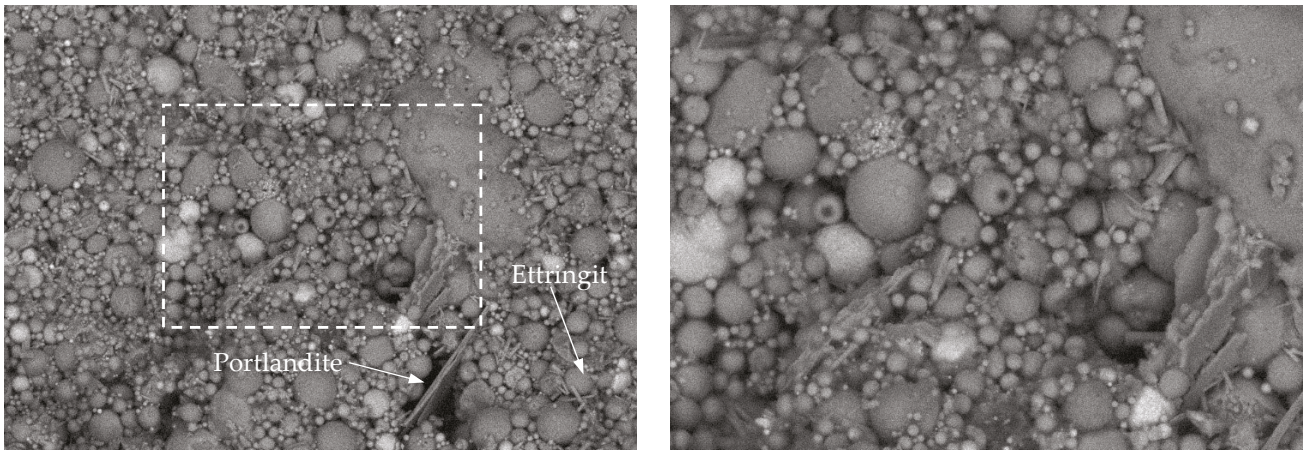


Figure 7. SEM images of hydrating cement blend with 20% fly ash after 60 days.

2.1. Moisture Content of Fly Ash

The moisture content of the fly ash was measured by weighing out 500 g each of the twelve samples and placing them inside an oven set to 105 °C for 24 h. The weight was measured again, and the moisture content was calculated.

2.2. Concrete Compressive Strength Assessment

Nine 100 × 100 × 100 mm concrete cubes were cast for each fly ash replacement level and subjected to compressive strength testing at 7, 28 and 56 days. All the mixes had a fixed w/c ratio of 0.5 and a total cement/binder content of 400 kg/m^3, with a design slump of between 100 and 150 mm. The CEM I cement used complied with BS EN 197-1 [3], and the fine and coarse aggregates were obtained from local sources in Ireland. The fine aggregate used was medium-grade sand, and the coarse aggregate was crushed limestone with a maximum size of 20 mm. A summary of the mixes is shown in Table 4.

Table 4. Mix proportions.

Mix ID	% PFA	Mass (kg/m^3)				
		Water	CEM I	FA	CA	
					10 mm	20 mm
1	0	200	400	0	350	700
2	10	200	360	40	350	700
3	25	200	300	100	350	700
4	35	200	260	140	350	700

Following mixing in a pan mixer, the concrete was poured into the moulds in 50 mm thick layers and vibrated on a vibrating table until no more air bubbles were visible on the surface. The cubes were cured for 24 h under a polythene sheet to trap evaporating moisture, demoulded and then placed into a water-filled curing tank set to 20 °C until testing.

3. Thermodynamic Modelling

Thermodynamic calculations were carried out using PHREEQC geochemical software [10,11]. The cemdata18 thermodynamic database [12] was used to model the predicted solid hydrates, pore solution chemistry and pH over time. The C-A-S-H phase was modelled using a number of Discrete Solid Phases (DSPs) based on the continuous solid solution between five end-members with different Ca/Si and Al/Si ratios, described by Shaji et al. [13]. Details on how DSPs are derived can be found in [14]. Holmes et al. [15] previously demonstrated this approach for the derivation of DSPs for the CSH-3T and CSHQ end-members. The thermodynamic data for the derivation of DSPs were taken from the cemdata18 database and copied directly into the PHREEQC input file. DSPs were also derived to model the siliceous (Si) hydrogarnet phases using the $C_3FS_{1.34}H_{3.32}$ and $C_3FS_{0.84}H_{4.32}$ end-members in cemdata18 [12], and can be found in Shaji et al. [13].

The amorphous/glass phase of the glass was modelled using phase equations following the methodology described in Shaji et al. [13]. Using the oxide proportions and phase compositions in Tables 2 and 3, respectively, the derived phase equations used in the thermodynamic calculations to account for the amorphous phase in the fly ash are listed below. These phases were added to the PHREEQC input file to represent the behaviour of the amorphous phases most accurately, rather than adding molar concentrations of the oxides found in the glass.

FA %	FA amorphous/glass phase equations (log_k for the reactive and inactive phases are +999 and −999, respectively)
5	$(SiO_2)_{9.167}(Al_2O_3)_{1.6678}(Fe_2O_3)_{0.8449}(CaO)_{1.3541}(MgO)_{0.5311}(K_2O)_{0.2218}(Na_2O)_{0.0002}(H_2O)_{1.4427}$ = + 9.167 SiO_2 + 3.3356 AlO_2^- + 1.6898 FeO_2^- + 1.3541 Ca^{+2} + 0.5311 Mg^{+2} + 0.4436 K^+ + 0.0004 Na^+ + 0.811 H^+ + 1.0372 H_2O
10	$(SiO2)_{9.219}(Al_2O_3)_{1.6537}(Fe_2O_3)_{0.8299}(CaO)_{1.3605}(MgO)_{0.5359}(K_2O)_{0.2238}(Na_2O)_{0.0002}(H_2O)_{1.4416}$ = + 9.219 SiO_2 + 3.3074 AlO_2^- + 1.6598 FeO_2^- + 1.3605 Ca^{+2} + 0.5359 Mg^{+2} + 0.4476 K^+ + 0.0004 Na^+ + 0.7264 H^+ + 1.0784 H_2O
15	$(SiO_2)_{9.2718}(Al_2O_3)_{1.6394}(Fe_2O_3)_{0.8145}(CaO)_{1.3671}(MgO)_{0.5407}(K_2O)_{0.2258}(Na_2O)_{0.0002}(H_2O)_{1.4405}$ = + 9.2718 SiO_2 + 3.2788 AlO_2^- + 1.629 FeO_2^- + 1.3671 Ca_{+2} + 0.5407 Mg^{+2} + 0.4516 K^+ + 0.0004 Na^+ + 0.6402 H^+ + 1.1204 H_2O
20	$(SiO_2)_{9.3257}(Al_2O_3)_{1.6248}(Fe_2O_3)_{0.7989}(CaO)_{1.3737}(MgO)_{0.5457}(K_2O)_{0.2279}(Na_2O)_{0.0002}(H_2O)_{1.4393}$ = + 9.3257 SiO_2 + 3.2496 AlO_2^- + 1.5978 FeO_2^- + 1.3737 Ca^{+2} + 0.5457 Mg^{+2} + 0.4558 K^+ + 0.0004 Na^+ + 0.5524 H^+ + 1.1631 H_2O
25	$(SiO_2)_{9.3805}(Al_2O_3)_{1.61}(Fe_2O_3)_{0.783}(CaO)_{1.3805}(MgO)_{0.5507}(K_2O)_{0.23}(Na_2O)_{0.0002}(H_2O)_{1.4382}$ = + 9.3805 SiO_2 + 3.22 AlO_2^- + 1.566 FeO_2^- + 1.3805 Ca^{+2} + 0.5507 Mg^{+2} + 0.46 K^+ + 0.0004 Na^+ + 0.4632 H^+ + 1.2066 H_2O
30	$(SiO_2)_{9.4364}(Al_2O_3)_{1.5949}(Fe_2O_3)_{0.7667}(CaO)_{1.3874}(MgO)_{0.5559}(K_2O)_{0.2321}(Na_2O)_{0.0002}(H_2O)1.437$ = + 9.4364 SiO_2 + 3.1898 AlO_2^- + 1.5334 FeO_2^- + 1.3874 Ca^{+2} + 0.5559 Mg^{+2} + 0.4642 K^+ + 0.0004 Na^+ + 0.372 H^+ + 1.251 H_2O
35	$(SiO_2)_{9.4933}(Al_2O_3)_{1.5794}(Fe_2O_3)_{0.7502}(CaO)_{1.3944}(MgO)_{0.5611}(K_2O)_{0.2343}(Na_2O)_{0.0002}(H_2O)_{1.4358}$ = + 9.4933 SiO_2 + 3.1588 AlO_2^- + 1.5004 FeO_2^- + 1.3944 Ca^{+2} + 0.5611 Mg^{+2} + 0.4686 K^+ + 0.0004 Na^+ + 0.2792 H^+ + 1.2962 H_2O

4. Results

4.1. Fly Ash Composition

The XRD patterns of four samples taken from Phase 1 in the ash field are shown in Figure 8. The amount of reactive silica and alumina in the ash is largely responsible for its reactivity, which has been noted by Alelweet et al. [16], who also studied the ash in Moneypoint. Previous work on fly ash mineralogy has identified up to 316 individual minerals and 188 mineral groups [16,17], with the most abundant phase being glass, with crystalline compounds such as quartz, mullite, magnetite, melilite, gehlenite, kalsilite, calcium sulphate and alkali sulphate accounting for 5–50% [18].

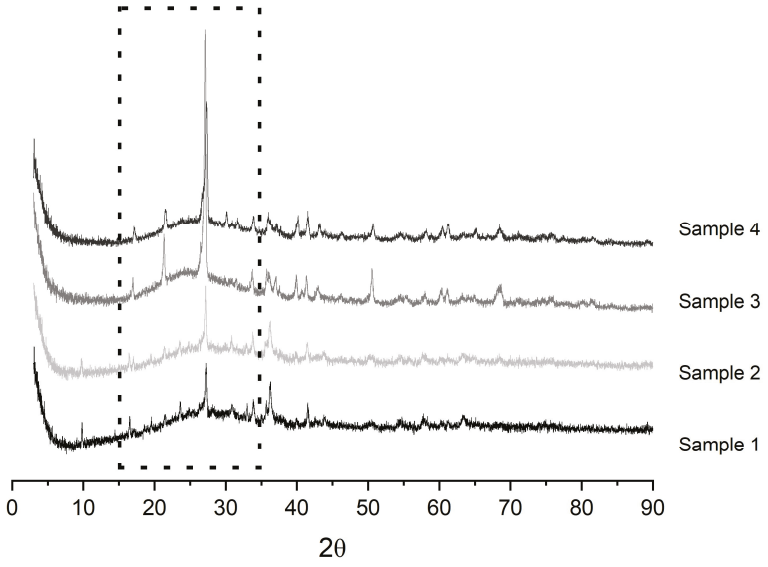


Figure 8. XRD pattern for fly ash in Phase 1. Significant amorphous content within highlighted area (15–35° 2θ).

As shown in Figure 8, there is significant glass in the fly ash. Alelweet et al. [16] calculated this to be between 40 and 60%, based on the background area between 15–35° 2θ. Here, the glass/amorphous content is calculated to be 81% using a Rietveld analysis, with amounts of quartz, mullite, hematite, calcite and magnetite. This is in broad agreement with previous studies on Moneypoint fly ash [16,19] and is summarised in Table 5. This also agrees with the previous literature, which reports quartz and mullite to be the two major crystalline phases in low-Ca (CaO < 8%) fly ash, with a crystalline mineral content in the range of 11–48 wt.% [17]. Alelweet et al. [16] concluded that the lack of sulphates and

calcium silicates in the Moneypoint fly ash is due to the composition of the subbituminous coal used in the power station, which is low in sulphur and calcium.

Table 5. Mineral composition of Moneypoint fly ash by Alelweet et al. [16].

Material	% Glass	% Crystalline	Mineral Composition
FA °C	40–60	60–40	Glass Quartz (SiO_2) Mullite ($2Al_2O_3.2SiO_2$)
FA 500 °C	10–30	70–90	Glass Quartz (SiO_2) Mullite ($2Al_2O_3.2SiO_2$)
FA 800 °C	10–30	70–90	Glass Quartz (SiO_2) Mullite ($2Al_2O_3.2SiO_2$)
FA 1000 °C	10–30	70–90	Glass Quartz (SiO_2) Mullite ($2Al_2O_3.2SiO_2$) Hematite (Fe_2O_3) Possible $Ca_3Al_2O_6$ and alkali sulphate

4.2. Fly Ash Moisture Content

The moisture content from the twelve flay ash samples taken is shown in Figure 9. As shown, the moisture contents ranges from 11.25% to 11.75%, with the average around 11.5%. This moisture content was considered during the concrete production, to ensure 0.5 w/c was achieved throughout, to ensure the design strengths were reached. The relatively high moisture content would indicate that the ash should be dried before use, or the free water content should be adjusted to account for the moisture within it.

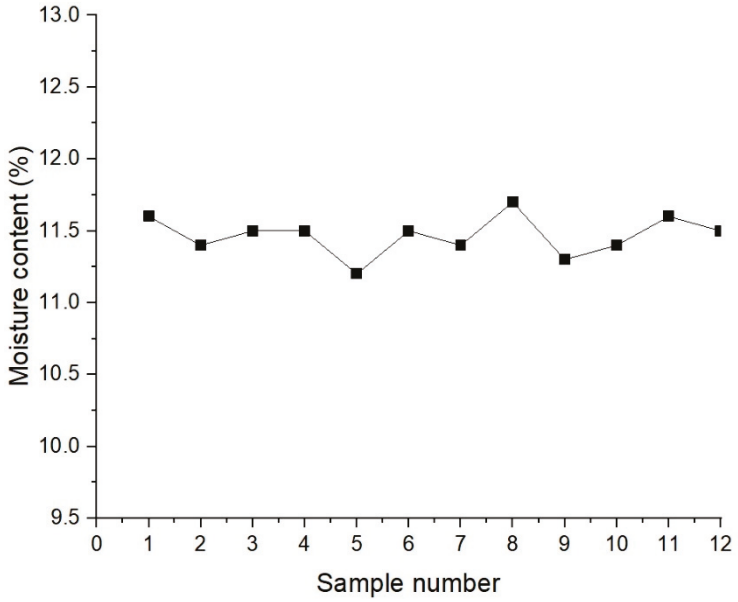


Figure 9. Fly ash samples moisture content.

4.3. Concrete Compressive Strength

The concrete compressive strength results are shown in Figure 10. As may be seen, the compressive strength results are not significantly affected with the addition of FA, compared with the CEM I only/0% FA samples at each age. However, the 35% FA samples do take longer to achieve similar strengths to CEM I only and to the other fly ash replacement levels. At 56 days, though, all compressive strengths appear to be similar.

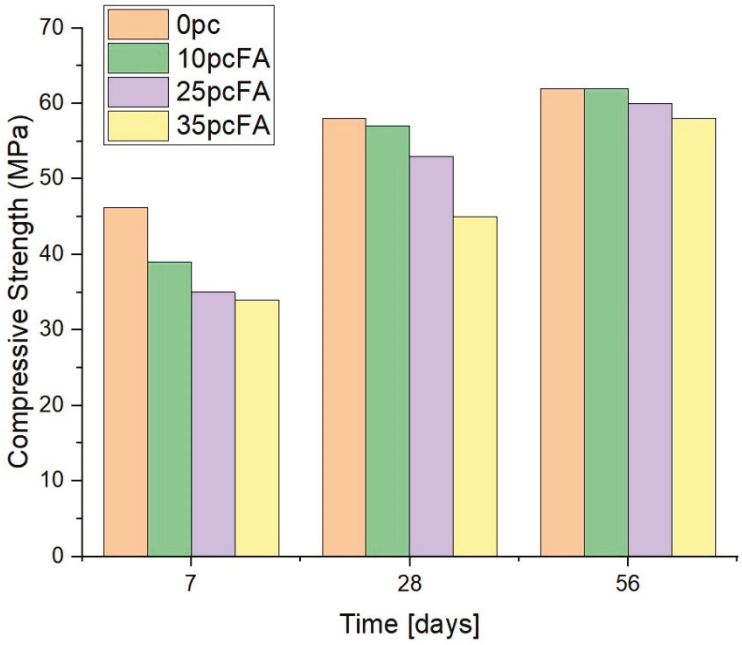


Figure 10. Concrete compressive strength results.

4.4. X-ray Diffraction

Figure 11 shows the XRD pattens for hydrating CEM I with no fly ash additions. The CEM I clinker peaks are shown at 12.1° 2θ (C_4AF), 31° 2θ (C_2S), 32.5° 2θ (mainly C_3S and C_2S) and 35° 2θ (C_3S). C_3S also overlaps with the calcite peak at 29.5° 2θ. C_2S can be difficult to identify in XRD patterns, and it appears to overlap with the C_3S peak at 32.5° 2θ, whereas C_3S is more abundant. C_3A, along with overlapping C_2S and C_3S, is observed at 32–33° 2θ.

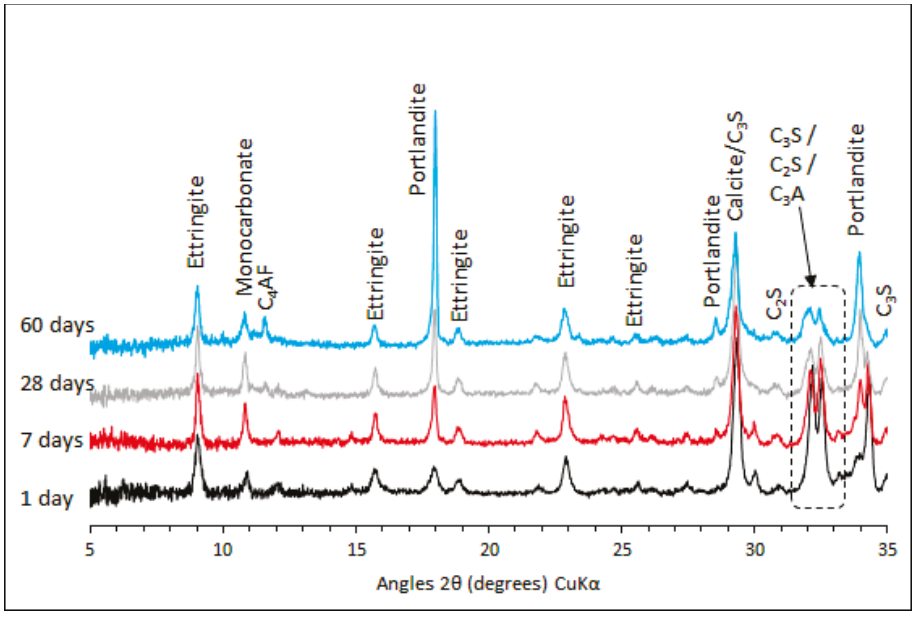


Figure 11. XRD patters from 5 to 35° 2θ for CEM I.

The main hydrates, including portlandite and ettringite, along with calcite, are observed as expected. Due to the presence of approximately 4.8 g/100 g of calcite in the clinker (see Table 3), permitted for CEM I cements under EN 197 [3], monocarbonate is the most abundant AFm phase [20,21], as shown by the peak at 10.8° 2θ, which remains

as hydration continues over time. Ettringite is the dominant AFt phase and is stable over time, with dominant peaks at 9, 15.8, 19 and 23° 2θ.

De Weerdt et al. [22] suggested that the main differences between plain and blended cements containing SCMs are best observed at low angles (8–13° 2θ), where the main peaks of the AFm and AFt phases are found. Figure 12 shows the XRD patterns at these low angles for the three cement replacements here after 1, 7, 28, 60 and 100 days of hydration. Monosulphate, which has been shown to diffract at 9.8° in the literature [23], is not shown in the patterns, whereas monocarbonate is precipitated at 11.5°, with a stable ettringite phase at 9.7° over time. Some hemicarbonate is shown at 11° at 7 days but decreases over time as monocarbonate is formed. These observations are consistent with previous studies [22–24]. Unfortunately, XRD patterns at 60 days for the 35% replacement samples are not available.

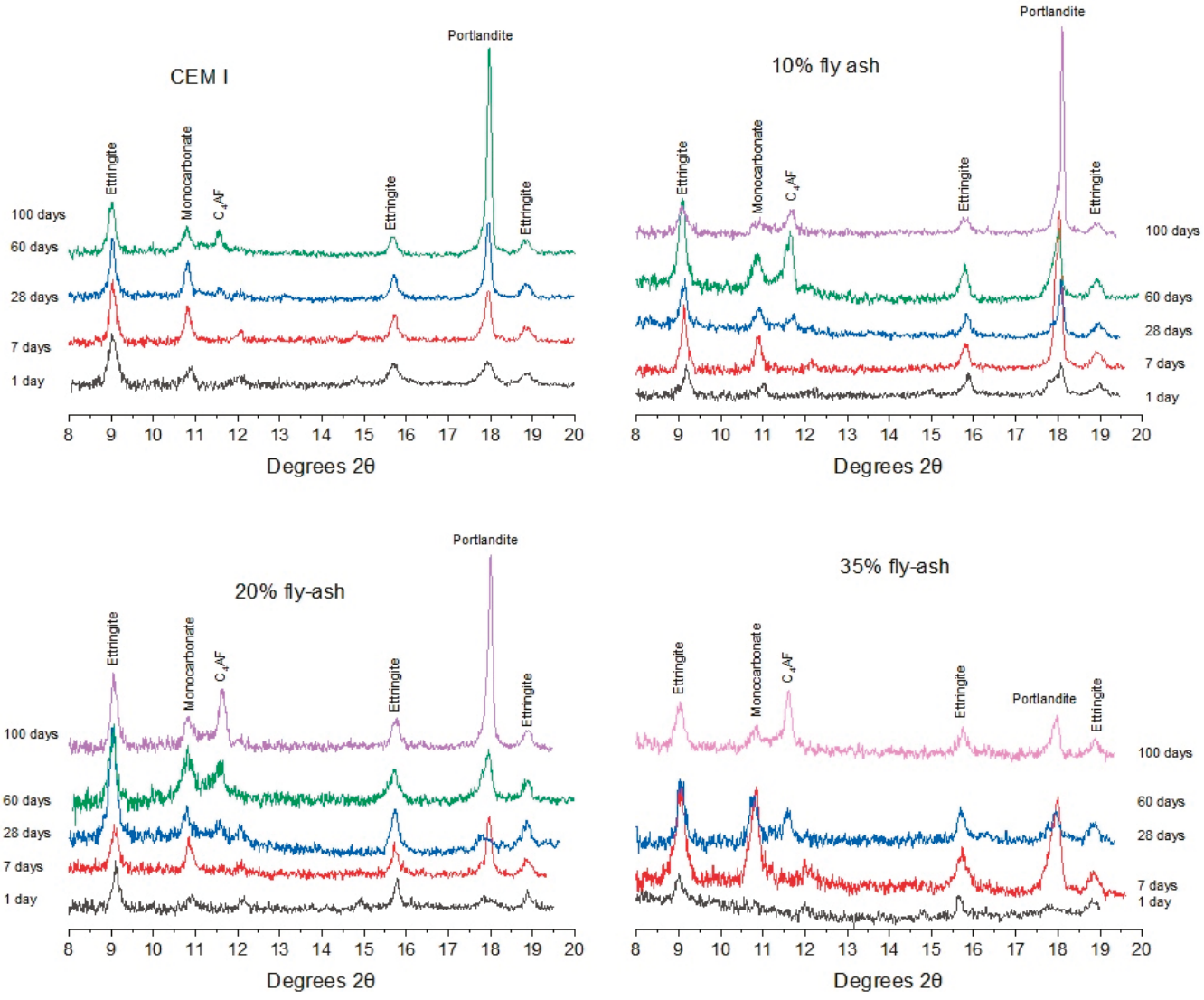


Figure 12. XRD patterns of blended fly ash cements with 0, 10, 20 and 35% replacement levels.

Another significant effect of blended fly ash cements is the reduction in portlandite over time due to pozzolanic activity, where it is converted to additional C-A-S-H with a lowering of the Ca:Si ratio. The increase in alumina may also lead to a reduction in ettringite and increase in AFm compared to 100% CEM I cement. This leads to a reduction in overall volume that could result in lower strengths, hence fly ash additions in cement standards being limited to 35%. This will be studied in the thermodynamic analysis.

4.5. Thermodynamic Modelling Analysis

The change in the solid phase assemblage predicted by PHREEQC over time is shown in Figure 13. The default output from PHREEQC is in moles. By multiplying this by the molar volume of each phase (using the SELECTED_OUTPUT and USER_PUNCH data blocks), the change in volume can be observed. The results show that the formation of monocarbonate with a stable ettringite phase is predicted, which agrees with the experimental observations. The formation of monocarbonate occurs at approximately 3 days, which is evident in the XRD patterns above and seen in the work by Lothenbach et al. [23]. Furthermore, with increasing fly ash, the volume of monocarbonate increases, which is due to additional calcium and aluminates being released into the solution and precipitating. De Weerdt et al. [22] showed that increasing fly ash in blended cements results in a faster OPC/CEM I reaction. Also confirmed is the reduction in portlandite as it reacts with silicates, along with additional alumina, to form additional C-A-S-H. Also, part of the additional aluminates will contribute additional ettringite and monocarbonate phases, as the sulphate content is lower in high-fly ash blended cement [22].

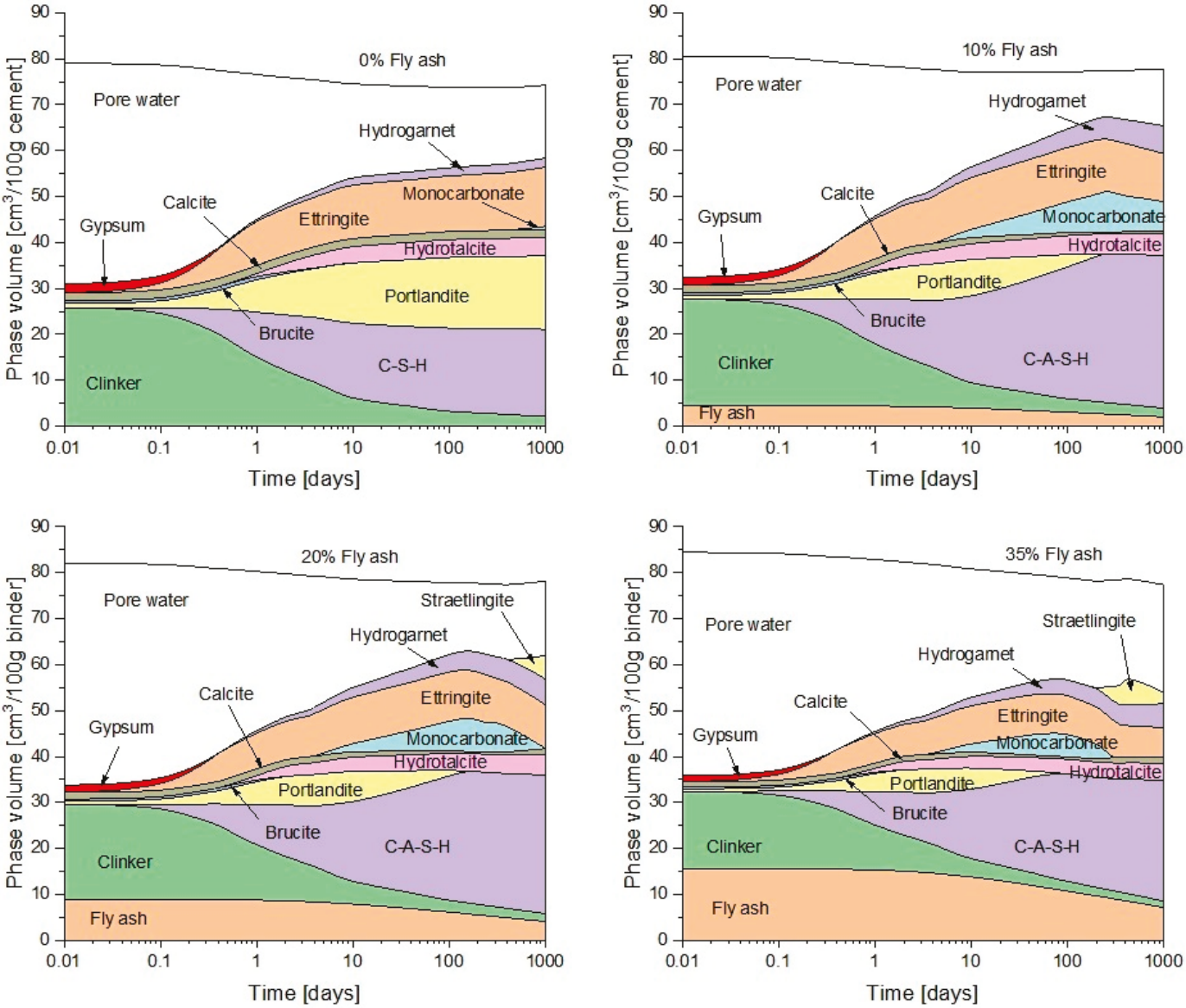


Figure 13. Phase assemblage changes over time for 0, 10, 20 and 35% FA replacement levels.

Lothenbach et al. [25] found that above 40% fly ash, monocarbonate and eventually ettringite both become unstable with the formation of strätlingite, depending on the reactivity of the fly ash, the Al_2O_3 content and Al uptake into the C–A-S–H. It was also found that, above 20% fly ash, portlandite was completely depleted. Strätlingite formation has not been observed in the experimental data but is evident in the thermodynamic simulations within the timeframe shown, at replacement levels at and above 20%, which agrees with previous research. Indeed, as seen in Figure 14, which depicts phase assemblages assuming full hydration at an infinite time in the future, strätlingite is thermodynamically predicted to form for fly ash blended cements ranging from 5 to 35%. Note that, although automatic peak identification assigns the reflection at 11.8° 2θ to the ferrite phase C4AF, we believe this to be erroneous. Our thermodynamic predictions suggest that this peak is due to the precipitation of gypsum, as shown in Figure 14, below.

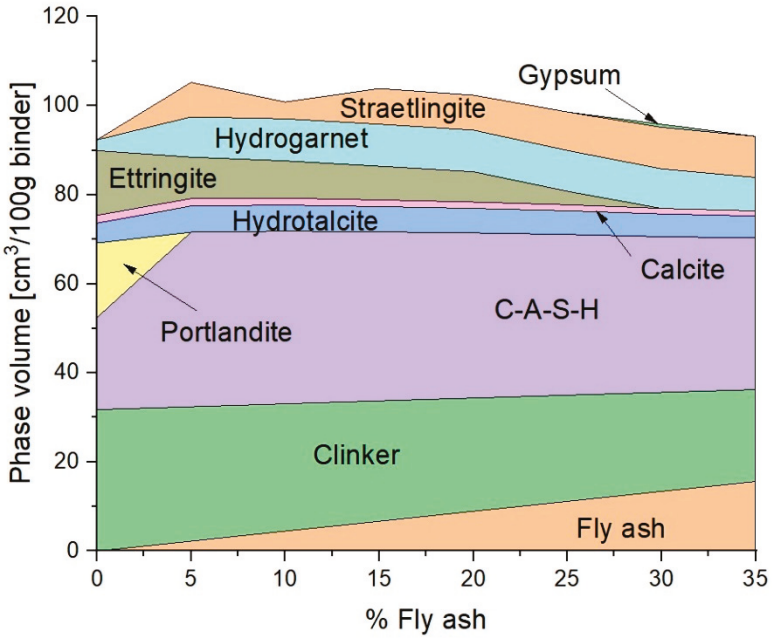


Figure 14. Phase assemblage for fully hydrated binder with fly ash replacements ranging from 0 to 35%.

As shown in Table 2, the SiO_2, Al_2O_3 and Fe_2O_3 contents are high, whereas CaO is low. According to ASTM C618 [6], with a combined SiO_2, Al_2O_3 and Fe_2O_3 of over 70% by mass, the ash belongs to the Class F family. It can be further classified as pozzolanic, and its reactivity is a function of aluminosilicate glass characteristics and particle fineness. The thermodynamic predictions here show portlandite completely depleted before 1000 days for fly ash blends over 10%, indicating that this source of ash is very reactive. This is observed in the XRD data, with the intensity of portlandite lowering over time for all replacement levels. Alelweet et al. [16] found that the ash is most reactive after approximately 20 h of hydration, using the method developed by Luxan et al. [26] and McCarter et al. [27], where the capacity of ash to combine with portlandite is a measure of its reactivity.

5. Discussion

The thermodynamic modelling of the fly ash blended cement appears to be in good agreement with other work in the literature in this area. The depletion of portlandite and precipitation of monocarbonate, co-existing with a stable ettringite phase, all appear to be as expected. These predictions are supported by the experimental data through XRD analysis. The depletion of portlandite and increase in C-A-S-H demonstrate the pozzolanic properties of the fly ash that can add to strength development over time. For all replacement levels at full hydration, portlandite and monocarbonate are shown to be fully exhausted

(Figure 14). Upon reflection, the peak assigned to C_4AF in Figure 12 may actually represent the re-precipitation of gypsum, as shown in Figure 14.

In terms of hydrates volume, replacement levels above 20% show a slight reduction. This has been observed in the literature [28–30], which found reductions in compressive and flexural strength in concrete samples when the fly ash replacement exceeded 20%. Small amounts of hemicarbonate are predicted in the 20% and 35% samples, which correspond with the slow reduction in monocarbonate. Previous works in the literature [23,31] also show small amounts of hemicarbonate, and Lothenbach et al. [23] postulated that the intermediate formation of hemicarbonate is due to the relatively slow dissolution of limestone and insufficient dissolved carbonate being available. While there is no clear XRD evidence for hemicarbonate in Figure 11, the amounts predicted in the model are very small. Not predicted in the thermodynamic predictions over time or the experimental data, at least within the timeframe here, is the existence of strätlingite. As may be seen in Figure 14, it is predicted to form after completing full hydration for all levels of fly ash replacement, due to the amount of soluble silicate in the ash.

The ash under investigation has been confirmed as Class F, in accordance with ASTM C618 [6]. In order for it to be classified a fly ash suitable as a cement replacement and for inclusion in concrete, masonry, mortar, etc., it must comply with the requirements set out in EN 450 [32].

6. Conclusions

The fly ash currently stored in Phase 1 (1985–1995) at the Moneypoint power station has shown to be a suitable Portland cement replacement. The ash is reactive and is shown here to be a pozzolanic material, contributing to solid phase assemblage and not just acting as a pore filler. This is demonstrated by the depletion of portlandite and increase in C-A-S-H in the thermodynamic predictions and experimental observations. Monocarbonate and ettringite appear stable over the timeframes considered here, with the former being removed from the phase assemblage, converting to strätlingite later, as shown by the predictions of the system after complete hydration.

The ash has also been shown, through its chemical properties (work is ongoing on the physical properties), that it meets the requirements of EN 450 to be considered suitable as a fly ash in structural concrete. Subsequent publications will investigate if the ash stored in Phase 2 (1995–2005) and Phase 3 (2005 to the present) are also suitable as a supplementary cementitious material in concrete.

Author Contributions: Conceptualization, N.S. and N.H.; methodology, N.S. and N.H.; software, N.S. and N.H.; validation, N.S., N.H. and M.T.; formal analysis, N.S.; investigation, N.S.; resources, N.H.; data curation, N.S.; writing—original draft preparation, N.S.; writing—review and editing, N.S., N.H. and M.T.; visualization, N.S.; supervision, N.H. and M.T.; project administration, N.H.; funding acquisition, N.H. All authors have read and agreed to the published version of the manuscript.

Funding: This research was funded by a TU Dublin Business Partners Research Scholarship.

Institutional Review Board Statement: Not applicable.

Informed Consent Statement: Not applicable.

Data Availability Statement: The raw data supporting the conclusions of this article will be made available by the authors on request.

Acknowledgments: The authors would like to acknowledge the valuable advice provided by the ESB Ireland staff at the Moneypoint power station for their assistance and to the technical staff at the FOCUS Research Centre in TU Dublin.

Conflicts of Interest: The authors declare no conflict of interest.

References

1. Ireland Energy Needs. Available online: https://www.seai.ie/about/irelands-energy-targets/ (accessed on 7 November 2023).
2. Making Concrete Change. Available online: https://www.chathamhouse.org/2018/06/making-concrete-change-innovation-low-carbon-cement-and-concrete (accessed on 7 November 2023).
3. *BS EN 197-1*; Cement: Composition, Specification and Conformity Criteria for Common Cements. European Committee for Standardization (CEN): Brussels, Belgium, 2011.
4. Snowdon, R.; Richardson, M. Influence of mix parameters on the permeability of PFA-concretes manufactured with PFA sourced in Ireland. In Proceedings of the Colloquium on Concrete Research in Ireland, Dublin, Ireland, 28 August 1997; pp. 3–9.
5. Lenehan, J.; Richardson, M.; O'Kiely, P. Evaluation of pulverised fuel ash as a cement replacer in concretes used in silage storage structures. *Irish J. Agric. Food Res.* **2001**, *39*, 489.
6. *ASTM C618-12*; Standard Specification for Coal Fly Ash and Raw or Calcined Natural Pozzolan for Use in Concrete. ASTM International: West Conshohocken, PA, USA, 2012.
7. *ASTM C1365-06*; Standard Test Method for Determination of the Proportion of Phases in Portland Cement and Portland-Cement Clinker Using X-ray Powder Diffraction Analysis. ASTM International: West Conshohocken, PA, USA, 2007.
8. Holmes, N.; Tyrer, M.; West, R.P.; Lowe, A.; Kelliher, D. Using PHREEQC to model cement hydration. *Constr. Build. Mater.* **2022**, *319*, 126–129. [CrossRef]
9. *BS EN 933-1*; Tests for Geometrical Properties of Aggregates. Determination of Particle Size Distribution. Sieving Method. European Committee for Standardization (CEN): Brussels, Belgium, 2012.
10. Parkhust, D.L.; Appelo, C.A.J. *A Computer Program for Speciation, Batch—Reaction, One—Dimensional Transport and Inverse Geochemical Calculations*; U.S. Geological Survey: Reston, VA, USA, 1999.
11. Parkhurst, D.J.; Appelo, C.A.J. *Description of Input and Examples for PHREEQC Version 3—A Computer Program for Speciation, Batch-Reaction, One-Dimensional Transport and Inverse Geochemical Calculations*; U.S. Geological Survey: Reston, VA, USA, 2013.
12. Lothenbach, B.; Kulik, D.A.; Matschei, T.; Balonis, M.; Baquerizo, L.; Dilnesa, B.; Miron, G.D.; Myers, R.J. Cemdata18: A chemical thermodynamic database for hydrated Portland cements and alkali-activated materials. *Cem. Concr. Res.* **2019**, *115*, 472–506. [CrossRef]
13. Shaji, N.; Holmes, N.; Tyrer, M. Derivation of fly-ash glass phase equations for use in thermodynamic models. In Proceedings of the Civil Engineering Research in Ireland, Galway, Ireland, 29–30 August 2024.
14. Walker, C.; Sutou, S.; Oda, C.; Mihara, M.; Honda, A. Calcium silicate hydrate (C-S-H) gel solubility data and a discrete solid phase model at 25 °C based on two binary non-ideal solid solutions. *Cem. Concr. Res.* **2016**, *79*, 1–30. [CrossRef]
15. Holmes, N.; Walker, C.; Tyrer, M.; Kelliher, D. Deriving discrete solid phases from CSH-3T and CSHQ end-members to model cement hydration in PHREEQC. In Proceedings of the Civil Engineering Research in Ireland (CERI) Conference, Dublin, Ireland, 25–26 August 2022; pp. 28–33.
16. Alelweet, O.; Pavia, S. Potential of a low-calcium fly ash (FA) for the production of alkali-activated materials. In Proceedings of the Civil Engineering Research in Ireland, Bishopstown, Ireland, 27–28 August 2020; pp. 162–167.
17. Xu, G.; Shi, X. Characteristics and applications of fly ash as a sustainable construction material: A state-of-the-art review. *Resour. Conserv. Recycl.* **2018**, *136*, 95–109. [CrossRef]
18. Shi, C.; Roy, D.; Krivenko, P. *Alkali-Activated Cements and Concretes*; CRC Press: Boca Raton, FL, USA, 2003.
19. Walker, R.; Pavía, S. Physical properties and reactivity of pozzolans, and their influence on the properties of lime–pozzolan pastes. *Mater. Struct.* **2011**, *44*, 1139–1150. [CrossRef]
20. Matschei, T.; Lothenbach, B.; Glasser, F.P. The role of calcium carbonate in cement hydration. *Cem. Concr. Res.* **2007**, *37*, 551–558. [CrossRef]
21. Holmes, N.; Russell, M.; Davis, G.; Tyrer, M. Comparing the Measured and Thermodynamically Predicted AFm Phases in a Hydrating Cement. *Appl. Sci.* **2022**, *12*, 10147. [CrossRef]
22. De Weerdt, K.; Haha, M.B.; Le Saout, G.; Kjellsen, K.O.; Justnes, H.; Lothenbach, B. Hydration mechanisms of ternary Portland cements containing limestone powder and fly ash. *Cem. Concr. Res.* **2011**, *41*, 279–291. [CrossRef]
23. Lothenbach, B.; Saout, G.L.; Gallucci, E.; Scrivener, K. Influence of limestone on the hydration of Portland cements. *Cem. Concr. Res.* **2008**, *38*, 848–860. [CrossRef]
24. Schöler, A.; Lothenbach, B.; Winnefeld, F.; Zajac, M. Hydration of quaternary Portland cement blends containing blast-furnace slag, siliceous fly ash and limestone powder. *Cem. Concr. Compos.* **2015**, *55*, 374–382. [CrossRef]
25. Lothenbach, B.; Scrivener, K.; Hooton, R.D. Supplementary cementitious materials. *Cem. Concr. Res.* **2011**, *41*, 1244–1256. [CrossRef]
26. Luxán, M.P.; Madruga, F.; Saavedra, J. Rapid evaluation of pozzolanic activity of natural products by conductivity measurement. *Cem. Concr. Res.* **1989**, *19*, 63–68. [CrossRef]
27. McCarter, W.J.; Tran, D. Monitoring pozzolanic activity by direct activation with calcium hydroxide. *Constr. Build. Mater.* **1996**, *10*, 179–184. [CrossRef]
28. Zhang, P.; Li, Q.; Zhang, H. Combined effect of polypropylene fiber and silica fume on mechanical properties of concrete composite containing fly ash. *J. Reinf. Plast. Compos.* **2011**, *30*, 1349–1358. [CrossRef]
29. Sun, J.; Shen, X.; Tan, G.; Tanner, J.E. Compressive strength and hydration characteristics of high-volume fly ash concrete prepared from fly ash. *J. Therm. Anal. Calorim.* **2019**, *136*, 565–580. [CrossRef]

30. Upadhyay, R.; Srivastava, V.; Arpan, H.; Mehta, P. Effect of Fly Ash on Flexural Strength of Portland Pozzolona Cement Concrete. *J. Acad. Ind. Res.* **2014**, *3*, 218–220.
31. Kuzel, H.-J.; Pöllmann, H. Hydration of C3A in the presence of $Ca(OH)_2$, $CaSO_4 \cdot 2H_2O$ and $CaCO_3$. *Cem. Concr. Res.* **1991**, *21*, 885–895. [CrossRef]
32. *EN 450-1:2012*; Fly Ash for Concrete—Part 1: Definition, Specifications and Conformity Criteria. European Committee for Standardization (CEN): Brussels, Belgium, 2012.

Disclaimer/Publisher's Note: The statements, opinions and data contained in all publications are solely those of the individual author(s) and contributor(s) and not of MDPI and/or the editor(s). MDPI and/or the editor(s) disclaim responsibility for any injury to people or property resulting from any ideas, methods, instructions or products referred to in the content.

applied sciences

MDPI

Article

Comparative Performance Analysis of Small Concrete Beams Reinforced with Steel Bars and Non-Metallic Reinforcements

Abel A. Belay , Julita Krassowska * and Marta Kosior-Kazberuk

Department of Building Structures and Structural Mechanics, Bialystok University of Technology, Wiejska 45A, 15-351 Bialystok, Poland; abel.belay@sd.pb.edu.pl (A.A.B.); m.kosior@pb.edu.pl (M.K.-K.)
* Correspondence: j.krassowska@pb.edu.pl

Abstract: This research investigates the performance of small concrete beams that are reinforced with glass fiber-reinforced polymer (GFRP) bars, basalt fiber-reinforced polymer (BFRP) bars, and traditional steel bars. It addresses the limitations of traditional steel reinforcement, emphasizing the need for alternative strategies. Fiber-reinforced polymer (FRP) materials, including GFRP and BFRP, are examined for their mechanical characteristics compared to steel. The experimental program focuses on ultimate load-bearing capacity, deflection, deformation at different load levels, and failure modes. The concrete specimens, prepared according to Eurocode, consist of six small concrete beams measuring 80 × 120 × 1100 mm with varied reinforcements. The study reveals that GFRP-reinforced beams outperform BFRP and steel reinforcements in ultimate load-bearing capacity, showcasing enhanced structural performance. The GFRP-reinforced beams exhibit capacity and resilience characteristics surpassing those of both BFRP and steel, whereas the deflection observed was higher on both fiber-reinforced beams than on the steel-reinforced beams. The examination of failure modes reveals that the concrete beams that were reinforced with FRP bars showed a bending property before failure, while those reinforced with steel broke easily without bending much. This comprehensive research contributes to advancing our understanding of FRP materials' application in concrete structures, paving the way for further optimization and overcoming limitations in reinforcement materials.

Keywords: BFRP bars; GFRP bars; concrete beam; steel bars

1. Introduction

Concrete, a commonly used building material, is often deficient in tension strength and susceptible to fractures from shrinkage and plastic deformation [1]. This inherent weakness in tension makes plain concrete unsuitable for many structural applications, as even structures under compressive pressures require sufficient tensile strength to prevent buckling. Steel, renowned for its remarkable tensile strength, has been widely employed in the construction industry to reinforce structural components, making it an ideal material for enhancing the strength of concrete buildings. Despite its widespread use, steel reinforcement comes with drawbacks, as highlighted by Mahadev Desai [2]. Corrosion vulnerability is a significant concern, with steel rusting over time when exposed to oxygen and moisture, compromising its structural integrity. Environmental factors, such as high seawater quantities in coastal areas or elevated humidity, can expedite the corrosion process, leading to fractures and spalling in the adjacent concrete, thereby impacting the overall structural stability. Another drawback is the substantial weight of the steel reinforcement due to its density, which contributes significantly to the overall weight of the construction when used in large quantities [3,4].

The inherent limitations in traditional steel reinforcement methods within construction have spurred a thorough exploration of alternative approaches, driven by significant advancements in science and technology. In response to this imperative, there has been a

surge of research interest surrounding the utilization of fiber reinforcements, with studies investigating the characteristics and tensile strengths of various fiber materials to augment their applicability in structural contexts [5,6].

Among the alternatives, fiber-reinforced polymer (FRP) materials have emerged as particularly promising contenders for different infrastructure projects. Their adoption is underpinned by a myriad of compelling advantages, including but not limited to rapid manufacturing and installation processes, inherent lightweight properties facilitating ease of handling, long-term cost-effectiveness due to reduced maintenance requirements, exceptional corrosion resistance, and an extended service life. Such attributes position FRP materials as versatile solutions that are amenable to a wide spectrum of applications across infrastructure construction domains [7–10].

In the realm of civil engineering, the utilization of four primary fiber materials—carbon, glass, aramid, and basalt—dominates the production of reinforced fibers. These fibers serve as the building blocks for the creation of distinct reinforced polymers, encompassing Carbon Fiber-Reinforced Polymer (CFRP), glass fiber-reinforced polymer (GFRP), Aramid Fiber-Reinforced Polymer (AFRP), and basalt fiber-reinforced polymer (BFRP). Each variant of reinforced polymer exhibits a unique array of properties, rendering them apt for specific applications within the civil engineering landscape [6,11–13]. This rich diversity in fiber reinforcement options underscores the nuanced and multifaceted nature of material selection processes within the realm of structural engineering.

Recently, numerous studies have explored the intricate properties of fiber-reinforced polymer (FRP)-reinforced concrete beams, as evidenced by a growing body of research [14–17]. Many of these investigations have focused on the behavior of concrete beams that are reinforced with a single type of fiber reinforcement, comparing their performance against that of conventional steel-reinforced concrete beams [16–22]. Conversely, other studies [23–29] have chosen to examine FRP bars in isolation, subjecting them to various conditions to elucidate their intrinsic properties without integration into concrete structures. While these studies offer valuable insights into the material properties of FRPs, there remains a notable gap in understanding how these materials function within the broader context of concrete elements. Additionally, a study comparing the adhesion properties of FRP fibers, coupled with analytical evaluations of material properties, was conducted [29]. However, the focus on standalone bar analysis overlooks the crucial aspect of comprehensively understanding the interaction between these materials and concrete elements, particularly in load-carrying scenarios.

Among the studies on the ultimate load-carrying capacity of concrete beams reinforced with FRP bars, Urbanski et al. [18] meticulously documented performance metrics, revealing that the average ultimate load of three concrete beams reinforced with 8 mm basalt fiber-reinforced polymer (BFRP) bars was 40 kN, while their steel-reinforced counterparts managed a load of 35 kN. This stark contrast signifies a notable 14.28% increase in the ultimate load-carrying capacity of BFRP-reinforced concrete beams compared to their steel-reinforced counterparts. The impressive tensile strength property inherent in FRP reinforcement is further underscored by the ACI Committee 440 [30].

Moreover, Sirimontree [22] conducted a parallel investigation, discovering that concrete beams reinforced with glass fiber-reinforced polymer (GFRP) bars exhibited an average ultimate load of 70.5 kN, nearly doubling that of steel-reinforced beams. Our research corroborates these findings, demonstrating that concrete beams reinforced with GFRP bars sustained an average ultimate load of 36.9 kN, while those reinforced with BFRP bars sustained 28.4 kN. These figures represent remarkable increases of 76.55% and 35.88%, respectively, compared to concrete beams reinforced with steel bars (20.9 kN).

Regarding the deflection property, some scholars [18,31] documented significantly greater deflections in beams reinforced with BFRP bars compared to reference beams. This phenomenon was attributed to the lower modulus of BFRP bars compared to steel bars. Furthermore, Kosior-Kazberuk et al. [16] reported that concrete beams reinforced with basalt fiber polymers exhibited substantially higher deformations, averaging three to four times more than steel-reinforced concrete beams. Notably, during the initial loading

phase, BFRP-reinforced concrete beams demonstrated a 40% increase in deflection relative to reference reinforced concrete (RC) beams, with this disparity increasing as the load intensified. Consequently, BFRP-reinforced concrete beams exhibited deflections twice as large as those of reference beams.

According to Krassowska et al. [31], concrete beams reinforced with BFRP bars have shown the largest amount of cracks with greater widths, with the first perpendicular crack occurring when the load reached 10% of the ultimate load-carrying capacity of the sample. However, the flexural capacity of beams reinforced with FRP reinforcement has shown significant improvement. In terms of failure modes, observations made by Ashour AF [20] are significant. Additionally, it is important to note that the ACI Committee 440 [30] has highlighted the comparatively low transverse shear resistance exhibited by FRPs. Furthermore, Urbanski et al. [18] observed that beams reinforced with basalt bars displayed cracks that were three to four times wider than those observed in traditionally reinforced concrete beams. This underscores the necessity for further research aimed at developing a comprehensive model to accurately predict the shear capacity of FRP-reinforced concrete beams. Such efforts are crucial for advancing our understanding and ensuring the structural integrity of FRP-reinforced concrete beams.

This research endeavors to bridge this gap in the scientific discourse by embarking on a comprehensive comparative analysis. The study seeks to explore and contrast concrete beams that are reinforced with two prevalent types of FRP—namely, glass- and basalt fiber-reinforced polymer—against beams that are reinforced with traditional steel bars. Importantly, all specimens will be subjected to identical loading and environmental conditions, facilitating a nuanced examination of their performance under standardized parameters. Through this comparative approach, the research endeavors to yield a more holistic understanding of the inherent material properties of each type of reinforcement by identifying areas of strength and potential improvement across various reinforcement methodologies.

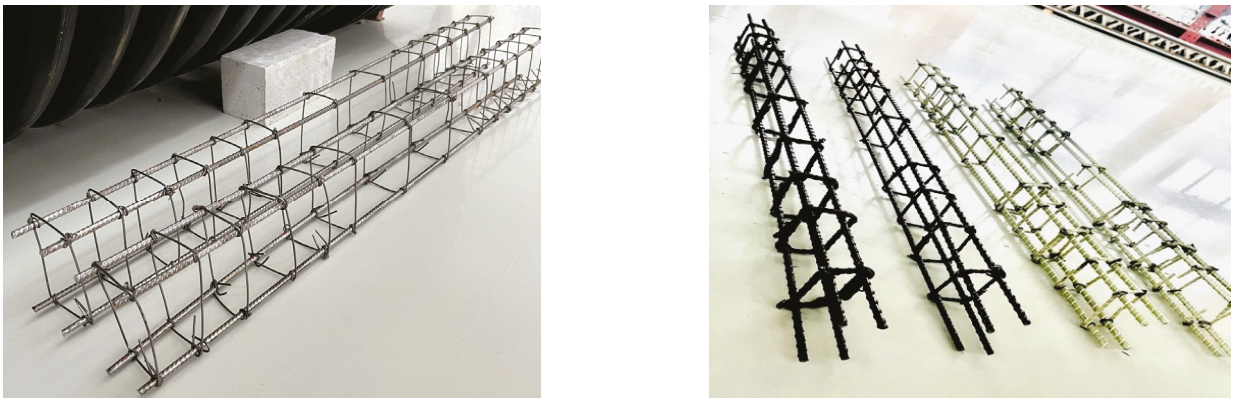
Furthermore, employing small-scale beam tests offers greater control over variables such as material properties and loading conditions, thereby enabling more precise comparisons between different reinforcement types.

This research empirically investigates small concrete beams that are reinforced with glass fiber-reinforced polymer (GFRP) bars, basalt fiber-reinforced polymer (BFRP) bars, and traditional steel reinforcement. The main objective is to analyze the performance of these materials within concrete beams, emphasizing strength, load-bearing capacity, failure modes, and deflection. Simultaneously, the research seeks to identify vulnerabilities in fiber-reinforced polymers (FRPs), laying the groundwork for future studies addressing these limitations and proposing improved reinforcement solutions for concrete beam structures.

2. Materials and Methods

2.1. Materials

The small beams were prepared using a concrete mixture containing CEM I 42.5R Portland cement. The cement content was set at 320 kg/m^3, with a water-to-cement ratio (w/c) of 0.5. The aggregate composition comprised 732 kg/m^3 of sand with a grain diameter of up to 2 mm and 1203 kg/m^3 of coarse natural aggregate with a grain diameter of up to 8 mm. To enhance the mixture, 3.2 kg/m^3 of superplasticizer was incorporated. For longitudinal reinforcement, 6 mm diameter S-500 steel bars with a tensile strength of 315 MPa, 6 mm diameter BFRPs with a tensile strength of 1180 MPa, and 8 mm diameter GFRPs with a tensile strength of 552 MPa were utilized, as depicted in Figure 1 below. The reinforcement design was made to resist the self-weight, with a safety factor of the concrete beam. The diameter variation between the two FRPs was used to achieve equivalent tensile strength and to counter the beam's own weight. This helped the investigation demonstrate the mechanical properties of the reinforcements under similar environmental conditions. All longitudinal reinforcements were prepared with a length of 940 mm.



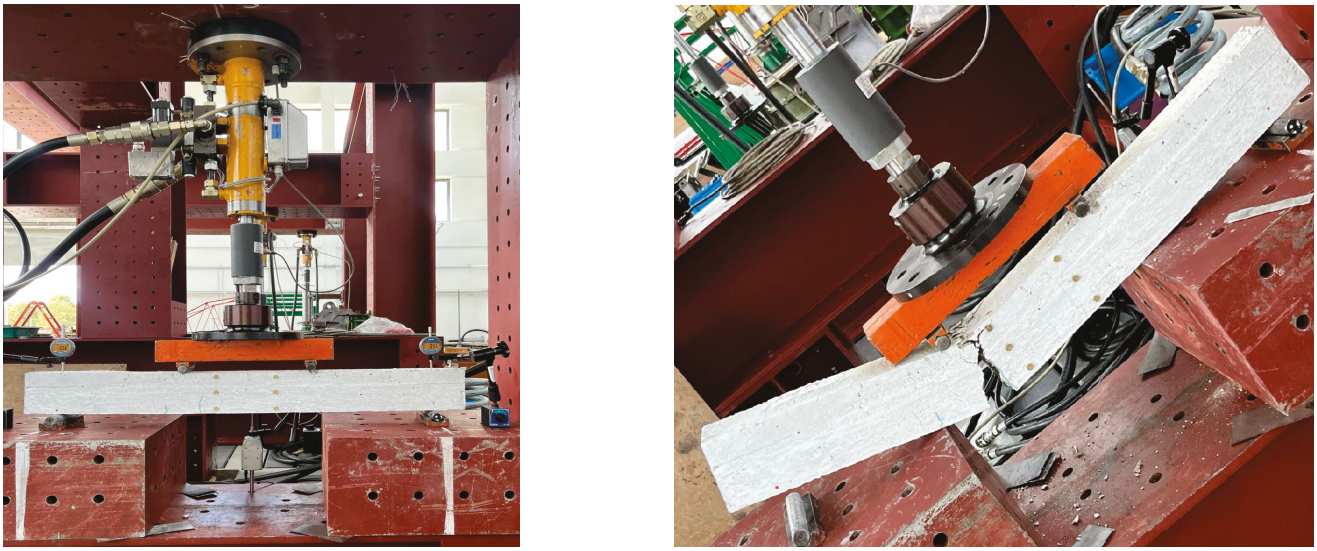
(**a**) (**b**)

Figure 1. Specimens' reinforcement setup: (**a**) steel reinforcement; (**b**) FRP reinforcement.

Before preparing the specimens, concrete strength tests were conducted to meet the required concrete standard based on strength. Three samples with a similar mix ratio were prepared for each strength test. Tests for the compressive strength of the concrete were executed following EN 12390-3:2009 [32], utilizing cubic samples with a side length of 100 mm. Tests for concrete tensile strength were carried out on samples measuring 100 × 100 × 400 mm, in accordance with EN 12390-5:2019 [33]. The modulus of elasticity was determined pursuant to EN 12390-13:2013 [34], using cylindrical specimens with a diameter of 160 mm and a height of 300 mm. The average test results were 59.66 MPa for compressive strength, 3.06 MPa for flexural strength, and 33.53 GPa for elastic modulus.

2.2. Description of Experimental Program

In order to enhance our comprehension of the performance of fiber-reinforced polymers in concrete beams, this research conducted an experimental program focusing on the ultimate load-bearing capacity; midspan deflection; average deformation at the top, middle, and bottom of concrete members under various load levels; and the failure modes of beams. The concrete specimens were mixed, cured, and tested in accordance with the EURO code. Six small beams measuring 80 × 120 × 1100 mm were employed in the study. These included two steel-reinforced beams (ABST-1 and ABST-2), two glass fiber-reinforced beams (ABGF-1 and ABGF-2), and two basalt fiber-reinforced beams (ABBF-1 and ABBF-2). The FRP-reinforced concrete beams were designed in accordance with the guidelines of ACI 440: 1R-06 standards [30]. The evaluation aimed to assess the mechanical characteristics and effectiveness of multiple reinforcing materials in enhancing the structural performance of concrete beams, as per the ACI 440.1R-06 standards [30]. All the beams were simply supported, with support points positioned 80 mm from the outer edge of the beams, resulting in span axes of 940 mm. Point loads are applied at 1/3 of the beam length on both sides. Throughout the test, the ultimate bending capacity of the element was determined, and various values were measured. These included deformations on the surface of the concrete member in the compressive, mid, and tensile zones, maximum deflection at midspan, and the development of cracks and failure modes of the beams. The beams underwent preloading with a 0 kN force. The force buildup occurred over 30 s per 2 kN, and the load was then held constant for approximately 30 s to record test readings. Subsequently, the force was incrementally increased by 2 kN until failure. The load application utilized a hydraulic cylinder, controlled from the control panel of the PZA machine. Deflection was gauged using inductive sensors from the Megatron-Munchen return spring, with specific locations designated for deflection measurements. Additionally, the progressive development of cracks and the shear capacity of the beams were meticulously recorded during the testing process. After each load phase until failure, every new crack was documented, and photographs were taken for the preparation of simulation drawings, as illustrated in Figure 2.



(**a**) (**b**)

Figure 2. Sample specimen under initial and final loading states: (**a**) test sample under initial applied load; (**b**) test sample post ultimate load failure.

3. Test Results and Discussion

3.1. Ultimate Load-Bearing Capacity

The ultimate load is defined as the maximum load achieved by the beam. The loads being supported by concrete beams that were reinforced with GFRP bars markedly exceeded those reinforced with BFRP and steel bars. The concrete beams that were reinforced with BFRP showcased a superior load-bearing capacity compared to those that were reinforced with steel bars. Despite steel-reinforced concrete beams enduring more load before the onset of initial cracks, they ultimately failed sooner. BFRP-reinforced concrete beams manifested the early initiation of cracks when contrasted with steel-reinforced concrete beams but exhibited a higher ultimate load-bearing capacity, trailing only behind GFRP-reinforced concrete beams. The ultimate load-carrying capacity of the beam specimens before failure is depicted in Figure 3 below.

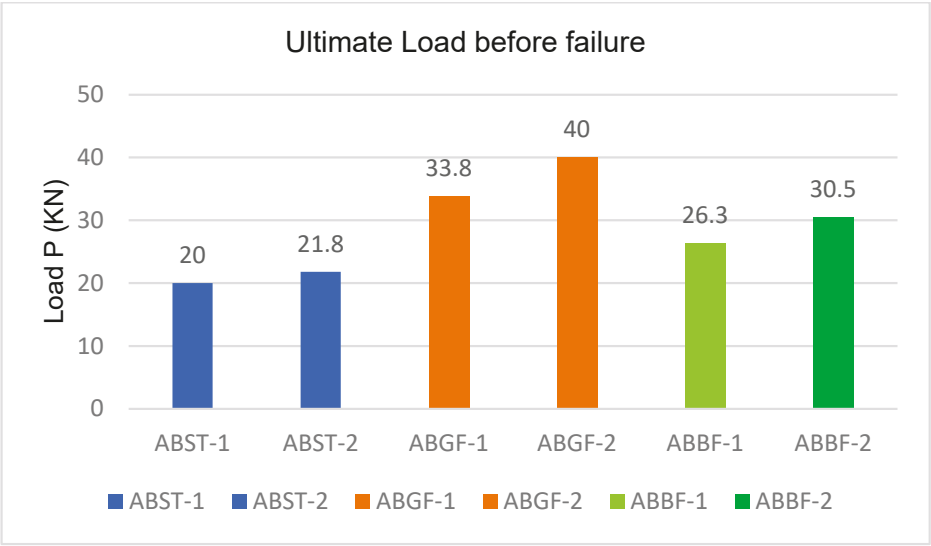


Figure 3. Ultimate load-bearing capacity of beam specimens.

Compared to concrete beams reinforced with steel bars, the average ultimate load-bearing capacity of the concrete beams reinforced with GFRP bars and BFRP bars increased by 76.5% and 35.8%, respectively. This increase can be attributed to the higher tensile strength of FRP bars compared to steel bars. One reason for the significant variation in the ultimate load-bearing capacity of beams reinforced with FRPs is the difference in the cross-sectional area of the reinforcements.

3.2. Deflection

The steel-reinforced concrete beams displayed similar behavior, experiencing failure at stresses of 20 kN and 21.8 kN, resulting in midspan deflections of 4.76 mm and 4.65 mm, respectively. Remarkably, the glass fiber-reinforced concrete beams exhibited remarkable strength, with ABGF-1 collapsing at 32 kN and ABGF-2 lasting until 40 kN. At the point of failure, midspan deflections measured 14.01 mm and 14.61 mm. The basalt fiber-reinforced concrete beams, performing between the steel- and GFRP-reinforced concrete beams, recorded failures at 26 kN (ABBF-1) and 30 kN (ABBF-2). The corresponding midspan deflections were 16.17 mm and 21.50 mm. Figure 4 illustrates the graphical implications of the maximum deflection observed in the sample specimens.

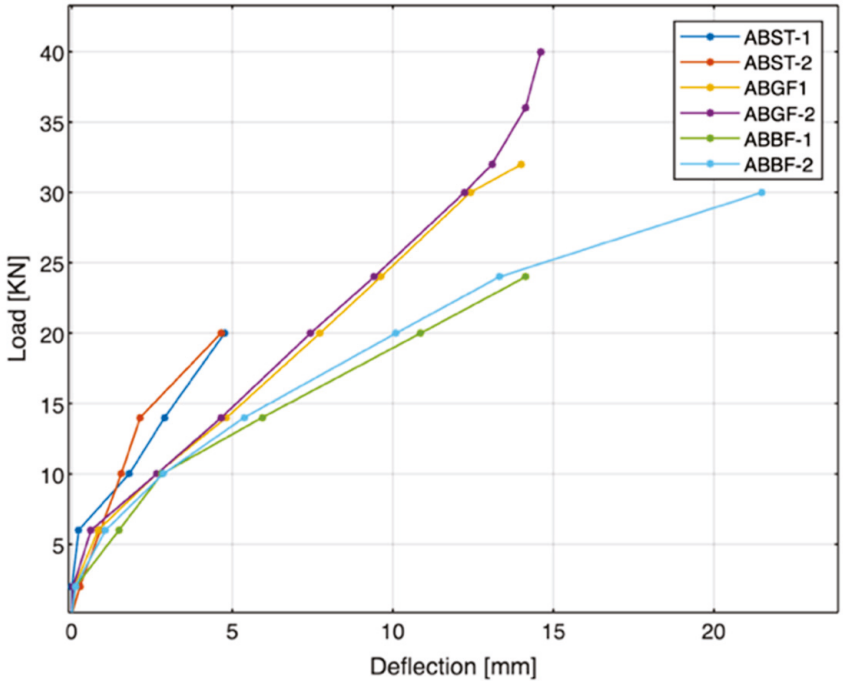


Figure 4. Load vs. deflection curves.

In this study, concrete beams that were reinforced with BFRP bars were found to exhibit higher deflection. Figure 5 illustrates the deflection of the beams under a regular load of 20 kN, where the GFRP-reinforced concrete beams displayed deflections of 7.73 mm (a 62% increase compared to the steel-reinforced beams) and 7.44 mm (a 60% increase compared to the steel-reinforced beams). On the other hand, the basalt fiber-reinforced beams demonstrated deflections of 10.87 mm (a 127% increase compared to the steel-reinforced beams and a 40% increase compared to the GFRP bar-reinforced concrete beams) and 10.10 mm (a 117% increase compared to the steel-reinforced concrete beams and a 35.75% increase compared to the GFRP-reinforced concrete beams). These findings underscore the greater flexibility of basal fiber-reinforced beams compared to glass fiber-reinforced beams.

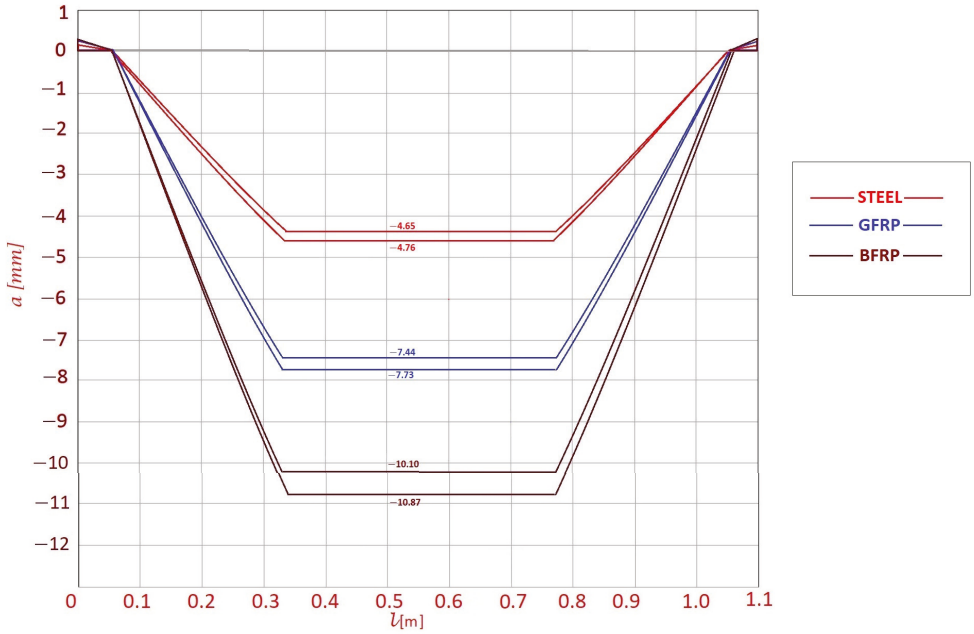


Figure 5. Deflection vs. position curves of beam specimens at 20 kN applied load (deflection data collected from gauges at the midpoint and both ends of the beams, measured at 2 kN load intervals).

3.3. Deformation of Concrete on the Surface of Different Sections of the Beam at Midspan

Figure 6 illustrates the deflection across different zones in the specimens. In Figure 6a, the compressive zone exhibited the least deformation: the steel-reinforced concrete beams measured 1.66 mm and 1.30 mm, the GFRP-reinforced concrete beams measured 1.45 mm and 2.73 mm, and the BFRP-reinforced beams measured 3.45 mm and 1.01 mm. In Figure 6c, the neutral zone demonstrated steel-reinforced concrete beams with 3.94 mm and 3.13 mm, GFRP-reinforced concrete beams with 3.77 mm and 4.38 mm, and BFRP-reinforced concrete beams with 6.86 mm and 7.95 mm. Figure 6c, representing the tensile zone, showed maximum deformation: the steel-reinforced concrete beams with 3.96 mm and 3.42 mm deformations, the GFRP-reinforced concrete beams with 7.04 mm and 9.05 mm, and the BFRP-reinforced concrete beams with 8.43 mm and 10.76 mm.

When comparing the values of concrete deformations at the same levels of beam loads, it was concluded that in the compressive zone, the highest deformations recorded in the case of concrete beams that were reinforced with BFRP and GFRP bars were 3.45‰ and 2.73‰, respectively. These values represented a 107.8% and 64.46% increase compared to the highest deformation recorded by the concrete beams that were reinforced with steel bars, which was 1.66‰. The most significant deformations in the compressive zone occurred in the case of concrete beams reinforced with GFRP bars.

In the mid-section of the beam, the highest deformation was recorded on concrete beams reinforced with BFRP, amounting to 7.95‰, which represented a 101.78% increase compared with the highest deformation recorded on concrete beams reinforced with steel bars, which was 3.94‰. Conversely, the highest deformation recorded for concrete beams reinforced with GFRP was 4.38‰, indicating an 11.17% increase from the deformation of concrete beams with steel reinforcement.

In the last section, which is the tensile zone, the highest deformation was observed for concrete beams that were reinforced with BFRP bars, measuring 10.76‰, and with GFRP bars, measuring 9.05‰. These values represented a 171.72% and 128.53% increase, respectively, compared to the highest deformation of concrete beams reinforced with steel bars, which was 3.96‰.

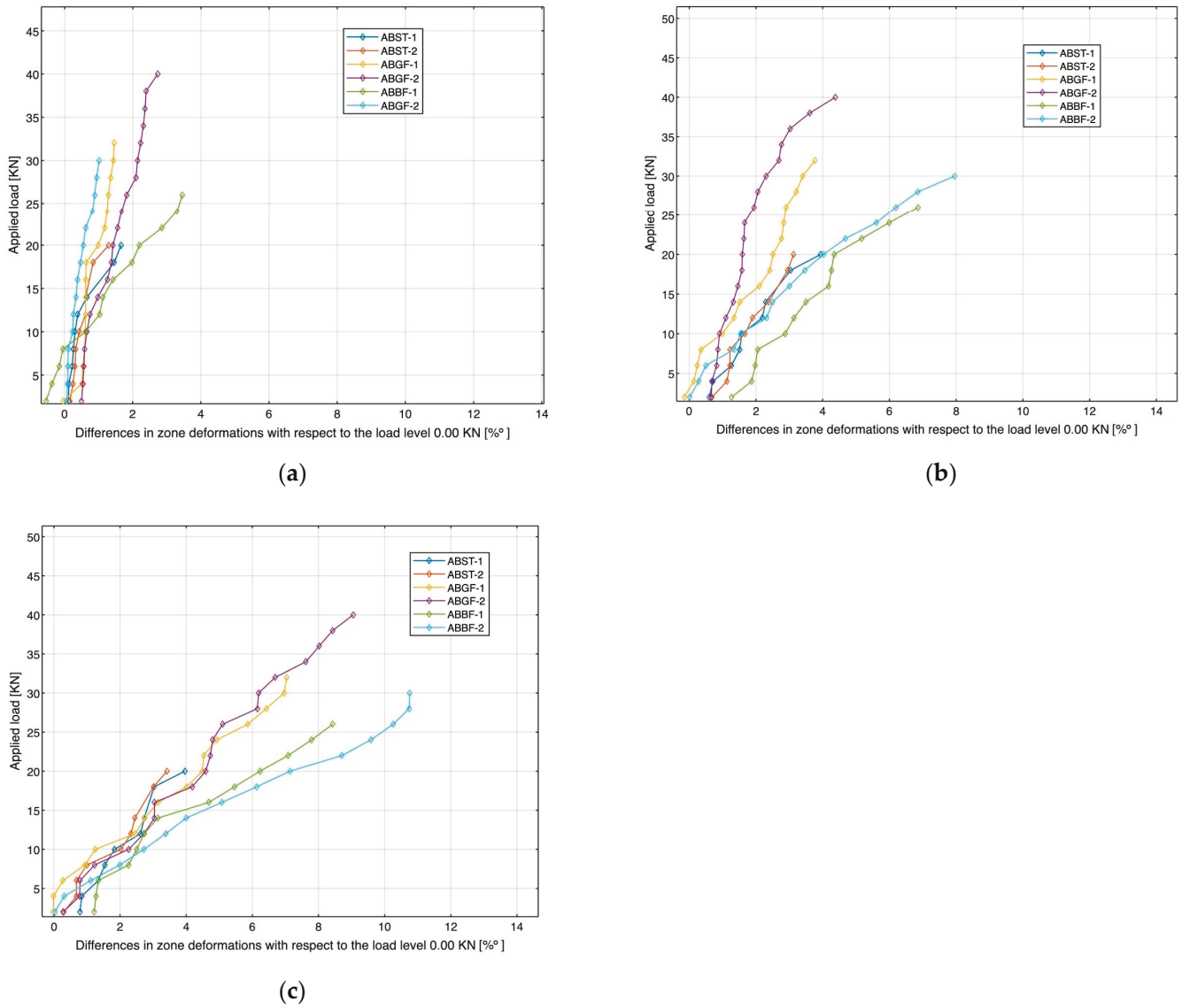


Figure 6. Deformation in different sections of beam specimens: (**a**) deformation in compressive zone; (**b**) deformation in mid-section; (**c**) deformation in tension zone.

3.4. Failure Modes

The analysis of various beam reinforcements unveiled a common pattern in the failure modes, providing valuable insights into their structural behavior under a load. Initially, cracks emerged in the flexural zone and midspan, accompanied by the development of additional vertical cracks within the shear span as the load intensified. Notably, steel-reinforced concrete beams exhibited midspan bending failure (Figure 7a,b), characterized by a premature failure.

In stark contrast, both the GFRP- and BFRP-reinforced concrete beams showcased ductile behavior, characterized by a gradual expansion of the cracks. Diagonal cracks were consistently observed in Figure 7c–f and were particularly notable in the GFRP- and BFRP-reinforced concrete beams, where they manifested as long diagonal cracks. The GFRP-reinforced concrete beams displayed significant deformations and wider crack widths compared to the steel-reinforced concrete beams. The BFRP-reinforced concrete beams exhibited a combination of diagonal tension and flexural failure modes.

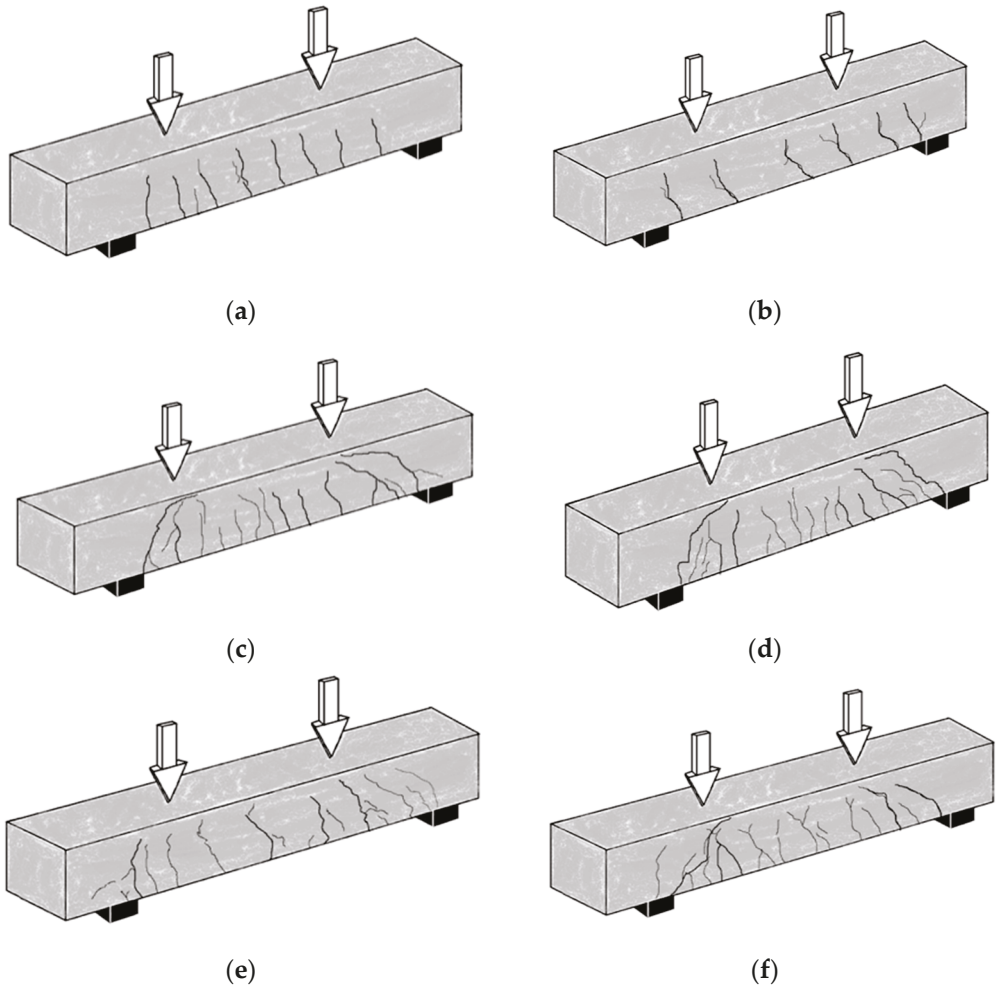


Figure 7. Crack development in tested concrete beams: (**a**) ABST-1; (**b**) ABST-2; (**c**) ABGF-1; (**d**) ABGF-2; (**e**) ABBF-1; (**f**) ABBF-2.

The failure modes exhibited distinct characteristics: the steel-reinforced concrete beams primarily failed due to flexural tension, while the GFRP-reinforced concrete beams demonstrated diagonal tension failure, subsequently leading to shear tension failure. The initiation of shear failure was marked by the emergence of a significant diagonal crack within the shear span, originating from the applied load. This crack propagated towards the point of GFRP reinforcement, eventually extending horizontally at the level of the GFRP bars towards the beam's support. Consequently, bond failure occurred between the longitudinal GFRP bars and the concrete, as illustrated in Figure 7. These detailed observations shed light on the intricate failure mechanisms that are inherent to different types of reinforced concrete beams.

In terms of failure modes, this study revealed a notable increase in crack formations within the FRP-reinforced concrete beams compared to their steel-reinforced counterparts. Specifically, beams reinforced with GFRP experienced shear failure, leading to longitudinal failure, with cracks propagating towards the support structures. The simulation images in Figure 7 provide a visual representation of the observed cracks in all the beam specimens before ultimate failure.

4. Conclusions

This research analyzes the critical shift from traditional steel reinforcement to the use of fiber-reinforced polymer (FRP) materials, specifically, glass fiber-reinforced polymer (GFRP) and basalt fiber-reinforced polymer (BFRP), in small concrete beams. Based on the experimental study, the following conclusions were drawn:

- A comprehensive investigation into the mechanical characteristics of GFRP- and BFRP-reinforced concrete beams in comparison to concrete beams that are reinforced with traditional steel bars was carried out.
- GFRP-reinforced concrete beams demonstrated an ultimate load-bearing capacity of 36.9 kN, outperforming BFRP-reinforced concrete beams and steel-reinforced concrete beams, which exhibited average ultimate load-bearing capacities of 28.4 kN and 20.9 kN, respectively.
- GFRP-reinforced concrete beams demonstrated notable strength and resilience, leading to later failure stages compared to their steel-reinforced counterparts.
- The deflection analysis highlighted the remarkable performance of GFRP-reinforced concrete beams, showcasing their superior strength and deformation properties in comparison to BFRP-reinforced concrete beams. However, both displayed higher deflections compared to concrete beams with steel reinforcement. On average, BFRP-reinforced concrete beams experienced a 122.85% increase in the maximum deflection, while GFRP-reinforced concrete beams exhibited a 61.21% increase when compared with steel-reinforced concrete beams.
- The examination of failure modes demonstrated that both GFRP- and BFRP-reinforced concrete beams exhibited a bending property before failure, while those that were reinforced with steel broke easily without bending much. This provides valuable insights into their distinct failure mechanisms.
- This study is limited to the examination of small concrete beams, which requires further studies regarding the applicability of the findings to full-sized beams. Additionally, further research and development of design models are recommended to address deflection issues associated with concrete beams reinforced by non-metallic reinforcements.

Author Contributions: Conceptualization: A.A.B., J.K. and M.K.-K.; Methodology and experiment: A.A.B., J.K. and M.K.-K.; Formal analysis and investigation: A.A.B.; Resources: A.A.B.; Writing—original draft preparation: A.A.B.; Writing—review and editing: J.K. and M.K.-K.; Supervision: J.K. and M.K.-K. All authors have read and agreed to the published version of the manuscript.

Funding: The research is funded from Bialystok University of Technology; Project number WI/WB-IIL/9/2023. This research work was financially supported by the National Centre for Research and Development, Poland; project number LIDER XIV Nr LIDER14/0206/2023.

Institutional Review Board Statement: Not applicable.

Informed Consent Statement: Not applicable.

Data Availability Statement: The original contributions presented in the study are included in the article, further inquiries can be directed to the corresponding author.

Conflicts of Interest: The authors declare no conflicts of interest.

References

1. Afroughsabet, V.; Biolzi, L.; Ozbakkaloglu, T. High-performance fiber-reinforced concrete: A review. *J. Mater. Sci.* **2016**, *51*, 6517–6551. [CrossRef]
2. Pros and Cons of Steel Reinforcement Bars, Mahadev Desai. Available online: https://gharpedia.com/blog/pros-and-cons-of-steel-reinforcement-bars/ (accessed on 11 November 2022).
3. PCA. *Types and Causes of Concrete Deterioration*; IS536; Portland Cement Association: Skokie, IL, USA, 2002.
4. Gkoumas, K.; Marques Dos Santos, F.L.; Van Balen, M.; Tsakalidis, A.; Ortega Hortelano, A.; Grosso, M.; Haq, G.; Pekár, F. *Research and Innovation in Bridge Maintenance, Inspection and Monitoring*; A European Perspective Based on Transport Research and Innovation Monitoring and Information System (TRIMIS), EUR 29650 EN; Publications Office of the European Union: Luxembourg, 2019; ISBN 978-92-79-99678-8. [CrossRef]
5. Solyom, S.; Di Benedetti, M.; Szijártó, A.; Balázs, G.L. Non-metallic reinforcements with different moduli of elasticity and surfaces for concrete structures. *Arch. Civ. Eng. Environ.* **2018**, *11*, 79–88. [CrossRef]
6. Rubino, F.; Nisticò, A.; Tucci, F.; Carlone, P. Marine Application of Fiber Reinforced Composites: A Review. *J. Mar. Sci. Eng.* **2020**, *8*, 26. [CrossRef]
7. Clyne, T.W.; Hull, D. *An Introduction to Composite Materials*, 3rd ed.; Cambridge University Press: Cambridge, UK, 2019; p. 345.

8. Hollaway, L.C. A review of the present and future utilisation of FRP composites in the civil infrastructure with reference to their important in-service properties. *Constr. Build. Mater.* **2010**, *24*, 2419–2445. [CrossRef]
9. Wang, Z.; Zhao, X.-L.; Xian, G.; Wu, G.; Raman, R.S.; Al-Saadi, S.; Haque, A. Long-term durability of basalt- and glass-fibre reinforced polymer (BFRP/GFRP) bars in seawater and sea sand concrete environment. *Constr. Build. Mater.* **2017**, *139*, 467–489. [CrossRef]
10. 5 Reasons to Use Fiber-Reinforced Polymer(FRP), Scott Reeve, 21 September 2022. Available online: https://www.creativecompositesgroup.com/blog/5-reasons-use-fiber-reinforced-polymer-frp (accessed on 6 May 2023).
11. Gudonis, E.; Timinskas, E.; Gribniak, V.; Kaklauskas, G.; Arnautov, A.K.; Tamulėnas, V. FRP reinforcement for concrete structures: State-of-the-art review of application and design. *Eng. Struct. Technol.* **2013**, *5*, 147–158. [CrossRef]
12. Ahmed, A.; Guo, S.; Zhang, Z.; Shi, C.; Zhu, D. A review on durability of fiber reinforced polymer (FRP) bars reinforced seawater sea sand concrete. *Constr. Build. Mater.* **2020**, *256*, 119484. [CrossRef]
13. Siddika, A.; Al Mamun, A.; Ferdous, W.; Alyousef, R. Performances, challenges and opportunities in strengthening reinforced concrete structures by using FRPs—A state-of-the-art review. *Eng. Fail. Anal.* **2020**, *111*, 104480. [CrossRef]
14. Adam, M.A.; Said, M.; Salah, A.; Elsheikh, A. Experimental and analytical study of high performance concrete beams reinforced with Basalt FRP bars. *Structures* **2023**, *55*, 510–530. [CrossRef]
15. Kudyakov, K.L.; Plevkov, V.S.; Nevskii, A.V. Strength and deformability of concrete beams reinforced by non-metallic fiber and composite rebar. *IOP Conf. Ser. Mater. Sci. Eng.* **2015**, *71*, 012030. [CrossRef]
16. Kosior-Kazberuk, M.; Krassowska, J. Analysis of deflection and cracking of concrete beams with non-metallic reinforcement. *Syst. Saf. Hum.-Tech. Facil.-Environ.* **2019**, *1*, 782–789. [CrossRef]
17. Elango, K.S.; Gopi, R.; Jayaguru, C.; Vivek, D.; Saravanakumar, R.; Rajeshkumar, V. Experimental investigation on concrete beams reinforced with basalt fiber reinforced polymer bars. *Mater. Today Proc.* **2021**, *45*, 2426–2429. [CrossRef]
18. Urbanski, M.; Lapko, A.; Garbacz, A. Investigation on concrete beams reinforced with basalt rebars as an effective alternative of conventional R/C structures. *Procedia Eng.* **2013**, *57*, 1183–1191. [CrossRef]
19. Krassowska, J.; Kosior-Kazberuk, M. The effect of steel and basalt fibers on the shear behavior of double-span fiber reinforced concrete beams. *Materials* **2021**, *14*, 6090. [CrossRef]
20. Ashour, A. Flexural and shear capacities of concrete beams reinforced with GFRP bars. *Constr. Build. Mater.* **2006**, *20*, 1005–1015. [CrossRef]
21. Kosior-Kazberuk, M.; Wasilczyk, R. Analiza ugięć i zarysowania betonowych belek ze zbrojeniem niemetalicznym. *Budownictwo Inżynieria Środowiska* **2017**, *8*, 172–183. Available online: https://pbc.biaman.pl/Content/54364/Budownictwo%20i%20In%C5%BCynieria%20%C5%9Arodowiska.%20Vol.8,%20no.4.pdf (accessed on 7 April 2024). (In Polish).
22. Sirimontree, S.; Keawsawasvong, S.; Thongchom, C. Flexural behavior, of concrete beam reinforced with GFRP bars compared to concrete beam reinforced with conventional steel reinforcements. *J. Appl. Sci. Eng.* **2021**, *24*, 883–890. [CrossRef]
23. Lebedev, M.P.; Startsev, O.V.; Kychkin, A.K. The effects of aggressive environments on the mechanical properties of basalt plastics. *Heliyon* **2020**, *6*, e03481. [CrossRef]
24. Ren, Y.; Wang, H.; Guan, Z.; Yang, K. Evaluation of the properties and applications of FRP bars and anchors: A review. *Rev. Adv. Mater. Sci.* **2023**, *62*, 20220287. [CrossRef]
25. Li, Y.; Yin, S.; Lu, Y.; Hu, C. Experimental investigation of the mechanical properties of BFRP bars in coral concrete under high temperature and humidity. *Constr. Build. Mater.* **2020**, *259*, 120591. [CrossRef]
26. Jin, Q.; Chen, P.; Gao, Y.; Du, A.; Liu, D.; Sun, L. Tensile strength and degradation of gfrp bars under combined effects of mechanical load and alkaline solution. *Materials* **2020**, *13*, 3533. [CrossRef] [PubMed]
27. Khan, Q.S.; Sheikh, M.N.; Hadi, M.N. Tension and compression testing of fibre reinforced polymer (FRP) bars. In Proceedings of the Joint Conference of the 12th International Symposium on Fiber Reinforced Polymers for Reinforced Concrete Structures (FRPRCS-12) & the 5th Asia-Pacific Conference on Fiber Reinforced Polymers in Structures (APFIS-2015), Nanjing, China, 14–16 December 2015; Wu, Z., Wu, G., Wang, X., Eds.; pp. 1–6. Available online: https://ro.uow.edu.au/eispapers/5008 (accessed on 7 April 2024).
28. Szmigiera, E.D.; Protchenko, K.; Urbański, M.; Garbacz, A. Mechanical properties of hybrid FRP bars and nano-hybrid FRP bars. *Arch. Civ. Eng.* **2019**, *65*, 97–110. [CrossRef]
29. Krassowska, J.; Wolka, P.; Protchenko, K.; Vidales-Barriguete, A. Testing the Influence of Metakaolinite and Zeolite on the Adhesion of BFRP and GFRP Bars to Concrete. *Materials* **2023**, *16*, 7435. [CrossRef] [PubMed]
30. *ACI 440.1R-06*; Guide for the Design and Construction of Concrete Reinforced with FRP Bars. ACI Committee 440. American Concrete Institute: Farmington Hills, MI, USA, 2006. Available online: https://www.concrete.org/Portals/0/Files/PDF/Previews/440_1R_15.pdf (accessed on 12 February 2024).
31. Krassowska, J.; Ramírez, C.P. Flexural Capacity of Concrete Beams with Basalt Fiber-Reinforced Polymer Bars and Stirrups. *Materials* **2022**, *15*, 8270. [CrossRef] [PubMed]
32. *EN 12390-3:2009*; Testing Hardened Concrete—Part 3: Compressive Strength of Test Specimens. European Committee for Standardization: Brussels, Belgium, 2009. Available online: https://i2.saiglobal.com/mpc2v/preview/497200114258.pdf?sku=855939_SAIG_NSAI_NSAI_2751255&nsai_sku=i-s-en-12390-3-2019-855939_saig_nsai_nsai_2751255 (accessed on 2 February 2024).

33. *EN 12390-5:2019*; Testing Hardened Concrete—Part 5: Flexural Strength of Test Specimens. European Committee for Standardization: Brussels, Belgium, 2019. Available online: https://cdn.standards.iteh.ai/samples/64401/9078b3193a544c26a16a278e66f0ae34/SIST-EN-12390-5-2019.pdf (accessed on 2 February 2024).
34. *EN 12390-13:2013*; Testing Hardened Concrete. Determination of Secant Modulus of Elasticity in Compression. European Committee for Standardization: Brussels, Belgium, 2013. Available online: https://knowledge.bsigroup.com/products/testing-hardened-concrete-determination-of-secant-modulus-of-elasticity-in-compression?version=standard (accessed on 2 February 2024).

Disclaimer/Publisher's Note: The statements, opinions and data contained in all publications are solely those of the individual author(s) and contributor(s) and not of MDPI and/or the editor(s). MDPI and/or the editor(s) disclaim responsibility for any injury to people or property resulting from any ideas, methods, instructions or products referred to in the content.

applied sciences

MDPI

Article

Effect of Data Augmentation Using Deep Learning on Predictive Models for Geopolymer Compressive Strength

Ho Anh Thu Nguyen [1], Duy Hoang Pham [2,*] and Yonghan Ahn [3,*]

[1] Department of Smart City Engineering, ERICA Campus, Hanyang University, 55 Hanyangdaehak-ro, Gyeonggi-do, Ansan 15588, Republic of Korea; thunguyen98@hanyang.ac.kr
[2] Center for Ai Technology in Construction, Hanyang University, Gyeonggi-do, Ansan 15588, Republic of Korea
[3] Department of Architecture Engineering, Hanyang University ERICA Campus, Gyeonggi-do, Ansan 15588, Republic of Korea
* Correspondence: phamduyhoang@hanyang.ac.kr (D.H.P.); yhahn@hanyang.ac.kr (Y.A.)

Abstract: In recent years, machine learning models have become a potential approach in accurately predicting the concrete compressive strength, which is essential for the real-world application of geopolymer concrete. However, the precursor system of geopolymer concrete is known to be more heterogeneous compared to Ordinary Portland Cement (OPC) concrete, adversely affecting the data generated and the performance of the models. To its advantage, data enrichment through deep learning can effectively enhance the performance of prediction models. Therefore, this study investigates the capability of tabular generative adversarial networks (TGANs) to generate data on mixtures and compressive strength of geopolymer concrete. It assesses the impact of using synthetic data with various models, including tree-based, support vector machines, and neural networks. For this purpose, 930 instances with 11 variables were collected from the open literature. In particular, 10 variables including content of fly ash, slag, sodium silicate, sodium hydroxide, superplasticizer, fine aggregate, coarse aggregate, added water, curing temperature, and specimen age are considered as inputs, while compressive strength is the output of the models. A TGAN was employed to generate an additional 1000 data points based on the original dataset for training new predictive models. These models were evaluated on real data test sets and compared with models trained on the original data. The results indicate that the developed models significantly improve performance, particularly neural networks, followed by tree-based models and support vector machines. Moreover, data characteristics greatly influence model performance, both before and after data augmentation.

Keywords: geopolymer concrete; compressive strength prediction; machine learning; deep learning; data augmentation; tabular GAN

1. Introduction

Concrete stands as the most extensively utilized man-made material worldwide [1]. The incessantly rising demand for concrete translates into a parallel surge in the need for cement, evidenced by a reported 12% increase in 2019 and an anticipated doubling by 2050 [2]. Nonetheless, the production of cement imposes diverse environmental repercussions [2]. Each ton of cement manufactured emits 0.6–1 ton of CO_2, contingent upon production methods, contributing 5–7% to global CO_2 emissions [1]. Additionally, limestone exploitation for cement production triggers water and land pollution, disturbing local ecosystems and biodiversity [3]. Therefore, numerous studies have been conducted to explore alternative materials to replace cement. In recent years, alkali-activated materials, such as geopolymers, have emerged as a promising alternative to OPC-based materials due to their lower carbon footprint and utilization of industrial by-products [4]. Geopolymers are polymeric aluminosilicate cementitious materials that involve industrial wastes (i.e., fly

ash, slag, and silica fume) as the precursors under the action of alkaline chemicals such as sodium hydroxide and sodium silicate [5].

Similar to OPC concrete, the strength of geopolymer concrete is influenced by various parameters, including both external and internal factors. External factors such as temperature, duration, curing types, humidity, and air containment play significant roles in determining the strength of geopolymer concrete [6]. On the other hand, internal factors, such as material quality and mixture compositions, also have a substantial impact. Because of the intricate relationships and inconsistencies in precursors and alkaline activators, a mixture proportion can yield a wide range of compressive strengths [7]. Therefore, calculating the distribution and predicting the intensity using empirical and theoretical methods pose significant challenges.

With the growth in ML applications, researchers are increasingly turning to ML to address the problem of compressive strength prediction for geopolymer concrete [8]. ML models heavily rely on large, high-quality datasets and models trained on datasets containing fewer than 1000 data points are prone to overfitting problems [9]. However, according to the research of Li et al. (2022) [9], only 11% of the studies on applying ML to concrete science utilize datasets containing more than 1000 samples. Also, the average sample size is estimated to be 174 [9]. To mitigate the challenge of data scarcity in concrete science, several studies have adopted generative models such as Generative Adversarial Networks (GANs) [10], Conditional Generative Adversarial Networks (CGANs) [11], Cycle-Consistent Deep Generative Adversarial Networks (CDGANs) [11], and TGANs [12,13] to generate synthetic data for ML models. The use of synthetic data has shown significant improvements in model performance, particularly noticeable with TGAN and CDGAN models [11,13]. However, existing research predominantly focuses on generating data for OPC concrete with less emphasis on geopolymer concrete. Meanwhile, geopolymer mixtures involve a more intricate ingredient system including alumino-silicate precursors and alkali activators, which are more complex than the cement–water system of OPC concrete [5]. Moreover, geopolymer precursors exhibit significant variations in chemical composition and reactivity across different factories, regions, and time periods [5]. Conversely, cement exhibits greater standardization in these aspects, resulting in more consistent data collection and synthesis. Consequently, the impact on generating and utilizing synthetic data on geopolymer strength prediction models may differ from that of OPC concrete. However, research focusing on the effectiveness of data augmentation specifically for geopolymer concrete remains limited.

Therefore, this study aims to investigate the ability of TGANs to generate data for geopolymers and the impacts of synthetic data on various algorithms with different mathematical principles and assumptions, including tree-based models, SVM, and neural networks. To achieve this objective, this study uses datasets collected from the open literature to ensure diversity in sources and the chemical composite of precursors. The dataset collected for this study consists of 930 instances. Specifically, 10 variables are considered as inputs, including the content of fly ash (FA), slag (S), sodium silicate (SS), sodium hydroxide (SH), superplasticizer (SP), fine aggregate (Fag), coarse aggregate (Cag), added water (W), curing temperature (CT), and specimen age (Age). The output of the models is the compressive strength (CS). Subsequently, a TGAN was employed to generate data pertaining to fly ash- and slag-based geopolymer concrete mixtures and their corresponding strengths based on the collected dataset. The generated data was then utilized to train different models, including LightGBM, SVM, and cascade forward neural networks (CFNNs). Next, models using synthetic data will be compared with models using original data with evaluation metrics such as R-squared (R^2), Mean Absolute Error (MAE), Root Mean Squared Error (RMSE), Mean Absolute Percentage Error (MAPE), Root Mean Square Residual (RSR), and Weighted Mean Absolute Percentage Error (WMAPE). Additionally, SHAP analysis was performed to facilitate the interpretation of model performance and data influence.

2. Literature Review

2.1. Machine Learning Models for Prediction

In recent years, there has been an increasing number of studies using ML to predict the strength of geopolymers. Among these, artificial neural networks (ANNs) have emerged as the most prominent, with numerous studies demonstrating promising prediction capabilities [14–16]. Alongside ANNs, convolutional neural networks (CNNs) [17] and deep neural networks (DNNs) [18] are also utilized. Additionally, tree-based algorithms including decision tree (DT) [19], random forest (RF) [20], LightGBM [20], and MP5-tree [21] are employed, showing advantages in model interpretation and handling skewed data. Similarly, recently emerged algorithms known as gene expression programming (GEP) [22] and its variants exhibit superior model interpretation capabilities compared to neural network models. SVM [15] is another popular algorithm that yields results comparable to ANN. To further enhance model performance, various optimization algorithms such as grey wolf optimizer (GWO) [23] and particle swarm optimization (PSO) [23] are employed. Additionally, stacked and ensemble models are utilized in several studies, demonstrating improved performance compared to individual models.

The input variables in these studies typically include mixture proportions, chemical compositions of precursors, specimen age, and external factors such as curing temperature and curing regimes. Table 1 presents the inputs, dataset sizes, and algorithms used in some related studies.

Table 1. Statistical description for the features in the dataset.

Refs.	ML Technology	Dataset	Inputs
[24]	LR, EL, SVMR, GPR, optimized EL, optimized SVMR, optimized GPR	275	Fly ash, coarse aggregate, fine aggregate, Na_2SiO_3, NaOH, SiO_2, molarity of NaOH and Na_2O
[19]	DT, AdaBoost, RF	363	Water/solids ratio, molarity of NaOH, gravel 4/10 mm, gravel 10/20 mm, Na_2SiO_3, NaOH, fly ash, GGBS, fag
[20]	RF, GB, AdaBoost, DT, lightGBM, XGB, kNN, MVR, GPR, CatB	158	Fly ash, superplasticizer, extra water added, Na_2SiO_3, NaOH, coarse aggregate, fine aggregate, slag, specimen age, rest period, curing temperature, molarity, alkali/binder, and Na_2SiO_3/NaOH
[14]	ANN, MLR, MNLR	289	Fly ash, slag, rest period, curing temperature, age, NaOH/Na_2SiO_3, superplasticizer, extra water, molarity of NaOH, alkali/binder, coarse aggregate, fine aggregate
[15]	SVM, DT, RFR	75	Molarity of NaOH, curing temperature, age, % of Na_2SiO_3, NaOH, fly ash, coarse aggregate, fine aggregate, Na_2SiO_3, NaOH
[25]	ANN, M5P, LR, MLR	220	Alkali/binder, fly ash, Si/Al of fly ash, GGBS, Si/Ca of GGBS, coarse aggregate, fine aggregate, Na_2SiO_3, NaOH, Na_2SiO_3/NaOH, molarity of NaOH
[26]	ANN, MARS	208	Water/solid ratio, alkali/binder, Na-Silicate/NaOH, fly ash/slag ratio, NaOH molarity
[27]	RF, GBR, AdaBoost	321	GGBS, Na_2SiO_3 + NaOH (total alkali), coarse aggregate, fine aggregate, water, water/binder, age
[23]	LR, GA, PSO, SVR, GWO, Differential Evolution	268	Water, curing temperature, water/binder, GGBFS/ binder, coarse aggregate, fine aggregate, superplasticizer
[28]	ANN	81	GGBS, silica fume
[16]	ANN, BLR	625	Na_2O:SiO_2, Na_2O:H_2O, GGBFS:H_2O, molarity of NaOH, Na_2SiO_3/NaOH, AS/GGBS, GGBS/water

Table 1. *Cont.*

Refs.	ML Technology	Dataset	Inputs
[29]	DT, Bagging, LightGBM	351	Specimen age, molarity of NaOH, natural zeolite, silica fume, GGBFS
[22]	ANFIS, ANNs, GEP	245	Chemical composition of fly ash, mixing procedures, curing regime, activator content, fine aggregate, coarse aggregate, water, activator/fly ash, and molarity of NaOH

LR: Linear Regression, EL: Elastic Net, SVM: Support Vector Machine, GPR: Gaussian Process Regression, DT: Decision Tree, AdaBoost: Adaptive Boosting, RF: Random Forest, GB: Gradient Boosting, lightGBM: Light Gradient Boosting Machine, XGB: XGBoost, kNN: k-Nearest Neighbors, MVR: Multivariate Regression, CatB: CatBoost, ANN: Artificial Neural Network, MLR: Multinomial Logistic Regression, MNLR: Multinomial Naive Bayes Logistic Regression, M5P: M5′ Model Tree, MARS: Multivariate Adaptive Regression Splines, GA: Genetic Algorithm, PSO: Particle Swarm Optimization, GWO: Grey Wolf Optimizer, BLR: Bayesian Linear Regression, Bagging: Bootstrap Aggregating, LSBoost: Least Squares Boosting, ANFIS: Adaptive Neuro-Fuzzy Inference System, GEP: Gene Expression Programming.

Table 1 indicates that neural network algorithms, tree-based models, and support vector algorithms are of significant interest. Furthermore, it is observed that the sample size in the majority of studies is insufficient for ML models, particularly when utilizing neural networks and deep learning. This scarcity of data, coupled with data complexity, can lead to high-dimensionality and data-bias problems [30]. Hence, data augmentation becomes essential in scenarios of limited experimental data availability.

2.2. Data Augmentation

In the field of concrete science, GANs are employed as powerful tools for data generation in conjunction with ML models. One notable application is the generation of images. For example, Yasuno et al. (2020) [10] utilized GANs to generate damaged images by mapping tri-categorical labels to real damaged images through image-to-image translation. In another study, Dunphi et al. (2022) [31] investigated the performance of a CNN architecture for multiclass damage detection on concrete surfaces.

Recently, several variants of GANs have been used for generating tabular data for concrete strength prediction problems. The study of Marani et al. (2020) [13] used TGAN to generate 6513 plausible synthetic data for RF, extra trees (ETR), and GBR models from 810 experimental instances. The results indicate that the developed models achieved outstanding predictive performance. GAN, DCGAN, and WGAN were used to generate data in the study by Chen et al., 2022 [11]. DCGAN performed better than the remaining models and helped improve the performance of deep learning models. In another study, TGAN was used in generating synthetic data on the shear capacity of FRP-reinforced concrete beams [13]. The study demonstrates that the TGAN technique could address the lack of availability of experimental datasets in engineering problems by synthesizing numerous probable data points.

The previous studies evidence that TGANs are a powerful tool for generating tabular data, particularly in the case of concrete gradation and strength. In light of this, the present study employs a TGAN for data generation to examine the effects of the synthetic data on the performance of various models.

3. Methodology

3.1. Tabular Generative Adversarial Networks

To address the scarcity of available data, GANs have been proposed as a solution for generating synthetic data from original data [32]. GANs draw inspiration from the concept of zero-sum games in game theory. In this framework, there exist two networks: a generator network (G) and a discriminator network (D). The GAN leverages the independent and adversarial relationship between G and D to train and produce specified data samples. G receives a random noise vector as input, from which it generates new relevant data. D, on the other hand, receives both the actual data and the data generated by G as input. These two networks engage in continuous competition, each pursuing its own objectives

independently. As the distribution of the generated data gradually converges to that of the real data, it becomes increasingly challenging for D to differentiate between them, signaling the completion of the GAN model training. Remarkably, various GAN variations have emerged for generating synthetic data, spanning images, text, and numerical data, among others. One notable advancement is the TGAN, which excels in generating both discrete and continuous tabular data simultaneously, showcasing promising efficiency [12].

TGANs employ the Adam optimizer for training, with a long short-term memory (LSTM) network acting as the generator and a multi-layer perceptron (MLP) functioning as the discriminator. One interesting feature of a TGAN is its capability to transform non-Gaussian distributions into continuous columns using a clever mode-specific normalization method. This enables it to capture the inherent distribution of the original data and effectively model the relationships between features. In the optimization phase, the loss function incorporates both KL divergence and cluster vector terms to enhance model stability. The formulation of the loss function is provided in Equations (1) and (2).

Generator:

$$Loss_G = -E_{z\ N(0,1)} logD(G(z)) + \sum_{i=1}^{n_c} KL(u'_i, u_i) + \sum_{i=1}^{n_c} KL(d'_i, d_i) \quad (1)$$

Discriminator:

$$Loss_D = -E_{v_{1:n_c}, u_{1:n_c}, d_{1:n_d}\ P(T)} logD(v_{1:n_c}, u1{:}n_c, d1{:}n_d) + E_{z\ N(0,1)} logD(G(z)) \quad (2)$$

where u'_i and d'_i are synthetic data, u_i and d_i are original data, and n_c and n_d are the numbers of continuous and discrete variables, respectively.

Figure 1 illustrates the architecture of a TGAN. In this investigation, a TGAN was trained utilizing the TGAN package implemented in Python.

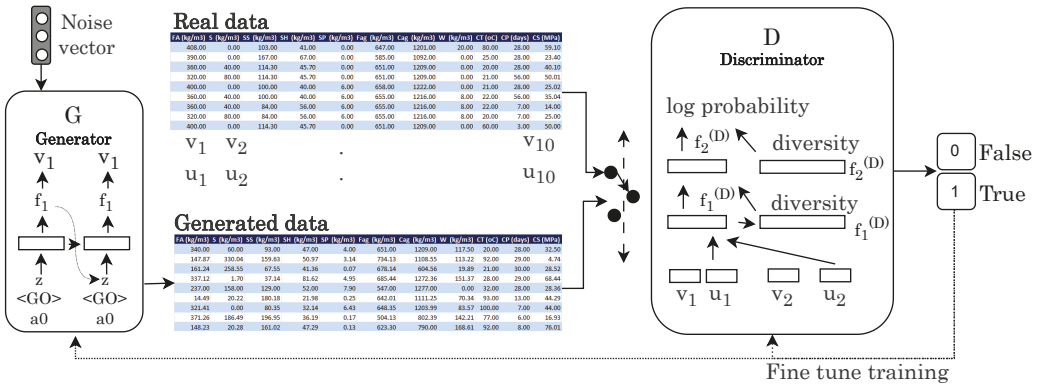


Figure 1. TGAN model in this study.

3.2. Machine Learning Predictive Models

Based on a preliminary literature review, this study recognizes tree-based algorithms, support vector algorithms, and neural networks as prominent choices for intensity prediction tasks in geopolymers. Consequently, the study intends to evaluate how the utilization of synthetic data impacts the performance of these models. Specifically, LightGBM, SVM, and CFNN were investigated to represent the aforementioned three algorithm groups. The advantages and disadvantages of these algorithms in compressive strength prediction scenarios are summarized in Table 2. In the context of this study, these ML techniques do not require the data to follow a normal distribution, making them suitable for the collected dataset in this study.

Table 2. Comparison of the three models.

Algorithms	Advantages	Disadvantages
LightGBM [33]	- Efficient and faster training compared to traditional gradient boosting algorithms - Handles large-scale data and high-dimensional features effectively - Automatically handles missing values - Resistant to overfitting and provides good accuracy and generalization performance	- Limited support for certain data types, such as text or images (requires feature engineering) - Can be sensitive to noise or outliers in the data - Model complexity can increase with the number of trees
SVM [34]	- Effective for high-dimensional data and can handle large feature spaces - Provides good generalization performance, even with limited training data - Robust to overfitting and works well with non-linear data by using kernel tricks	- Training time can be slow for large datasets - Not well-suited for large datasets with noise or outliers - Limited interpretability compared to some other models
CFNN [35,36]	- Highly versatile and can model complex non-linear relationships - Capable of automatic feature extraction and learning hierarchical representations - Scalable to large datasets with the availability of computational resources	- Require large amounts of training data to achieve good performance - Can be computationally expensive, especially for deep architectures - Limited interpretability and often considered as "black boxes"

3.3. LightGBM

Light GBM, developed by Microsoft Research [37], is a variant of Gradient Boosting Decision Trees based on a decision-tree technique. LightGBM constructs trees leaf by leaf, employing a histogram-based technique to partition leaf nodes. This approach yields notable efficiency and memory savings [38]. Although the leaf-wise tree growth enhances model complexity, LightGBM can achieve greater accuracy improvements with each iteration of the algorithm. However, this method poses a significant risk of overfitting, which is addressed through regularization terms. To render LightGBM a swift, effective, and dependable ensemble method, two strategies are employed: gradient-based one-side sampling (GOSS) and exclusive feature bundling (EFB) [38]. GOSS selectively retains samples with higher gradients during the training phase, as they contribute more to information gain, discarding those with lower gradients. Consequently, compared to traditional methods like DT, RF, and gradient boosted decision trees (GBDT) that examine all data for information gain calculation, LightGBM with GOSS significantly reduces computation time. On the other hand, EFB clusters exclusive features together in a sparse feature space, reducing dimensionality and enhancing efficiency. Particularly in scenarios involving high feature dimensions, LightGBM combined with EFB substantially enhances model efficiency and scalability compared to standard approaches (e.g., RF, DT, and GBDT). Consequently, this adaptation markedly accelerates the computation process and minimizes memory usage while preserving prediction accuracy.

To enhance the performance of the LightGBM in this study, grid search cross-validation was employed to explore various hyperparameter combinations for LightGBM, resulting in the selection of optimal values: n_estimators = 300, learning_rate = 0.3, max_depth = 10, num_leaves = 30, and min_child_samples = 20.

3.4. Support Vector Machine (SVM)

The SVM method employs non-linear decision boundaries to carry out regression and classification tasks, offering significant flexibility within the feature space where these boundaries reside. It relies on principles of statistical learning and structural risk reduction. However, SVM parameters are not predetermined, and there is no prior knowledge about the distribution of inputs and outputs. During training, input and output values are aligned in training sets, enabling the derivation of decision functions to classify new datasets based on these alignments. The equation representing the SVM-derived plane is expressed as Equation (4) [39].

$$f(x) = (w, x) + b \tag{3}$$

In this context, the weight vector w and the scalar constant b play crucial roles. The training data is denoted by n-dimensional vector x. By computing the dot product of w and x, and adding the scalar b, the function's result is obtained. Each training datum is represented by an n-dimensional vector. The dataset, comprising m data points, assigns each data point to one of the elements in the set $y \in \{+1, -1\}$. The SVM model illustrates class samples as points in space, aiming to separate instances of different classes with an open vector, maximizing the space between them [39].

In this work, SVM hyperparameters were fine-tuned, leading to optimal parameters: C = 133, epsilon = 0.02, and gamma = 0.7.

3.5. Cascade forward Neural Networks (CFNNs)

CFNN is a specialized form of the MLP with a unique network structure. Generally, CFNN includes an input layer, one or more hidden layers, and an output layer, mirroring the architecture of the MLP model. However, unlike the MLP, which employs a feedforward network structure to transmit data from the input to output layers via hidden layers, CFNN introduces additional direct connections between the input and output layers [40]. This difference results in CFNN having a denser interconnection of weights and biases compared to the traditional MLP. The CFNN architecture in this study is depicted in Figure 2.

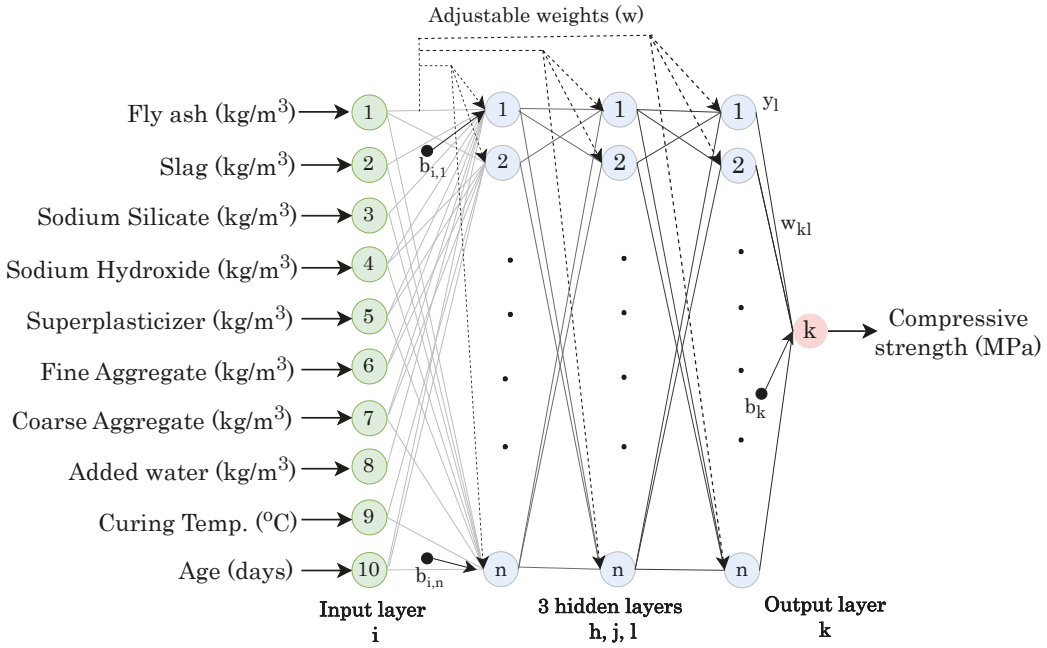


Figure 2. CFNN architecture in this study.

The CFNN model constructs its cascade architecture within the network by incorporating newly added neurons and their connections. The additional connections between the input layer and subsequent layers potentially enhance the learning rate of the network by adjusting the weights of the newly formed neurons exclusively [40]. The total inputs of the jth hidden node from the ith input node are described as Equation (5):

$$n_{inputs,j} = \sum_{i=1}^{N} w_{ij} u_i \quad 1 \le j \le N \tag{4}$$

where N represents the count of input variables; w_{ij} signifies the weight connecting the ith input node to the jth hidden node; and u_i is the ith input.

The output of the jth hidden node is determined as Equation (6).

$$O_{hidden,j} = f(n_{\text{input},j}) \tag{5}$$

Ultimately, the output of the CFNN model is calculated as Equation (7).

$$Y_n = g(\sum_{j=1}^{M} w_{jn}^2 O_j + \sum_{i=1}^{N} w_{i,n}^3 u_i) \quad \text{for } 1 \le n \le N \tag{6}$$

where M is the number of hidden nodes.

To improve the CFNN, the architecture and training parameters of the model were optimized using the GWO, specifying the number of neurons, learning rate, batch size, and epochs for two networks. The parameter bounds were set to [(0.0001, 0.01), (8, 128), (8, 128), (8, 128)] with 50 iterations and 20 wolves. After tuning, the model commences with an input layer that matches the dimensionality of the feature space (10 neurons), followed by the first hidden layer comprising 26 neurons. Subsequently, two additional hidden layers are introduced in a cascaded fashion, with 128 and 21 neurons, respectively. Each of these hidden layers is connected to the input layer and all the preceding hidden layers. The activation function employed for the hidden layers is the Rectified Linear Unit (ReLU), which introduces non-linearity into the model and enables it to learn complex patterns present in the data. The output layer consists of a single neuron, aiming to predict the compressive strength of the geopolymer concrete. During the training process, the Adam optimizer is utilized. The MSE serves as the loss function, optimizing the model to minimize the squared differences between the predicted and actual compressive strength values.

To measure the performance of the predictive models, six types of indicators are utilized, namely, R^2, MAE, RMSE, MAPE, RSR, and WMAPE. The chosen evaluation metrics offer specific benefits in comparing the models. R^2 elucidates how well each model captures the variance in the target variable, crucial for assessing predictive capability and overall model fit. MAE and RMSE provide tangible measures of prediction accuracy, enabling direct comparison of error magnitudes and helping identify which model yields predictions closer to actual values. RSR normalizes errors by dataset variability, facilitating assessment of model fit relative to inherent data characteristics, which is particularly valuable when dealing with datasets of varying scales or levels of variability. WMAPE, by considering the weighted average of absolute percentage errors, offers a nuanced evaluation that accounts for the relative importance of different observations and scales of data, thus providing insight into model performance across diverse subsets. These metrics collectively provide a comprehensive understanding of the strengths and weaknesses of models trained on both authentic and synthetic data. These metrics are presented in the following equations:

$$R^2 = 1 - \frac{\sum_{i=1}^{n}(y_i - \hat{y}_i)^2}{\sum_{i=1}^{n}(y_i - \bar{y})^2} \tag{7}$$

$$MAE = \frac{1}{n}\sum_{i=1}^{n}|y_i - \hat{y}_i| \tag{8}$$

$$RMSE = \sqrt{\frac{1}{n}\sum_{i=1}^{n}(y_i - \hat{y}_i)^2} \tag{9}$$

$$MAPE = \frac{1}{n}\sum_{i=1}^{n}\left|\frac{y_i - \hat{y}_i}{y_i}\right| \times 100\% \tag{10}$$

$$RSR = \frac{\sum_{i=1}^{n}(y_i - \hat{y}_i)^2}{\sum_{i=1}^{n}(y_i - \bar{y})^2} \tag{11}$$

$$WMAPE = \frac{\sum_{i=1}^{n} w_i|y_i - \hat{y}_i|}{\sum_{i=1}^{n} w_i} \times 100\% \tag{12}$$

wherein y_i and $\hat{y}_i$ are observed and predicted value of the dependent variable for the ith observation; $\bar{y}$ presents the mean of the observed values of the dependent variable y; and w_i in WMAPE equation is weight assigned to observation i.

3.6. Study Framework

This study investigates the effect of synthetic data on various ML models. Figure 3 illustrates the process of developing and assessing TGAN, as well as ML models for predicting geopolymer compressive strength. Initially, the data is partitioned into training (80%) and testing (20%) sets. Models including LightGBM, SVR, and CFNNs are constructed in Python and trained with the training set and evaluated using metrics such as R^2, MAE, RMSE, MAPE, RSR, and WMAPE. Concurrently, the training set is used to train a tabular GAN model to generate synthetic data. This dataset, including the original training set and 1000 newly generated data points, is utilized to train LightGBM, SVR, and CFNNs models. Subsequently, these models are evaluated on the original test set using the same metrics. By analyzing the obtained results, this study derives and presents insights into the impact of employing synthetic data across various algorithmic forms in the following section.

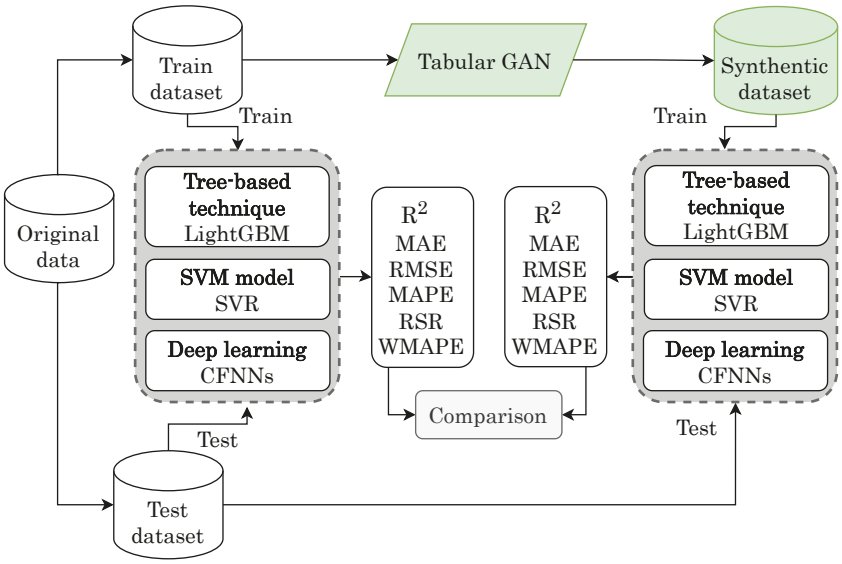


Figure 3. Evaluation flowchart of data augmentation and predictive models.

4. Results and Discussion

4.1. Data Collection and Preparation

This study utilized 930 data points derived from laboratory experiments to develop and test prediction models. The data, extracted from peer-reviewed articles [41–59], pertained to mixtures and compressive strength of alkali-activated concrete using fly ash and slag. The data were manually curated from text, tables, and figures within the publications. The dataset comprises 10 input variables and 1 output as depicted in Table 3. Notably, natural aggregates served as both coarse and fine aggregates for the model. Additionally, the concrete specimen sizes varied across articles according to adopted standards, namely cube size (150 mm) and cylinder size (150 mm × 300 mm, 100 mm × 200 mm). Since the size of the testing sample influences compressive strength, all data points were standardized to a consistent size (150 mm × 300 mm cylinder) using the Elwel table [60].

To understand the details of the variables in the collected dataset, a statistical analysis was performed with IBM SPSS Statistics 27.0. Based on the initial analysis, the distributions of the SP and CP were skewed and contained significant numbers of outliers, which could severely reduce the performance of ML models. To address this issue, the interquartile range (*IQR*) method was employed to identify and remove outliers from these two parameters. The interquartile range is a robust measure of scale that is not influenced by outliers [61]. It

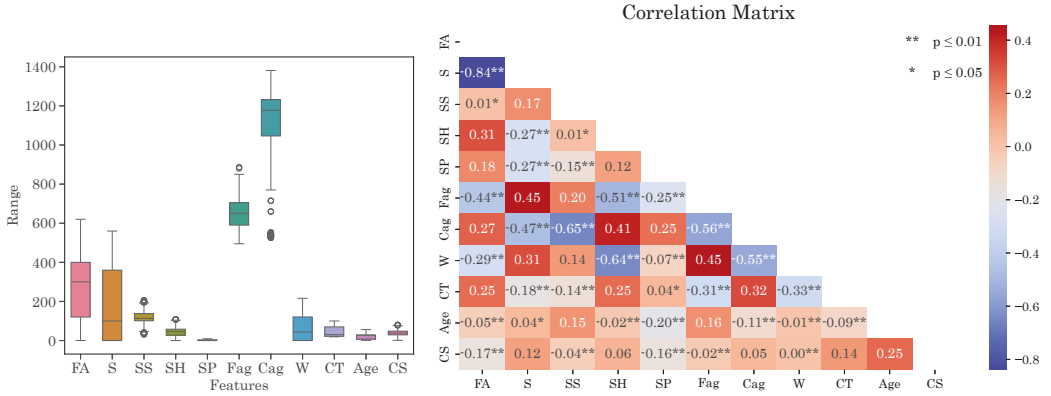
is calculated as the difference between the 75th percentile ($Q3$) and the 25th percentile ($Q1$) of the data:

$$IQR = Q3 - Q1 \tag{13}$$

For the SP and CP parameters, the IQR was calculated, and any data point that fell outside the range of [$Q1 - 1.5 \times (IQR)$, $Q3 + 1.5 \times (IQR)$] was identified as an outlier and removed from the dataset [61]. After removing the outliers from the SP and CP, the remaining data points in the dataset were used for further analysis and modeling. Figure 4a depicts the box plot of the dataset after outlier removal.

The Pearson correlation coefficients between all pairs of input parameters were calculated and illustrated in the correlation matrix shown in Figure 4b. The heatmap indicates that there are no parameters having strong linear relationship with each other. So, all the parameters are kept to construct the train and test datasets.

The statistical description of the dataset after outlier removal is presented in Table 3. The content of fly ash and GGBS varied significantly, with values ranging from 0 to 620 kg/m^3 and 560 kg/m^3, respectively. This wide range is attributed to the dataset including mixtures utilizing solely FA or GGBS, as well as combinations of both materials. The age of the concrete ranged from 1 to 56 days and the compressive strength ranged from 1.25 to 80.51 MPa.



(**a**) (**b**)

Figure 4. Data analysis. (**a**) Box plot after outlier removal. (**b**) Correlation matrix.

Table 3. Statistical description for the features in the dataset.

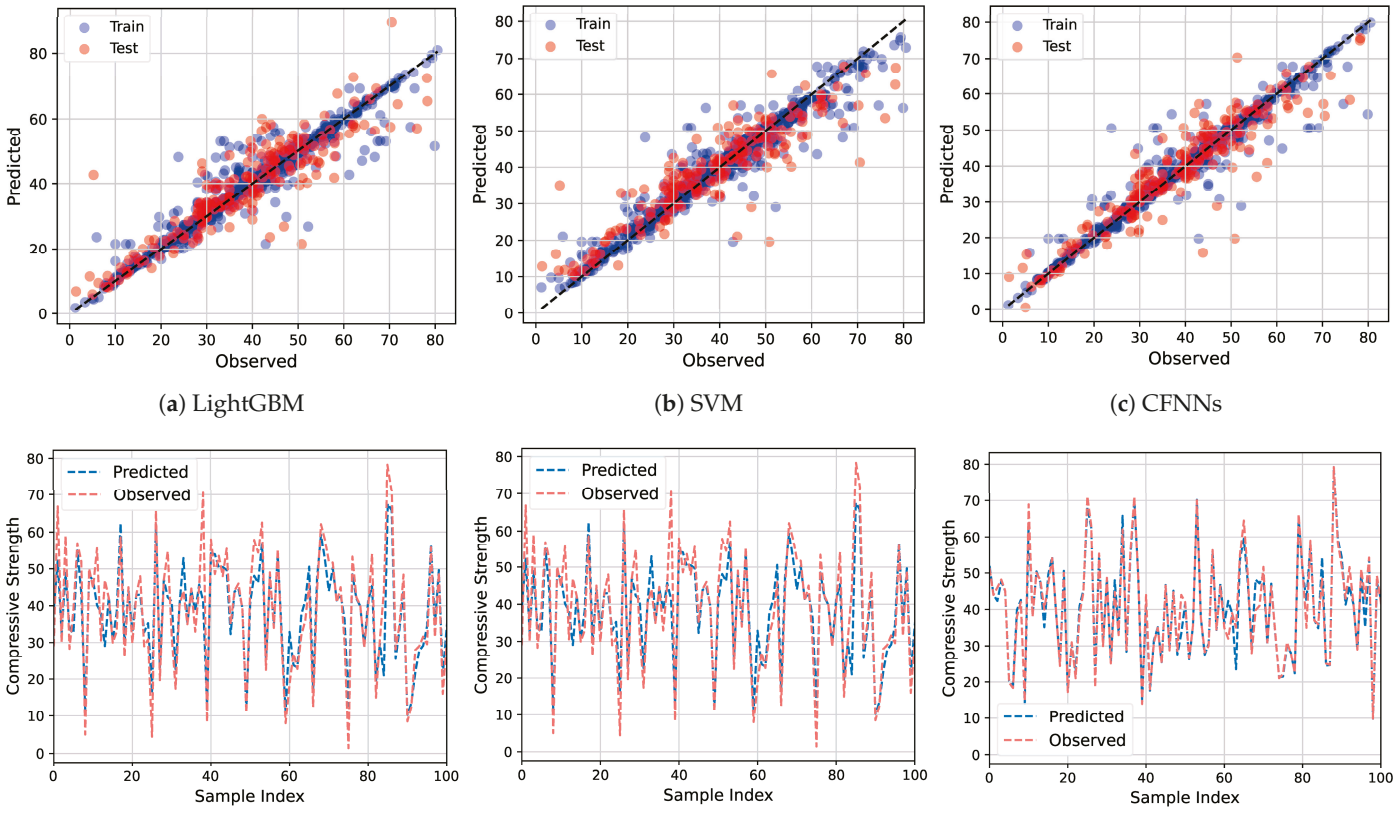
Feature Name	Symbol	Unit	Mean	STD	Min	Max	Skewness
Fly ash	FA	kg/m^3	246.72	159.99	0.00	620.00	−0.3385
GGBS	GGBS	kg/m^3	176.27	177.38	0.00	560.00	0.4777
Sodium silicate	SS	kg/m^3	117.56	36.08	32.00	205.50	0.2317
Sodium hydroxide	SH	kg/m^3	44.78	22.51	0.00	108.00	0.1219
Superplasticizer	SP	kg/m^3	1.52	2.57	0.00	9.00	1.3455
Fine aggregate	fag	kg/m^3	656.26	81.65	495.00	887.00	0.3134
Coarse aggregate	cag	kg/m^3	1082.58	239.87	525.40	1381.35	−1.3052
Added water	w	kg/m^3	64.72	62.10	0.00	216.00	0.4727
Curing temperature	CT	°C	48.16	28.21	19	100	0.4981
Curing period	CP	days	21.76	14.99	1	56	0.6225
Compressive strength	CS	MPa	38.45	14.95	1.25	80.51	0.1296

In summary, the analysis of box plots, correlation heatmaps, and various statistical parameters reveals that the dataset contains few outliers and can accommodate all 10 input variables without multicollinearity issues. However, certain variables exhibit high skewness, indicating non-normal data distribution. This deviation from normality contradicts the assumptions of classical ML algorithms [62] like linear regression and Gaussian Naive Bayes. Therefore, the algorithms applied should be non-parameter algorithms or neural networks which do not explicitly assume that the input features (independent variables) are normally distributed or have a symmetric distribution [62].

4.2. Performance of Models before Data Augmentation

Figure 5 show the results of the three models (LightGBM, SVM, and CFNN) before data augmentation. The scatter plots in Figure 5a–c visually depict the models' performance by comparing the predicted and observed values for both the training and test sets. Figure 5a demonstrates that LightGBM provides a moderate fit to the data. Figure 5b, which represents the SVM model, exhibits more scattered points that deviate further from the ideal line, indicating a poorer performance compared to LightGBM. Figure 5c, corresponding to the CFNN model, reveals that the data points are more tightly clustered around the ideal line, suggesting the best fit among the three models.

The time series plots in Figure 5d–f depict the tendency of the models in the test set. In Figure 5d, corresponding to the LightGBM model, the predicted values show some deviations from the observed values, indicating over- or underestimation tendencies for certain samples. Figure 5e, representing the SVM model, exhibits more pronounced deviations between the predicted and observed values, with noticeable over- or underestimation for some samples. Figure 5f, corresponding to the CFNN model, shows that the predicted values closely follow the observed values, suggesting minimal over- or underestimation tendencies across the test set samples.



(**a**) LightGBM (**b**) SVM (**c**) CFNNs

(**d**) Tendency in test set LightGBM (**e**) Tendency in test set SVM (**f**) Tendency in test set CFNNs

Figure 5. Model performance before data augmentation.

Table 4 provides an overview of the performance of models trained on the original dataset in predicting the compressive strength of geopolymer concrete. Accordingly, the CFNN model exhibited superior performance across all evaluation metrics. It achieved the highest R^2 values of 0.902 and 0.842 for the training and test sets, respectively. Additionally, the CFNN model had the lowest error values, with an MAE of 2.973 and 3.940, and an RMSE of 3.348 and 6.442 for the training and test sets, respectively. The CFNN model also demonstrated low percentage errors, with a MAPE of 6.00% for the training set and 18.00% for the test set. Furthermore, the RSR value of 0.411 for the test set suggests a relatively low standardized RMSE compared to the standard deviation of the measured

data. The LightGBM model showed a reasonably good fit with R^2 values of 0.819 and 0.805 for the training and test sets, respectively. However, it exhibited higher error values, with an MAE of 4.357 and 5.593, and an RMSE of 6.287 and 7.24 for the training and test sets, respectively. The MAPE was 17.50% for the training set and 20.10% for the test set, suggesting relatively low percentage errors. The RSR value of 0.600 for the test set indicates a moderate standardized RMSE compared to the standard deviation of the measured data. Similarly, the SVM model displayed signs of overfitting, with a high R^2 of 0.893 on the training set but a lower value of 0.783 on the test set. Despite the lower R^2 on the test set, the model had lower MAE and RMSE values compared to LightGBM, with an MAE of 3.945 and 4.918, and an RMSE of 5.277 and 7.309 for the training and test sets, respectively. The MAPE was 26.00% for the training set and 22.00% for the test set, indicating low percentage errors. The RSR value of 0.496 for the test set suggests a relatively low standardized RMSE. Overall, the CFNN model demonstrated the most promising performance in predicting the compressive strength of geopolymer concrete among the models evaluated.

Table 4. Model performance before data augmentation.

Model	Dataset	R^2	MEA	RMSE	MAPE	RSR	WMAPE
LightGBM	Train	0.819	4.357	6.287	17.50%	0.409	11.067%
	Test	0.805	5.593	7.24	20.10%	0.600	14.921%
SVM	Train	0.893	3.945	5.277	26.00%	0.333	11.276%
	Test	0.783	4.918	7.309	22.00%	0.496	13.749%
CFNN	Train	0.902	2.973	3.348	6.00%	0.227	3.444%
	Test	0.842	3.940	6.442	18.00%	0.411	10.758%

4.3. Synthetic Dataset

Table 5 demonstrates a statistical description of the synthetic compared to original data. The mean values of the features in the synthesized data closely approximated those of the original dataset, indicating that the TGAN model effectively captured the central tendencies inherent in the data. Additionally, the standard deviations exuded by the generalized data were compatible with those of the original data, subsuming that the TGAN model successfully replicated the disposition or variability present in the dataset. The examination of the minimum and maximum values of each feature further revealed that the range spread by the synthetic data aligned well with that of the original data, ensuring that the synthetic data does not contain any unrealistic outliers or values outside the valid range. Furthermore, skewness, a measure of asymmetry in the distributions, was highly similar between the two datasets, indicating that the TGAN model retained the shape characteristics of the original data distributions. The fact that the mean, standard deviation, minimum, maximum, and skewness values of the features in the synthetic data are effectively the same as those of the original data suggests that the generated data points capture the key statistical properties and patterns present in the real dataset.

Table 5. Comparison of original and synthetic datasets.

Symbol	Unit	Mean		STD		Min		Max		Skewness	
		Original	Synthetic	Original	Synthetic	Original	Synthetic	Original	Synthetic	Original	Synthetic
FA	kg/m^3	246.72	238.01	159.99	150.28	0.00	0.00	620.00	546.91	−0.34	−0.20
GGBS	kg/m^3	176.27	188.92	177.38	172.51	0.00	0.00	560.00	560.00	0.48	0.40
SS	kg/m^3	117.56	119.44	36.08	36.01	32.00	33.11	205.50	203.66	0.23	0.23
SH	kg/m^3	44.78	48.60	22.51	23.93	0.00	3.26	108.00	108.00	0.12	0.09
SP	kg/m^3	1.52	1.69	2.57	2.54	0.00	0.00	9.00	8.33	1.35	1.13
fag	kg/m^3	656.26	656.37	81.65	80.66	495.00	496.07	887.00	859.69	0.31	0.18
cag	kg/m^3	1082.58	1063.82	239.87	246.23	525.40	528.40	1381.35	1351.08	−1.31	−1.08
w	kg/m^3	64.72	70.93	62.10	60.39	0.00	0.00	216.00	212.41	0.47	0.29
CT	°C	48.16	49.90	28.21	28.09	19.00	19.00	100	100.00	0.50	0.41
CP	days	21.76	22.54	14.99	14.44	1.00	1.00	56	56.00	0.62	0.63
CS	MPa	38.45	35.05	14.95	16.48	1.25	0.00	80.51	80.51	0.13	0.12

Figure 6 presents a t-SNE plot comparing the original data and the synthetic data generated by the TGAN model. The t-SNE algorithm is a dimensionality reduction tech-

nique that projects high-dimensional data into a lower-dimensional space (in this case, a 2D plane) while preserving the local structure and relationships between data points [11]. In the t-SNE plot, each data point is represented as a colored dot, with the original data points shown in one color (e.g., blue) and the synthetic data points generated by the TGAN model shown in another color (e.g., orange). The proximity of the data points in the plot indicates their similarity in the high-dimensional feature space. The t-SNE plot shows that the synthetic data points generated by the TGAN model are well-distributed and intermixed with the original data points. This suggests that the TGAN model has successfully captured the underlying patterns and distributions present in the original data, and the generated synthetic data points share similar characteristics and relationships with the real data points.

The ability of the TGAN model to generate high-quality synthetic data is crucial for data augmentation techniques, as it can help increase the size and diversity of the training dataset without introducing unrealistic or inconsistent data points. By generating 1000 additional data points using the TGAN model, the total training dataset size has been increased, potentially improving the performance and generalization capabilities of the ML models trained on this augmented dataset.

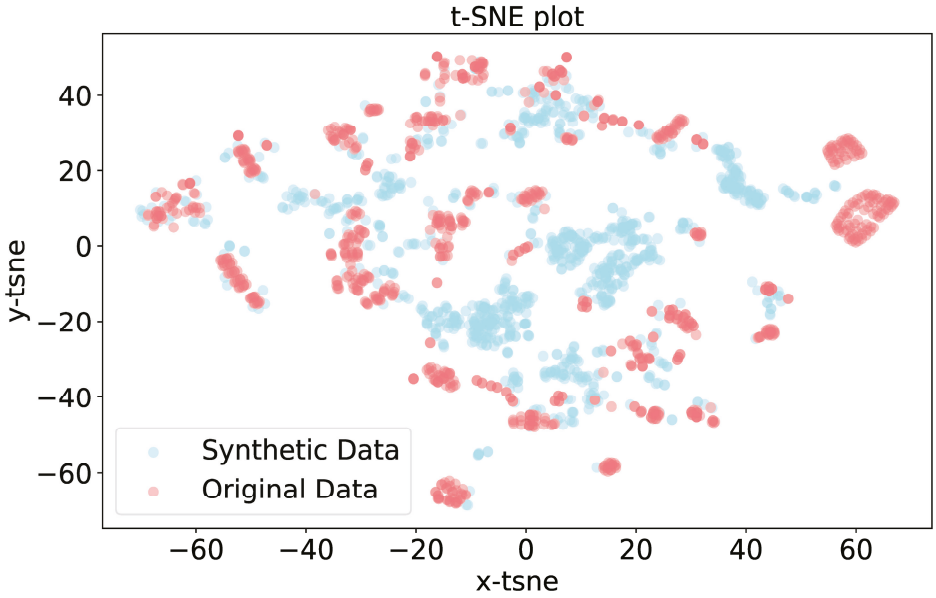


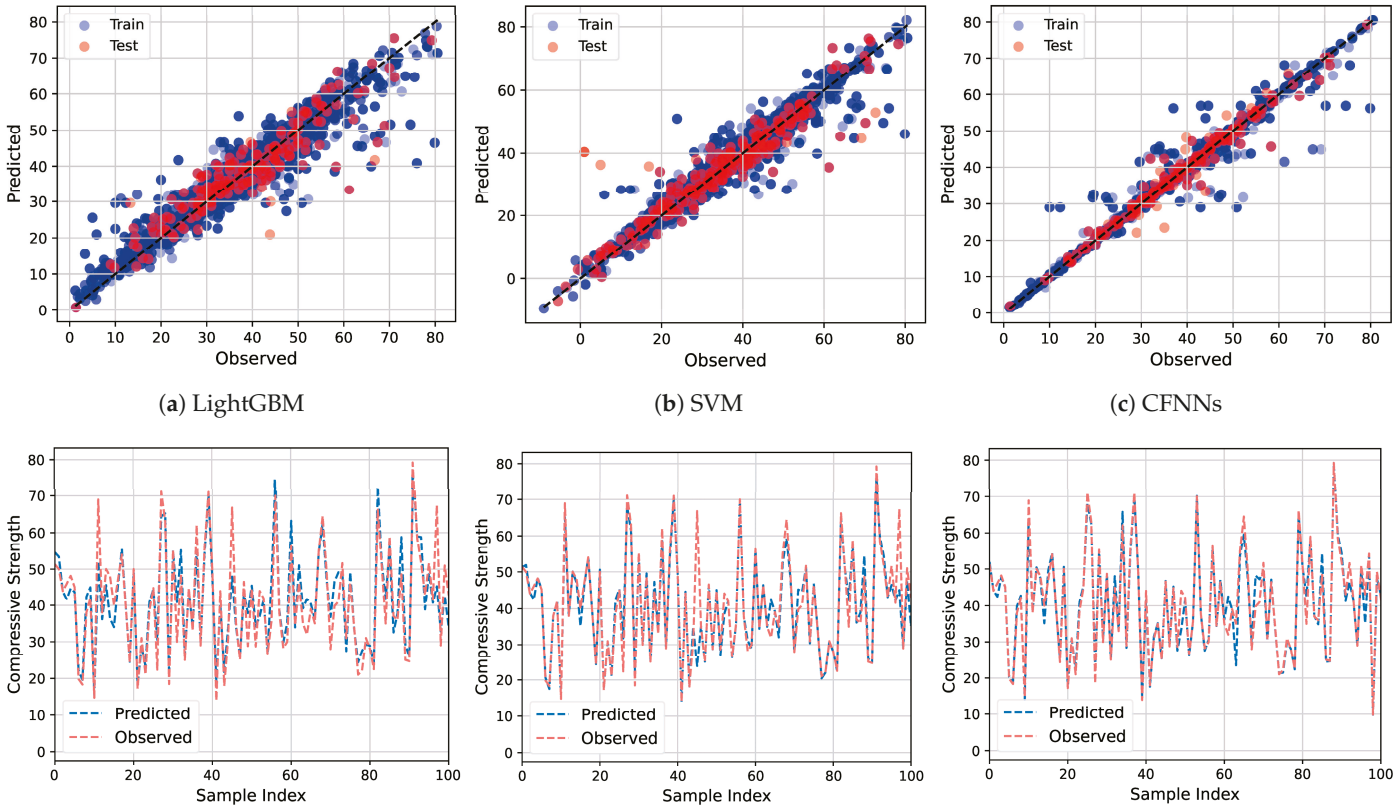
Figure 6. t-SNE visualization of the synthetic and original data.

4.4. Performance of Models after Data Augmentation

The data augmentation approach using the tabular GAN to generate synthetic samples led to substantial improvements in the predictive performance of all three models, as evidenced by Figure 7. The scatter plots show that the data points representing the predicted versus observed compressive strength values lie much closer to the ideal line after augmentation, indicating a stronger agreement between predictions and observations across the entire data range. The LightGBM and SVM models also exhibit improved performance with reduced scatter compared to their pre-augmentation results; their predictions still deviate more from the ideal line, particularly for higher strength values. For the CFNN model, the augmented data enabled the model to learn more robust patterns. This suggests that the CFNN model benefited more from the augmented data in capturing the underlying complexities and nuances of the problem.

The tendency plots in Figure 7d–f further corroborate these observations. For the CFNN, the predicted values closely track the actual observed values across the entire test set, with minimal discrepancies on a sample-by-sample basis. In contrast, the LightGBM and SVM models, while improved, still exhibit noticeable fluctuations and deviations from

the observed values, indicating a higher propensity for over- or underestimation on certain test samples.



(**a**) LightGBM (**b**) SVM (**c**) CFNNs

(**d**) Tendency in test set LightGBM (**e**) Tendency in test set SVM (**f**) Tendency in test set CFNNs

Figure 7. Model performance after data augmentation.

Also, the performance of the models is demonstrated in more detail in Table 6. Overall, the models achieved better performance after data augmentation. The CFNN model exhibited substantial improvements across all metrics after data augmentation. The R^2 increased from 0.902 to 0.956 on the training set and 0.842 to 0.942 on the test set, indicating better explained variance and goodness of fit. The MAE decreased from 2.973 to 1.037 MPa on the training set and 3.940 to 1.546 MPa on the test set, representing reductions of 65.12% and 60.74% respectively. Similarly, the RMSE dropped from 3.348 to 2.982 MPa on the training set (10.9% reduction) and 6.442 to 3.836 MPa on the test set (40.5% reduction). The MAPE saw a notable decrease from 6.00% to 18.10% on the training set, though it improved from 18.00% to 5.283% on the test set. The RSR also reduced from 0.227 to 0.181 on the training set and 0.411 to 0.194 on the test set, indicating smaller errors relative to data variability. Overall, the CFNN demonstrated consistent and substantial improvements across all metrics after augmentation.

For LightGBM, the R^2 increased from 0.819 to 0.913 on the training set and 0.805 to 0.877 on the test set after augmentation. The MAE decreased from 4.357 to 3.004 MPa (31.1% reduction) on the training set and 5.593 to 3.366 MPa (39.9% reduction) on the test set. The RMSE also saw improvements, dropping from 6.287 to 4.676 MPa (25.7% reduction) on the training set and 7.240 to 4.657 MPa (35.6% reduction) on the test set. The MAPE decreased from 0.175% to 0.1% on the training set and 0.201% to 0.10% on the test set. Lastly, the RSR improved from 0.409 to 0.282 on the training set and 0.600 to 0.413 on the test set. While LightGBM showed improvements across all metrics, the magnitude of improvement was generally smaller compared to the CFNN model.

The SVM model also benefited from data augmentation, with the R^2 increasing from 0.893 to 0.922 on the training set and 0.783 to 0.863 on the test set. The MAE improved

from 3.945 to 1.373 MPa (39.9% reduction) on the training set and 4.918 to 2.897 MPa (41.1% reduction) on the test set. The RMSE decreased from 5.277 to 3.256 MPa (38.2% reduction) on the training set and 7.309 to 5.61 MPa (23.2% reduction) on the test set. The MAPE remained relatively unchanged at 0.06% on the training set but improved from 0.18% to 0.21% on the test set. Finally, the RSR saw improvements, decreasing from 0.333 to 0.281 on the training set and 0.411 to 0.399 on the test set.

Table 6. Model performance.

Model	Dataset	R^2	MAE	RMSE	MAPE	RSR	WMAPE
LightGBM	Train	0.913	3.004	4.676	10.00%	0.282	7.679%
	Test	0.877	3.366	4.657	10.32%	0.413	9.413%
SVM	Train	0.922	2.373	4.256	12.00%	0.281	4.323%
	Test	0.863	2.897	4.61	21.00%	0.399	5.757%
CFNN	Train	0.956	1.037	2.982	18.10%	0.181	2.717%
	Test	0.942	1.546	3.836	22.83%	0.194	3.265%

4.5. Discussion and Limitations

The comparison of model performance before and after data augmentation is visualized in Figure 8. The findings align with relevant studies that have utilized synthetic data for ML models in predicting the compressive strength of concrete [11,13]. Research conducted by Chen et al. (2022) [11] highlights the effectiveness of integrating synthetic data, showcasing a significant improvement in the accuracy of deep learning models (i.e., CNNs), compared to traditional ML models. Similarly, this study underscores the efficacy of data augmentation methods in enhancing model predictive capabilities, particularly for CFNNs, despite the inherent variability in precursor chemicals. Additionally, the results suggest that the implementation of data augmentation techniques for SVMs leads to more substantial improvements compared to tree-based models, although the distinction may not be immediately apparent. While the use of synthetic data has proven effective in enhancing the performance of the LightGBM and CFNN models, as evidenced by the improvements in metrics such as MAE, RMSE, RSR, and WMAPE, its impact on the MAPE of the SVM model remains limited. This can be attributed to the inherent sensitivity of SVM models to the presence of outliers in the dataset [63]. Consequently, the outliers observed in the coarse aggregate and fine aggregate features may have adversely influenced the SVM model's performance relative to the LightGBM and CFNN models.

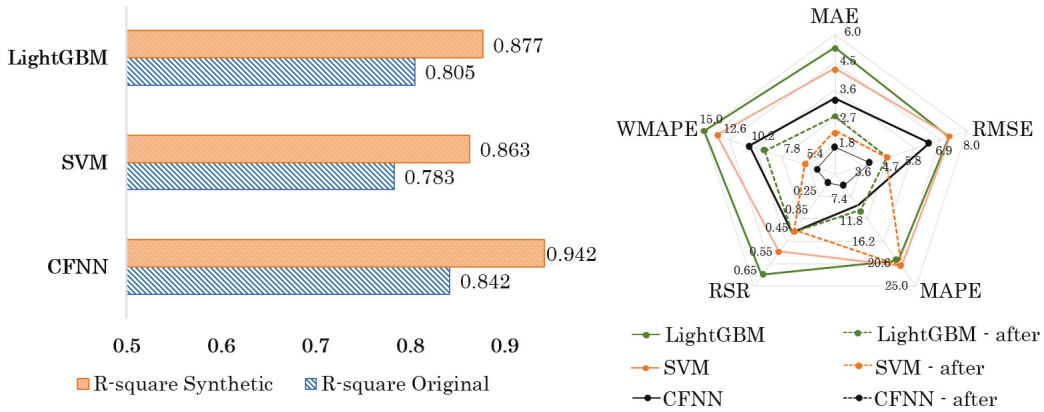


Figure 8. Comparison of R^2 and error indices of the models before and after data augmentation.

Notwithstanding the observed enhancements in model performance, it is crucial to acknowledge that the generation of synthetic data in this study does not necessarily augment the generalizability of the models. As demonstrated in Table 5, the minimum, maximum, and skewness values of the synthetic data are either reduced or maintained at the same level as the original dataset. However, it is worth noting that generating data

with broader coverage may potentially introduce model uncertainty due to extrapolation, thus necessitating further investigation to assess the trade-offs between model performance and generalizability.

Despite the high performance in the test set, it should be noted that the test set and training set in this study are constructed using the same dataset obtained from open literature. This can cause overoptimistic performance estimates because the data distribution in both sets is identical. Additionally, it is important to consider that data sourced from previous studies may not always be reliable and the presence of measurement biases among multiple studies further adds to the uncertainty of prediction outcomes. Moreover, the data collected in this study is confined to specific countries and regions, notably China, India, Iran, and Australia, where geopolymer research has received considerable attention. Consequently, the dataset lacks comprehensive international representation, thereby limiting its scope and exhaustiveness.

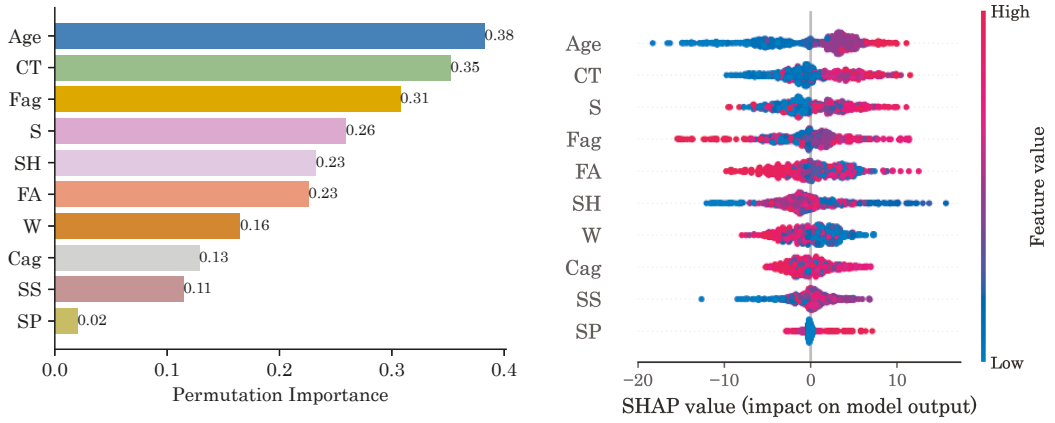
To interpret the developed model effectively, permutation feature importance and SHapley Additive exPlanations (SHAP) were adopted, shedding light on the intricate interplay between input features and their influence on compressive strength. These two interpretability techniques were conducted within CFNNs, recognized as the most promising model. Permutation feature importance evaluates the variation in prediction error resulting from the permutation of feature values. If prediction error remains unchanged after shuffling values, the feature is considered 'unimportant,' signifying the model's disregard for it in prediction. This approach offers a concise, comprehensive understanding of the model's behavior. SHAP, grounded in coalitional game theory, conceptualize prediction as a game, with features akin to players. The SHAP value assigned to each feature delineates its average marginal contribution across all conceivable coalitions, thereby elucidating its impact on attaining a heightened or diminished final prediction outcome.

Figure 9 presents the overall importance of the features. The most influential features for predicting compressive strength are the specimen age and curing temperature, with permutation importance of 0.38 and 0.35, respectively. Similar results were observed in the SHAP analysis, with slight discrepancies in the influence of slag and fine aggregate content between the two analyses. SHAP analysis presents that higher slag content generally results in increased compressive strength, denoted by the prominent red coloring on the right side of the slag feature. Conversely, higher fly ash content tends to have a detrimental effect on compressive strength, as evidenced by the pink coloring on the right side of the fly ash feature. The impact of fine aggregate content is more nuanced, with both positive and negative effects depending on the specific value of the feature. Other features, such as sodium hydroxide, water content, coarse aggregate, and sodium silicate, exhibit relatively smaller impacts on compressive strength prediction, as indicated by their narrower ranges of SHAP values and lower permutation importance. Superplasticizer content demonstrates a significantly smaller influence compared to the other features (permutation importance = 0.02).

It can be observed that that variables of specimen age and curing temperature are the most important features in the decision making of the CFNN model. These factors are expressed in integers and have a high frequency of repetition according to the curing regime. Therefore, the TGAN model can capture features and generate better data. Meanwhile, factors with many outliers such as superplasticizer and coarse aggregate are the least influential features. These may be the reasons why the CFNN model benefits a lot from synthetic data. Additionally, a study conducted by Rahmati et al. (2022) [64] highlights the impact of curing time and curing method (i.e., oven, steam) on the prediction of ML models. However, these factors were not considered in the current study due to the problem of high dimensionality associated with the complexity of the dataset. Incorporating these factors with larger datasets can improve the accuracy of the prediction model.

Considering model characteristics and limitations, a process for deploying and enhancing models was proposed in Figure 10. The developed TGAN and predictive models can be refined using real data from users labeled with the prediction results. The effectiveness

of using the results of the ML model to further improve the model is demonstrated in the research of Ford et al. (2022) [61]. This ongoing learning process ensures that the deployed models can enhance generalization and mitigate temporal and measurement uncertainties, ultimately improving their performance and reliability over time.



(**a**) (**b**)

Figure 9. The importance of each feature of CFNN model. (**a**) Permutation importance. (**b**) SHAP value.

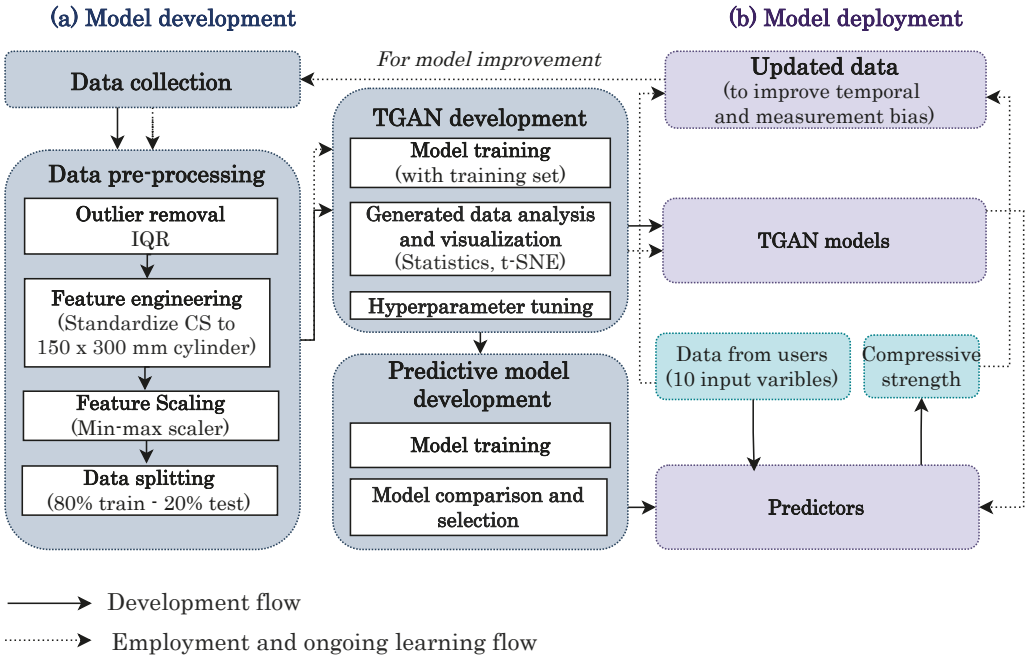


Figure 10. Schematic diagram of model deployment and improvement process.

5. Conclusions and Future Works

This study examines the impact of using synthetic data on ML models that predict the compressive strength of geopolymer concrete. For this purpose, 930 data points were collected from the open literature. The TGAN method was employed to generate geopolymer mixture and compressive strength data. The ML model consists of LightGBM, SVM, and CFNN algorithms, representing tree-based, support vector, and neural network algorithms, respectively. These models were trained using the generated data and subsequently evaluated using the real dataset. A comparison was made with the corresponding model using the original dataset. Based on the obtained results, the following conclusions can be drawn:

- TGAN proves capable of generating mixture and compressive strength data for geopolymer concrete. The synthetic data significantly improves the performance

of ML models, as evident from the increased R^2 values and reduced error indices such as MAE, RMSE, MAPE, RSR, and WMAPE. The CFNN model exhibited the most improvement, followed by LightGBM and SVM.
- The enhanced performance of the models indicates that the heterogeneity in the type or quality of precursors in the collected data does not significantly affect the data generation ability and performance of ML models.
- Due to the presence of numerous outliers and skewed characteristics of the data, the SVM model was greatly impacted in both the original and synthetic datasets.
- The generated data statistics demonstrate that the characteristics of the data are quite similar to the original data. This indicates that the TGAN model generated reliable data. However, it is important to note that using such data merely improves accuracy without enhancing the generalization capabilities of the models.
- In addition, this study demonstrates limitations concerning the generalizability of the model, the scope of inputs, the absence of validation with actual experimental data, and regional bias within the dataset.

Several avenues for future research can be pursued to address the limitations identified in this study. Firstly, prioritizing exploration of generator architectures within GANs or employing of bounded GANs could enable better control over the range of generated data. Furthermore, the generalization capability of the models can be enhanced through the implementation of regularization techniques (e.g., dropout, and L1 and L2 regularization), cross-validation, and the adaptation of open-source algorithms tailored to the characteristics of the data. Instead of solely relying on integration algorithms, future research should focus on enhancing existing algorithms to better align with the characteristics of data. To assess practical effectiveness, the developed TGAN and predictive models necessitate further verification through experimental data or real-world project implementation. Moreover, expanding the scope of input variables, such as the chemical and physical composition of precursors, curing duration, and methodologies, could potentially improve the predictive accuracy of the models. Expanding the dataset to include geopolymer research across diverse regions and countries also serves to enhance the internationality and generalizability of the model. The aggregation of a comprehensive dataset holds promise for broadening the scope of output variables to encompass additional mechanical properties, including tensile strength, flexural strength, durability, and the effects of aging on geopolymer concrete.

Author Contributions: Conceptualization, H.A.T.N. and D.H.P.; Data curation, H.A.T.N.; Writing—original draft, H.A.T.N.; Writing—review & editing, D.H.P.; Visualization, H.A.T.N.; Supervision, Y.A. All authors have read and agreed to the published version of the manuscript.

Funding: This work was supported by the National Research Foundation of Korea (NRF) grant funded by the Korea government (MSIT) (No. RS-2023-00217322).

Institutional Review Board Statement: Not applicable.

Informed Consent Statement: Not applicable.

Data Availability Statement: The raw data supporting the conclusions of this article will be made available by the authors on request.

Acknowledgments: This work was supported by the National Research Foundation of Korea (NRF) grant funded by the Korea government (MSIT) (No. RS-2023-00217322).

Conflicts of Interest: The authors declare no conflicts of interest.

References

1. Habert, G.; Miller, S.A.; John, V.M.; Provis, J.L.; Favier, A.; Horvath, A.; Scrivener, K.L. Environmental impacts and decarbonization strategies in the cement and concrete industries. *Nat. Rev. Earth Environ.* **2020**, *1*, 559–573. [CrossRef]
2. Nwankwo, C.O.; Bamigboye, G.O.; Davies, I.E.; Michaels, T.A. High volume Portland cement replacement: A review. *Constr. Build. Mater.* **2020**, *260*, 120445. [CrossRef]
3. Scrivener, K.L.; John, V.M.; Gartner, E.M. Eco-efficient cements: Potential economically viable solutions for a low-CO_2 cement-based materials industry. *Cem. Concr. Res.* **2018**, *114*, 2–26. [CrossRef]

4. Zhuang, X.Y.; Chen, L.; Komarneni, S.; Zhou, C.H.; Tong, D.S.; Yang, H.M.; Yu, W.H.; Wang, H. Fly ash-based geopolymer: Clean production, properties and applications. *J. Clean. Prod.* **2016**, *125*, 253–267. [CrossRef]
5. Zakka, W.P.; Lim, N.H.A.S.; Khun, M.C. A scientometric review of geopolymer concrete. *J. Clean. Prod.* **2021**, *280*, 124353. [CrossRef]
6. Dwibedy, S.; Panigrahi, S.K. Factors affecting the structural performance of geopolymer concrete beam composites. *Constr. Build. Mater.* **2023**, *409*, 134129. [CrossRef]
7. Li, N.; Shi, C.; Zhang, Z.; Wang, H.; Liu, Y. A review on mixture design methods for geopolymer concrete. *Compos. Part B Eng.* **2019**, *178*, 107490. [CrossRef]
8. Gupta, T.; Rao, M.C. Prediction of compressive strength of geopolymer concrete using machine learning techniques. *Struct. Concr.* **2022**, *23*, 3073–3090. [CrossRef]
9. Li, Z.; Yoon, J.; Zhang, R.; Rajabipour, F.; Srubar III, W.V.; Dabo, I.; Radlińska, A. Machine learning in concrete science: Applications, challenges, and best practices. *npj Comput. Mater.* **2022**, *8*, 127. [CrossRef]
10. Yasuno, T.; Nakajima, M.; Sekiguchi, T.; Noda, K.; Aoyanagi, K.; Kato, S. Synthetic image augmentation for damage region segmentation using conditional GAN with structure edge. *arXiv* **2020**, arXiv:2005.08628.
11. Chen, N.; Zhao, S.; Gao, Z.; Wang, D.; Liu, P.; Oeser, M.; Hou, Y.; Wang, L. Virtual mix design: Prediction of compressive strength of concrete with industrial wastes using deep data augmentation. *Constr. Build. Mater.* **2022**, *323*, 126580. [CrossRef]
12. Liu, K.H.; Xie, T.Y.; Cai, Z.K.; Chen, G.M.; Zhao, X.Y. Data-driven prediction and optimization of axial compressive strength for FRP-reinforced CFST columns using synthetic data augmentation. *Eng. Struct.* **2024**, *300*, 117225. [CrossRef]
13. Marani, A.; Jamali, A.; Nehdi, M.L. Predicting ultra-high-performance concrete compressive strength using tabular generative adversarial networks. *Materials* **2020**, *13*, 4757. [CrossRef] [PubMed]
14. Sharma, U.; Gupta, N.; Verma, M. Prediction of the compressive strength of Flyash and GGBS incorporated geopolymer concrete using artificial neural network. *Asian J. Civ. Eng.* **2023**, *24*, 2837–2850. [CrossRef]
15. Gupta, P.; Gupta, N.; Goyal, S. Predicting compressive strength of calcined clay, fly ash-based geopolymer composite using supervised learning algorithm. *Adv. Appl. Math. Sci.* **2022**, *21*, 4151–4161.
16. Jafari, A.; Toufigh, V. Developing a comprehensive prediction model for the compressive strength of slag-based alkali-activated concrete. *J. Sustain. Cem.-Based Mater.* **2024**, *13*, 256–273. [CrossRef]
17. Kumar, P.; Pratap, B.; Sharma, S.; Kumar, I. Compressive strength prediction of fly ash and blast furnace slag-based geopolymer concrete using convolutional neural network. *Asian J. Civ. Eng.* **2024**, *25*, 1561–1569. [CrossRef]
18. Huynh, A.T.; Nguyen, Q.D.; Xuan, Q.L.; Magee, B.; Chung, T.; Tran, K.T.; Nguyen, K.T. A machine learning-assisted numerical predictor for compressive strength of geopolymer concrete based on experimental data and sensitivity analysis. *Appl. Sci.* **2020**, *10*, 7726. [CrossRef]
19. Wang, Q.; Ahmad, W.; Ahmad, A.; Aslam, F.; Mohamed, A.; Vatin, N.I. Application of soft computing techniques to predict the strength of geopolymer composites. *Polymers* **2022**, *14*, 1074. [CrossRef]
20. Tran, V.Q. Data-driven approach for investigating and predicting of compressive strength of fly ash–slag geopolymer concrete. *Struct. Concr.* **2023**, *24*, 7419–7444. [CrossRef]
21. Ahmed, H.U.; Mohammed, A.S.; Mohammed, A.A. Proposing several model techniques including ANN and M5P-tree to predict the compressive strength of geopolymer concretes incorporated with nano-silica. *Environ. Sci. Pollut. Res.* **2022**, *29*, 71232–71256. [CrossRef] [PubMed]
22. Nazar, S.; Yang, J.; Amin, M.N.; Khan, K.; Ashraf, M.; Aslam, F.; Javed, M.F.; Eldin, S.M. Machine learning interpretable-prediction models to evaluate the slump and strength of fly ash-based geopolymer. *J. Mater. Res. Technol.* **2023**, *24*, 100–124. [CrossRef]
23. Ahmed, H.U.; Mostafa, R.R.; Mohammed, A.; Sihag, P.; Qadir, A. Support vector regression (SVR) and grey wolf optimization (GWO) to predict the compressive strength of GGBFS-based geopolymer concrete. *Neural Comput. Appl.* **2023**, *35*, 2909–2926. [CrossRef]
24. Kumar, A.; Arora, H.C.; Kapoor, N.R.; Kumar, K. Prognosis of compressive strength of fly-ash-based geopolymer-modified sustainable concrete with ML algorithms. *Struct. Concr.* **2023**, *24*, 3990–4014. [CrossRef]
25. Ahmed, H.U.; Mohammed, A.A.; Mohammed, A. Soft computing models to predict the compressive strength of GGBS/FA-geopolymer concrete. *PLoS ONE* **2022**, *17*, e0265846. [CrossRef] [PubMed]
26. Gunasekara, C.; Lokuge, W.; Keskic, M.; Raj, N.; Law, D.; Setunge, S. Design of alkali-activated slag-fly ash concrete mixtures using machine learning. *Mater. J.* **2020**, *117*, 263–278.
27. Gogineni, A.; Panday, I.K.; Kumar, P.; Paswan, R.k. Predictive modelling of concrete compressive strength incorporating GGBS and alkali using a machine-learning approach. *Asian J. Civ. Eng.* **2024**, *25*, 699–709. [CrossRef]
28. Nukah, P.D.; Abbey, S.J.; Booth, C.A.; Oti, J. Evaluation of the structural performance of low carbon concrete. *Sustainability* **2022**, *14*, 16765. [CrossRef]
29. Kina, C.; Tanyildizi, H.; Turk, K. Forecasting the compressive strength of GGBFS-based geopolymer concrete via ensemble predictive models. *Constr. Build. Mater.* **2023**, *405*, 133299. [CrossRef]
30. Parhi, S.K.; Panigrahi, S.K. Alkali–silica reaction expansion prediction in concrete using hybrid metaheuristic optimized machine learning algorithms. *Asian J. Civ. Eng.* **2024**, *25*, 1091–1113. [CrossRef]
31. Dunphy, K.; Fekri, M.N.; Grolinger, K.; Sadhu, A. Data augmentation for deep-learning-based multiclass structural damage detection using limited information. *Sensors* **2022**, *22*, 6193. [CrossRef] [PubMed]

32. Goodfellow, I.; Pouget-Abadie, J.; Mirza, M.; Xu, B.; Warde-Farley, D.; Ozair, S.; Courville, A.; Bengio, Y. Generative adversarial nets. *Adv. Neural Inf. Process. Syst.* **2014**, *27*, 2672–2680.
33. Jia, J.F.; Chen, X.Z.; Bai, Y.L.; Li, Y.L.; Wang, Z.H. An interpretable ensemble learning method to predict the compressive strength of concrete. *Structures* **2022**. *46*, 201–213. [CrossRef]
34. Çalışkan, A.; Demirhan, S.; Tekin, R. Comparison of different machine learning methods for estimating compressive strength of mortars. *Constr. Build. Mater.* **2022**, *335*, 127490. [CrossRef]
35. Hasanipanah, M.; Jamei, M.; Mohammed, A.S.; Amar, M.N.; Hocine, O.; Khedher, K.M. Intelligent prediction of rock mass deformation modulus through three optimized cascaded forward neural network models. *Earth Sci. Inform.* **2022**, *15*, 1659–1669. [CrossRef]
36. Mijwel, M.M. Artificial neural networks advantages and disadvantages. *Mesopotamian J. Big Data* **2021**, *2021*, 29–31. [CrossRef]
37. Sun, L.; Koopialipoor, M.; Jahed Armaghani, D.; Tarinejad, R.; Tahir, M. Applying a meta-heuristic algorithm to predict and optimize compressive strength of concrete samples. *Eng. Comput.* **2021**, *37*, 1133–1145. [CrossRef]
38. Liang, M.; Chang, Z.; Wan, Z.; Gan, Y.; Schlangen, E.; Šavija, B. Interpretable Ensemble-Machine-Learning models for predicting creep behavior of concrete. *Cem. Concr. Compos.* **2022**, *125*, 104295. [CrossRef]
39. Ling, H.; Qian, C.; Kang, W.; Liang, C.; Chen, H. Combination of Support Vector Machine and K-Fold cross validation to predict compressive strength of concrete in marine environment. *Constr. Build. Mater.* **2019**, *206*, 355–363. [CrossRef]
40. Pwasong, A.; Sathasivam, S. A new hybrid quadratic regression and cascade forward backpropagation neural network. *Neurocomputing* **2016**, *182*, 197–209. [CrossRef]
41. Joseph, B.; Mathew, G. Influence of aggregate content on the behavior of fly ash based geopolymer concrete. *Sci. Iran.* **2012**, *19*, 1188–1194. [CrossRef]
42. Nath, P.; Sarker, P.K. Effect of GGBFS on setting, workability and early strength properties of fly ash geopolymer concrete cured in ambient condition. *Constr. Build. Mater.* **2014**, *66*, 163–171. [CrossRef]
43. Vora, P.R.; Dave, U.V. Parametric studies on compressive strength of geopolymer concrete. *Procedia Eng.* **2013**, *51*, 210–219. [CrossRef]
44. Demie, S.; Nuruddin, M.F.; Shafiq, N. Effects of micro-structure characteristics of interfacial transition zone on the compressive strength of self-compacting geopolymer concrete. *Constr. Build. Mater.* **2013**, *41*, 91–98. [CrossRef]
45. Lee, N.; Lee, H.K. Setting and mechanical properties of alkali-activated fly ash/slag concrete manufactured at room temperature. *Constr. Build. Mater.* **2013**, *47*, 1201–1209. [CrossRef]
46. Nuaklong, P.; Sata, V.; Chindaprasirt, P. Influence of recycled aggregate on fly ash geopolymer concrete properties. *J. Clean. Prod.* **2016**, *112*, 2300–2307. [CrossRef]
47. Rajarajeswari, A.; Dhinakaran, G. Compressive strength of GGBFS based GPC under thermal curing. *Constr. Build. Mater.* **2016**, *126*, 552–559. [CrossRef]
48. Su, H.; Xu, J.; Ren, W. Mechanical properties of geopolymer concrete exposed to dynamic compression under elevated temperatures. *Ceram. Int.* **2016**, *42*, 3888–3898. [CrossRef]
49. Tennakoon, C.; Shayan, A.; Sanjayan, J.G.; Xu, A. Chloride ingress and steel corrosion in geopolymer concrete based on long term tests. *Mater. Des.* **2017**, *116*, 287–299. [CrossRef]
50. Wardhono, A.; Gunasekara, C.; Law, D.W.; Setunge, S. Comparison of long term performance between alkali activated slag and fly ash geopolymer concretes. *Constr. Build. Mater.* **2017**, *143*, 272–279. [CrossRef]
51. Reddy, M.S.; Dinakar, P.; Rao, B.H. Mix design development of fly ash and ground granulated blast furnace slag based geopolymer concrete. *J. Build. Eng.* **2018**, *20*, 712–722. [CrossRef]
52. Nguyen, K.T.; Le, T.A.; Lee, K. Evaluation of the mechanical properties of sea sand-based geopolymer concrete and the corrosion of embedded steel bar. *Constr. Build. Mater.* **2018**, *169*, 462–472. [CrossRef]
53. Li, N.; Shi, C.; Zhang, Z.; Zhu, D.; Hwang, H.J.; Zhu, Y.; Sun, T. A mixture proportioning method for the development of performance-based alkali-activated slag-based concrete. *Cem. Concr. Compos.* **2018**, *93*, 163–174. [CrossRef]
54. Nagaraj, V.K.; Venkatesh Babu, D.L. Assessing the performance of molarity and alkaline activator ratio on engineering properties of self-compacting alkaline activated concrete at ambient temperature. *J. Build. Eng.* **2018**, *20*, 137–155.
55. Morsy, A.M.; Ragheb, A.M.; Shalan, A.H.; Mohamed, O.H. Mechanical characteristics of GGBFS/FA-based geopolymer concrete and its environmental impact. *Pract. Period. Struct. Des. Constr.* **2022**, *27*, 04022017. [CrossRef]
56. Gunasekera, C.; Setunge, S.; Law, D.W. Correlations between mechanical properties of low-calcium fly ash geopolymer concretes. *J. Mater. Civ. Eng.* **2017**, *29*, 04017111. [CrossRef]
57. Sukmak, P.; Horpibulsuk, S.; Shen, S.L. Strength development in clay–fly ash geopolymer. *Constr. Build. Mater.* **2013**, *40*, 566–574. [CrossRef]
58. Somna, K.; Jaturapitakkul, C.; Kajitvichyanukul, P.; Chindaprasirt, P. NaOH-activated ground fly ash geopolymer cured at ambient temperature. *Fuel* **2011**, *90*, 2118–2124. [CrossRef]
59. Suksiripattanapong, C.; Horpibulsuk, S.; Chanprasert, P.; Sukmak, P.; Arulrajah, A. Compressive strength development in fly ash geopolymer masonry units manufactured from water treatment sludge. *Constr. Build. Mater.* **2015**, *82*, 20–30. [CrossRef]
60. Talaat, A.; Emad, A.; Tarek, A.; Masbouba, M.; Essam, A.; Kohail, M. Factors affecting the results of concrete compression testing: A review. *Ain Shams Eng. J.* **2021**, *12*, 205–221. [CrossRef]

61. Taffese, W.Z.; Abegaz, K.A. Prediction of compaction and strength properties of amended soil using machine learning. *Buildings* **2022**, *12*, 613. [CrossRef]
62. Benavoli, A.; Corani, G.; Mangili, F. Should we really use post-hoc tests based on mean-ranks? *J. Mach. Learn. Res.* **2016**, *17*, 152–161.
63. Chowdhary, C.L.; Mittal, M.; P, K.; Pattanaik, P.A.; Marszalek, Z. An efficient segmentation and classification system in medical images using intuitionist possibilistic fuzzy C-mean clustering and fuzzy SVM algorithm. *Sensors* **2020**, *20*, 3903. [CrossRef] [PubMed]
64. Rahmati, M.; Toufigh, V. Evaluation of geopolymer concrete at high temperatures: An experimental study using machine learning. *J. Clean. Prod.* **2022**, *372*, 133608. [CrossRef]

Disclaimer/Publisher's Note: The statements, opinions and data contained in all publications are solely those of the individual author(s) and contributor(s) and not of MDPI and/or the editor(s). MDPI and/or the editor(s) disclaim responsibility for any injury to people or property resulting from any ideas, methods, instructions or products referred to in the content.

applied sciences

MDPI

Article

Geochemical Evolution of Mg-Bentonite Affected by the Contact of Carbon Steel and a Hydrothermal Gradient

Carlos Mota-Heredia *, Jaime Cuevas and Raúl Fernández

Department of Geology and Geochemistry, Faculty of Sciences, Autonomous University of Madrid, Cantoblanco, 28049 Madrid, Spain; jaime.cuevas@uam.es (J.C.); raul.fernandez@uam.es (R.F.)
* Correspondence: carlos.mota@uam.es

Abstract: Carbon steel and bentonite are materials selected as engineered barriers for high-level radioactive waste confinement. Their long-term interaction must be evaluated to confirm the barrier's stability. Three laboratory experiments of the carbon steel—Mg-bentonite interaction were conducted for 1, 6, and 22 months under a hydrothermal gradient. Changes in bentonite's water content, specific surface area, and cation exchange capacity were measured. Mineralogy was studied by X-ray diffraction and scanning electron microscopy. The redistribution of aqueous species and the redox state of iron were determined across the bentonite columns. Results indicated water saturation after 22 months. The specific surface area of bentonite was reduced near contact with the steel, while the cation exchange capacity mostly decreased at 3–6 mm from the steel interface. The corrosion rate decreased with time and bentonite enriched in Fe in the first 1.5 mm from the steel contact. The formation of new Fe-bearing minerals, such as di-tri ferri-sudoite, magnetite, hematite, maghemite, lepidocrocite, siderite and ankerite was observed. Aqueous species redistributed in the porewater of bentonite with decreasing concentrations of Fe and Cl as a function of time and increasing concentrations of Na, Ca and SO_4 after 22 months. This occurs under conditions where the bentonite is saturated with Mg, which conditioned the formation and nature of iron clay minerals with time.

Keywords: Mg-montmorillonite; carbon steel; bentonite; hydrothermal gradient

1. Introduction

Bentonite is a clay material proposed for use as an engineered barrier in deep geological repositories (DGRs). Deep geological disposal consists of isolating high-level radioactive waste (HLRW) from the biosphere by keeping it in underground galleries, normally at a depth of 300 to 1000 m depending on the specific location, within stable host geological formations. The low solubility and solid form of the waste is considered a barrier itself. The waste is encapsulated in a metallic container, a second barrier, that depending on each DGR concept can be made of copper–copper alloys (e.g., Swedish and Finnish concept) or carbon steel (e.g., as considered in Switzerland, the United Kingdom, France or Germany) [1]. The canisters are placed within the galleries and surrounded by barriers of compacted clay, typically composed of bentonite, until all of the galleries are completely sealed. In clayey formations, it is essential to insert a concrete barrier between the bentonite layer and the geological formation to provide structural support for the galleries' construction. The combination of mechanical and physicochemical protection is referred to as the engineering barrier (third barrier), while the natural geological formation or bedrock is considered a natural barrier (fourth barrier). Ensuring safety requires ongoing and proper long-term maintenance, along with vigilant monitoring of the installation [2–6].

Carbon steel is the metal chosen by countries, such as Spain, Switzerland, Japan or Belgium to manufacture the canister that insulates the HLRW [2,7–9]. This material has been studied, showing good properties for use in DGRs, such as a low corrosion rate or a long lifetime [10,11].

Bentonite is a clay rock frequently produced by the hydrothermal alteration or diagenesis of acidic-to-intermediate chemistry volcanic glass [12]. Under these conditions, montmorillonite is the main clay mineral, a phyllosilicate belonging to the smectite group [13]. Due to the properties of smectite, such as high swelling capacity, high cation exchange capacity and high chemical stability, bentonite is a competitive material used as an engineered barrier in HLRW management in DGRs [7,14,15].

HLRW will generate heat due to the decay of radionuclides. This heat will be transferred to the container for decades. The temperature is expected to rise to 100 °C at the surface of the canisters, although higher temperatures have recently been considered to reduce galleries spacing [16,17]. Due to the elevated temperature, geochemical interactions between the metal vessel and the bentonite will occur [10,18].

The canister should keep its structural integrity without cracks for at least 1000 years. The corrosion of the canister will depend on the environmental conditions. Temperature, groundwater, bentonite's porewater chemistry, especially the pH and the concentrations of chlorides, sulfur species and carbonates, the redox conditions, including the effect of gamma radiation, microbial activity and the degree of bentonite saturation are factors that will influence the formation of corrosion products as well as the corrosion rate [1,14].

The bentonite barrier will be subjected to hydration conditions in contact with the bedrock. Therefore, the location of the DRG is also a variable to consider, since the hydrogeochemical conditions of the host rock will affect the bentonite barrier, providing hydration with variable salt content. Low saline host rocks (e.g., Grimsel granite formations in Switzerland), high saline rocks (e.g., clay formations in Switzerland, France or Spain) or even marine-type porewater formations (e.g., granite formations in the Forsmark area, Sweden) have been studied [19–22].

It is predictable that full saturation of the bentonite barrier will be reached before dissipation of the thermal gradient, which will take place between 100 and 1000 years after deposition, depending on the particular characteristics of the repository [7,23–27]. In addition, the water vapor produced in the hot part of the bentonite, close to the canister, could recondense in cooler areas, influencing the redistribution of aqueous species in bentonite's porewater [28]. The saturation of the bentonite barrier involves a swelling process that redistributes the mass, changing the dry density, and as a consequence, the porewater chemistry, that is in equilibrium with the mineralogy [29,30]. Also, changes in the water content and chemistry mainly modify the exchangeable cation distribution and, in general, aqueous ion concentrations like Cl^-, SO_4^{2-}, Na^+, K^+, Ca^{2+}, Mg^{2+} or $Fe^{2+/3+}$ [31,32].

Due to the interaction between the steel and bentonite, redox reactions will occur on the surface of the steel and resulting soluble species and Eh/pH conditions will be transferred to the bentonite, generating potential mineral changes. Due to the variability of the existing candidate bentonites, with different mineralogies and exchangeable cation distributions [6,32–35], and the particular geochemical conditions that may occur depending on the design of the DGR, steel–bentonite interactions may produce different effects [36].

The interaction between steel and bentonite can lead to alteration processes like dissolution or re-precipitation of accessory minerals, i.e., short-term dissolution of $CaCO_3$ followed by precipitation of magnesium or iron carbonates due to cation exchange, where Mg or Fe ions replace Ca cations [37]. In addition, accessory silica minerals such as cristobalite and quartz, as well as montmorillonite, can undergo dissolution processes, contributing to the formation of iron silicates, such as nontronite or ferric chlorite [38]. Pignatelli et al. [39] reported the formation of iron-rich T–O phyllosilicates like greenalite and cronstedtite, in addition to magnetite, illite and chlorite, in an experiment in which Callovo-Oxfordian clay was mixed with metallic iron and iron powder, kept at 90 °C for 6 months, and then the temperature gradually reduced by 10 °C monthly until reaching 40 °C. The variety of Fe-bearing minerals that could be formed depends on Fe/Si and Al/Si ratios and pH but also could be mediated by silica dissolution and carbonates [39–41].

Experimental investigations have shown the accumulation of Mg in the hotter zone of bentonite, near the canister surface, regarding FEBEX in situ experiments [18]. The same trend was also found in several bentonite analyses in the ABM-II experiment explained by the increase in exchangeable Mg near the hot steel–bentonite interface [41,42] and by the precipitation of $MgSO_4$ in evaporation surfaces near this interface [36]. This accumulation, displacing cations such as Ca^{2+}, promotes the formation of 2:1 magnesium silicate mineral. Fernandez et al. [43] reported the formation of trioctahedral saponite and chlorite phases or brucite-like sheet phases from montmorillonite modification mediated by high Mg and Fe content in porewater. Svensson [44] also observed saponite formation at the iron–bentonite interface in in situ experiments performed at the hard rock laboratory in Äspö, Sweden. A modeling simulation of the iron–bentonite interaction provided by Savage et al. [45] suggested a sequence of predominancy of Fe-bearing minerals over time, with magnetite prevailing at the first stage. The magnetite led to cronstedtite (kaolinite-serpentine group) with a general formula $(Fe^{2+},Fe^{3+})_3(Si,Fe^{3+})_2O_5(OH)_4$ that dominated the corrosion products for the first 500 years. The next Fe-bearing minerals transformation was reported to form berthierine and, in some cases, chlorite. Wilson et al. [46] reported the formation of iron-rich saponite or 1:1 minerals at <150 °C through geochemical modeling. Other studies reported the formation of chlorite or non-swelling minerals in hydrothermal systems and consequently, the reduction of the swelling capacity of smectite [47,48]. The formation of magnetite and siderite as corrosion products was also predicted by a carbon steel–bentonite interaction model [48].

It is accepted that reservoir conditions will evolve with time, with temperatures at the canister–bentonite interface expected to increase to ~100 °C for the first 10–100 years after DGR post-closure [1]. This temperature is estimated to be maintained for up to 1000 years [49], after which the temperature is estimated to gradually decrease to 80–50 °C, over a period of 1000 to 10,000 years [37]. Numerous studies, performed either at laboratory scale or long-term in situ experiments and geochemical modeling, reported the migration of Mg in the bentonite to the hottest zones near the canister surface [18]. That caused the enrichment in Mg at the canister–bentonite interface, allowing interaction with ions in solution like Fe^{2+}, Fe^{3+}, Na^+, K^+ or Ca^{2+}, and forming minerals like saponite, chlorite group or ankerite ($Ca(Fe^{2+},Mg)(CO_3)_2$) [37,44,50]. Mg enrichment in bentonite has also been observed by diffusion towards the alkaline interface of cement-based materials used as engineered barriers in some DGR concepts [6,51,52]. Despite all these studies, the interaction between magnesium bentonite and carbon steel under conditions of saturated and depleted Mg DGR is not well known.

This research aims to improve the understanding of the interaction between carbon steel and Mg-bentonite under hydrothermal conditions at an evolved scenario in a DGR, where Mg-montmorillonite is assumed to be the dominant mineral. The research employed compacted bentonites that were hydrated with a saline solution and heated at 100 °C from a steel plate, creating a hydrothermal gradient in opposite directions (heat and hydration). Laboratory-scale experiments were conducted for periods of 1, 6 and 22 months using FEBEX Mg-bentonite, pretreated with $MgCl_2$, with the objective to examine the behavior of this bentonite and the development of corrosion products at the steel plate surface.

2. Materials and Methods

2.1. Experimental Setup

Cylindrical bentonite blocks were created using homogeneous bentonite powder with its natural moisture content. The blocks were 21 mm in height and 50 mm in diameter and were compressed uniaxially within a steel mold to a dry density of 1.65 $g \cdot cm^{-3}$. Each block of 77.5 g was weighed before placing it in the cell. This mass was determined considering a 14 wt.% of bentonite's natural moisture content stored in the laboratory.

The experiments were performed using hydrothermal cells of in-house design (Figure 1), as described in Mota-Heredia et al. [53]. The cells were maintained in a glove box under N_2 atmosphere during the whole experimental time to prevent oxidation in case of a potential

leakage in the system and to favor dismantling under anoxic conditions. A thermal gradient was established by setting constant temperatures of 100 °C at the heater (lower bentonite column end) and 40 °C at the hydration zone (upper bentonite column end). Three cells were studied after reaction for 1, 6 and 22 months.

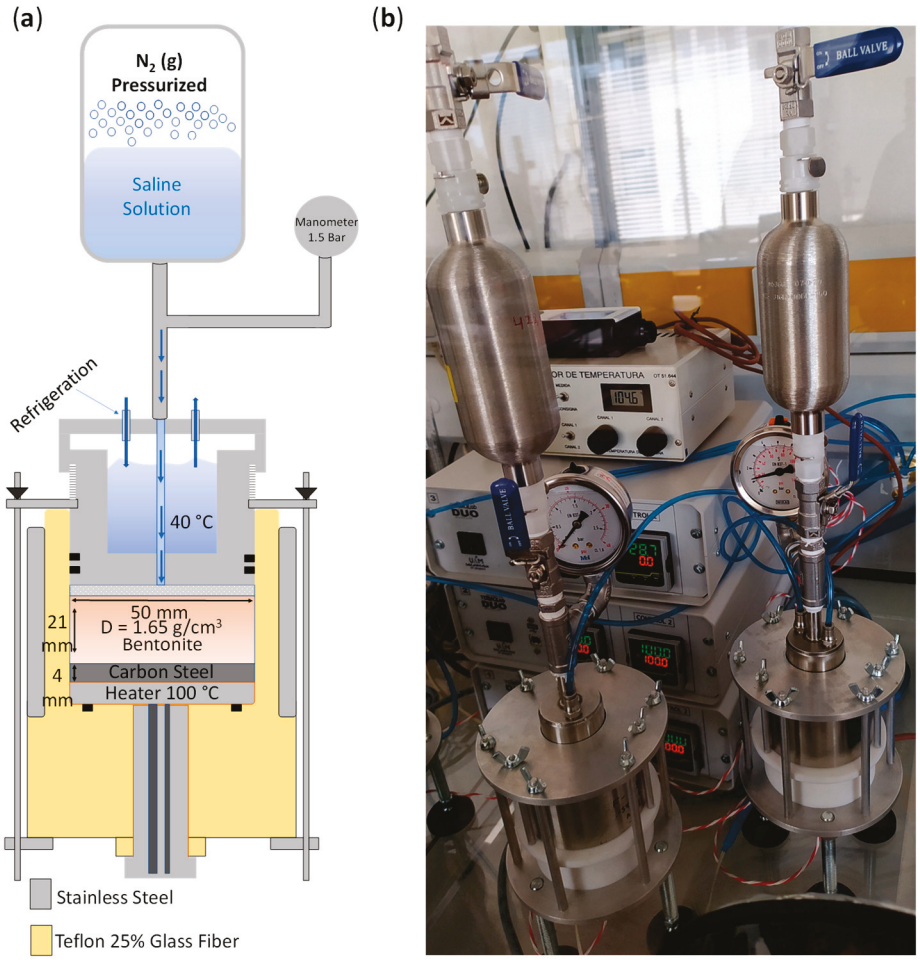


Figure 1. (**a**) Scheme of a hydrothermal cell, and (**b**) photograph of the experimental setup showing two cells and the electronic temperature controls at the back.

2.2. Materials

To simulate hydration from the clayey host rock, a synthetic saline solution of dominant Na-Cl-SO_4-type water, described in Mota-Heredia et al. [53] was used.

In this study, FEBEX bentonite from Cortijo de Archidona, Serrata de Níjar, Almería, Spain [54,55], considered the standard buffer material for radioactive waste storage in Spain [56], was pre-treated to produce Mg-bentonite. Natural bentonite contains 85 ± 10 wt.% montmorillonite [57], and accessory minerals, such as quartz, cristobalite, calcite and feldspars. It also contains traces of Fe minerals such as magnetite and goethite. The exchangeable complex of montmorillonite is composed of approximately 1/3 Ca^{2+}-, 1/3 Na^{+}- and 1/3 Mg^{2+}-mol fractions. In this study, FEBEX bentonite was pre-treated with $MgCl_2$ with the objective to replace exchangeable Ca^{2+}, Na^{+} and K^{+} with Mg^{2+}. The pre-treatment process was described in detail in Fernandez et al. [52].

TStE 355 carbon steel discs were used to simulate the canister surface. The dimensions were 50 mm in diameter and 4 mm thick. Before settling in the cells, the c-steel discs were cleaned with ethanol and sonicated. Fe is present at more than 97 wt.% but small amounts of C, Cr, Mo and Mn are present in the steel composition.

2.3. Sample Segmentation

The three cells were dismantled after 1, 6 and 22 months. The steel–bentonite columns were embedded with a low-viscosity epoxy resin Araldite 2020™ to avoid the deformation and dehydration of bentonite and to keep the samples away from atmospheric oxygen. The embedded samples were cured at room temperature in the glove box until resin hardening was achieved. Samples were then suitable for cutting and segmentation.

A Struers™ (Champigny sur Marne, France) Secotom-6 saw machine was used to cut the cells using a cooling oil that covered the external bentonite surface while cutting. This oil did not chemically interact with bentonite but prevented exposure to atmospheric oxygen. Longitudinal cuts, parallel to the steel–bentonite interface, were performed in cylindrical bentonite samples with the Secotom-6 saw, while a cutter was used for cross-sections, perpendicular to the interface. To analyze reactivity along the hydrothermal gradient, samples were cut to ensure that sufficient material was available for each characterization technique, in agreement with the sampling method previously used by Mota-Heredia et al. [53].

2.4. Analytical Methods

The water content was calculated by mass difference of samples before and after heating to a constant weight at 105 °C. The specific surface area (SSA) was determined by nitrogen adsorption using a Gemini V analyzer from Micrometrics Corporate (Norcross, GA, USA) and calculated by the BET method. The samples were ground and dried at 90 °C for 24 h. Subsequently, the samples were degassed at 90 °C for at least two hours using a nitrogen gas stream and analyzed using the 5-point isotherm method as in Cuevas et al. [51].

The cation exchange capacity (CEC) was determined using the Cu-trien method [58], with modifications made for clays as in Ammann et al. [59]. The absorbance was measured at 577 nm using the UV–Visible Spectrophotometer Genesys 150 from Thermoscientific (Thermo Fisher Scientific, Waltham, MA, USA).

Analysis of major ions including Na^+, K^+, Ca^{2+}, Mg^{2+}, Cl^- and $SO_4{}^{2-}$ was performed using a Metrohm 802™ compact IC plus (from Metrohm, Herisau, Switzerland) through ion chromatography. A 0.15 solid/liquid ratio was used to mix the samples with deionized water in order to obtain the aqueous extracts. The samples were then subjected to 24 h of interaction with water on a shaker, followed by centrifugation for 30 min at 10,000 rpm. Finally, the aqueous extracts were filtered using syringe filters with a pore size < 0.45 μm.

Longitudinal thin section samples were prepared for scanning electron microscopy (SEM) and energy-dispersive X-ray (EDX) analyses. Each sample was dried by immersion in liquid nitrogen inside a vacuum chamber. After that, the samples were embedded and polished. The procedure is detailed in Mota-Heredia et al. [53]. A Q150T-S Quorum sputter coater system from Quorum Technologies (Lewes, UK) was used to coat the samples with Au.

Surface and morphology images were captured using a Hitachi S–3000N SEM (Hitachi, Japan) that was coupled with an EDX XFlash® 6130 Bruker detector (Bruker Corporation, Billerica, MA, USA) for semi-quantification analyses of chemical composition. Internal standard quantitative analyses were used for EDX quantification. The equipment operated under high vacuum conditions with an accelerating voltage of 20 keV, a lifetime of 40 s, a working distance of 15.0 to 18.5 mm and a beam current of 300 mA.

A study was conducted to determine the chemical composition in a longitudinal profile of bentonite, in the direction from the heater to the hydration zone. The images were largely magnified at the hottest zone where chemical variations were expected to be more significant. About 20 analyses were conducted over a thickness of 2 mm at the steel–bentonite interface, 15 analyses over a thickness of 3 mm at the hydration zone and 60 analyses at the intermedium zone over a thickness of 16 mm, although the number of analyses and thicknesses may vary slightly from sample to sample. EDX analyses were used to observe the diffusion of Fe along the bentonite and concentration changes of elements such as Mg, Ca, Na, K, Cl, S and Fe. The data were processed by removing

C and O from the concentrations and recalculating the rest of the elements to achieve 100 wt.%. The mineralogy of bentonite was also analyzed on fresh fractured samples to observe the morphologies of the reaction products. Small samples that either fell apart or were manually separated were used for this study.

To compare the redox state of Fe along the bentonite block in the longest experiment (after 22 months), the 1,10-phenanthroline photochemical method was used [60,61]. This method allowed for discrimination between ferrous and total iron in mineral samples. The Fe^{3+} was calculated by the difference between total Fe and Fe^{2+}.

To study the mineralogical changes in the bentonite block and at the steel interface, X-ray diffraction (XRD) was conducted using a Bruker D8 Discover diffractometer with a Ge monochromator and a lynxeye XE-T fast detector (Bruker Corporation, Billerica, MA, USA). The patterns were measured within a 3–70° θ/2θ range, with 0.02° angular increments and 1 s times. The device was set at 40 kV and 40 mA. Bentonite mineralogy was studied over five sections, sampled with respect to the distance to the carbon steel. The samples were ground and XRD powder was measured.

To study the corrosion product crusts at the carbon steel–bentonite interfaces, the crusts were studied without grinding and additional extra samples of the bentonites in contact with the corrosion crusts were ground and analyzed. To prevent the oxidation of possible reduced compounds during the sampling and XRD analyses, the low background airtight Bruker holder A100B138-B141 was used for the sections closest to the crust to analyze the powder and non-ground crust.

3. Results

Physical–Chemical Characterization

The bentonite's water content after 1 and 6 months of reaction remained similar to the initial 15 wt.% (Figure 2a) but after 22 months increased to 31–33 wt.% along the whole column. A strong decrease in the bentonite's SSA (Figure 2b) was observed in the sections close to the heater, decreasing from 79 m^2/g to 4.6–11.1 m^2/g at the contact with the steel (a SSA reduction of 75–88%). The SSA trend in the three experiments was similar, decreasing towards both ends of the bentonite column but more intensely near the heater. The SSA values after 1 month were lower than those after 6 and 22 months, respectively, but considering the standard deviation of the measurements, this might not be relevant.

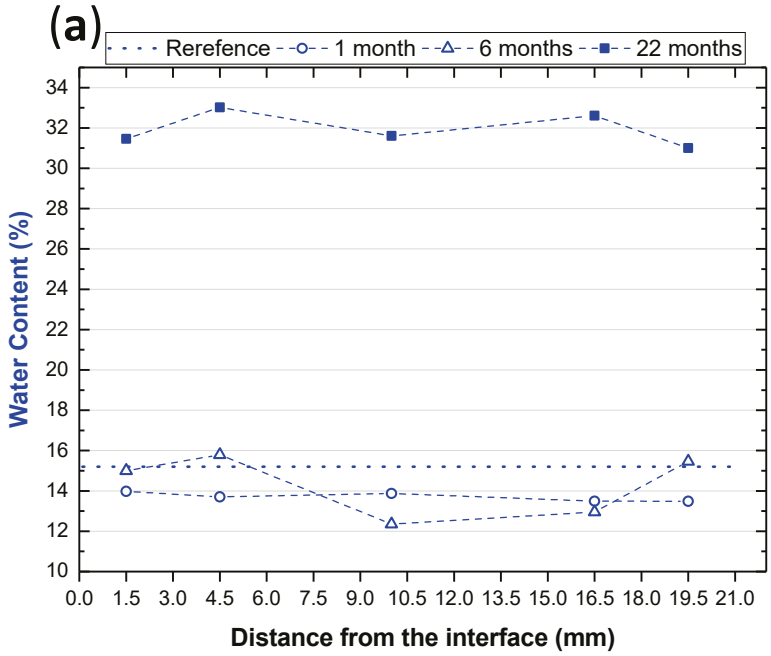


Figure 2. *Cont.*

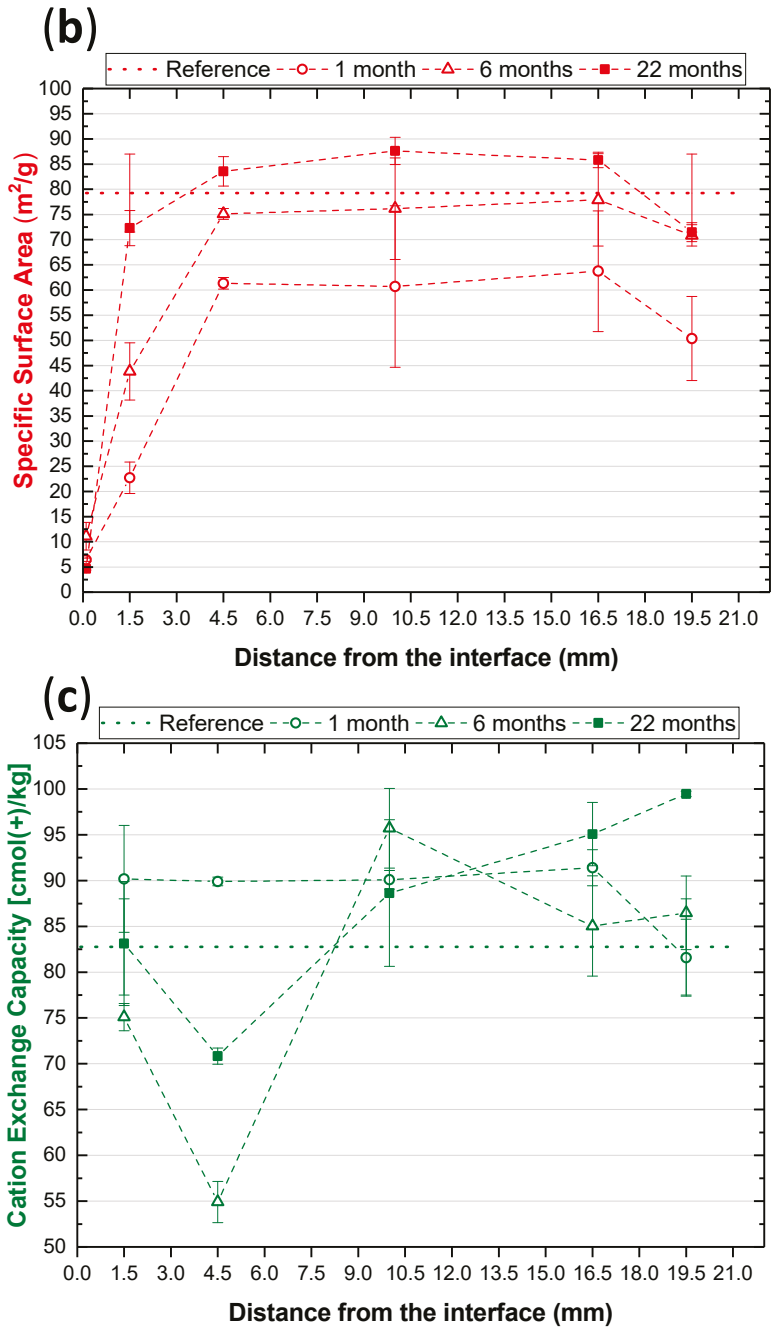
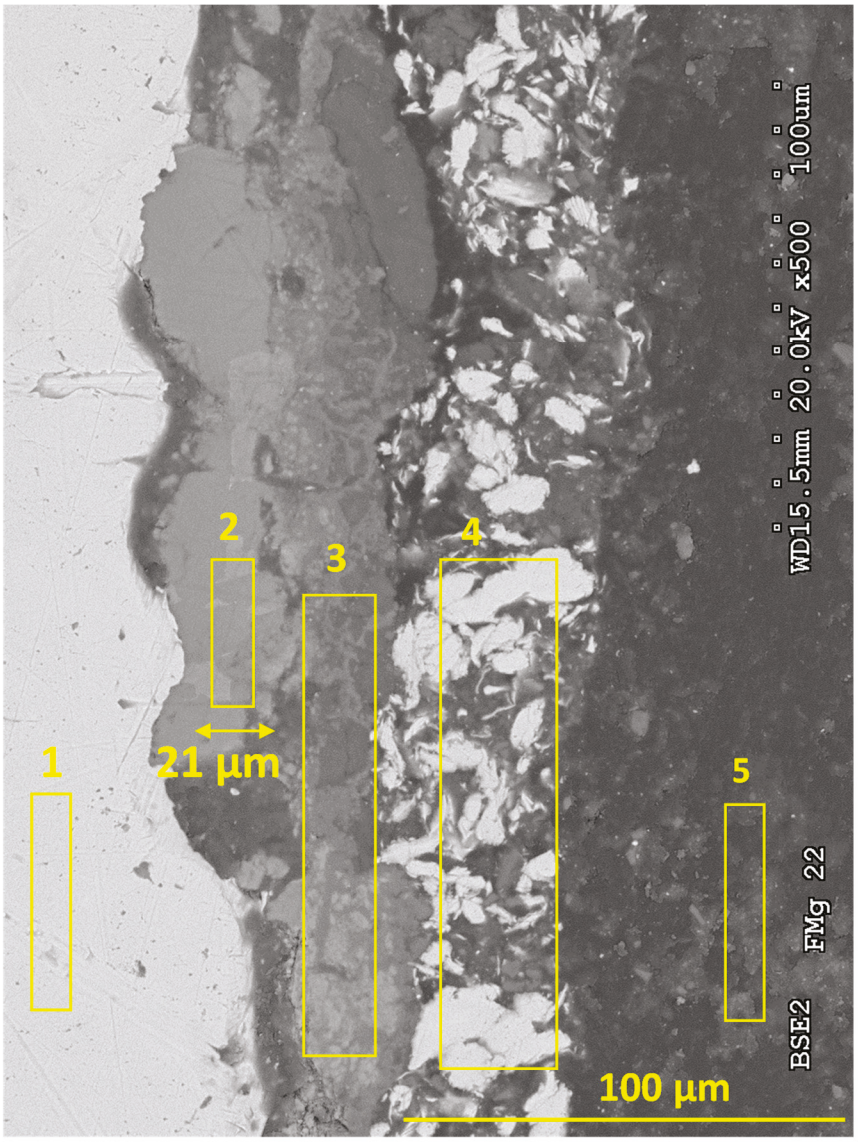


Figure 2. Evolution of physical–chemical properties along the bentonite blocks after 1, 6 and 22 months: (**a**) water content (wt.%); (**b**) specific surface area (m^2/g); (**c**) cation exchange capacity (cmol(+)/kg).

Independently of the reaction time, the bentonite's CEC remained close to the initial reference value (83 ± 5 cmol(+)/kg) except in the section at 3–6 mm from the heater, where a relevant decrease was observed after 6 and 22 months, achieving values of 55 and 71 cmol(+)/kg, respectively (Figure 2c).

The corrosion rate calculated by measurements of corrosion thickness at the steel discs by SEM-EDX (Figure 3) indicated certain passivation with time. The measurements of the corrosion thickness considered the gray compact rim formed at the bright steel surface (Figure 3). A corrosion rate of 39.6 µm/year was calculated after 1 month of reaction, 20.0 µm/year after 6 months and 4.8 µm/year after 22 months (Figure 3).



Zone 1: C-Steel (98 Fe, 1 Si, 1 Mn, 0.3 Cr)
Zone 2: Steel corrosion (88 Fe, 9 Si, 2 Mg, 1 Cr, 0.6 Mn)
Zone 3: Steel corrosion–bentonite (41 Fe, 25 Si, 16 Mg, 10 Al, 4 Ca, 4 Mn)
Zone 4: Steel fragments (74 Fe, 17 Si, 6 Al, 2 Mg, 0.6 Mn, 0.5 Ca)
Zone 5: Resin–bentonite (19 Fe, 60 Si, 12 Al, 6 Mg, 3 Cl)

Figure 3. Backscattered electron image of FEBEX-Mg after 22 months, distinguishing four altered zones from the steel left part) and confirmed by the EDX composition shown below the image. The atomic % of each zone is given to differentiate the observed materials.

The concentration of the major elements in bentonite (Fe, Al and Si), determined by EDX analyses, remained stable over time, but a remarkable decrease in Al and Si, in agreement with an increase in Fe, was observed at 1–2 mm from the interface with the steel. Specifically, the increase in iron reached 1 mm from the interface after 1 month, 1.25 mm after 6 months and 1.5 mm after 22 months (Figure 4a,b). Quantitatively, Fe increased from an averaged 7.2 ± 0.7 wt.% to values > in a range 10–30 wt.% in a thickness of 0–5–1.5 mm from the interface, and values >80 wt.% at a very short distance from the interface (<0.2 mm).

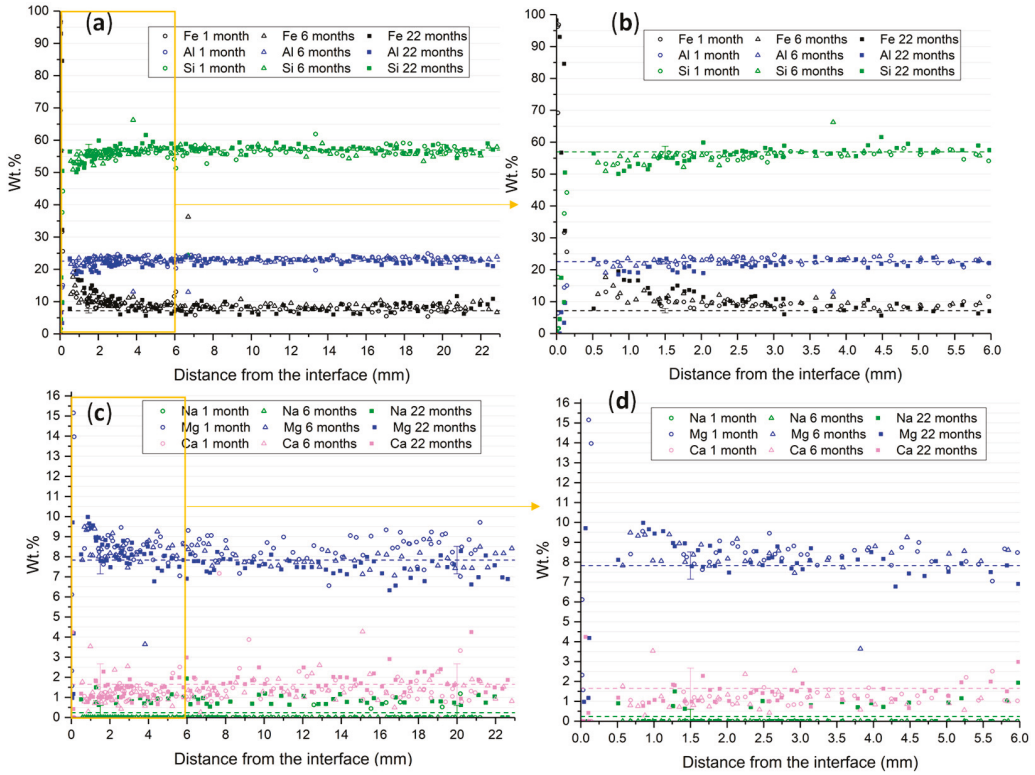


Figure 4. EDX chemical profiles in bentonite, expressed in wt.%: (**a**) Fe, Al and Si after 1, 6 and 22 months; (**b**) detail of (**a**) showing the first 6 mm from the steel interface; (**c**) Na, Mg and Ca after 1, 6 and 22 months; (**d**) detail of (**c**) showing the first 6 mm from the steel interface. Reference values represented by dash lines.

The evolution of Ca and Na, on the contrary, decreased over the first 1.5 mm from the interface, averaged values of 1.7 and 0.2%, respectively, from the original reference bentonite value. Inversely, Mg concentrated at this region and remained at relatively stable values beyond 1.5 mm from the interface (Figure 4c,d).

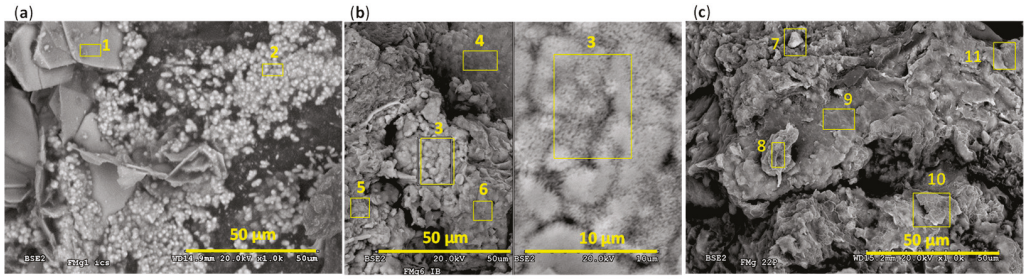
SEM images and EDX analyses performed on fresh fractured bentonite samples close to the steel interface showed incorporation of Fe into the smectite. Figure 5 shows the aspect of clay aggregates presumably produced during bentonite alteration and oxides found attached to the steel plate after 1, 6 and 22 months, which had evidence of formation of new Fe-rich silicates. Secondary mineral phases, with different morphologies, formed on the smectite surface (Figure 5a). EDX analyses expressed in atomic percentage showed that laminar morphologies (analysis 1) contained approximately 79% Fe and 21% Cl, while small micrometric spheres contained 95% Fe and 5% Cl. Both phases were attributed to the precipitation of iron oxides with variable amounts of chloride. After 6 months, iron oxide with additional chloride was observed (analysis 3), nucleating on aggregates with multidirectional micrometer fibers (Figure 5b). The altered clay shown by the morphologies observed in analyses 4, 5 and 6 presented high Fe content (>40%) and a Si/Fe ratio close to 1. Considering the atomic concentrations obtained by EDX, structural formulas were calculated using the model of a di-trioctahedral chlorite (i.e., [62]) structure, assuming the possibility of hydroxide precipitation in a previous dioctahedral smectite interlayer. They were calculated based on the anionic base ($-O_{10}(OH)_8$), distributing Al in the tetrahedral layer (T2 sites) [62,63] and in the octahedral layer (M1, M2 sites). Likewise, Fe was assigned as Fe^{2+} in the trioctahedral brucitic layer (M3, M4); assuming that the charge compensating the sum of the charges generated in T2 and M1, M2 must be produced due to the existence of a certain proportion of Fe^{3+} in the brucitic layer. Mg and part of the Fe and Al, not assignable to T2, M3 and M4, were assigned to the octahedral layer (M1, M2).

Analysis 4: $(Fe^{3+}_{0.33}Fe^{2+}_{0.67})(OH)_2)_3(Al_{0.22}Mg_{0.40}Fe_{1.51})_2(Si_3Al_1)_4O_{10}(OH)_2$
Analysis 5: $(Fe^{3+}_{0.34}Fe^{2+}_{0.66})(OH)_2)_3(Al_{0.25}Mg_{0.92}Fe_{1.09})_2(Si_{3.12}Al_{0.88})_4O_{10}(OH)_2$
Analysis 6: $(Fe^{3+}_{0.37}Fe^{2+}_{0.63}(OH)_2)_3(Al_{0.8}Mg_{0.6}Fe_{0.6})_2(Si_{3.5}Al_{0.5})_4O_{10}(OH)_2$

The calculation reasonably corresponds to the intercalation of iron hydroxide into a smectite structure, although the iron proportions slightly exceed those present in the original octahedral sheet of FEBEX montmorillonite (Ca^{+2} homoionised: $(K_{0.04\_0.01}Ca_{0.24\_0.06}(Fe_{0.09}Al_{1.41}Mg_{0.50})Si_{3.94}Al_{0.05}(O_{10}(OH)_2)$ [64]. The substitution of aluminum in the tetrahedral sheet significantly increased compared to the average montmorillonite, while octahedral Mg remained in similar proportions as in the reference FEBEX.

Analyses on fresh fractured bentonite samples close to the interface after 22 months revealed a larger coating of smectite aggregates (Figure 5c), with a high content of Fe and Mg. The Si/Fe ratio calculated for analyses shown in Figure 5c exceeded 4, except for analysis 7, and differentiated by a single aggregate of brighter color that was 0.75. The structural formula calculated for analysis 7 was $(Fe^{3+}_{0.425}Fe^{2+}_{0.575}(OH)_2)_3(Al_{0.48}Mg_{0.61}Fe_{1.02})_2(Si_3Al_1)_4O_{10}(OH)_2$, compatible again with the di-trioctahedral chlorite structure used to simulate an iron (II, III) hydroxide interlayer simulation. The iron proportion increased over the expected for intercalation. Some mixing of iron oxides and formation of new iron silicates could not be discarded.

Analyses 8–11 showed phyllosilicates rich in Mg and Fe and Si/Fe ratios higher than 4, revealing the necessary presence of iron oxides in the mixture.



(a1)	Cl	Fe
1	21.3	78.7
2	4.8	95.2

(b1)	Mg	Al	Si	Cl	Fe	Si/Fe
3	1.1	2.2	8.0	9.8	78.9	0.1
4	4.4	13.4	32.9	0.0	49.4	0.7
5	9.9	12.1	33.5	0.5	43.9	0.8
6	7.1	14.2	39.4	0.0	39.3	1.0

(c1)	Na	Mg	Al	Si	Cl	K	Ca	Fe	Si/Fe
7	-	6.5	15.6	31.8	1.1	1.2	1.3	42.5	0.8
8	-	10.0	28.3	43.2	3.4	3.0	1.6	10.6	4.1
9	-	13.3	24.0	52.1	-	0.6	0.8	9.1	5.7
10	1.8	13.2	25.1	49.6	0.5	1.8	0.8	7.7	6.4
11	-	14.1	24.6	48.5	-	0.6	2.4	9.9	4.9

Figure 5. SEM images of details taken in fresh fractures close to the steel plate interface: (**a**) 1 month; (**b**) 6 months; (**c**) 22 months. (**a1**,**b1**,**c1**) include the composition of the zones marked in the respective subfigures. Data presented in atomic %. –: data below detection limits.

Figure 6 shows the concentrations of Fe^{2+}, Fe^{3+} and Fe_{total} along the bentonite column after 22 months. An increase in Fe^{2+}, Fe^{3+} and Fe_{total} was observed in a thickness of 2 mm from the interface with steel, compared to the reference concentrations in FEBEX-Mg-bentonite. A similar trend was observed for Fe^{2+} and Fe^{3+} over the whole bentonite column. At the hydration zone, 12–21 mm from the interface with steel, the concentrations decreased slightly below the reference values. Most of the increase in iron was presumably related to the presence of iron (III) oxides as there was an increase in Fe^{2+} from 0.13 ± 0.05 wt.% to 0.26 ± 0.08 wt.% in the section closest to the heater (0–1 mm). Fe^{3+} also increased in contact with the steel, from 3.0 ± 0.4 wt.% determined in the reference Mg-bentonite to 4.03 ± 0.04 wt.%. In the following section (1–2 mm), Fe^{2+} and Fe^{3+} concentrations decreased by 0.17 ± 0.01 wt.% and 3.85 ± 0.6 wt.%, respectively. At the 2–3 mm section from the heater, the Fe^{2+} and Fe^{3+} values remained in the order of the reference Mg-bentonite.

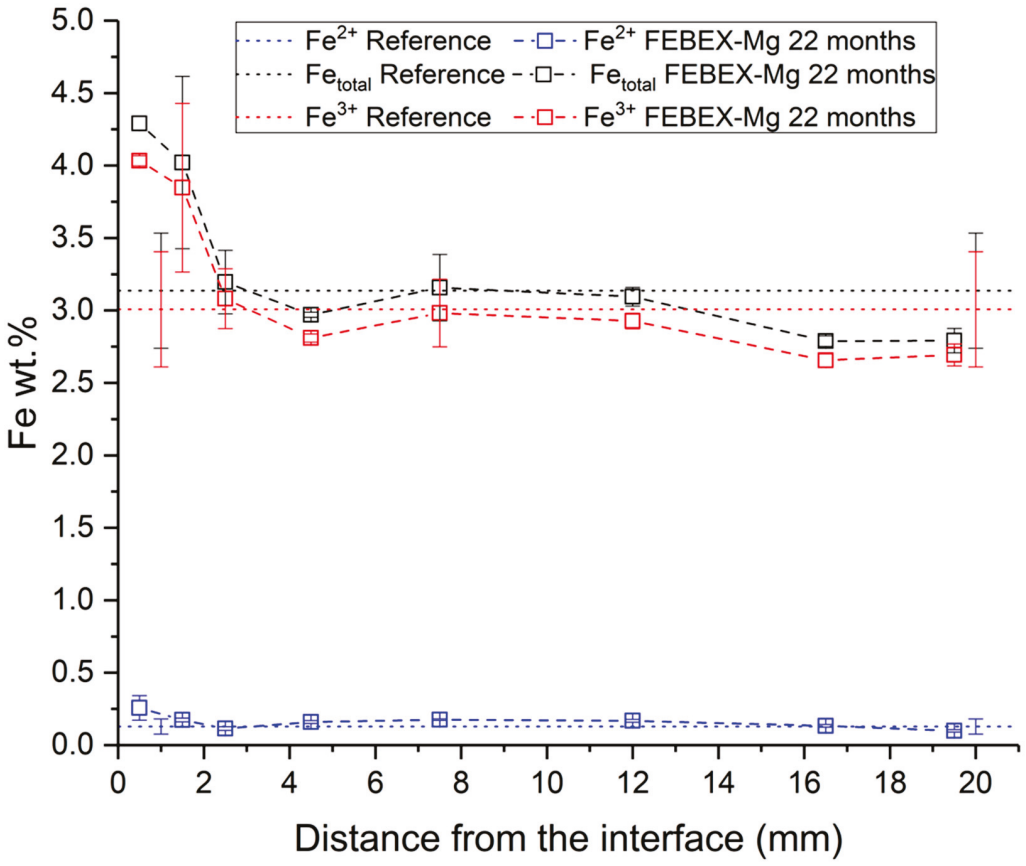


Figure 6. Concentrations of Fe^{2+}, Fe^{3+} and Fe_{total} along the bentonite column after 22 months. Units expressed in wt.%, referred to dry mass of solid sample.

The mineralogy of FEBEX-Mg-bentonite experienced minor changes over time (Figure S1, Supplementary Materials) considering the whole thickness of the bentonite disc. The main FEBEX-Mg-smectite XRD reflections were detected at 14.8 Å (001), 4.45 Å (020), 2.58 Å (110), 1.70 Å (210) and 1.50 Å (060). The reference material also presented quartz (4.25, 3.34 Å), cristobalite (4.04 Å), calcite (3.0 Å), and traces of magnetite (2.53 Å) and maghemite (2.52 Å), (Figure 7). The main mineralogical changes were observed near the steel interface (<3 mm). After 1 month, no minerals other than those present in the reference bentonite were detected, except ankerite, a Ca,Fe^{II},Mg-carbonate (2.90 Å) in the section <3 mm from the steel interface. After 6 months, also in the section <3 mm from the steel interface, low-intensity reflections of ankerite and maghemite were also detected. After 22 months, the presence of a 7.05 Å reflection and the enhancement of a 4.8–4.7 Å band supported some evidence of di-tri ferric chlorite presence, presumably ferri-sudoite-like (in agreement with the SEM-EDX data). It is known that the 14 Å reflection of ferric (hydroxide layer) aluminous (octahedral layer) chlorite displayed a very small intensity compared to 7 and 4.74 Å reflections (i.e., [65]). The 14.8–14.6 Å basal spacing reflection predominant in most DRX patterns could contain smectite and the minor chlorite reflection. Ankerite (2.90 Å) was detected close to the steel interface (<3 mm). In the section at 3–6 mm, lepidocrocite (γ-$Fe^{3+}O(OH)$) (6.25 Å) and hematite (Fe_2O_3) (2.70 Å) were detected. Lepidocrocite was also detected in the section at 6–15 mm (Figure 7). Accessory minerals like muscovite (illite) and albite (plagioclases), present in the reference Mg-bentonite raw material, were randomly detected due to their heterogeneous distribution in bentonite.

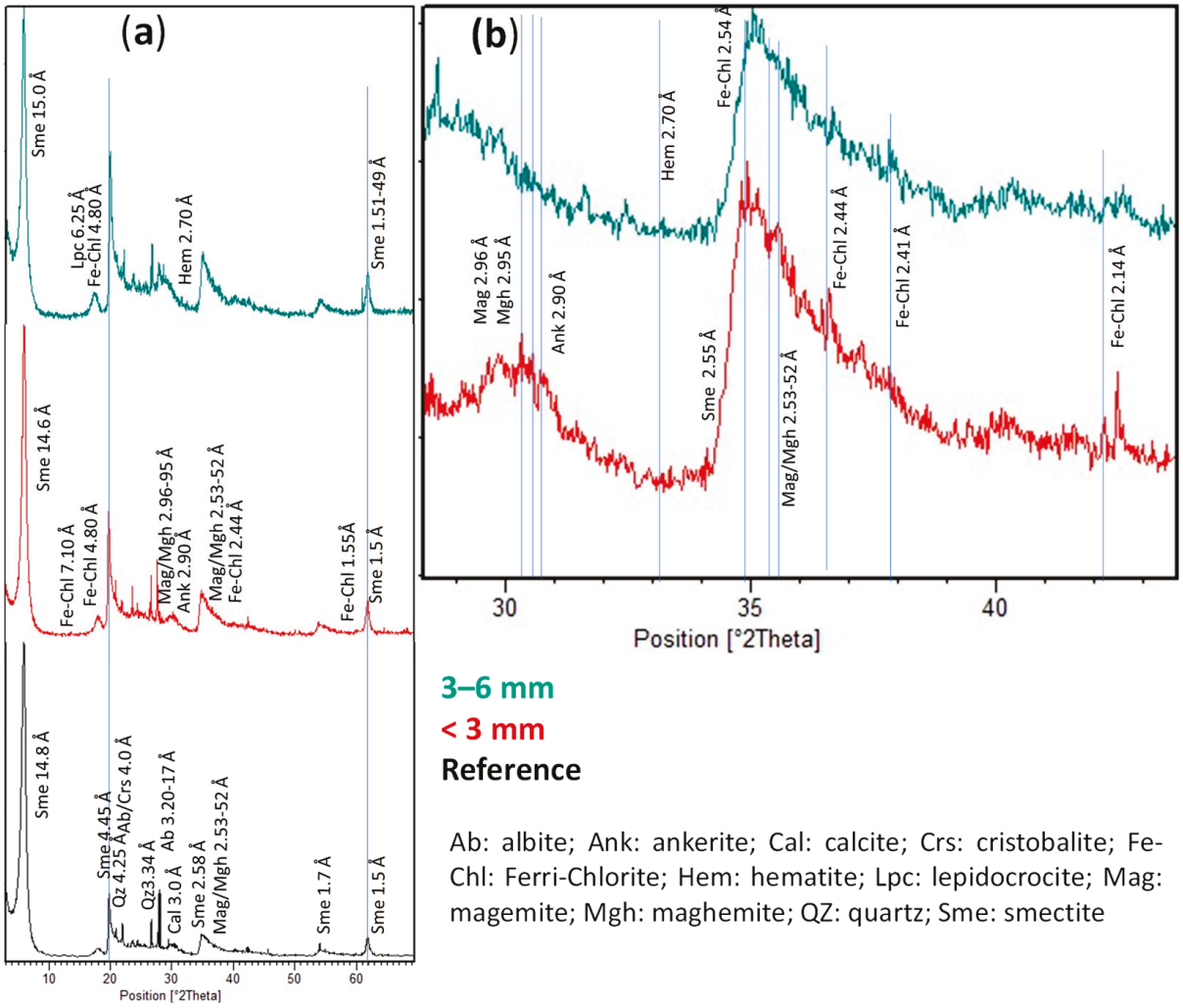


Figure 7. XRD on FEBEX-Mg sections from the steel interface after 22 months. (**a**) section at 3–6 mm (green upper diffractogram); section at 0–3 mm (red middle diffractogram); reference FEBEX-Mg (black bottom diffractogram); (**b**) zoom of the 29–44 2θ range.

The XRD patterns corresponding to the corrosion crusts that formed at the steel–bentonite interface were measured on both sides, the contact with steel (colored in fuchsia) and the contact with the bentonite (colored in orange) (Figure 8). Several intense reflections, observed at 6.40, 5.35, 4.84 and 3.52 Å, identified after 1 month, were not related to any mineral alteration but attributed to the adhesive used to fix the corrosion crust on the airtight holder. In addition, hematite (2.70 Å, 2.51 Å) and maghemite (2.94 Å, 2.52 Å) were detected, and siderite at a low intensity (2.79 Å). At the contact with the bentonite side, low-intensity reflections of ankerite (2.90 Å) and hematite (2.70 Å) were identified as corrosion products at the corrosion crust. The ferric chlorite phase (ferri-sudoite) (7 and 4.8 Å) was barely identified with other compatible reflections at 2.65 Å and 2.44 Å. Low-intensity reflections of magnetite/maghemite were observed.

After 6 months, reflections attributed to green rust (7.5 Å, 3.75 Å), maghemite and magnetite (2.96–95 Å and 2.53–2.51 Å) and siderite (low-intensity reflections at 2.79 Å) were observed in the corrosion crust at the contact with steel. Smectite, albite and quartz, already present in the original bentonite were detected. Ferri-sudoite was detected by the reflections at 7.05 Å, 4.80, 2.80 and 2.44. At the bentonite side, ferri-sudoite was detected too. Ankerite (2.90 Å), hematite (2.70 Å) and a maghemite/magnetite mix were identified as corrosion products. Siderite was not identified on this side.

After 22 months, more clear and intense reflections were observed regarding the altered products. The crust analyzed in contact with steel showed a main composition of siderite (2.79 Å). Smectite, ferri-sudoite and albite were detected as minor minerals. On the bentonite side, the main reflections were associated with ferri-sudoite (7.05 Å, 4.80 Å, 3.53 Å, 2.44 Å, 2.14 Å and 1.55 Å) and green rust (7.5 Å and 3.76 Å), but low-intensity reflections at 2.90 Å and 2.51 Å were attributed to ankerite and maghemite, respectively.

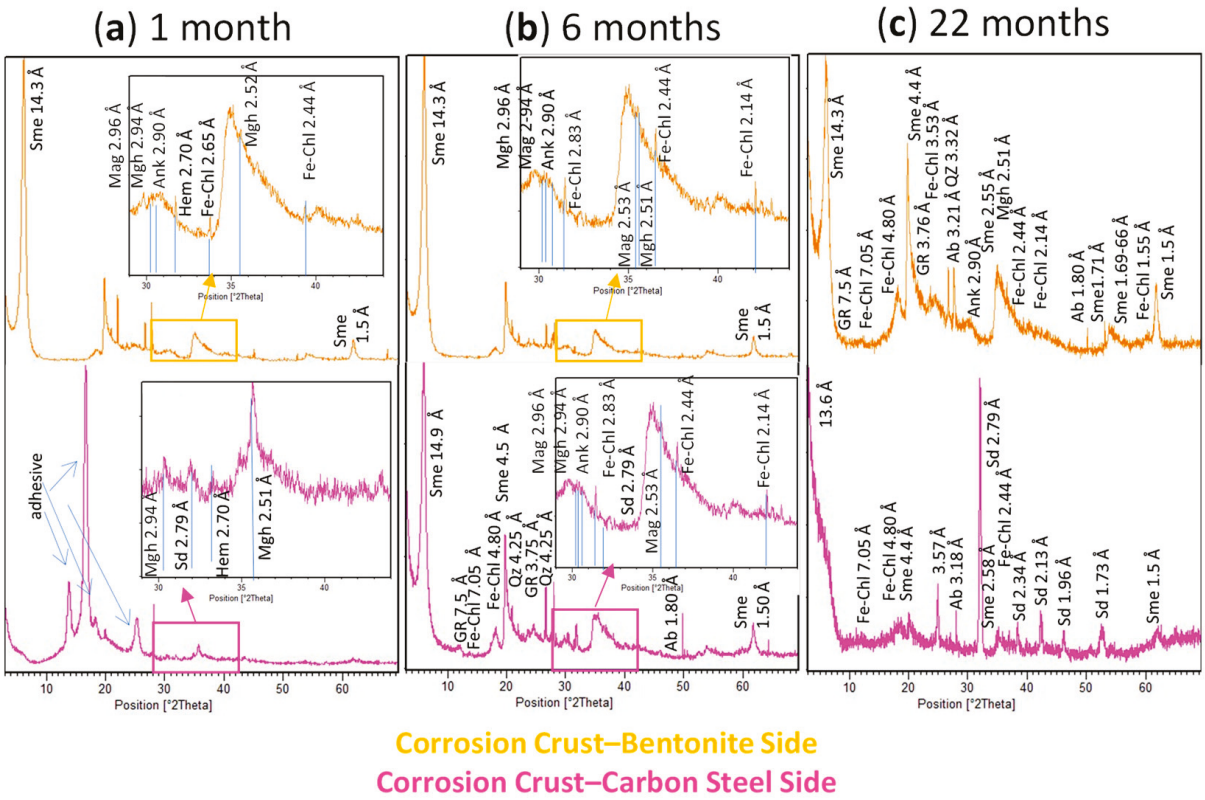


Figure 8. XRD of corrosion crusts examined from the contact with steel (fuchsia) and with bentonite (orange) after (**a**) 1 month; (**b**) 6 months; and (**c**) 22 months. Ab: albite; Ank: ankerite; Crs: cristobalite; GR: green rust; Hem: hematite; Mag: magnetite; Mgh: maghemite; Qz: quartz; Sd: siderite; Sme: smectite; Sud: sudoite.

Aqueous extracts were analyzed to study the redistribution of aqueous species in the bentonite porewater (Figure 9). After 1 month Cl^- varied within a range between 395 and 483 mM, similar to the reference FEBEX-Mg (455 ± 2 mM), concentrating at the middle of the bentonite column (6–15 mm). The same tendency was observed after 6 months but within a lower concentration range (220–280 mM). After 22 months, Cl^- decreased to lower concentrations, within a range of 54–58 mM. Mg^{2+} maintained concentrations close to the reference FEBEX-Mg (130 ± 6 mM), within a range between 100 and 166 mM after 1 and 6 months, but after 22 months Mg^{2+} concentrations decreased within a narrow range of 28–36 mM along the bentonite column. The rest of the ions analyzed (Na^+, Ca^{2+}, $SO_4{}^{2+}$ and K^+) were in a lower concentration range (3–58 mM). A general decrease of concentrations was observed with the increasing reaction time. After 22 months, Na^+ was determined to be within a range between 36 and 40 mM, while the reference Na^+ concentration was 15 ± 9 mM; Ca^{2+} increased up to 11–16 mM from the initial reference of 9 ± 2 mM; $SO_4{}^{2-}$ increased to 9–12 mM from the reference of 5 ± 1 mM, and K^+ decreased from 10 ± 1 mM to 4 mM.

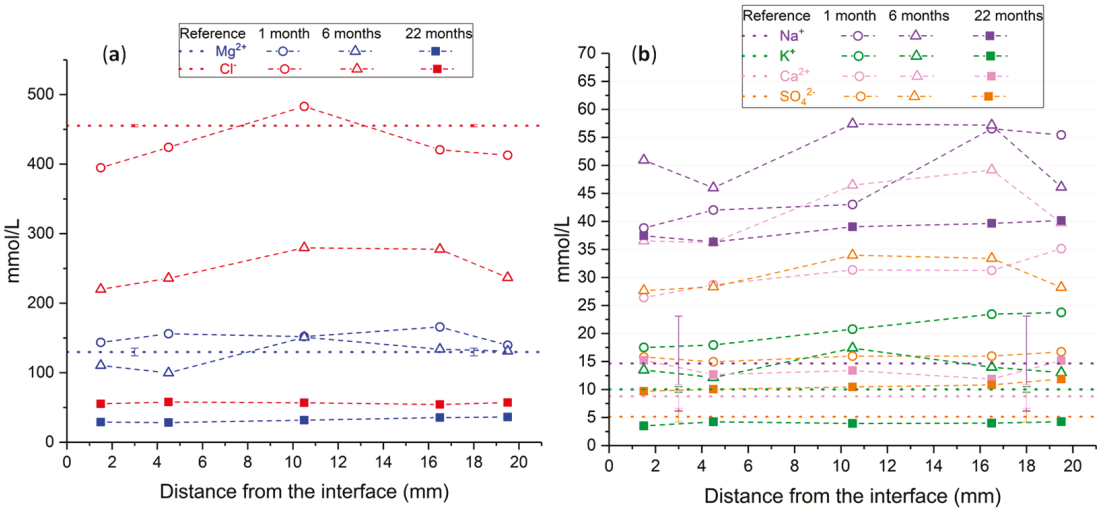


Figure 9. Ionic concentrations of aqueous extracts in bentonite sections parallel to the steel interface. (**a**) Mg^{2+} and Cl^{-}; (**b**) Na^{+}, K^{+}, Ca^{2+} and $SO_4{}^{2-}$. References values represented by dotted lines.

4. Discussion

The experimental design provided data after 1, 6 and 22 months, allowing for the study of the temporal evolution of steel–bentonite interactions. The temporal evolution described how the progressive passivation of the steel surface occurred, visibly decreasing the corrosion rate with time. The longest experiment, performed for 22 months, unusually for this type of laboratory experiment, permitted the formation of a well-defined cemented crust at the steel–bentonite interface due to the precipitation of iron corrosion products that could be analyzed from both faces.

Due to the hydrothermal gradient, the bentonite's physical–chemical properties were modified. A rather homogeneous increase in water content was observed after 22 months (close to 30 wt.%) without apparent water content decrease as a function of distance to the heat contact. Similar experiments using natural FEBEX bentonite showed a slightly higher water content range (20–25 wt.%), achieved during a short time in the whole column (1 and 6 months) [53]. Since the pressure of water injection was relatively low (0.15 MPa) and the swelling properties of the Mg-saturated bentonite were homogeneous, hydration progressed very slow. The material was previously wetted and reprocessed to be Mg-saturated, so final mineral grains and grain size were artificially homogenized to <1 mm compared to natural FEBEX bentonite, which usually provided grains <5 mm with a visible heterogeneity of grain colors and different altered rock preserved grains (i.e., [66]). The great homogeneity, at small time lapses, could produce resistance to hydration at the swelling interface. There was no evidence of water loss associated with the thermal treatment or gradient in the short term that would have resulted in the dehydration of the bentonite near the heater, a phenomenon that was not detected, with values close to the initial moisture level being maintained. On the other hand, hydration was completed after 22 months, allowing for comparison of the short term (1 and 6 months) with the long-term (22 months), once the hydration front progressed. The bentonite's SSA remained in a range close to the initial reference values, except near the steel interface, due to the presence of corrosion products and modifications on the smectite, as observed by SEM-EDX and XRD, where minerals identified to be of the chlorite group and iron-rich were detected, mixed with the smectite matrix. Chlorite minerals were detected in a FEBEX in situ experiment by Wersin et al. [49] at a temperature of 50 °C and were synthesized at 300 °C in the presence of metallic Fe powder facing MX-80 bentonite [67], showing compositions and XRD powder patterns similar to those shown in this study.

The composition of materials corresponding to iron silicates, seeking locations free of chloride and analyzed by SEM-EDX, is compatible with ferric chlorites. Their elemental

proportions are consistent with the predominance of a di-octahedral character in the octahedral layer and tri-octahedral character with partially oxidized Fe^{2+} in the brucitic layer. Assuming the already described distribution model, the presence of typical reflections of ferric chlorites outlining a main reflection at 7 Å could be explained with a composition characteristic of ferri-sudoite (Figure 7).

The CEC remained within a range similar to the reference bentonite, except in the section at 3–6 mm from the steel interface that decreased after 6 and 22 months. This phenomenon is typically connected to the dissolution of montmorillonite and the neoformation of other non-swelling minerals such as chlorite or iron oxides. Fe^{3+} predominated over Fe^{2+}, which increased slightly by approximately 0.2 wt.% over the first 1.5 mm of bentonite from the steel interface. This was in agreement with the presence of tri-(Fe^{2+}),di-(Al^{3+})-chlorite mineral in minor amounts, coexisting with Fe(III) oxides, evidenced by the presence of hematite on the bentonite side and Fe^{3+}/Fe^{2+} oxides, mainly magnetite, within the steel corrosion products. The decline in CEC observed in the present study was attributed to the formation of mixed iron oxides in the material rather than montmorillonite dissolution, as no peak broadening XRD evidence supported such dissolution (Figure S1).

After being exposed to a carbon–steel heater at 100 °C for 18 years in the in situ FEBEX experiment, a reduction in CEC was also observed in FEBEX bentonite [43]. That decrease was attributed to one of the following factors: an increase in the smectite layer charge, the reduction of Fe^{III}-bearing smectite, which induced the collapse of clay particles (not observed in the present research), or the shrinkage of lamellar particles induced by high salinity. In FEBEX bentonite, the salinity was nearly constant at each reaction time, except in the section closest to the hydration zone. Therefore, the decrease in CEC could not be ascribed to higher salinity resulting from direct contact with the saline solution. Dohrmann et al. [68] proposed that the potential decrease in CEC could be attributed to the increased experimental temperature and/or the development of corrosion products within the bentonite matrix. In the current set of experiments, it was noted that smectite aggregates at the steel–bentonite interface were coated with iron oxides, as illustrated in Figure 5, in agreement with the interpretation by Dohrman et al. [68].

The characterization of aqueous extracts from the bentonite porewater showed a decrease in K^+ concentrations after 22 months. It could have occurred due to a fixation of K^+ in the interlayer during the initial stages of illitization, as suggested by Kumar et al. [68,69], although the low general K^+ concentration provided no visible evidence for this, extracted from the XRD patterns. Another explanation for the general salinity reduction involving the remaining ions over the long term could be attributed to the formation of iron oxides, wherein ions subsequently associated to form complex minerals, such as green rust, producing an overall reduction of ions (chloride) in solution, as observed after 22 months of reaction.

Fe-silicates and Fe-Cl corrosion products were detected, evidencing chloritization processes, as confirmed by XRD after 22 months of reaction. The formation of Fe-spicules or fibrous Fe-silicates was reported by Kaufhold et al. [70] in their SEM study on Fe–bentonite interactions. Previous experiments with MX-80 and FEBEX bentonite conducted for 1 and 6 months under the same experimental conditions showed similar precipitation of iron oxides in the corrosion layer at the steel–bentonite contact. The authors reported the formation of magnetite, maghemite and goethite after 1 and 6 months [53].

The increase in Fe content within the montmorillonite structure could be elucidated through various mechanisms, such as adsorption within the interlayer via cation exchange, adsorption at the edge sites of montmorillonite or association with corrosion products [36]. Additionally, redox reactions may have occurred, leading to the precipitation of Fe^{III}-oxides or mixed Fe^{II}/Fe^{III}-oxides and Fe^{II}-carbonates like ankerite and siderite. Soluble Fe^{2+} migrated into the bentonite as oxygen from the bentonite pores diffused to the steel surface. The interaction of iron with oxygen could have resulted in oxidation and subsequent precipitation on montmorillonite surfaces, forming iron (hydr)oxides like lepidocrocite. The calculated corrosion rate showed a reduction with increasing time, in agreement with

other studies [71–74]. Wersin et al. [75] reviewed the corrosion rates of four different in situ experiments, the FEBEX in situ experiment being one of them. A range of corrosion rates between 6 and 11 μm/year were calculated for this experiment, conducted for 18 years at 70 °C, using carbon steel and FEBEX bentonite. In the present research at 100 °C and over the short term, compared to the FEBEX in situ experiment, the final corrosion rate was nearly in the same range or even lower but within the same order of magnitude as observed after 18 years. The Mg-saturated bentonite could enhance passivation, which will presumably be confirmed by ongoing longer-term experiments.

Taking into account the mineralogical observations, a scheme showing the reaction products at the steel–bentonite interface after at the three experimental times (1, 6 and 22 months) is presented in Figure 10. This scheme is based on those presented by Wersin et al. [75] and Hadi et al. [73]. Wersin et al. [75] studied corrosion in eight bentonites pre-saturated with Äspö groundwater heated to 130 °C in the ABM2 in situ experiment. Hadi et al. [73] studied the steel–bentonite interactions in the FEBEX in situ experiment, in which carbon steel, in contact with FEBEX bentonite, was heated at 100 °C for 18 years. The proposed scheme tries to visualize the different mineral phases detected after 1, 6 (presumably under unsaturated water vapor migration conditions) and 22 months (under water saturated conditions at the end of the experiment). The alteration thicknesses are not presented at scale but indicate the transformation of some phases into others. The increase of siderite with time as well as the presence of Fe^{2+}-silicates in a wider region after 22 months than after 1 and 6 months were observed by XRD. Although each zone is represented by solid colors, a mixture of minerals was observed at the interfaces of each zone.

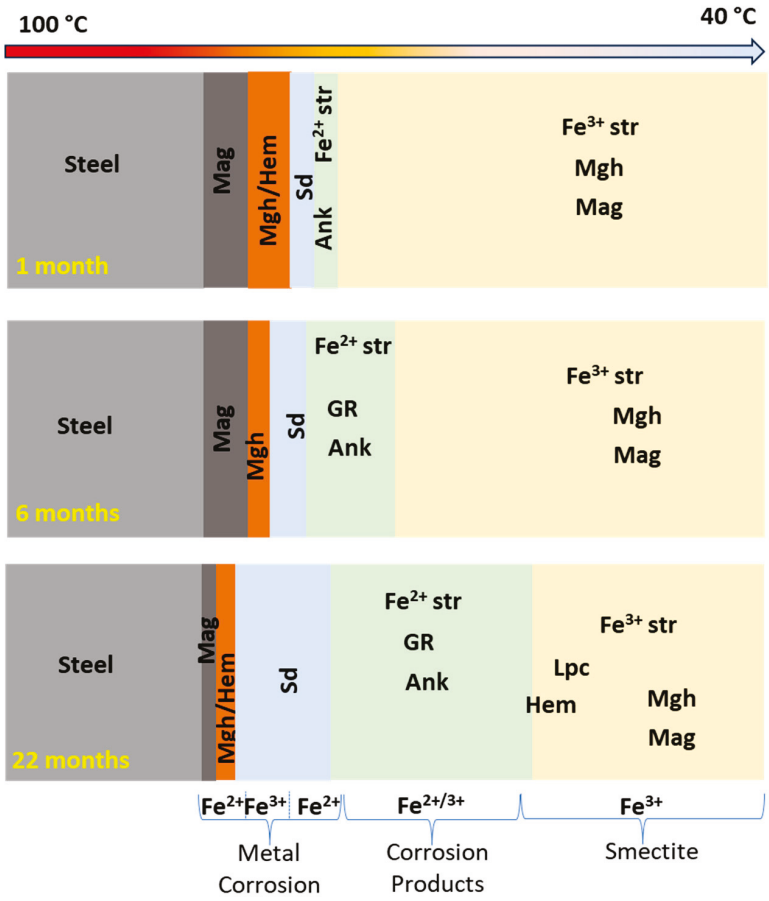


Figure 10. Proposed mineral phase evolution scheme for steel–FEBEX-Mg interface after 1, 6 and 22 months. Mag: magnetite; Mgh: maghemite; Hem: hematite; Sd: siderite; GR: green rust; Ank: ankerite; Lpc: lepidocrocite; using similar scheme and colors as in Hadi et al. [73].

Determinations on the iron redox state in bentonite, analyzed after 22 months of reaction, showed an increase of Fe^{2+} and Fe^{3+} near the steel interface (<2 mm), presumably affecting a larger thickness compared to less humid and earlier times (1 and 6 months under the same conditions). Magnetite formed as the main steel corrosion mineral, as observed in several water-saturated environments under reducing conditions (i.e., Schelegel et al. [76]). The determination of redox potential in the clay–metal-iron interface in a transient oxic to anoxic state is complex and ambiguous as many Fe^{3+} and Fe^{2+} minerals are involved and present in small quantities, making them difficult to identify.

Robinson et al. [77] established the presence of magnetite/maghemite-coupled minerals mainly controlling the Fe^{2+} redox solution equilibrium at pH 6.5–8.5, exhibiting more negative potential than the corresponding lepidocrocite and hematite at progressively less negative potentials. The expansion of the reducing front towards the bentonite may have led to the presence of these Fe^{3+} iron oxides in regions relatively far (up to 2 mm) from the interface where Fe^{3+} predominated. The potential intercalation of Fe^{2+} ions as hydroxide in a chloritic structure added complexity and probably further enhanced the transport of Fe^{2+} to the clay material. Wersin et al. [18] mostly identified the iron in the zone closest to the heater as Fe^{3+}, which was consistent with the detection of hematite, magnetite, maghemite and lepidocrocite in this zone. Fe^{2+} was oxidated partially to Fe^{3+} in the middle sections of the bentonite column, coexisting both species, although concentrations of Fe^{3+} were higher than Fe^{2+}.

5. Conclusions

Bentonite was slightly altered after 1 and 6 months, but the main alterations were observed after 22 months of reaction and well-defined mineralogical changes could be identified. The formation of secondary minerals coating the smectite were argued to explain the bentonite-specific surface area decreases at the steel interface. The enrichment in Fe in the bentonite was detected over the first 3 mm from the steel interface. However, the corrosion rate decreased to <5 μm/year with the reaction time up to 22 months. Minor changes were noticed along the bentonite column beyond the first 3 mm from the steel interface, maintaining its original properties. The iron–bentonite interactions allowed the formation of corrosion products, several iron oxides like magnetite, maghemite or hematite, and iron carbonates like siderite, ankerite and green rust (containing chloride) to be identified. The geochemical evolution of bentonite promoted the formation of a chlorite phase of ferri-sudoite-like composition through the montmorillonite modification. The use of X-ray diffraction, the photochemical method with 1,10-phenanthroline and scanning electron microscopy analyses allowed the identification of these minerals.

The main mineralogical changes were found at the steel–bentonite interface, where the bentonite properties studied were modified by the precipitation of corrosion products, forming a low-porosity layer that could potentially clog bentonite pores and affect subsequent reactivity. Negligible smectite alteration was found in previous experiments of the Fe–bentonite interaction at low liquid/solid ratios, leading to uncertainties over the Fe-phyllosilicates that could form in such systems. However, the use of a bentonite containing Mg-smectite has favored the identification of bentonite mineral alteration, producing chlorite-type minerals that should be considered in future geochemical modeling of Fe–bentonite systems.

Supplementary Materials: The following supporting information can be downloaded at https://www.mdpi.com/article/10.3390/app14031259/s1: Figure S1: XRD of sections from the steel interface: (a) 1 month; (b) 6 months; (c) 22 months.

Author Contributions: Conceptualization, C.M.-H., R.F. and J.C.; methodology, C.M.-H., R.F. and J.C.; software, C.M.-H., R.F. and J.C.; validation, R.F. and J.C.; formal analysis, C.M.-H.; investigation, C.M.-H., R.F. and J.C.; resources, C.M.-H., R.F. and J.C.; data curation, C.M.-H., R.F. and J.C.; writing—original draft preparation, C.M.-H.; writing—review and editing, R.F., J.C. and C.M.-H.; visualization, C.M.-H., R.F. and J.C.; supervision, R.F. and J.C.; project administration, J.C.; funding acquisition, J.C. All authors have read and agreed to the published version of the manuscript.

Funding: This research has been developed by the UAM AcMe research group to support the WP.2 EURAD-ACED project results, which has received funding from the European Union's Horizon 2020 research and innovation program under grant agreement No. 847593.

Data Availability Statement: The data presented in this study are available on request from the corresponding author.

Acknowledgments: The authors acknowledge the contribution of two anonymous reviewers for their suggestions to improve the quality of the manuscript.

Conflicts of Interest: The authors declare no conflicts of interest.

References

1. King, F. 13—Nuclear Waste Canister Materials: Corrosion Behavior and Long-Term Performance in Geological Repository Systems. In *Geological Repository Systems for Safe Disposal of Spent Nuclear Fuels and Radioactive Waste*, 2nd ed.; Apted, M.J., Ahn, J., Eds.; Woodhead Publishing: Cambridge, UK, 2017; pp. 365–408, ISBN 978-0-08-100642-9.
2. NUMO. *Safety of the Geological Disposal Project 2010*; NUMO: Tokyo, Japan, 2013; p. 148.
3. Hellä, P.; Pitkänen, P.; Löfman, J.; Partamies, S.; Vuorinen, U.; Wersin, P. *Safety Case for the Disposal of Spent Nuclear Fuel at Olkiluoto Definition of Reference and Bounding Groundwaters, Buffer and Backfill Porewaters*; POSIVA OY: Olkiluoto, Finland, 2014.
4. Chapman, N.A. Geological Disposal of Radioactive Wastes—Concept, Status and Trends. *J. Iber. Geol.* **2006**, *32*, 7–14.
5. *Status and Trends in Spent Fuel and Radioactive Waste Management*; Nuclear Energy Series; International Atomic Energy Agency: Vienna, Austria, 2022; ISBN 978-92-0-130521-3.
6. Fernández, R. Engineered Barriers for Radioactive Waste Confinement. *Mater. Construcción* **2011**, *61*, 485–492. [CrossRef]
7. ENRESA. *Evaluación Del Comportamiento y de La Seguridad de Un Almacenamiento Geológico Profundo En Granito*; ENRESA: Madrid, Spain, 1997; p. 179.
8. Pirot, V. *ONDRAF/NIRAS Research, Development and Demonstration (RD&D) Plan for the Geological Disposal of High-Level and/or Long-Lived Radioactive Waste Including Irradiated Fuel If Considered as Waste, State-of-the-Art Report as of December 2012*; ONDRAF/NIRAS: Brussels, Belgium, 2013; p. 413.
9. Patel, R.; Punshon, C.; Nicholas, J.; Bastid, P.; Zhou, R.; Schneider, C.; Bagshaw, N.; Howse, D.; Hutchinson, E.; Asano, R.; et al. *Canister Design Concepts for Disposal of Spent Fuel and High Level Waste*; NAGRA: Wettingen, Switzerland, 2012; p. 245.
10. King, F.; Kolář, M.; Keech, P.G. Simulations of Long-Term Anaerobic Corrosion of Carbon Steel Containers in Canadian Deep Geological Repository. *Corros. Eng. Sci. Technol.* **2014**, *49*, 456–459. [CrossRef]
11. Necib, S.; Schlegel, M.L.; Bataillon, C.; Daumas, S.; Diomidis, N.; Keech, P.; Crusset, D. Long-Term Corrosion Behaviour of Carbon Steel and Stainless Steel in Opalinus Clay: Influence of Stepwise Temperature Increase. *Corros. Eng. Sci. Technol.* **2019**, *54*, 516–528. [CrossRef]
12. Christidis, G.E.; Huff, W. Geological Aspects and Genesis of Bentonites. *Elements* **2009**, *5*, 93–98. [CrossRef]
13. Bergaya, F.; Lagaly, G. Chapter 1—General Introduction: Clays, Clay Minerals, and Clay Science. In *Developments in Clay Science*; Bergaya, F., Lagaly, G., Eds.; Elsevier: Amsterdam, The Netherlands, 2013; Volume 5, pp. 1–19. ISBN 1572-4352.
14. Bildstein, O.; Claret, F. Chapter 5—Stability of Clay Barriers Under Chemical Perturbations. In *Natural and Engineered Clay Barriers*; Tournassat, C., Steefel, C.I., Bourg, I.C., Bergaya, F., Eds.; Developments in Clay Science; Elsevier: Amsterdam, The Netherlands, 2015; Volume 6, pp. 155–188.
15. Villar, M.V. *Thermo-Hydro-Mechanical Characterisation of a Bentonite from Cabo de Gata. A Study Applied to the Use of Bentonite as a Sealing Material in High Level Waste Repositories*; ENRESA: Madrid, Spain, 2002; p. 277.
16. Huertas, F.; Fariña, P.; Farias, J.; García-Siñéroz, J.L.; Villar, M.V.; Fernández, A.M.; Martín, P.L.; Elorza, F.J.; Gens, A.; Sánchez, M.; et al. *Full-Scale Engineered Barriers Experiment. Updated Final Report 1994-2004*; ENRESA: Madrid, Spain, 2006; p. 590.
17. Zeng, Z.; Shao, J.; Sun, D.; Lyu, H.; Xu, Y.; Yang, C. Effect of Thermal Ageing on Physical Properties of MX80 Bentonite under High-Temperature Conditions. *Eng. Geol.* **2022**, *308*, 106822. [CrossRef]
18. Wersin, P.; Kober, F. *FEBEX-DP Metal Corrosion and Iron-Bentonite Interaction Studies*; NAGRA: Wettingen, Switzerland, 2017; p. 300.
19. Garralón, A.; Gómez, P.; Turrero, M.J.; Torres, E.; Buil, B.; Sánchez, L.; Peña, J. *Hydrogeochemical Characterisation of the Groundwater in the FEBEX Gallery*; NAGRA: Wettingen, Switzerland, 2017; p. 125.
20. Turrero, M.J.; Fernández, A.M.; Peña, J.; Sánchez, M.D.; Wersin, P.; Bossart, P.; Sánchez, M.; Melón, A.; Garralón, A.; Yllera, A.; et al. Pore Water Chemistry of a Paleogene Continental Mudrock in Spain and a Jurassic Marine Mudrock in Switzerland: Sampling Methods and Geochemical Interpretation. *J. Iber. Geol.* **2006**, *32*, 233–258.
21. Ragvald, J. *Hydrochemical Groundwater Monitoring Results from Water Sampling in the Forsmark Area 2016*; SKB: Seoul, Republic of Korea, 2018; p. 90.
22. Navarro, V.; Yustres, Á.; Asensio, L.; De la Morena, G.; González-Arteaga, J.; Laurila, T.; Pintado, X. Modelling of Compacted Bentonite Swelling Accounting for Salinity Effects. *Eng. Geol.* **2017**, *223*, 48–58. [CrossRef]

23. ANDRA. *Agence Nationale pour la Gestion des Dechets Radioactifs—Andra, 1/7, Rue Jean Monnet, Parc de la Croix-Blanche, 92298 Chatenay-Malabry Cedex (France). Dossier 2005 Granite—Tome Phenomenological Evolution of a Geological Repository December 2005*; Andra: Châtenay-Malabry, France, 2006; p. 198.
24. ANDRA. *Agence Nationale pour la Gestion des Dechets Radioactifs—Andra, 1/7, Rue Jean Monnet, Parc de la Croix-Blanche, 92298 Chatenay-Malabry Cedex (France). Dossier 2005 Argile—Tome Phenomenological Evolution of a Geological Repository December 2005*; Andra: Châtenay-Malabry, France, 2006; p. 527.
25. King, F.; Ahonen, L.; Taxen, C.; Vuorinen, U.; Werme, L. *Copper Corrosion under Expected Conditions in a Deep Geologic Repository*; Swedish Nuclear Fuel and Waste Management Co.: Stockholm, Sweden, 2001; p. 171.
26. National Cooperative for the Disposal of Radioactive Waste (NAGRA). *W. (Switzerland) Project Opalinus Clay—Safety Report—Demonstration of Disposal Feasibility for Spent Fuel, Vitrified High-Level Waste and Long-Lived Intermediate-Level Waste (Entsorgungsnachweis)*; Nagra: Wettingen, Switzerland, 2002; p. 472.
27. Kim, J.-S.; Kwon, S.-K.; Sanchez, M.; Cho, G.-C. Geological Storage of High Level Nuclear Waste. *KSCE J. Civ. Eng.* **2011**, *15*, 721–737. [CrossRef]
28. Villar, M.V.; Martín, P.L.; Bárcena, I.; García-Siñeriz, J.L.; Gómez-Espina, R.; Lloret, A. Long-Term Experimental Evidences of Saturation of Compacted Bentonite under Repository Conditions. *Eng. Geol.* **2012**, *149–150*, 57–69. [CrossRef]
29. Bradbury, M.H.; Baeyens, B. Porewater Chemistry in Compacted Re-Saturated MX-80 Bentonite. *J. Contam. Hydrol.* **2003**, *61*, 329–338. [CrossRef] [PubMed]
30. Carlsson, T.; Muurinen, A.; Matusewicz, M.; Root, A. Porewater in Compacted Water-Saturated MX-80 Bentonite. *MRS Online Proc. Libr.* **2012**, *1475*, 397–402. [CrossRef]
31. Bohác, P.; Delavernhe, L.; Zervas, E.; Königer, F.; Schuhmann, R.; Emmerich, K. Cation Exchange Capacity of Bentonite in a Saline Environment. *Appl. Geochem.* **2019**, *100*, 407–413. [CrossRef]
32. Hadi, J.; Tournassat, C.; Ignatiadis, I.; Greneche, J.M.; Charlet, L. Modelling CEC Variations versus Structural Iron Reduction Levels in Dioctahedral Smectites. Existing Approaches, New Data and Model Refinements. *J. Colloid Interface Sci.* **2013**, *407*, 397–409. [CrossRef] [PubMed]
33. Brigatti, M.F.; Galán, E.; Theng, B.K.G. Chapter 2—Structure and Mineralogy of Clay Minerals. In *Developments in Clay Science*; Bergaya, F., Lagaly, G., Eds.; Elsevier: Amsterdam, The Netherlands, 2013; Volume 5, pp. 21–81. ISBN 1572-4352.
34. Kale, R.C.; Ravi, K. A Review on the Impact of Thermal History on Compacted Bentonite in the Context of Nuclear Waste Management. *Environ. Technol. Innov.* **2021**, *23*, 101728. [CrossRef]
35. Laloui, L.; Ferrari, A.; Bosch, J.A. Bentonite Clay Barriers in Nuclear Waste Repositories. *E3S Web Conf.* **2020**, *205*, 01003. [CrossRef]
36. Wersin, P.; Hadi, J.; Jenni, A.; Svensson, D.; Grenèche, J.-M.; Sellin, P.; Leupin, O.X. Interaction of Corroding Iron with Eight Bentonites in the Alternative Buffer Materials Field Experiment (ABM2). *Minerals* **2021**, *11*, 907. [CrossRef]
37. Mosser-Ruck, R.; Cathelineau, M.; Guillaume, D.; Charpentier, D.; Rousset, D.; Barres, O.; Michau, N. Effects of Temperature, pH, and Iron/Clay and Liquid/Clay Ratios on Experimental Conversion of Dioctahedral Smectite to Berthierine, Chlorite, Vermiculite, or Saponite. *Clays Clay Miner.* **2010**, *58*, 280–291. [CrossRef]
38. Chaparro, M.C.; Finck, N.; Metz, V.; Geckeis, H. Reactive Transport Modelling of the Long-Term Interaction between Carbon Steel and MX-80 Bentonite at 25 °C. *Minerals* **2021**, *11*, 1272. [CrossRef]
39. Pignatelli, I.; Bourdelle, F.; Bartier, D.; Mosser-Ruck, R.; Truche, L.; Mugnaioli, E.; Michau, N. Iron–Clay Interactions: Detailed Study of the Mineralogical Transformation of Claystone with Emphasis on the Formation of Iron-Rich T–O Phyllosilicates in a Step-by-Step Cooling Experiment from 90 °C to 40 °C. *Chem. Geol.* **2014**, *387*, 1–11. [CrossRef]
40. Bourdelle, F.; Mosser-Ruck, R.; Truche, L.; Lorgeoux, C.; Pignatelli, I.; Michau, N. A New View on Iron-Claystone Interactions under Hydrothermal Conditions (90 °C) by Monitoring in Situ pH Evolution and H2 Generation. *Chem. Geol.* **2017**, *466*, 600–607. [CrossRef]
41. Kaufhold, S.; Dohrmann, R.; Sandén, T.; Sellin, P.; Svensson, D. Mineralogical Investigations of the First Package of the Alternative Buffer Material Test—I. Alteration of Bentonites. *Clay Miner.* **2013**, *48*, 199–213. [CrossRef]
42. Dohrmann, R.; Kaufhold, S. Characterization of the Second Package of the Alternative Buffer Material (ABM) Experiment—II Exchangeable Cation Population Rearrangement. *Clays Clay Miner.* **2017**, *65*, 104–121. [CrossRef]
43. Fernández, A.M.; Kaufhold, S.; Sánchez-Ledesma, D.M.; Rey, J.J.; Melón, A.; Robredo, L.M.; Fernández, S.; Labajo, M.A.; Clavero, M.A. Evolution of the THC Conditions in the FEBEX in Situ Test after 18 Years of Experiment: Smectite Crystallochemical Modifications after Interactions of the Bentonite with a C-Steel Heater at 100 °C. *Appl. Geochem.* **2018**, *98*, 152–171. [CrossRef]
44. Svensson, D. Saponite Formation in the ABM2 Iron-Bentonite Field Experiment at Äspö Hard Rock Laboratory, Sweden. In Proceedings of the 8th International Conference on Clays in Natural and Engineered Barriers for Radioactive Waste Confinement, Brussels, Belgium, 23–26 March 2015; pp. 168–169.
45. Savage, D.; Watson, C.; Benbow, S.; Wilson, J. Modelling Iron-Bentonite Interactions. *Appl. Clay Sci.* **2010**, *47*, 91–98. [CrossRef]
46. Wilson, J.; Cressey, G.; Cressey, B.; Cuadros, J.; Ragnarsdottir, K.V.; Savage, D.; Shibata, M. The Effect of Iron on Montmorillonite Stability. (II) Experimental Investigation. *Geochim. Cosmochim. Acta* **2006**, *70*, 323–336. [CrossRef]
47. Wilson, J.; Savage, D.; Cuadros, J.; Shibata, M.; Ragnarsdottir, K.V. The Effect of Iron on Montmorillonite Stability. (I) Background and Thermodynamic Considerations. *Geochim. Cosmochim. Acta* **2006**, *70*, 306–322. [CrossRef]

48. Wilson, J.C.; Benbow, S.; Sasamoto, H.; Savage, D.; Watson, C. Thermodynamic and Fully-Coupled Reactive Transport Models of a Steel–Bentonite Interface. *Appl. Geochem.* **2015**, *61*, 10–28. [CrossRef]
49. Wersin, P.; Johnson, L.H.; McKinley, I.G. Performance of the Bentonite Barrier at Temperatures beyond 100 °C: A Critical Review. *Phys. Chem. Earth Parts A/B/C* **2007**, *32*, 780–788. [CrossRef]
50. Al Dabbas, A.; Kopecsko, K. Corrosion of ISG by Mg-Si Precipitation in Presence of Ankerite. *Pollack Period.* **2022**, *17*, 56–61. [CrossRef]
51. Cuevas, J.; Ruiz, A.I.; Fernández, R.; Torres, E.; Escribano, A.; Regadío, M.; Turrero, M.J. Lime Mortar-Compacted Bentonite–Magnetite Interfaces: An Experimental Study Focused on the Understanding of the EBS Long-Term Performance for High-Level Nuclear Waste Isolation DGR Concept. *Appl. Clay Sci.* **2016**, *124–125*, 79–93. [CrossRef]
52. Fernández, R.; Mäder, U.K.; Rodríguez, M.; Vigil de la Villa, R.; Cuevas, J. Alteration of Compacted Bentonite by Diffusion of Highly Alkaline Solutions. *Eur. J. Mineral.* **2009**, *21*, 725–735. [CrossRef]
53. Mota-Heredia, C.; Cuevas, J.; Ruiz, A.I.; Ortega, A.; Torres, E.; Turrero, M.J.; Fernández, R. Geochemical Interactions at the Steel-Bentonite Interface Caused by a Hydrothermal Gradient. *Appl. Clay Sci.* **2023**, *240*, 106984. [CrossRef]
54. Caballero, E.; Jiménez de Cisneros, C.; Huertas, F.J.; Huertas, F.; Pozzuoli, A.; Linares, J. Bentonites from Cabo de Gata, Almeria, Spain: A Mineralogical and Geochemical Overview. *Clay Miner.* **2005**, *40*, 463–480. [CrossRef]
55. Fernández, A.M.; Baeyens, B.; Bradbury, M.; Rivas, P. Analysis of the Porewater Chemical Composition of a Spanish Compacted Bentonite Used in an Engineered Barrier. *Phys. Chem. Earth* **2004**, *29*, 105–118. [CrossRef]
56. FEBEX. *Bentonite: Origin, Properties and Fabrication of Blocks*; ENRESA: Madrid, Spain, 1998; Volume PT-4/98.
57. Cuevas, J.; Cabrera, M.Á.; Fernández, C.; Mota-Heredia, C.; Fernández, R.; Torres, E.; Turrero, M.J.; Ruiz, A.I. Bentonite Powder XRD Quantitative Analysis Using Rietveld Refinement: Revisiting and Updating Bulk Semiquantitative Mineralogical Compositions. *Minerals* **2022**, *12*, 772. [CrossRef]
58. Meier, L.P.; Kahr, G. Determination of the Cation Exchange Capacity (CEC) of Clay Minerals Using the Complex of Copper (II) Ion with Triethylenetetramine and Tetraethylenepentamine. *Clays Clay Miner.* **1999**, *47*, 386–388. [CrossRef]
59. Ammann, L.; Bergaya, F.; Lagaly, G. Determination of the Cation Exchange Capacity of Clays with Copper Complexes Revisited. *Clay Miner.* **2005**, *40*, 441–455. [CrossRef]
60. Stucki, J.W. The Quantitative Assay of Minerals for Fe^{2+} and Fe^{3+} Using 1,10-Phenanthroline: II. A Photochemical Method. *Soil Sci. Soc. Am. J.* **1981**, *45*, 638–641. [CrossRef]
61. Stucki–, J.W.; Anderson, W.L. The Quantitative Assay of Minerals for Fe^{2+} and Fe^{3+} Using 1,10-Phenanthroline: I. Sources of Variability. *Soil Sci. Soc. Am. J.* **1981**, *45*, 633–637. [CrossRef]
62. Trincal, V.; Lanari, P. Al-Free Di-Trioctahedral Substitution in Chlorite and a Ferri-Sudoite End-Member. *Clay Miner.* **2016**, *51*, 675–689. [CrossRef]
63. Masci, L.; Dubacq, B.; Verlaguet, A.; Chopin, C.; De Andrade, V.; Herviou, C. A XANES and EPMA Study of Fe^{3+} in Chlorite: Importance of Oxychlorite and Implications for Cation Site Distribution and Thermobarometry. *Am. Mineral.* **2019**, *104*, 403–417. [CrossRef]
64. Cuevas, J.; Ruiz, A.; Fernández, R. Investigating the Potential Barrier Function of Nanostructured Materials Formed in Engineered Barrier Systems (EBS) Designed for Nuclear Waste Isolation. *Chem. Rec.* **2018**, *18*, 1065–1075. [CrossRef]
65. Jeans, C.V. MOORE, D. M. & REYNOLDS, R. C., Jr. 1997. X-ray Diffraction and the Identification and Analysis of Clay Minerals, 2nd Ed. Xviii + 378 pp. Oxford, New York: Oxford University Press. Price £27.95 (Spiral-Bound Paperback). ISBN 0 19 508713 5. *Geol. Mag.* **1998**, *135*, 819–842. [CrossRef]
66. Cuevas, J.; Villar, M.V.; Martín, M.; Cobeña, J.C.; Leguey, S. Thermo-Hydraulic Gradients on Bentonite: Distribution of Soluble Salts, Microstructure and Modification of the Hydraulic and Mechanical Behaviour. *Appl. Clay Sci.* **2002**, *22*, 25–38. [CrossRef]
67. Guillaume, D.; Neaman, A.; Cathelineau, M.; Mosser-Ruck, R.; Peiffert, C.; Abdelmoula, M.; Dubessy, J.; Villiéras, F.; Baronnet, A.; Michau, N. Experimental Synthesis of Chlorite from Smectite at 300 °C in the Presence of Metallic Fe. *Clay Miner.* **2003**, *38*, 281–302. [CrossRef]
68. Dohrmann, R.; Kaufhold, S. Cation Exchange and Mineral Reactions Observed in MX 80 Buffer Samples of the Prototype Repository In Situ Experiment in Äspö, Sweden. *Clays Clay Miner.* **2014**, *62*, 357–373. [CrossRef]
69. Sudheer Kumar, R.; Podlech, C.; Grathoff, G.; Warr, L.N.; Svensson, D. Thermally Induced Bentonite Alterations in the SKB ABM5 Hot Bentonite Experiment. *Minerals* **2021**, *11*, 1017. [CrossRef]
70. Kaufhold, S.; Schippers, A.; Marx, A.; Dohrmann, R. SEM Study of the Early Stages of Fe-Bentonite Corrosion—The Role of Naturally Present Reactive Silica. *Corros. Sci.* **2020**, *171*, 108716. [CrossRef]
71. Uyama, M.; Hitomi, T.; Hayagane, S.; Kadota, N.; Saito, H.; Okamoto, S.; Aoshima, K.; Osawa, M. Analysis of Corrosion Mechanisms of Carbon Steel in Contact with FEBEX Bentonite. *Geol. Soc. Lond. Spec. Publ.* **2019**, *482*, 301–312. [CrossRef]
72. Hadi, J.; Wersin, P.; Serneels, V.; Greneche, J.-M. Eighteen Years of Steel–Bentonite Interaction in the FEBEX in Situ Test at the Grimsel Test Site in Switzerland. *Clays Clay Miner.* **2019**, *67*, 111–131. [CrossRef]
73. Hadi, J.; Wersin, P.; Jenni, A.; Greneche, J.M. *Redox Evolution and Fe-Bentonite Interaction in the ABM2 Experiment, Äspö Hard Rock Laboratory*; Nagra: Wettingen, Switzerland, 2017; p. 330.
74. Wersin, P.; Jenni, A.; Mäder, U.K. Interaction of Corroding Iron with Bentonite in the ABM1 Experiment at Äspö, Sweden: A Microscopic Approach. *Clays Clay Miner.* **2015**, *63*, 51–68. [CrossRef]

75. Wersin, P.; Hadi, J.; Kiczka, M.; Jenni, A.; Greneche, J.-M.; Diomidis, N.; Leupin, O.; Svensson, D.; Smart, N.; Zhang, Z. Unravelling the Corrosion Processes at Steel/Bentonite Interfaces in in Situ Tests. *Mater. Corros.* **2023**, *74*, 1716–1727. [CrossRef]
76. Schlegel, M.L.; Martin, F.; Fenart, M.; Blanc, C.; Varlet, J.; Foy, E.; Prêt, D.; Trcera, N. Corrosion at the Carbon Steel-Clay Compact Interface at 90 °C: Insight into Short- and Long-Term Corrosion Aspects. *Corros. Sci.* **2019**, *152*, 31–44. [CrossRef]
77. Robinson, T.C.; Latta, D.E.; Leddy, J.; Scherer, M.M. Redox Potentials of Magnetite Suspensions under Reducing Conditions. *Environ. Sci. Technol.* **2022**, *56*, 17454–17461. [CrossRef]

Disclaimer/Publisher's Note: The statements, opinions and data contained in all publications are solely those of the individual author(s) and contributor(s) and not of MDPI and/or the editor(s). MDPI and/or the editor(s) disclaim responsibility for any injury to people or property resulting from any ideas, methods, instructions or products referred to in the content.

applied sciences

MDPI

Article

Influence of Warm Mix Asphalt Additives on the Physical Characteristics of Crumb Rubber Asphalt Binders

Munder Bilema [1,2,*], Choon Wah Yuen [1,2], Mohammad Alharthai [3,4], Zaid Hazim Al-Saffar [5], Salam Ridha Oleiwi Aletba [6] and Nur Izzi Md Yusoff [7]

[1] Centre for Transportation Research, Universiti Malaya, Kuala Lumpur 50603, Malaysia; yuencw@um.edu.my
[2] Department of Civil Engineering, Faculty of Engineering, Universiti Malaya, Kuala Lumpur 50603, Malaysia
[3] Department of Civil Engineering, Najran University, Najran 66462, Saudi Arabia; maalharthai@nu.edu.sa
[4] Science and Engineering Research Center, Najran University, Najran 66462, Saudi Arabia
[5] Building and Construction Engineering Department, Engineering Technical College of Mosul, Northern Technical University, Mosul 41002, Iraq; zaid.alsaffar@ntu.edu.iq
[6] Civil Engineering Department, University of Technology-Iraq, Alsina'a Street, Baghdad 10066, Iraq; 40372@uotechnology.edu.iq
[7] Department of Civil Engineering, Universiti Kebangsaan Malaysia, Bangi 43600, Selangor, Malaysia; izzi@ukm.edu.my
* Correspondence: munderbilema@um.edu.my or munderbilema@gmail.com

Abstract: This investigation is centered around the application of warm mix asphalt (WMA) technologies to address workability concerns linked to rubberized asphalt binders. The primary aim of incorporating crumb rubber (CR) and WMA additives is to establish a robust paving method that fosters energy conservation, efficient waste management, noise reduction, and improved overall performance. The current study aims to comprehensively characterize and differentiate the physical attributes of rubberized asphalt binders by employing three distinct WMA additives: Sasobit, Cecabase RT and Rediset WMX. These additives are introduced into eight unique asphalt binders. Laboratory assessments are carried out to evaluate the workability and physical properties of these binders. The evaluation encompasses penetration, softening point, penetration index, penetration viscosity number, storage stability, ductility, viscosity, and stiffness modulus analyses. The findings indicate that the rubberized asphalt binder enhanced with Sasobit demonstrates the highest levels of both hardness and softening point in comparison to asphalt binders supplemented with alternative WMA additives. The evaluation of storage stability underscores the satisfactory stability across all modified asphalt binders. Both the unmodified and modified binders meet the requirements stipulated by the ductility test; the rubberized asphalt binder modified with Rediset falls short. The rubberized asphalt binder improved with Sasobit displays the most notable enhancement in workability. Furthermore, the blend of crumb rubber and Sasobit binder reveals the highest stiffness modulus values under conditions of intermediate and high temperatures with 1.88 and 0.46 MPa, respectively. In summation, the rubberized asphalt binder incorporating crumb rubber with Sasobit showcases superior improvements in both stiffness and workability compared to counterparts modified with Cecabase RT and Rediset WMX.

Keywords: warm mix asphalt (WMA); crumb rubber (CR); WMA additives; physical properties; workability; stiffness modulus

1. Introduction

Authorities across the globe are dealing with limited budgets for constructing and maintaining infrastructures by implementing cost-saving strategies that utilize recycled materials [1,2]. Pavement researchers are still looking for cost-effective solutions that reduce project expenditures by incorporating waste material into road pavements [3]. Several studies have examined the performances of pavements modified with waste materials,

including recycled asphalt shingles (RAS), reclaimed asphalt pavement (RAP), glass, steel slag, waste frying oil (WFO), waste engine oil (WEO), and crumb rubber (CR) [4–7].

The rapid growth of the automotive sector and the number of vehicles on the road each year has increased the demand for tires. Globally, 1.5 billion tires are produced, and 4.0 billion tires are disposed of annually [8]. The decomposition of discarded tires, sometimes known as black pollution, could be worse than plastic or white pollution. The thermosetting nature of natural and synthetic rubbers, which seldom degrade in typical climate conditions, makes scrap tire disposal challenging. The conventional methods for disposing of waste tires are landfilling and burning. The landfilling of scrap tires poses health risks and can cause unintentional fires, while burning scrap tires pollutes the environment. In short, waste tire dumping causes environmental, economic, health, and social issues [9]. Recycling scrap tires in asphalt pavements is a cost-effective and environmentally responsible approach to disposing of these waste materials [10,11]. The usage of crumb rubber (CR) is advantageous for environmental reasons (i.e., noise isolation). The exposure to emissions in asphalt-rubber production was the same as in traditional asphalt production. Moreover, in comparison to the influence of other factors, the effect of CRM on emissions may be minimal. The dryer's fueling rate, mix temperature, asphalt throughput rate, and binder content are some of those factors [12].

The wet and dry methods exist for integrating crumb rubber into asphalt pavements [13,14]. Wet bitumen modification techniques involve blending the asphalt binder and CR at temperatures between 160 °C and 200 °C, adhering to specific shear rates and durations [15]. At these elevated temperatures, crumb rubber particles rapidly expand due to the absorption of the lighter components of the bitumen during mixing [16]. The incorporation of crumb rubber into asphalt binders significantly enhances the characteristics of the modified binder. Various factors, including raw material properties and interaction conditions, exert an influence on the properties of rubberized binders. Researchers have extensively employed CR to ameliorate the performance of rubberized asphalt pavements while upholding environmental considerations [17]. CR-modified asphalt binders exhibit augmented viscosity, heightened resistance to rutting, cracking, and moisture susceptibility, as well as elevated manufacturing and laying temperatures (approximately 10 °C) in comparison to conventional blends [18]. However, challenges associated with CR-modified asphalt pavements encompass reduced workability and heightened temperature prerequisites at asphalt manufacturing facilities [19]. Recent studies have concentrated on mitigating production and laying temperatures and enhancing workability. On the other hand, the absence of a universally standardized warm mix asphalt (WMA) mix design underscores the necessity to comprehend the fundamental mechanisms through which additives operate within the mixture. The insufficiency of information concerning the capabilities and dynamics of WMA, prevalent in various global regions, is attributed to factors such as the variation in WMA additives, suggested quantities, and technological approaches. This knowledge gap can be attributed in part to the limited understanding of WMA additives, which impedes the cultivation of expertise in WMA practices among industry professionals [20].

In recent years, warm mix asphalt has been gaining popularity due to its benefits, including reduced fossil fuel consumption, reduced greenhouse gas emissions, lower manufacturing, and laying temperatures [20]. Many studies and field cases have demonstrated the eco-friendliness, superior performance, and economic benefits of WMA technologies, such as improved compaction and mixing temperatures, longer hauling distances, and paving workability [18,21], which contributed to the rapid increase of its market share. In the United States, WMA asphalt made up about 38.9% of the total paving, the equivalent of 147.4 million tons in 2017 [22]. There was a 26% increase in WMA output between 2016 and 2017. The production in Europe, Japan, Canada, and South Africa is still insufficient. The data from the European Asphalt Pavement Association showed that, between 2013 and 2017, several European countries allowed the use of WMA, which leads to increasing use of WMA technology year after year [18].

In recent studies, three distinct WMA techniques have been devised: (a) utilization of foaming additives, (b) incorporation of chemical additives (surfactants), and (c) inclusion of non-foaming additives. Recent examinations conducted in both laboratory settings and in the field have demonstrated that pavements constructed using WMA exhibit equivalent or improved performance compared to those constructed using hot mix asphalt (HMA) [23]. Researchers have observed that the introduction of additives for WMA into asphalt blends leads to a notable reduction in the temperatures required for mixing and compaction, with temperature decreases ranging between 20 °C and 40 °C [19,24]. WMA technologies that employ fluidifying additives to lower the viscosity of bitumen during mixture production temperatures, while upholding bitumen functionality, offer a potential resolution to challenges linked with crumb rubber-modified (CRM) binders. Incorporating WMA additives into CR asphalt binders has shown the potential to decrease mixing and compaction temperatures by 15 to 30 °C [25,26]. Numerous WMA additives have demonstrated the capacity to lower the production temperature of rubberized binder mixtures by reducing viscosity and enhancing the workability of the rubberized binder [27,28]. A sustainable paving approach has been developed by researchers, involving the use of WMA asphalt to modify rubberized asphalt binders, thereby contributing to environmental preservation and performance enhancement [29]. The integration of Sasobit into the rubberized binder leads to a decrease in the high-temperature viscosity and low-temperature ductility of rubber asphalt, while also resulting in an increase in the softening point. This combination of effects is beneficial for enhancing workability and promoting high-temperature stability [30]. In a prior investigation conducted by Sesay et al. [31], a comparative analysis was carried out involving three distinct WMA additives: Sasobit, Rediset, and Alube. These additives were introduced into the rubberized asphalt binder to assess their influence on high and intermediate temperature performance. The study revealed that the rubberized asphalt binder incorporating Sasobit exhibited superior high-temperature performance in comparison to the rubberized asphalt binder with Alube. Conversely, concerning intermediate-temperature performance, the rubberized asphalt binder with Rediset displayed the most favorable outcomes.

The available literature reveals a dearth of investigations concerning the collective impact of various CR asphalt binders modified with optimal quantities of WMA additives. Addressing this gap, the present study aims to investigate the physical attributes of diverse CR binders, each modified with Sasobit, Rediset, and Cecabase. The aim of this investigation is to identify a suitable WMA additive that enhances the workability of the rubberized binder while maintaining a stiffness value higher than that of the original asphalt binder.

2. Material and Methods

2.1. Asphalt Binder

The bitumen binder employed in this research possesses a 60/70 penetration grade and is supplied by the Kemaman Bitumen Company Sdn. Bhd, Selangor, Malaysia. This binder boasts a flash point of 240 °C and a density of 1.02 gm/cm^3.

2.2. Crumb Rubber

The Malaysian supplier, Miroad Rubber Industries Sdn Bhd, furnishes crumb rubber powder with a mesh size of 20 (passing 0.15 mm). The crumb rubber modifier (CRM) is manufactured through a process of mechanical shredding followed by grinding at ambient temperature.

2.3. WMA Additives

This research used three warm mix additives, an organic additive (Sasobit), and two chemical additives (Rediset WMX and Cacebase). The dosage of the WMA additives followed the recommendations of previous studies [32–34]. Figure 1 shows all warm mix asphalt additives and crumb rubber used in this study. Table 1 shows the physical characteristics of the warm mix asphalt additives used in this research.

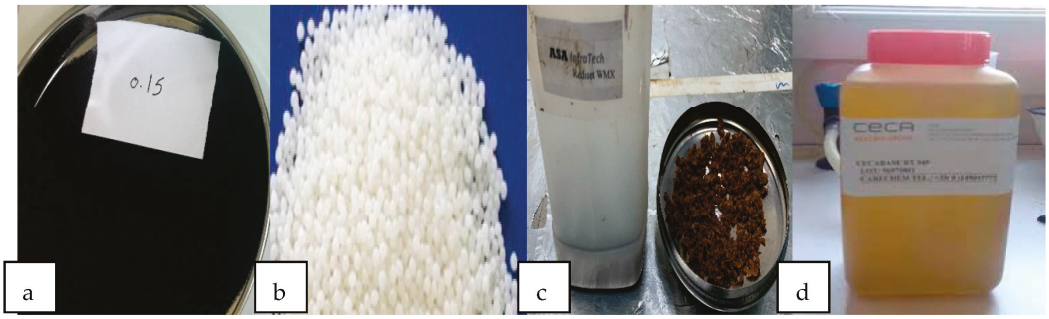


Figure 1. The additives used in this research. (**a**) Crumb rubber. (**b**) Sasobit. (**c**) Rediset WMX. (**d**) Cecabase.

Table 1. Properties of the WMA additives.

Properties	Sasobit	Cecabase RT 975	Rediset WMX
Appearance at 25 °C	Pastille flakes	Liquid	Pastilles
Density at 25 °C (g/cm^3)	0.9	0.997	0.55
Color	Off-white	Dark amber liquid	Light brown
Melting point (°C)	100–120	-	80–90
Flash point (°C)	285	>200	253

2.3.1. Sasobit

Sasobit, among the pioneering WMA additives, was introduced for pavement production. Its inaugural field trial occurred in Hamburg, Germany in 1997. Sasobit, a synthetic paraffin wax, is synthesized using the Fischer–Tropsch technique, involving the combination of heated coal and natural gas with steam and a catalyst [18]. Its viscosity surpasses that of the binder below its melting point. The manufacturer recommends a dosage range of 0.8% to 3% by weight of the binder [35].

2.3.2. Cecabase RT 975

Cecabase RT 975 is a chemical additive produced by the Arkema Group in France. It is liquid at 25 °C and can reduce the asphalt mixing and laydown temperatures by 20–40 °C. Cecabase RT 975 is one of the most popular liquid WMA additives with a recommended dose of 0.2–0.5% and does not require curing in the mixing process. It is pumped directly into the asphalt mixture or mixed with the asphalt binder [36].

2.3.3. Rediset WMX

Rediset WMX is a blend of organic additives and surface-active chemicals produced by a Dutch firm, Akzo Nobel. Rediset WMX was first proposed in 2007 to resolve the reported flaws in the warm mix asphalts, including the effects of water on warm asphalt mixes and their lower hardness compared to hot mixes, and the unpredictability of their low-temperature characteristics. Rediset WMX is mixed with the asphalt binder or mixture at a dosage of 0.5 to 2.5% by weight of the asphalt binder [34].

2.4. Preparation of the CR Binders Containing the WMA Additives

The virgin asphalt binders were placed in a container and heated in a 110 °C oven for 60 min. The asphalt binder was added with 5% CR for 30 min at 700 rpm and 177 °C. Then, the hot plate was left for five minutes to reach the desired temperature before the next addition, which adjusted the temperature to 120 °C [32]. The required amounts of the WMA additives were added at 1000 rpm and 120 °C for 10 min to ensure that the asphalt binders were sufficiently fluid, uniform, and consistent [37]. The modified binders were placed in the containers for investigation. Table 2 presents the composition of all asphalt binders, and Figure 2 shows the high-shear mixer used to mix the modified asphalt binders.

Table 2. Composition of the modified and virgin asphalt binders.

Binder	ID	Asphalt Binder (%)	Crumb (%)	Warm Mix Additive (%)
Virgin 60/70	V	100	-	-
Crumb rubber	CR	100	5	-
Sasobit	SA	100	-	1.5
Cecabase	CE	100	-	0.44
Rediset	RE	100	-	1.5
Sasobit + crumb rubber	SECR	100	5	1.5
Cecabase + crumb rubber	CECR	100	5	0.44
Rediset + crumb rubber	RECR	100	5	1.5



Figure 2. The high-shear mixer for blending the modified asphalt binders.

2.5. Testing Program

Table 3 summarizes the penetration, softening point, penetration index, storage stability, ductility, loss on heating, and viscosity tests performed in this research to determine the properties of the conventional asphalt binder. The softening point and penetration values were used to compute the penetration index (*PI*) using Formula (1).

$$PI = \frac{1952 - 500loglog\ PEN - 20SP}{50loglog\ PEN - SP - 120}, \quad (1)$$

where *PI* is the penetration index, *PEN* is the penetration value (0.1 mm), and *SP* is the softening point value (°C). The viscosity and penetration values were used to compute the penetration viscosity number (*PVN*) using Formula (2).

$$PVN = \frac{4.258 - 0.7967\ log\ P - loglog\ V}{(0.795 - 0.1858\ log\ P)} \quad (2)$$

where *PVN* is the penetration viscosity number, *V* is the viscosity in centistokes measured at 135 °C (cp), and *P* is the penetration value at 25 °C (0.1 mm).

Table 3. The physical properties tests conducted in this research.

Asphalt Binder Test (Unit)	Test Standard	Specification
Penetration at 25 °C (0.1 mm)	ASTM D5	60–70
Softening point (°C)	ASTM D36	48–52
Penetration index	-	−2 to 2
Penetration viscosity number	-	-
Storage stability (°C)	ASTM D5892	<2.2
Ductility at 25 °C (cm)	ASTM D113	Min. 100
Loss on heating (%)	AASHTO T240	Max. 1.00
Viscosity at 120 and 135 °C (cp)	ASTM D4402	-
Stiffness modulus (MPa)	-	-

Van der Poel [38] introduced the concept of stiffness modulus, which represents the ratio between a consistent uniaxial stress and the resultant uniaxial strain at a specified time. By examining the outcomes of tests conducted on 47 bitumens, Van der Poel constructed a graphical tool, known as a nomograph, designed to ascertain the stiffness of asphalt binder, accounting for temperature and loading time (or frequency), given knowledge of the softening temperature and penetration. For the practical determination of binder stiffness, the BitProps program is a useful tool. This program utilizes a digitized version of Van der Poel's nomograph, developed by G. Rowe and M. Sharrock [39], facilitating the ease of calculation. The study evaluated the stiffness characteristics of eight distinct asphalt binders, both unmodified and modified, across varying temperature conditions: low, intermediate, and high. This assessment employed five distinct loading scenarios, considering outcomes from penetration and softening point tests. The selected temperatures for this investigation corresponded to the low, intermediate, and high temperature ranges observed in Kuala Lumpur, Malaysia. Figure 3 shows the flowchart of the research.

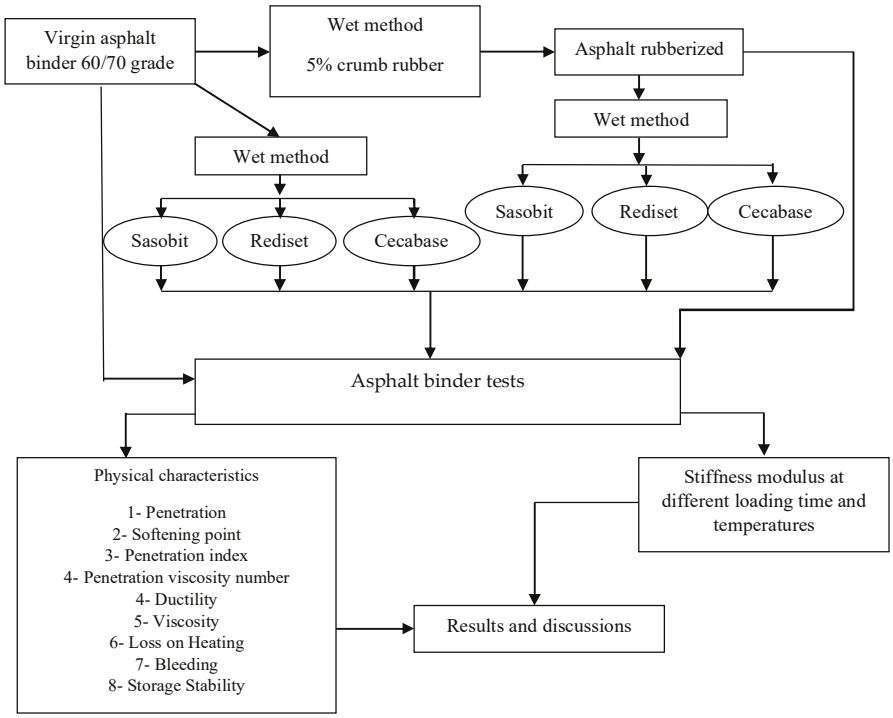


Figure 3. The flowchart of the study.

3. Results and Discussion

3.1. Penetration

The assessment of asphalt binder characteristics involves multiple tests to determine their properties. Figure 4 illustrates the penetration values of various asphalt binders at 25 °C, which serve as an indicator of their hardness or softness. A lower penetration value in CR asphalt binders corresponds to increased hardness. Previous research [40] highlighted that introducing crumb rubber into asphalt binders led to a significant reduction in penetration values, contingent on CR content. Among WMA additives, Cecabase exhibited minimal impact on asphalt binder hardness, with the modified binder's penetration value aligning closely with that of the virgin binder. This was confirmed by Awazhar et al. [41], who noted Cecabase's limited influence on penetration values. In contrast, Sasobit and Rediset exerted more substantial effects on asphalt binder hardness than Cecabase. The liquid form of Cecabase had minimal impact on the hardness of the CECR asphalt binder. The SECR asphalt binder demonstrated the lowest penetration value due to the combined influence of Sasobit and crumb rubber, which augmented the binder's hardness. Bilema et al. [37] reported comparable findings regarding the combined effect of crumb rubber and Sasobit on penetration values, consistent with our current study.

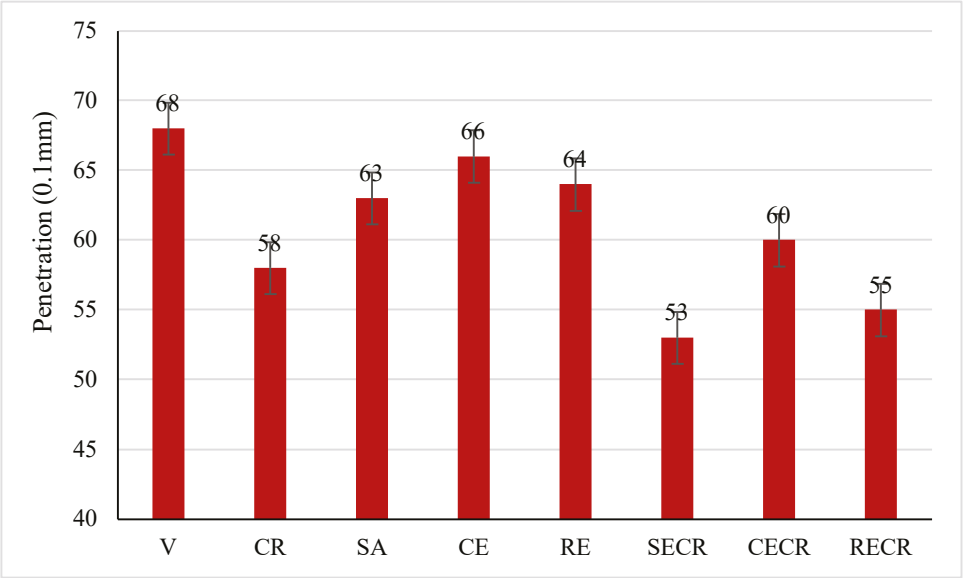


Figure 4. The penetration of the asphalt binders.

3.2. Softening Point

The outcome of the softening point test, presented in Figure 5, reveals the temperature at which asphalt binders transition from semi-solid to soft states. Higher softening points are preferable for greater resilience in warm conditions. CR-modified asphalt binders exhibited higher penetration values, aligning with previous research [42]. Among WMA additives, Cecabase demonstrated the lowest softening point (47.5 °C), while Sasobit exhibited the highest (50.5 °C). The CECR asphalt binder displayed a relatively low softening point, whereas the SECR binder exhibited the highest value (54 °C), attributed to the combined influence of crumb rubber and Sasobit, resulting in higher melting temperatures. Kök et al. [43] obtained similar results, concluding that Sasobit enhanced softening points. In a preceding study undertaken by Akpolat [44], it was determined that the incorporation of Sasobit additive in combination with CR leads to an elevation in the value of softening points. This concurs with the findings observed in the current research.

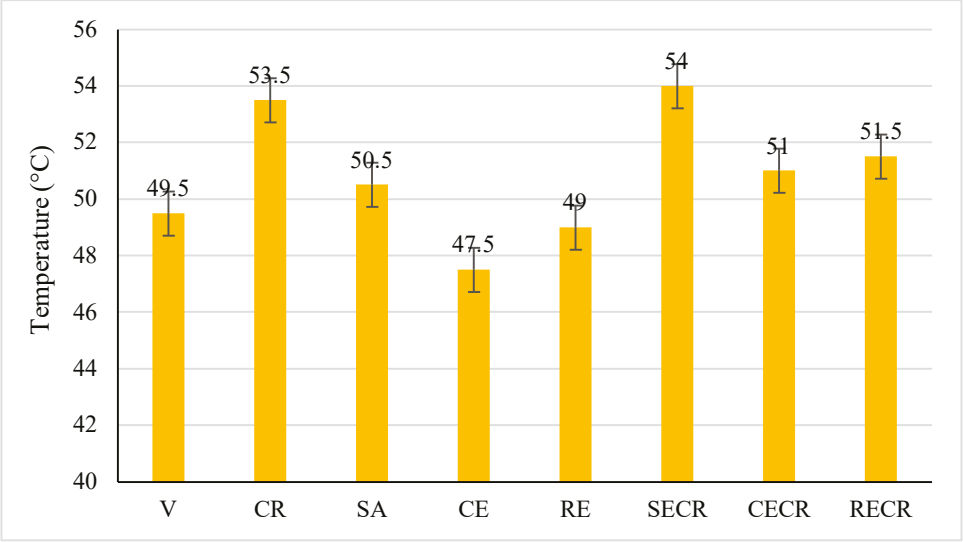


Figure 5. The softening point result of the asphalt binders.

3.3. Viscosity

The Brookfield rotational viscosity test gauges asphalt binder workability at temperatures of 120 and 135 °C, determining their capacity to withstand shear forces. Figure 6 displays viscosities for virgin and modified asphalt binders. At the higher test temperature of 135 °C, asphalt binders demonstrated reduced viscosity values. CR asphalt binders exhibited the highest viscosity values at both temperatures, attributed to crumb rubber particle behavior. Elevated viscosity of aged binders can decline asphalt mixture workability, causing reduced adhesion between aggregates and binders [45]. Higher viscosity demands elevated laying, compaction, and mixing temperatures, consuming more energy, as noted by Sengoz and Isikyakar [46]. WMA additives lowered viscosities across asphalt binders. Sasobit had the most significant influence on binder workability, whereas Rediset had a limited effect. Viscosity in all asphalt binders, with crumb rubber and WMA additives, was akin to virgin asphalt binders. SECR asphalt binder exhibited the lowest viscosity values at both temperatures due to Sasobit's substantial workability enhancement, consistent with Veeraiah and Nagabhushanarao's findings [47].

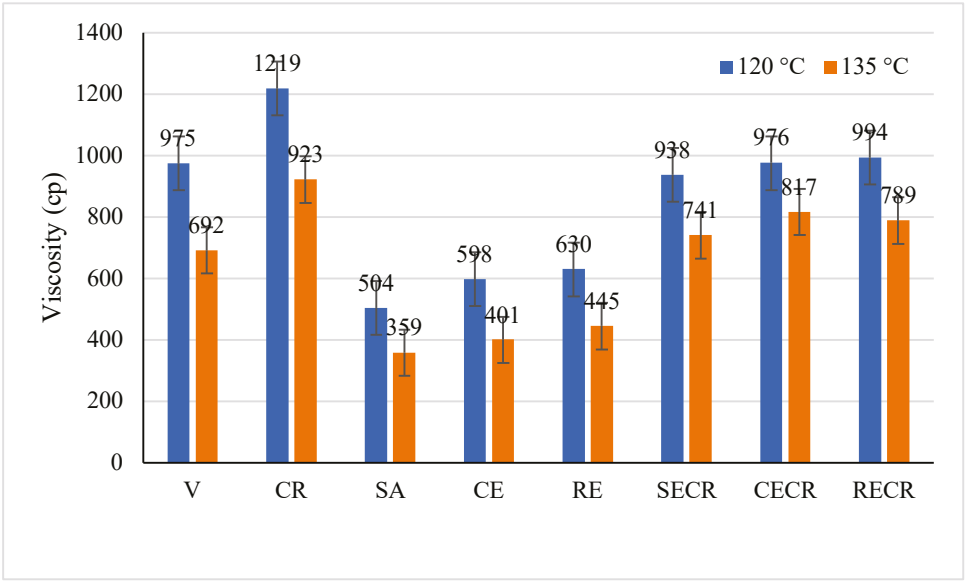


Figure 6. The viscosity of the asphalt binders at 120 and 135 °C.

3.4. Temperature Susceptibility

Temperature susceptibility of modified asphalt binders was assessed using the penetration index (*PI*) and penetration viscosity number (*PVN*) based on penetration and softening point at 25 °C and viscosity at 135 °C. Higher *PI* and *PVN* values indicated reduced temperature susceptibility. *PI* classified asphalt binder type and suitability for highway construction, while *PVN* gauged temperature susceptibility. The findings in Table 4 indicate that both *PI* and *PVN* values increased with crumb rubber addition, signifying lower temperature susceptibility in CR asphalt binders. Except for Sasobit, WMA additives displayed similar behavior in raising temperature susceptibility values. Asphalt binders modified with WMA additives and crumb rubber exhibited temperature susceptibility akin to virgin asphalt binders. The utilization of Sasobit in the rubberized asphalt binder leads to an elevation in the PI value, accompanied by a reduction in the *PVN* value. This aligns with the outcomes observed in the present study [48]. Table 4 shows the outcome of the *PVN* and *PI* of all asphalt binders in the study.

Table 4. The PI and PVN for all asphalt binders.

ID	PI	PVN
V	−0.54	−0.06
CR	0.04	0.39
SA	−0.49	−0.92
CE	−1.17	−0.69
RE	−0.83	−0.59
SECR	−0.02	0.004
CECR	−0.48	0.23
RECR	−0.62	0.07

3.5. Storage Stability

The storage stability test, depicted in Figure 7, was conducted to assess the success of binder modification and its stability during storage. Acceptable storage stability demands a minimal temperature difference between sample top and bottom. All asphalt binders showed adequate stability without significant separation, owing to slight variations in softening points within 2.2 °C. Virgin and WMA-modified asphalt binders exhibited lower storage stability, with a 0.5 °C difference. RECR asphalt binder exhibited the highest storage asphalt due to the crumb rubber's contribution. Elevated crumb rubber content decreased modified binder stability, aligning with prior studies [21].

3.6. Ductility

The outcome of the ductility test, depicted in Figure 8, illustrates the evaluation of asphalt binder flexibility and deformation. The figure indicates that the inclusion of CR resulted in a decrease in asphalt binder ductility. This reduction in ductility was attributed to the absorption of the asphalt binder's oily components by the rubber powder, leading to an increase in the mass of rubber particles. Consequently, the CR asphalt binder exhibited a greater thickness compared to unmodified asphalt binder samples, aligning with the observations made by Mashaan et al. [49]. Across all asphalt binders, the introduction of WMA additives brought about a reduction in ductility. Sasobit had a minimal effect on asphalt binder ductility, while Rediset produced the highest difference in the ductility values. Sedaghat et al. [50] reported that Sasobit reduced the ductility value, which is consistent with the result of this research. The 109 and 101 cm ductility values of the SECR and CECR asphalt binder fulfilled the ductility test requirement. However, the RECR asphalt binder did not meet the ductility test requirement of 98 cm.

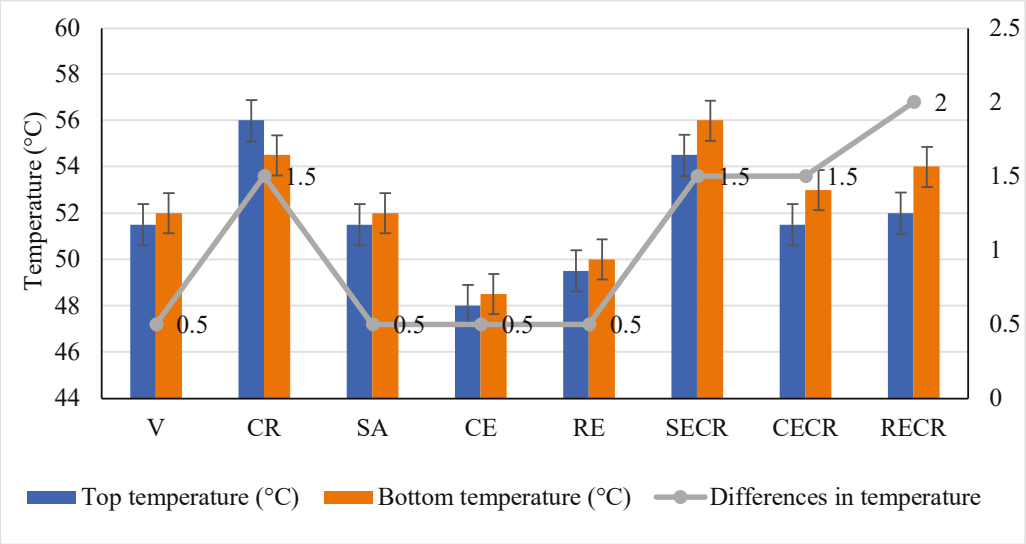


Figure 7. The storage stability of the asphalt binders.

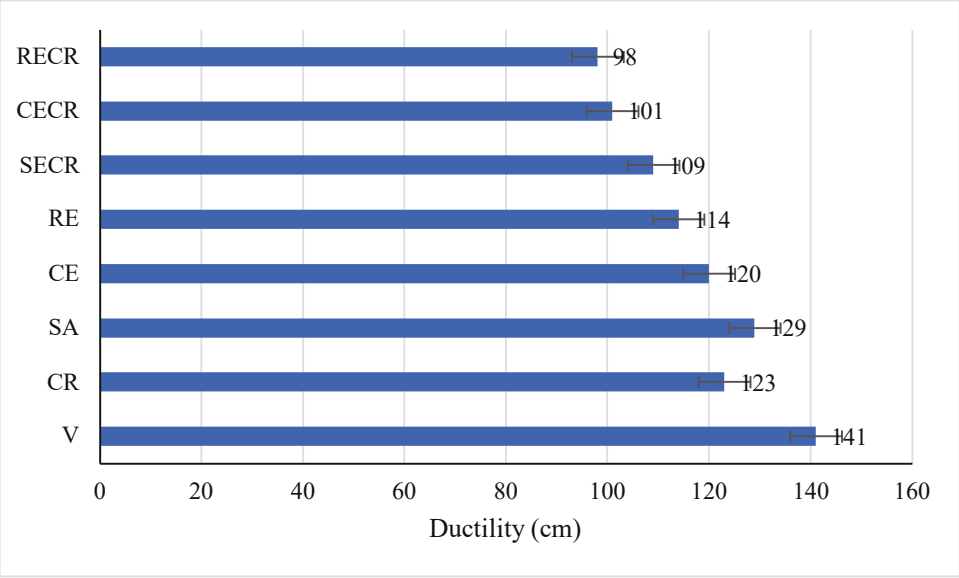


Figure 8. The ductility of the asphalt binders.

3.7. Loss on Heating

This research conducted the Rolling Thin Film Oven (RTFO) test to determine the mass loss on heating when the samples were exposed to high temperatures and pressures. The impurities and particles in the asphalt binders became volatile and escaped into the air at high temperatures, causing the asphalt binder to lose some mass. Loss on heating is a critical factor since a considerable loss on heating can cause problems with the asphalt binder's workability. The loss on heating typically ranges from 0.05 to 0.5%, and the maximum loss on heating is 1.0%. Figure 9 presents the loss on heating for all asphalt binders. All asphalt binders in this study fulfilled the 0.05 to 0.5% requirement for the loss on heating test and showed a lower loss on heating than the virgin asphalt binder since the blending process exposed them to a high temperature for a particular period. In a prior investigation conducted by Li et al. [48], it was determined that various dosages of rubberized asphalt binder and Sasobit yielded comparable outcomes to the original asphalt binder, as the percentages fell within the designated test range. These findings correspond harmoniously with the results observed in the current study.

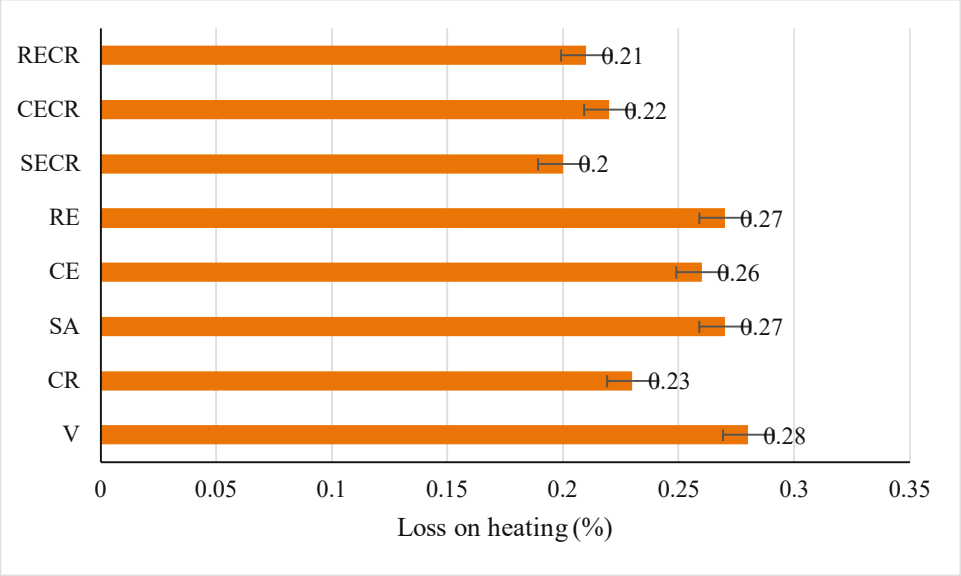


Figure 9. The loss on heating for the asphalt binders.

3.8. Stiffness Modulus

Table 5 presents two predominant patterns: as test temperatures rise, stiffness values decline, whereas stiffness values increase as loading time decreases. Notably, at a loading time of 10 s, the SECR exhibits the most elevated stiffness modulus figures under intermediate and low temperatures, measuring 0.07 and 0.49 MPa, respectively. Conversely, the CE displays the least stiffness among all unmodified and modified asphalt binders at intermediate temperatures, registering 0.03 MPa. Similar trends in stiffness modulus emerge at loading times of 5, 1, and 0.5 s, mirroring the observations at a 10 s loading time. At the lowest loading times and temperatures explored in this study, modified asphalt binders manifest distinct behavior. Specifically, the RECR demonstrates the highest stiffness values at low temperatures, reaching 11.31 MPa. Among the warm mix asphalt additives without crumb rubber, Sasobit records the highest stiffness values across all temperatures and loading times, except at low temperatures and loading times of 0.5 and 0.1 s, where stiffness values for CE measure 3.23 and 9.93 MPa, respectively. Comparable stiffness values are observed between RECR and SECR. The influence of loading time on stiffness values is evident from the data in Table 5, revealing a notable impact. Reducing the loading time enables a deeper exploration of asphalt binder stiffness behavior. The presence of crumb rubber yields higher stiffness values compared to warm mix asphalt additives, attributed to the combination of low penetration and elevated softening point values. Table 5 shows stiffness modulus values for virgin and modified asphalt binders at different loading times and temperatures.

Table 5. The stiffness modulus for unmodified and modified asphalt binders.

Asphalt ID	Stiffness (MPa) at Loading Time: 10 (s)		
	High Temperature	Intermediate Temperature	Low Temperature
V	0.01	0.04	0.31
CR	0.01	0.06	0.43
SA	0.01	0.05	0.36
CE	0.00	0.03	0.31
RE	0.01	0.04	0.34
SECR	0.01	0.07	0.49
CECR	0.01	0.05	0.39
RECR	0.01	0.06	0.44

Table 5. *Cont.*

Asphalt ID	Stiffness (MPa) at Loading Time 5 (s)		
	High Temperature	Intermediate Temperature	Low Temperature
V	0.01	0.07	0.47
CR	0.02	0.11	0.7
SA	0.01	0.08	0.54
CE	0.01	0.06	0.48
RE	0.01	0.07	0.5
SECR	0.02	0.13	0.83
CECR	0.01	0.09	0.61
RECR	0.02	0.1	0.73
Asphalt ID	**Stiffness (MPa) at Loading Time: 1 (s)**		
	High Temperature	**Intermediate Temperature**	**Low Temperature**
V	0.05	0.32	1.48
CR	0.07	0.37	1.93
SA	0.05	0.31	1.71
CE	0.04	0.24	1.7
RE	0.05	0.28	1.71
SECR	0.08	0.42	2.51
CECR	0.06	0.34	1.87
RECR	0.07	0.38	2.35
Asphalt ID	**Stiffness (MPa) at Loading Time: 0.5 (s)**		
	High Temperature	**Intermediate Temperature**	**Low Temperature**
V	0.08	0.42	2.58
CR	0.13	0.56	3.48
SA	0.09	0.47	3.09
CE	0.07	0.4	3.23
RE	0.08	0.43	3.16
SECR	0.15	0.67	4.17
CECR	0.1	0.49	3.45
RECR	0.11	0.58	4.11
Asphalt ID	**Stiffness (MPa) at Loading Time: 0.1 (s)**		
	High Temperature	**Intermediate Temperature**	**Low Temperature**
V	0.3	1.23	7.81
CR	0.42	1.64	9.24
SA	0.35	1.44	8.67
CE	0.26	1.31	9.93
RE	0.3	1.39	9.43
SECR	0.46	1.88	11.04
CECR	0.37	1.57	9.17
RECR	0.41	1.8	11.31

4. Conclusions

This research investigated the effects of three warm mix additives on the physical properties of rubberized asphalt binder by performing physical tests, namely the penetration, softening point, penetration index, penetration viscosity number, storage stability, ductility, viscosity test, and stiffness modulus. Based on the research results, the researchers draw the following conclusions.

- Enhanced asphalt binders, resulting from modifications, display increased levels of hardness. Notably, the binder that underwent modification through the introduction of crumb rubber and Sasobit showcases the most pronounced hardness.
- All rubberized asphalt binders modified with warm mix asphalt (WMA) techniques manifest elevated values of softening points in comparison to the original asphalt binder. Among these alternatives, the rubberized asphalt binder that incorporates Sasobit stands out with the highest softening point.
- The penetration index, penetration viscosity number, and loss on heating of crumb rubber with WMA additives closely resemble those of the virgin asphalt binder.
- The modified asphalt binders exhibit commendable stability over the course of storage.
- With the exception of the rubberized asphalt binder adjusted with Rediset, all other modified asphalt binders adhere to the criteria set by the ductility test.
- All pairings of rubberized asphalt binder and WMA additives contribute to the reduction of viscosity values. Notably, the rubberized asphalt binder with Sasobit showcases superior workability compared to its counterparts employing alternative WMA additives.
- Among the assortment of asphalt binders, the combination that involves crumb rubber and Sasobit-modified binder presents the highest stiffness modulus values under conditions of intermediate and high temperatures.
- When subjected to lower temperatures and briefer loading periods, the blend of Rediset and crumb rubber produces the most significant stiffness modulus values.

The findings suggest that employing crumb rubber with Sasobit could be effectively implemented in nations with hot weather conditions, whereas the combination of crumb rubber and Rediset could be suitable for countries experiencing colder climates. For forthcoming studies, it is recommended to center attention on examinations conducted at lower temperatures, specifically emphasizing tests like the Bending Beam Rheometer (BBR) and the Direct Tension Test (DTT). Furthermore, an augmentation of the investigation could involve the incorporation of a broader collection of warm-mix asphalt additives.

Author Contributions: Conceptualization, N.I.M.Y.; Methodology, M.B.; Validation, C.W.Y.; Investigation, M.B. and Z.H.A.-S.; Data curation, C.W.Y.; Writing—original draft, M.B.; Writing—review & editing, Z.H.A.-S. and S.R.O.A.; Visualization, M.A. and S.R.O.A.; Supervision, N.I.M.Y.; Funding acquisition, M.A. All authors have read and agreed to the published version of the manuscript.

Funding: This work was funded by Science and Engineering Research Center at Najran University with grant (NU/RCP/SERC/12/3).

Institutional Review Board Statement: Not applicable.

Informed Consent Statement: Not applicable.

Data Availability Statement: All data used in this research can be provided upon request.

Acknowledgments: The authors are thankful to the Deanship of Scientific Research under supervision of the Science and Engineering Research Center at Najran University for funding this work under the research centers funding program with grant (NU/RCP/SERC/12/3). The authors would like to thank Universiti Malaya for their continuous support.

Conflicts of Interest: The authors have no conflict of interest to declare.

References

1. Fakhri, M.; Javadi, S.; Sedghi, R.; Arzjani, D.; Zarrinpour, Y. Effects of deicing agents on moisture susceptibility of the WMA containing recycled crumb rubber. *Constr. Build. Mater.* **2019**, *227*, 116581. [CrossRef]
2. Pouranian, M.R.; Shishehbor, M. Sustainability Assessment of Green Asphalt Mixtures: A Review. *Environments* **2019**, *6*, 73. [CrossRef]
3. Rahman, M.T.; Mohajerani, A.; Giustozzi, F. Recycling of Waste Materials for Asphalt Concrete and Bitumen: A Review. *Materials* **2020**, *13*, 1495. [CrossRef] [PubMed]
4. Bilema, M.; Aman, M.Y.; Hassan, N.A.; Memon, Z.A.; Omar, H.A.; Yusoff, N.I.M.; Milad, A. Mechanical Performance of Reclaimed Asphalt Pavement Modified with Waste Frying Oil and Crumb Rubber. *Materials* **2021**, *14*, 2781. [CrossRef]

5. Cheng, Y.; Chai, C.; Liang, C.; Chen, Y. Mechanical Performance of Warm-Mixed Porous Asphalt Mixture with Steel Slag and Crumb-Rubber–SBS Modified Bitumen for Seasonal Frozen Regions. *Materials* **2019**, *12*, 857. [CrossRef]
6. Bilema, M.; Aman, Y.B.; Hassan, N.A.; Al-Saffar, Z.; Ahmad, K.; Rogo, K. Performance of Aged Asphalt Binder Treated with Various Types of Rejuvenators. *Civ. Eng. J.* **2021**, *7*, 502–517. [CrossRef]
7. Tahmoorian, F.; Samali, B.; Yeaman, J.; Crabb, R. The Use of Glass to Optimize Bitumen Absorption of Hot Mix Asphalt Containing Recycled Construction Aggregates. *Materials* **2018**, *11*, 1053. [CrossRef]
8. Wang, M.; Zhang, L.; Li, A.; Irfan, M.; Du, Y.; Di, W. Comparative pyrolysis behaviors of tire tread and side wall from waste tire and characterization of the resulting chars. *J. Environ. Manag.* **2019**, *232*, 364–371. [CrossRef]
9. Dong, R.; Zhao, M.; Tang, N. Characterization of crumb tire rubber lightly pyrolyzed in waste cooking oil and the properties of its modified bitumen. *Constr. Build. Mater.* **2019**, *195*, 10–18. [CrossRef]
10. Thives, L.P.; Pais, J.C.; Pereira, P.A.A.; Palha, C.A.O.F.; Trichês, G. Contribution of Asphalt Rubber Mixtures to Sustainable Pavements by Reducing Pavement Thickness. *Materials* **2022**, *15*, 8592. [CrossRef]
11. Presti, D.L. Recycled Tyre Rubber Modified Bitumens for road asphalt mixtures: A literature review. *Constr. Build. Mater.* **2013**, *49*, 863–881. [CrossRef]
12. Caltrans & CIWMB Partnered Research. *Guide, Asphalt Rubber Usage. "Caltrans"*; State of California Department of Transportation: Sacramento, CA, USA, 2003; pp. 94612–95819.
13. Bilema, M.; Aman, M.; Hassan, N.; Haloul, M.; Modibbo, S. Influence of crumb rubber size particles on moisture damage and strength of the hot mix asphalt. *Mater. Today Proc.* **2021**, *42*, 2387–2391. [CrossRef]
14. Milad, A.; Ahmeda, A.G.F.; Taib, A.M.; Rahmad, S.; Solla, M.; Yusoff, N.I.M. A review of the feasibility of using crumb rubber derived from end-of-life tire as asphalt binder modifier. *J. Rubber Res.* **2020**, *23*, 203–216. [CrossRef]
15. Attia, M.; Abdelrahman, M. Enhancing the performance of crumb rubber-modified binders through varying the interaction conditions. *Int. J. Pavement Eng.* **2009**, *10*, 423–434. [CrossRef]
16. Wang, H.; Liu, X.; Erkens, S.; Skarpas, A. Experimental characterization of storage stability of crumb rubber modified bitumen with warm-mix additives. *Constr. Build. Mater.* **2020**, *249*, 118840. [CrossRef]
17. Airey, G.; Rahman, M.; Collop, A.C. Crumb Rubber and Bitumen Interaction as a Function of Crude Source and Bitumen Viscosity. *Road Mater. Pavement Des.* **2011**, *5*, 453–475. [CrossRef]
18. Ozturk, H.I.; Kamran, F. Laboratory evaluation of dry process crumb rubber modified mixtures containing Warm Mix Asphalt Additives. *Constr. Build. Mater.* **2019**, *229*, 116940. [CrossRef]
19. Caputo, P.; Abe, A.A.; Loise, V.; Porto, M.; Calandra, P.; Angelico, R.; Rossi, C.O. The Role of Additives in Warm Mix Asphalt Technology: An Insight into Their Mechanisms of Improving an Emerging Technology. *Nanomaterials* **2020**, *10*, 1202. [CrossRef]
20. Woszuk, A.; Franus, W. A Review of the Application of Zeolite Materials in Warm Mix Asphalt Technologies. *Appl. Sci.* **2017**, *7*, 293. [CrossRef]
21. Bilema, M.A.; Aman, M.Y.; Hassan, N.A.; Ahmad, K.A.; Elghatas, H.M.; Radwan, A.A.; Shyaa, A.S. Moisture Sensitivity of Crumb Rubber Modified Modifier Warm Mix Asphalt Additive for Two Different Compaction Temperatures. *IOP Conf. Ser. Earth Environ. Sci.* **2018**, *140*, 012072. [CrossRef]
22. Williams, B.A.; Willis, J.R.; Shacat, J. *Asphalt Pavement Industry Survey on Recycled Materials and Warm-Mix Asphalt Usage: 2019*; NAPA: Greenbelt, MD, USA, 2020.
23. Cheng, D.; Hicks, R.; Teesdale, T. Assessment of Warm Mix Technologies for Use with Asphalt Rubber Paving Applications. *Mater. Sci.* **2011**.
24. Rubio, M.C.; Martínez, G.; Baena, L.; Moreno, F. Warm mix asphalt: An overview. *J. Clean. Prod.* **2012**, *24*, 76–84. [CrossRef]
25. Moreno, F.; Sol, M.; Martín, J.; Pérez, M.; Rubio, M.C. The effect of crumb rubber modifier on the resistance of asphalt mixes to plastic deformation. *Mater. Des.* **2013**, *47*, 274–280. [CrossRef]
26. Leng, Z.; Yu, H.; Zhang, Z.; Tan, Z. Optimizing the mixing procedure of warm asphalt rubber with wax-based additives through mechanism investigation and performance characterization. *Constr. Build. Mater.* **2017**, *144*, 291–299. [CrossRef]
27. Oliveira, J.R.M.; Silva, H.M.R.D.; Abreu, L.P.F.; Fernandes, S.R.M. Use of a warm mix asphalt additive to reduce the production temperatures and to improve the performance of asphalt rubber mixtures. *J. Clean. Prod.* **2013**, *41*, 15–22. [CrossRef]
28. Ameri, M.; Yazdipanah, F.; Yengejeh, A.R.; Afshin, A. Production temperatures and mechanical performance of rubberized asphalt mixtures modified with two warm mix asphalt (WMA) additives. *Mater. Struct.* **2020**, *53*, 113. [CrossRef]
29. Turbay, E.; Martinez-Arguelles, G.; Navarro-Donado, T.; Sánchez-Cotte, E.; Polo-Mendoza, R.; Covilla-Valera, E. Rheological Behaviour of WMA-Modified Asphalt Binders with Crumb Rubber. *Polymers* **2022**, *14*, 4148. [CrossRef]
30. Wang, T.; Yang, R.; Li, A.; Chen, L.; Zhou, B. Effects of Sasobit and Its Adding Process on the Performance of Rubber Asphalt. *Chem. Eng. Trans.* **2016**, *51*, 181–186. [CrossRef]
31. Sesay, T.; You, Q.; Chuan, J.; Qiao, H.; Zhang, H.; Tian, S. High and intermediate temperature performance of warm asphalt rubber containing conventional warm mix additives and novel chemical surfactant. *Constr. Build. Mater.* **2023**, *394*, 132214. [CrossRef]
32. BILEMA, M.A.; Aman, M.Y.; Hassan, N.A.; Al-Saffar, Z.; Rogo, K.; Abdullah, N.F.A. Influence of crumb rubber incorporating different warm mix asphalt additives on the mechanical performance of the WMA mixture. *J. Rehabil. Civ. Eng.* **2021**, *9*, 1–11. [CrossRef]
33. Hamzah, M.O.; Golchin, B.; Jamshidi, A.; Chailleux, E. Evaluation of Rediset for use in warm-mix asphalt: A review of the literatures. *Int. J. Pavement Eng.* **2014**, *16*, 809–831. [CrossRef]

34. Vaitkus, A.; Čygas, D.; Laurinavičius, A.; Perveneckas, Z. Analysis and Evaluation of Possibilities for the Use of Warm Mix Asphalt in Lithuania. *Balt. J. Road Bridge Eng.* **2009**, *4*, 80–86. [CrossRef]
35. Hurley, G.C.; Prowell, B.D. Evaluation of Sasobit®for Use in Warm Mix Asphalt. *NCAT Rep.* **2005**, *5*, 1–27.
36. Abdullah, M.E.; Zamhari, K.A.; Buhari, R.; Abu Bakar, S.K.; Kamaruddin, N.H.M.; Nayan, N.; Hainin, M.R.; Hassan, N.A.; Hassan, S.A.; Yusoff, N.I.M. Warm Mix Asphalt Technology: A Review. *J. Teknol.* **2014**, *71*, 39–52. [CrossRef]
37. Bilema, M.A.M.; Aman, M.Y.; Ahmad, K.A. Investigating the rheological and physical properties for unaged of crumb rubber-modified binders containing warm mix asphalt additive. In Proceedings of the 1st Global Civil Engineering Conference 1, Kuala Lumpur, Malaysia, 25–28 July 2017; Springer: Singapore, 2019; Volume 9, pp. 1389–1400. [CrossRef]
38. Van Poel, C.D. A general system describing the visco-elastic properties of bitumens and its relation to routine test data. *J. Appl. Chem.* **1954**, *4*, 221–236. [CrossRef]
39. Abatech Inc. Available online: https://www.abatech.com/ (accessed on 12 August 2023).
40. Mashaan, N.S.; Ali, A.H.; Karim, M.R.; Abdelaziz, M. Effect of crumb rubber concentration on the physical and rheological properties of rubberised bitumen binders. *Int. J. Phys. Sci.* **2011**, *6*, 684–690. Available online: http://www.academicjournals.org/IJPS (accessed on 17 July 2021).
41. Awazhar, N.A.; Khairuddin, F.H.; Rahmad, S.; Fadzil, S.M.; Omar, H.A.; Yusoff, N.I.M.; Badri, K.H. Engineering and leaching properties of asphalt binders modified with polyurethane and Cecabase additives for warm-mix asphalt application. *Constr. Build. Mater.* **2020**, *238*, 117699. [CrossRef]
42. Mohamed, M.; Zumrawi, E. Effect of Crumb Rubber Modifiers (CRM) on Characteristics of Asphalt Binders in Sudan. *Int. J. Mater. Sci. Appl.* **2017**, *6*, 1. [CrossRef]
43. Kök, B.V.; Yilmaz, M.; Akpolat, M. Evaluation of the conventional and rheological properties of SBS + Sasobit modified binder. *Constr. Build. Mater.* **2014**, *63*, 174–179. [CrossRef]
44. Akpolat, M.; Akpolat, M. Investigation of rutting, fatigue and cracking resistance parameters of CR modified warm asphalt binders compare with SBS modified binders. *Rev. Construcción* **2022**, *21*, 309–328. [CrossRef]
45. Bilema, M.; Aman, M.Y.; Hassan, N.A.; Al-Saffar, Z.; Mashaan, N.S.; Memon, Z.A.; Milad, A.; Yusoff, N.I.M. Effects of Waste Frying Oil and Crumb Rubber on the Characteristics of a Reclaimed Asphalt Pavement Binder. *Materials* **2021**, *14*, 3482. [CrossRef]
46. Sengoz, B.; Isikyakar, G. Analysis of styrene-butadiene-styrene polymer modified bitumen using fluorescent microscopy and conventional test methods. *J. Hazard. Mater.* **2008**. [CrossRef] [PubMed]
47. Veeraiah, H.K.; Nagabhushanarao, S.S. Effect of optimized short-term aging temperature on rheological properties of rubberized binders containing warm mix additives. *Constr. Build. Mater.* **2020**, *261*, 120019. [CrossRef]
48. Li, M.; Lv, A.; Ran, J.; Li, Q. Testing and Evaluation of Sasobit on the Performances of Asphalt Rubber. In *ICCTP 2011: Towards Sustainable Transportation Systems, Proceedings of the 11th International Conference of Chinese Transportation Professionals, Nanjing, China, 14–17 August 2011*; ASCE: Reston, VA, USA, 2011; pp. 3502–3509. [CrossRef]
49. Mashaan, N.S.; Karim, M.R. Investigating the rheological properties of crumb rubber modified bitumen and its correlation with temperature susceptibility. *Mater. Res.* 2013. [CrossRef]
50. Sedaghat, B.; Taherrian, R.; Hosseini, S.A.; Mousavi, S.M. Rheological properties of bitumen containing nanoclay and organic warm-mix asphalt additives. *Constr. Build. Mater.* **2020**, *243*, 118092. [CrossRef]

Disclaimer/Publisher's Note: The statements, opinions and data contained in all publications are solely those of the individual author(s) and contributor(s) and not of MDPI and/or the editor(s). MDPI and/or the editor(s) disclaim responsibility for any injury to people or property resulting from any ideas, methods, instructions or products referred to in the content.

applied sciences

MDPI

Review

A Comprehensive Review on Clay Soil Stabilization Using Rice Husk Ash and Lime Sludge

Hamid Reza Manaviparast [1,*], Nuno Cristelo [2], Eduardo Pereira [3] and Tiago Miranda [4]

[1] Department of Civil Engineering, University of Minho, 4800-058 Guimarães, Portugal
[2] School of Science and Technology, University of Trás-os-Montes e Alto Douro, 5000-801 Vila Real, Portugal; ncristel@utad.pt
[3] IB-S/ISISE, University of Minho, 4800-058 Guimarães, Portugal; eduardo.pereira@civil.uminho.pt
[4] Institute for Sustainability and Innovation in Structural Engineering (ISISE), Associate Laboratory Advanced Production and Intelligent Systems (ARISE), Department of Civil Engineering, University of Minho, 4800-058 Guimares, Portugal; tmiranda@civil.uminho.pt
* Correspondence: id8028@alunos.uminho.pt

Abstract: Soil stabilization is vital in construction to enhance soil strength and durability. While conventional stabilizers like cement and lime improve soil properties, they contribute to significant carbon emissions. Given their widespread use, exploring eco-friendly alternatives is crucial. This review examines rice husk ash (RHA) and lime sludge (LS) as sustainable substitutes. Previous studies have evaluated their effectiveness in stabilizing clay soil, but a more application-focused approach, along with a detailed cost and sustainability evaluation, is needed. Standard Proctor compaction, California Bearing Ratio, and unconfined compression strength tests were analyzed from the existing literature to determine the optimal ratio of these additives for maximum soil strength. The results were compared to determine the most effective quantities of RHA and LS, either separately or combined, and inferences about their influences on clay soil attributes were drawn. Additionally, comprehensive life cycle assessment (LCA) and cost evaluation were reviewed. Finally, it was concluded that increasing the amounts of RHA and LS and combining them enhanced the strength of clay soil. Moreover, using RHA and LS for soil stabilization proved to be a cost-effective alternative to traditional methods, providing economic and environmental advantages.

Keywords: clay soil stabilization; sustainability; rice husk ash; lime sludge; strength test

1. Introduction

Soil stabilization is a process used to improve the engineering characteristics of the soil to make it more suitable for construction purposes [1]. It involves various techniques and materials applied to the soil to enhance its strength, durability, and load-bearing capacity [2]. The main goal of soil stabilization is to create a stable surface to support structures and prevent undesirable settlement or failure [3].

1.1. Stabilization History

Soil stabilization has been used for centuries, demonstrating its longstanding history. Humans have been using various techniques to enhance the strength and stability of soil for construction purposes and to prevent soil erosion [4,5]. Around 2500 BCE, the Egyptians used soil stabilization techniques to construct buildings and monuments. They mixed mud with straw to strengthen the soil properties and create more durable structures [6]. Ancient Greeks and Romans used lime and pozzolanic materials such as volcanic ash to

stabilize the soil and enhance its strength and durability [7]. In ancient China, rammed earth construction was widely used, where soil was compacted in layers with wooden frames, creating durable structures like the Great Wall. They also mixed lime and clay to improve soil strength [8]. In ancient India, stabilization methods that included using lime, ash, and organic materials to strengthen soil were prevalent [9]. During the Middle Ages, lime stabilization became popular in Europe to improve the soil properties [10]. With the advent of the Industrial Revolution in the 18th century, new methods and materials for soil stabilization emerged [11]. Cement was produced on a larger scale and started to be used to stabilize soil, while lime also remained in use [12,13]. In the early 20th century, engineers began experimenting with chemical additives for soil stabilization [14,15]. Materials, including bitumen and asphalt emulsions, were deployed to improve soil properties and make them appropriate for road construction [16–18]. In the mid-20th century, the development of geotextiles and geosynthetics provided new opportunities for soil stabilization [19]. These materials, typically made of synthetic fibers, were utilized to reinforce soil [20]. In recent years, soil stabilization techniques have made significant strides in their development. Innovations such as using polymer additives, cementitious binders, and a range of chemical agents have emerged to improve soil properties [21–23]. Today, the soil stabilization process is an essential aspect of construction and civil engineering projects [24].

1.2. Stabilization Methods

The specific soil stabilization technique deployed in every project depends on the soil's characteristics and the project's requirements. Mechanical, chemical, and geosynthetic stabilization and soil mixing are the most common soil stabilization methods [25,26]. Different types of soils require specific soil stabilization techniques to address their unique properties and challenges. Some common soil stabilization techniques for different soil types are reviewed: clay soils can be stabilized using chemical additives such as lime, cement, or fly ash [27]. These additives react with the clay particles, reducing their plasticity, improving their strength, and increasing their stability [28]. Sandy soils can be stabilized through chemical additives, like cement, and mechanical methods, such as compaction or densification [29]. Compaction increases soil density, while techniques like vibro-compaction or dynamic compaction can enhance load-bearing capacity [30]. Also, geosynthetic materials, such as geotextiles or geogrids, can reinforce sandy soils, improving their stability, preventing erosion, and enhancing slope stability [31]. Like clay soils, silty soils can be stabilized using chemical additives like lime or cement, improving their strength and reducing their compressibility [32]. Soil mixing with additives can also be efficient for silty soils to generate a more stable and homogenous soil mixture [33]. For organic soils, preloading and surcharging can be deployed: preloading with the placement of temporary surcharges can be used to consolidate and improve strength over time. The weight of the surcharge compresses the soil and expels water, reducing settlement potential [34]. Geosynthetic materials can also be used in organic soils to provide reinforcement and prevent excessive deformations [35]. Expansive soils, which are prone to swell and shrink with moisture changes, can be treated with chemical additives like lime, cement, or fly ash to reduce their volume change potential [36]. Proper moisture control techniques, such as drainage systems or moisture barriers, can be implemented to minimize moisture fluctuations in expansive soils [37].

1.3. Conventional Stabilizers

In construction projects, Ordinary Portland Cement (OPC) is primarily utilized as a binding agent in producing concrete, mortar, and grout. It is mixed with aggregates and

water to create a paste that hardens and develops strength over time. OPC-based concrete structures are widely utilized for building structural elements [38]. In the soil stabilization process, OPC can be deployed as an additive to improve the engineering properties of the soil. Adding OPC to the soil can enhance mechanical characteristics [39]. The process typically involves thoroughly mixing the OPC with the soil, forming a cementitious matrix that binds the soil particles together. This improves soil cohesion and increases its resistance to erosion [40]. The effectiveness of OPC as a soil stabilizer depends on factors such as the soil type, moisture content, and the desired outcome of the stabilization. It is commonly used for stabilizing cohesive soils such as clay or silt [41].

Calcium silicate hydrate (CSH) is the main product of the hydration of Portland cement [42]. CSH is the primary binder and the main component responsible for the strength and durability of cement-based materials [43]. It forms through a chemical reaction between cementitious materials such as Portland cement and water. CSH is responsible for developing the hardened cement paste's strength. It reacts with water and the soil particles, improving cohesion, increasing strength, reducing permeability, and improving stability. It helps to bind the soil particles together and create a more stable and compacted soil matrix [44]. Calcium aluminum silicate hydrate (CASH) is another hydrated mineral compound formed in cementitious materials. CASH is a specific type of calcium silicate hydrate that contains additional alumina (Al_2O_3) in its structure [45]. It forms when cement containing alumina-rich materials, such as fly ash or slag, undergoes hydration. It is the primary product of the chemical reaction between cementitious materials, such as Portland cement and water, during hydration [46]. It is responsible for developing the strength and durability of hardened cement paste. CASH is an amorphous material composed of calcium, aluminum, silicon, and oxygen atoms, with water molecules trapped within its structure [47]. It forms a gel-like substance that fills the spaces between cement particles, providing cohesiveness and strength to the cement matrix. While both CSH and CASH contribute to the strength and durability of cementitious materials, CASH can exhibit different properties compared to traditional CSH due to the presence of alumina [48]. The addition of alumina can affect the structure and mechanical properties of the hydrated phases, influencing the overall performance of the cementitious material [49].

Conventional stabilizers, including cement, are widely used in construction but contribute significantly to carbon emissions, raising serious environmental concerns. As sustainability becomes a priority, finding eco-friendly alternatives is essential to reduce the environmental impact of such materials. Consequently, efforts are being made within the cement industry to reduce its carbon footprint and mitigate carbon dioxide (CO_2) emissions by:

(1) Using alternative fuels, such as biomass or waste-derived fuels, which can help lower CO_2 emissions. Additionally, using alternative raw materials, such as industrial byproducts, can reduce the need for limestone extraction and decrease associated emissions [50,51].
(2) Implementing energy-efficient technologies and practices can reduce the overall energy consumption and emissions from cement production. This includes optimizing kiln operations, improving heat recovery systems, and employing more efficient grinding processes [52].
(3) Carbon capture and storage (CCS) technologies aim to capture CO_2 emissions from cement plants, store them underground, or utilize them in other industrial processes. CCS is still in the early stages of deployment in the cement industry but holds promise for significant emissions reduction [53].
(4) Development efforts are underway to develop and promote low-carbon or carbon-neutral cement alternatives. These include cement made from supplementary ce-

mentitious materials like fly ash, blast furnace slag, or pozzolanic materials [54]. By implementing these measures, the cement industry can reduce its carbon footprint and contribute to global efforts to mitigate climate change.

1.4. Sustainable Stabilizers

Byproduct materials, such as rice husk ash (RHA) and lime sludge (LS), can play a significant role in soil stabilization applications. These materials provide several benefits, including environmental sustainability, cost-effectiveness, and improved engineering properties of the stabilized soil [55]. RHA contains high amounts of amorphous silica (SiO_2), contributing to its pozzolanic properties. RHA can be used in soil stabilization as an additive to improve soil properties, including strength, durability, and permeability. It reacts with calcium hydroxide, a byproduct of lime, to form additional calcium silicate hydrates (CSH) gel. This pozzolanic reaction improves cementitious properties, such as increased strength and reduced permeability [56]. Utilizing RHA as a sustainable utilization in soil stabilization provides an environmentally friendly solution by recycling agricultural waste material to reduce waste generation and promote sustainable practices [57].

Lime sludge (LS), also known as lime waste or lime byproduct, possesses cementitious properties that make it suitable for soil stabilization. LS is rich in calcium hydroxide ($Ca(OH)_2$), which is the main compound responsible for its cementitious properties [58]. Calcium hydroxide is an alkaline compound that reacts with silicates and other compounds to form cementitious products. LS exhibits pozzolanic activity, which refers to its ability to react with calcium hydroxide and water to form additional cementitious compounds. This reaction, known as the pozzolanic reaction, produces calcium silicate hydrates (CSH) gel, which contributes to the strength of the stabilized soil. LS interacts with clay minerals in soils, causing chemical and physical changes to the soil structure. This reaction decreases the plasticity of the clay minerals while enhancing their stability [59]. This reaction enhances the soil characteristics, including strength, workability, and load-bearing capacity. LS can be utilized as a stabilizing agent to enhance soil properties, mainly clayey or cohesive soils. When LS is added to these soils, it reacts with the clay minerals, resulting in improved compaction characteristics, reduced soil plasticity, increased strength, reduced swell-shrink behavior, and enhanced load-bearing capacity [60]. Lime sludge can be self-cement or self-harden when mixed with water. This property allows it to bind and stabilize soil particles, improving cohesion and strength within the stabilized soil or construction material [61]. Utilizing lime sludge in soil stabilization as a waste management solution provides a means of repurposing a waste material that might otherwise pose disposal challenges. It offers an opportunity for sustainable waste management practices and reduces the demand for traditional construction materials. When RHA and LS are used together, LS provides the calcium needed for stabilizing clay, while RHA increases the soil's strength and durability by contributing additional pozzolanic reactions. This combination reduces soil plasticity, minimizes shrink-swell behavior, and improves compaction, making it suitable for infrastructure projects in areas with clay soils. The process involves blending appropriate amounts of LS and RHA with the soil and allowing time for curing to achieve optimal soil stabilization [62].

The produced waste of rice husk ash and lime sludge can have detrimental environmental effects [63]. Proper management and disposal of RHA and LS byproducts are essential. Inadequate disposal methods, such as open dumping or uncontrolled release, can lead to soil and water pollution, posing ecosystem risks [64]. Both RHA and LS can have environmental implications if not properly managed. RHA may contain heavy metals, such as lead, cadmium, arsenic, and mercury; if not properly managed, these metals can leach into the soil or water bodies, posing a risk to ecosystems and human health. RHA

contains amorphous silica, and if fine RHA particles become airborne during handling or mixing, there is potential for inhalation. Prolonged inhalation of silica dust may pose health risks, such as respiratory issues or lung disease, caused by silica exposure. Therefore, wearing protective masks, using dust suppression techniques, and handling RHA in controlled environments can minimize health risks [65]. RHA contains a high percentage of silica, which can be released as airborne particulate matter during handling or processing. Inhalation of silica dust can cause respiratory issues, including lung damage. It may also contain organic contaminants, such as polycyclic aromatic hydrocarbons (PAHs) or volatile organic compounds (VOCs), which can harm the environment and human health [66].

LS can contain heavy metals like chromium, lead, cadmium, and nickel, so improper disposal or release of LS into the environment can contaminate soil and water bodies. Lime in LS is mildly caustic, and direct skin or eye contact can cause irritation or burns. Proper safety measures, such as wearing gloves, goggles, and protective clothing, should be in place for workers handling lime sludge. Additionally, the fine particles of LS can become airborne during handling, potentially causing respiratory irritation if inhaled. However, proper dust control and protective equipment can manage these risks effectively [67]. Lime sludge has high alkalinity due to its calcium hydroxide content. Discharging untreated lime sludge into water bodies can increase pH levels, affecting aquatic organisms and disrupting the ecosystem's natural balance [68]. LS often contains elevated levels of nutrients, particularly phosphorus. When released into water bodies, it can contribute to eutrophication, leading to excessive algae growth, oxygen depletion, and harm to aquatic life [69].

Proper management practices should be followed to mitigate the potential environmental impact of RHA and LS. This includes appropriate storage, transportation, and disposal methods to prevent the release of impurities into the environment. Additionally, environmental regulations should be followed, and treatment techniques should be employed to minimize the impact on ecosystems and human health.

Past studies have explored the effectiveness of clay soil stabilization using eco-friendly alternative materials, including RHA and LS [70]. However, this review bridges research gaps by comprehensively analyzing laboratory test results (UCS, CBR, Mr, and Proctor tests) on RHA and LS as soil stabilizers to promote the reuse of agricultural and industrial byproducts. By identifying optimal proportions for specific applications like structural foundations and roadways, we provide engineers and researchers with precise data to enhance stabilization solutions tailored to project needs. Additionally, it provides an in-depth evaluation of sustainability and cost factors, highlighting its unique contribution to promoting sustainable practices in civil engineering to support the shift toward greener construction. By evaluating lifecycle factors, such as energy use and waste reduction, along with cost savings from locally sourced byproducts, valuable insights for policymakers and stakeholders are provided. This study provides a strong foundation for future studies by offering precise guidelines and test result analyses. It encourages further exploration of RHA and LS in combination with other additives and supports regional case studies that address local soil and waste availability, paving the way for more tailored and effective soil stabilization strategies.

To conclude, this review aims to assess the efficacy of clay soil stabilization using rice husk ash (RHA) and lime sludge (LS) to determine the optimum quantity of RHA and LS to be used based on comprehensive geotechnical tests, as well as research on cost-effectiveness and sustainability.

2. Materials

Disposing of waste materials, such as rice husk ash and lime sludge, resulting from industrial processes poses environmental concerns when deposited in landfills. However, these materials can be repurposed and utilized beneficially, particularly in geotechnical and other engineering projects [71,72]. This review focuses on applying RHA and LS in clay soil stabilization, exploring their properties, and investigating their chemical composition, as documented by various researchers who worked in the field of using green alternative materials for clay stabilization. Results of laboratory tests, including standard Proctor compaction, unconfined compression strength (UCS), and California Bearing Ratio (CBR) related to soil samples with various mixed proportions of admixtures among different papers, are discussed.

2.1. Rice Husk Ash (RHA)

Rice husk ash is a byproduct obtained from the combustion or incineration of rice husks [73]. Rice husks are the protective coverings of rice grains and are generated during the rice milling process. It constitutes around 20–23% of the total weight of the rice grain [74]. Rice husks are agricultural trash that accounts for nearly one-fifth of the world's yearly gross rice production of 545 million metric tons [75]. Due to the high calorific power of rice husk (approximately 16,720 kJ/kg), it is increasingly used as a fuel source for heat generation in rice drying [76]. Rice husk ash is mainly produced by burning rice husks at around 450–700 °C for 1–3 h under controlled conditions [77]. During high-temperature combustion, the organic components of rice husk, including cellulose, hemicellulose, and lignin, are more effectively burned, leaving behind a higher percentage of silica-rich ash [78]. In contrast, during lower-temperature combustion, the combustion may be less efficient, and a more significant fraction of the organic matter may remain in the RHA, leading to higher carbon content [79].

Based on the requirements, the collected RHA may undergo additional processing steps, including grinding or sieving, to achieve the desired particle size distribution and remove impurities. The resulting RHA is a fine, light powder with high silica content (60 to 90%) [80]. RHA primarily consists of amorphous silica (SiO_2) and is chemically reactive. It contains a high percentage of siliceous elements, indicating its potential for exhibiting pozzolanic characteristics [81]. RHA does not possess inherent cementitious qualities; therefore, it is not used alone for soil stabilization and is commonly utilized as supplementary material in soil stabilization processes [82]. The addition of RHA can significantly influence macro aggregate production, while it has been observed that the addition of RHA decreases the fraction of micro aggregates smaller than 0.25 mm in size. The aggregation of clay particles with RHA can create larger pores, known as macropores, which help to drain the soil better, while it might not significantly impact the smallest-sized pores, known as crytopores [83]. To sum up, rice husk ash, as agricultural waste, shows remarkable potential for stabilizing clay soils.

To determine the elemental composition of rice husk ash, the results of the various chemical analyses of RHA performed by X-ray fluorescence (XRF) tests are given in Table 1. Furthermore, the mean and standard deviation (SD) were calculated to determine the average chemical composition and measure the variability of the data for RHA.

Table 1. Chemical composition of RHA obtained by XRF (in percent).

Source	CaO	SiO_2	Na_2O	MgO	Al_2O_3	Fe_2O_3	K_2O	TiO_2	LOI
[84]	0.578	96.235	0.054	0.269	0.281	1.366	0.454	-	-
[85]	0.82	80.82	0.96	-	0.25	0.38	1.25	-	12.70
[86]	0.37	87.49	0.01	0.01	0.05	0.04	0.8	0.01	11.21
[87]	0.62	89.69	1.02	0.57	1.01	0.23	0.81	4.06	-
[88]	0.82	80.02	0.01	0.74	1.81	0.79	1.01	0.43	10.62
Mean	0.6416	86.8508	0.4108	0.39725	0.6804	0.5612	0.8648	2.245	11.51
SD	0.1675	5.96	0.474	0.279	0.861	0.387	0.265	2.11	1.07

LOI = Loss on Ignition.

Extracted results indicate that Silica (SiO_2) is the major component of RHA, ranging from 80% to 96%. Silica in RHA is highly reactive and can contribute to pozzolanic reactions in cementitious materials. Potassium oxide (K_2O) and sodium oxide (Na_2O) are found in small amounts, less than 2%. Calcium oxide (CaO) content can vary, but it has been found in small quantities, less than 1%, contributing to the overall pozzolanic activity. Iron oxide (Fe_2O_3) content can vary depending on the rice husk source and burning conditions, below 2%. These percentages can vary based on the source of the rice husk, the burning temperature, and the combustion conditions. XRF analysis quantitatively measures these elements, helping to characterize RHA for its potential use in various applications, especially in the construction industry [89,90].

2.2. Lime Sludge (LS)

Lime sludge is a byproduct produced in various industrial processes, mainly in the paper industry and water treatment plants. In the pulp and paper industry, a significant source of lime sludge, approximately 100–200 kg of LS, can be generated per ton of pulp produced. Global pulp production is around 185 million tons annually, which could imply around 18.5 to 37 million tons of lime sludge per year from this sector alone [91]. Lime sludge can vary in composition depending on the specific industrial process and the impurities in the treated lime. However, it primarily contains calcium carbonate ($CaCO_3$) [92]. LS can have beneficial applications as a waste material, as adopted and illustrated in Figure 1, particularly in soil stabilization and construction materials [93].

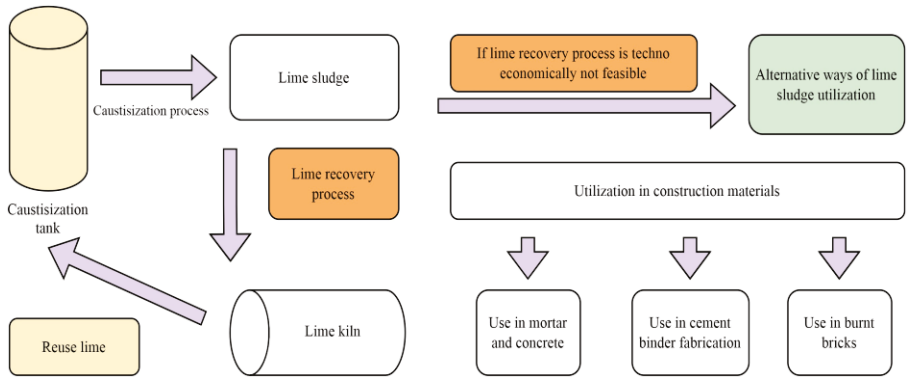


Figure 1. Utilization possibilities of LS [93].

Lime sludge can be deployed as a stabilizing agent to amend the engineering properties of soil or as a raw material in the production of cementitious materials [94]. However, proper waste management of lime sludge is necessary to prevent environmental pollution. Lime sludge can be deployed to change the engineering properties of fine-grained soils and the fine-grained fractions of granular soils [95]. It can reduce the plasticity of fine-grained

soils, such as clay, resulting in reduced potential for shrinkage and swelling and improved soil workability, strength, drainage, and permeability, making the soil more stable [96]. The lime sludge treatment effectively stabilizes plastic clays and other fine-grained soils with high water storage capacity. Soils with higher plasticity or water content generally require a higher lime sludge dosage for effective stabilization [97]. However, as a general guideline, a lime sludge content of 3–10 percent by dry weight is sufficient to achieve adequate stabilization [98]. The results of the chemical analysis of LS using the X-ray fluorescence (XRF) test are given in Table 2.

Table 2. Chemical composition of LS obtained by XRF (in percent).

Source	CaO	SiO_2	Al_2O_3	Fe_2O_3	MgO	So_3	Na_2O	LOI
[99]	92.25	0.06	0.56	0.45	0.03	-	0.26	6.39
[100]	95.03	0	0.13	0.08	0.25	0.02	0.05	4.33
[101]	70.85	1.19	0.69	0.12	0.53	-	0.25	26.1
[102]	40.74	5.78	0.18	0.15	0.41	0.28	2.03	-
Mean	74.72	1.76	0.39	0.20	0.31	0.15	0.65	12.27
SD	25.10	2.74	0.28	0.17	0.22	0.18	0.93	12.02

LOI = Loss on Ignition.

The results obtained from different studies demonstrate that calcium oxide (CaO) is a major component, reflecting the high calcium content derived from the lime used in treatment processes. The concentration can vary widely but often ranges from 40% to 95% depending on how much lime was used and how completely it reacted. Silica (SiO_2) is present in varying amounts, from 0% to 5%. Iron oxide (Fe_2O_3) is present in smaller quantities, less than 1%, and can come from various sources, including the treatment process or impurities in the lime. Magnesium oxide (MgO) is found in smaller amounts, less than 1%. It can come from the mineral composition of the lime or other additives used in the treatment process. Sodium oxide (Na_2O) is in smaller amounts, less than 3%. The exact composition of lime sludge can vary based on factors such as the source of the water being treated, the type of lime used, and the specifics of the treatment process. XRF provides a detailed elemental analysis that helps understand and manage lime sludge for various applications or disposal methods [103,104].

3. Laboratory Tests

The success or failure of enhancing the geotechnical properties of soils using different admixtures is typically determined through experimental or laboratory tests. These tests provide a means to evaluate the effectiveness of the admixtures in improving soil characteristics. The most widely used tests to evaluate the effectiveness of a soil improvement procedure include the standard Proctor compaction test, the unconfined compressive strength (UCS) test, and the California Bearing Ratio (CBR) test. In the present review, these tests are used to assess the performance of RHA and LS in clay soil improvement.

3.1. Standard Proctor Compaction Test

Assessing the compaction characteristics of soils for stabilization purposes is commonly used in geotechnical engineering. Different studies were reviewed to determine the Optimum Moisture Content (OMC) and Maximum Dry Density (MDD) of stabilized soil samples using the standard Proctor compaction test [98,105–112]. The results from the literature show that the OMC of soil samples increases and the MDD of soil samples decreases as the LS and RHA content increases in soil stabilization processes. During the pozzolanic reaction, the hydration of LS and RHA particles occurs, forming cementitious compounds such as CSH and CASH gels. This reaction consumes water, necessitating a

higher water content to maintain an appropriate moisture level for the reaction to take place, leading to an increase in the OMC of the soil. Simultaneously, adding LS and RHA also influences the soil particle arrangement. The cementitious compounds formed help to fill void spaces and enhance the development of a more compacted soil structure, leading to an increase in the MDD of the soil. The analyzed results show that increasing the LS percentage in the soil sample from 5% to 10% resulted in a sudden decrease in the MDD value. Deploying RHA alone as an admixture in clay soil samples results in an increase in the OMC and a decrease in the MDD due to the lower density of rice husk ash compared to the expansive soil. Similarly, incorporating LS as a binding material with RHA and the soil sample also leads to an increase in the OMC and a decrease in the MDD value. In this context, the decrease in the MDD value can be attributed to the lower density of lime sludge compared to the expansive soil. To clarify the results obtained from the literature, the variation in OMC and MDD based on different admixtures is shown in Figures 2–7. Methodological differences can impact the findings when comparing different results across different studies on clay soil stabilization using green alternative materials. These differences, such as clay mineralogy, soil gradation, soil preparation, curing duration, and environment, may influence the measured variations in results between studies. However, for the sake of simplicity, when comparing the results, methodological differences are not considered.

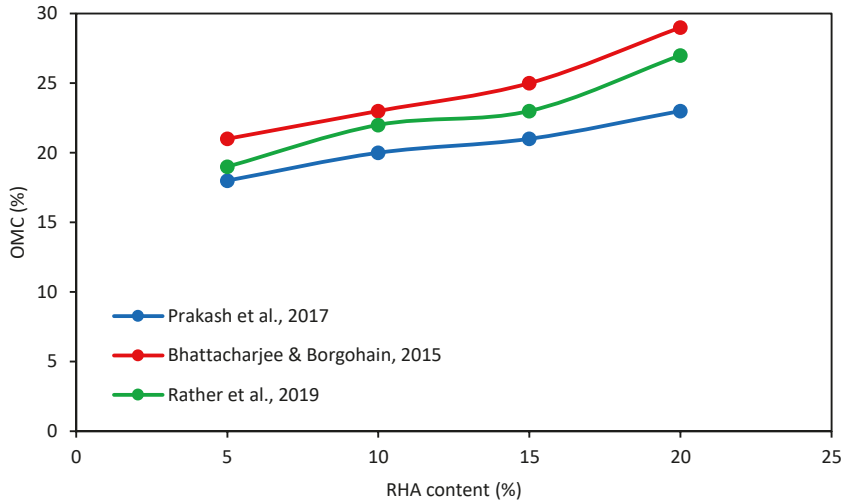


Figure 2. Effect of RHA in OMC [105–107].

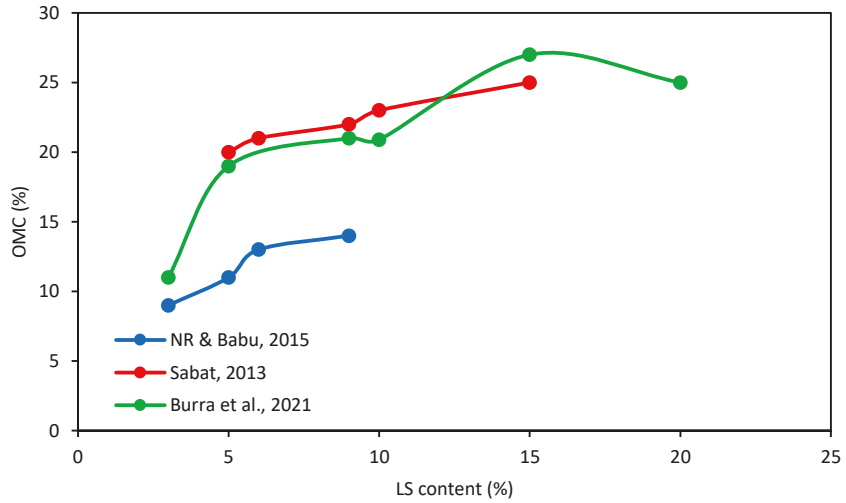


Figure 3. Effect of LS in OMC [108–110].

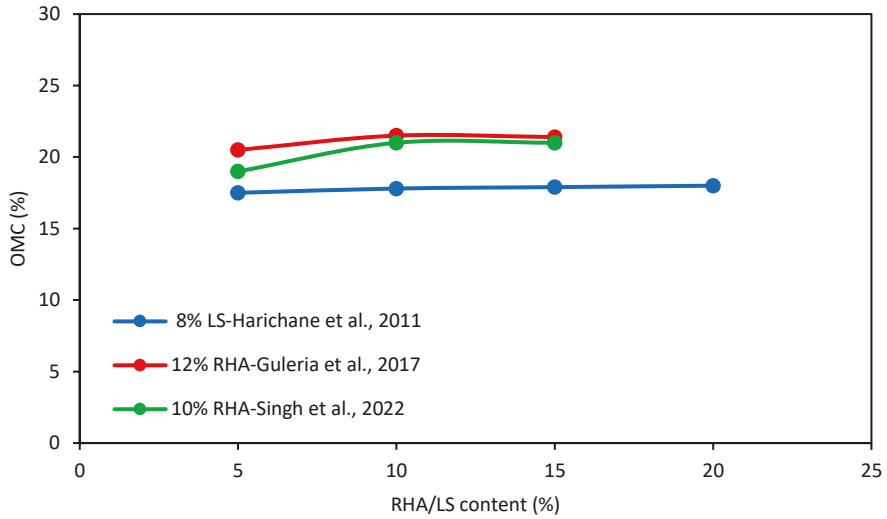


Figure 4. Effect of RHA and LS in OMC [98,111,112].

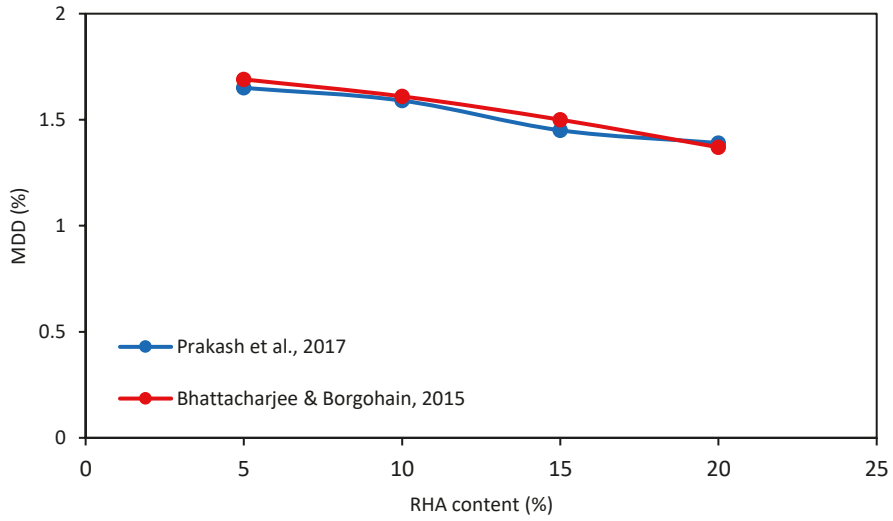


Figure 5. Effect of RHA in MDD [105,106].

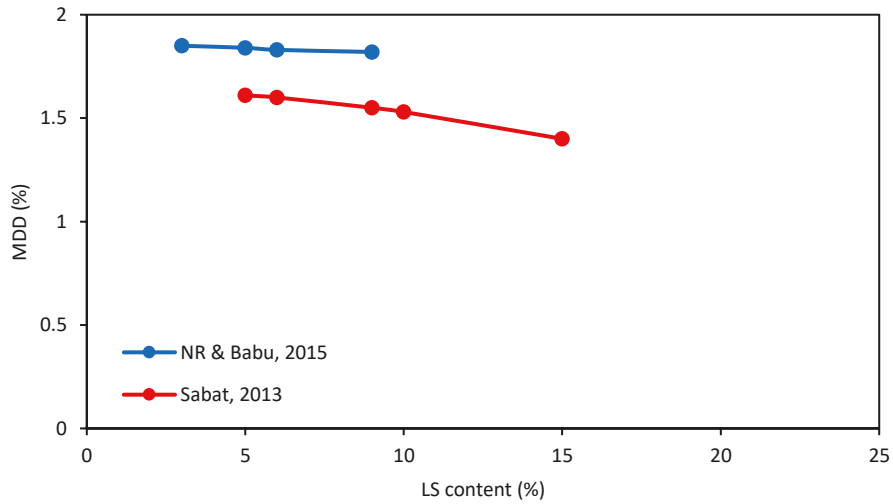


Figure 6. Effect of LS in MDD [108,109].

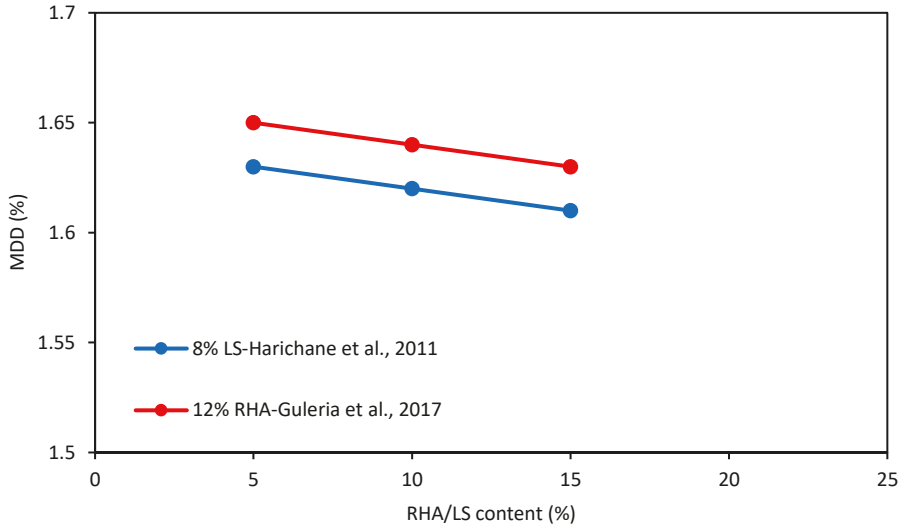


Figure 7. Effect of RHA and LS in MDD [98,111].

The results of the analysis of the drawn graphs from the standard Proctor compaction tests are provided below. Figure 2 demonstrates that with the increase in the percentage of RHA content added to the clay soil samples, the OMC of the soil increases. This increase in OMC with higher RHA content is due to RHA's porous and lightweight nature, which absorbs more water and requires higher moisture for compaction. Moreover, adding 10–20% of RHA content significantly increases the OMC of the soil samples. Figure 3 shows that by increasing the amount of LS content, the OMC of the soil increases due to the water-absorbing capacity of the admixtures. Additionally, it is evident that adding 10–15% of LS content escalates the OMC value in soil samples, and by adding more than 15% of LS content, a sudden drop in OMC value is observed. This is because, beyond a certain threshold of LS content (more than 15%), the soil structure becomes overly rigid, reducing its ability to retain moisture, thereby leading to a lower OMC since less water is required for compaction. Figure 4 reveals that incorporating RHA and LS into the soil samples enhances the OMC. It is observed that OMC increases progressively with the higher amount of admixtures added due to the high water absorption capacity of both materials, which increases the overall water demand for proper compaction. Additionally, the pozzolanic reaction between RHA, LS, and clay soil minerals consumes water, further increasing OMC. Figures 5–7 demonstrate a decrease in the MDD of the soil samples as the percentage of RHA and LS content increases. This reduction in MDD can be attributed to the lower specific gravity of the admixtures, which is less than the natural soil [113]. Additionally, reduced MDD indicates less strength of the matrix, which is compensated by the binding effect of the RHA and/or LS, increasing cohesion. The MDD decreases when RHA and LS are incorporated because both materials increase the void spaces within the soil matrix, making it less compact and requiring more water for lubrication, further reducing dry density. The pozzolanic reaction between RHA, LS, and clay soil also leads to the formation of cementitious compounds, which create a more open, flocculated soil structure, contributing to the reduction in MDD.

3.2. Unconfined Compressive Strength (UCS)

The unconfined compressive strength test is a laboratory test to determine improved soil strength and load-bearing capacity. The UCS test is commonly performed on cylindrical soil specimens under axial compression without lateral confinement. Different references were reviewed to present the relationships between the UCS values of different mixtures

and varying amounts of RHA and LS content added to the soil samples [111,114–118]. The review of the extracted results is shown in Figures 8–10.

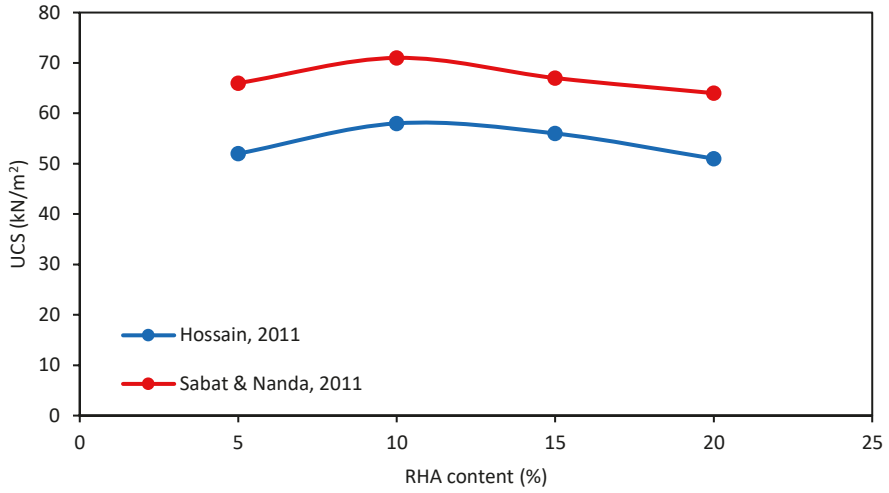


Figure 8. Effect of RHA in UCS [116,117].

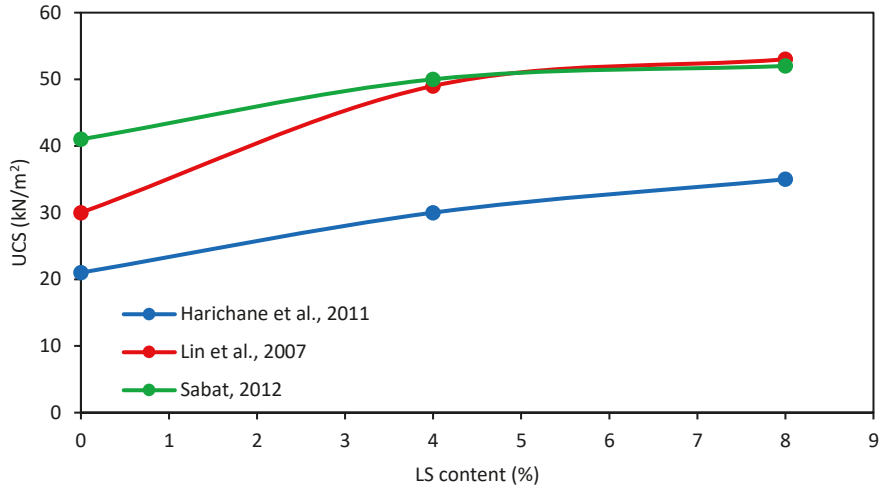


Figure 9. Effect of LS in UCS [111,114,115].

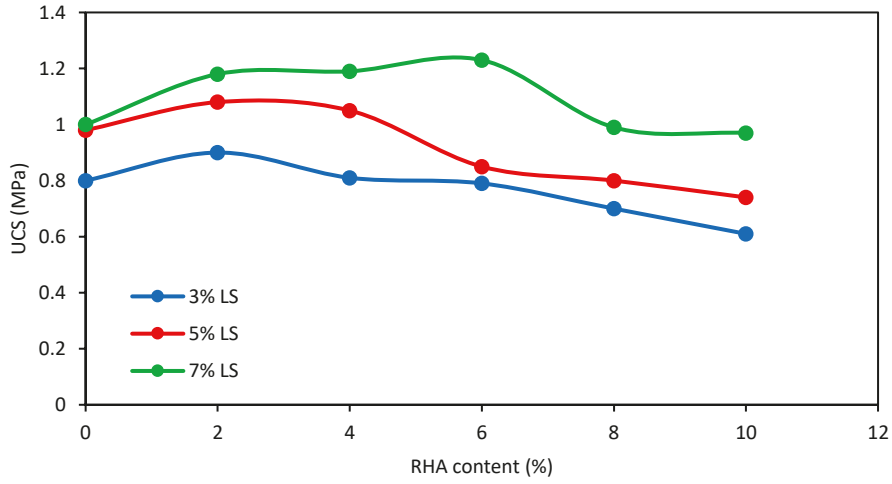


Figure 10. Effect of RHA and LS in UCS [118].

The results of the analysis of the drawn graphs from the UCS tests are provided below. Figure 8 shows the variation of the UCS value with respect to the RHA content. It

demonstrates that the UCS value of the soil samples shows an increase with the addition of RHA up to 10%. However, beyond this threshold, it is seen that the UCS of the clay soil starts to decline due to the reduction of cohesion and internal friction of the soil, consequently leading to a decrease in the soil's ability to resist deformation and load. When the amount of RHA exceeds the optimal level, there might be too much binder relative to the amount of soil available for the reaction. The extra RHA particles can start to act as a filler rather than a reactive component, leading to a reduction in the overall strength of the mixture. Additionally, excess RHA can increase the porosity of the mixture due to its lightweight and relatively high specific surface area. Higher porosity can reduce the density and, consequently, the strength of the soil. Figure 9 shows the variation of the UCS value with respect to the LS content. It indicates that an increase in the LS content increases the UCS value of the soil samples due to better bonding of soil and lime. Adding LS content up to 4% can increase the UCS value. Figure 10 shows the variation of the UCS value with respect to the combined RHA and LS content. The combined use of RHA and LS can have a significant influence, leading to a notable increase in the UCS value of the soil. However, it is indicated that above 6% RHA content, the strength decreases independently of LS content, which seems to be an upper threshold for RHA. Also, it can be seen that the higher the LS, the higher the strength, which conforms with the Figure 9 analysis. Figure 8 shows an optimized value of RHA of 10%, but when mixed with LS, this threshold is clearly lower.

3.3. California Bearing Ratio (CBR)

California Bearing Ratio is a laboratory test to evaluate the strength and load-bearing capacity of soils commonly used in geotechnical engineering, particularly in road construction. The compaction process uses a specific compaction effort to achieve the desired density and moisture content representative of the in-situ conditions. Proper compaction at the OMC ensures that the soil is compacted to its optimum condition for bearing capacity and strength, which is crucial for the design and construction of roads, embankments, and other civil engineering structures. The curing period, another significant governing parameter in the CBR test, directly impacts the CBR value obtained. CBR values increase with increasing curing periods, resulting in more accurate representations of the soil performance under the applied loads [119]. The CBR values, as shown in Figure 11, were determined by analyzing the results obtained from different references [109,120,121].

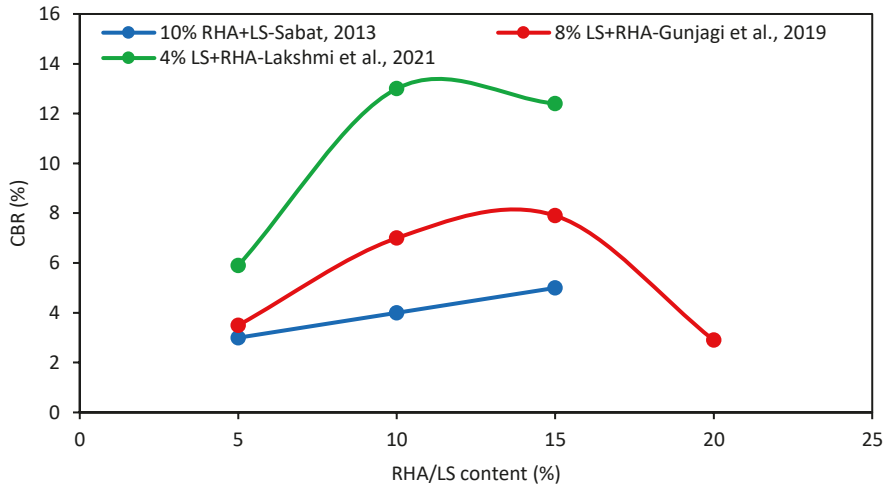


Figure 11. Effect of RHA and LS in CBR [109,120,121].

The results of the analysis of the drawn graph from the CBR tests are provided below. Figure 11 illustrates the results of various studies related to the impact of RHA plus LS on

the CBR parameters of soil samples. The results indicate that 4% of LS plus RHA content increases the CBR value compared to 8%. It is clear that there is a decrease in the CBR value after increasing the percentage of RHA content above 15%. However, by incorporating both RHA and LS content, the CBR value was increased overall. Higher amounts of LS aim to improve soil properties by increasing CBR, enhancing soil strength and load-bearing capacity, and reducing plasticity, but excessive use of LS can potentially lead to adverse effects if not properly managed.

The UCS and CBR are both indicators of the strength and load-bearing capacity of soils, but they measure different properties and are deployed for various purposes. CBR is usually more focused on pavement or roadway purposes, while UCS is generally more precise and relevant for clay soils, giving a more fundamental measure of compressive strength for structural purposes such as foundations or slope stability. Hence, the choice depends on the type of project.

Furthermore, the resilient modulus (M_r) is a critical parameter in road and pavement applications, as it directly reflects the elastic behavior of soil under repeated loading, which is more representative of the stresses experienced in actual pavement conditions. The CBR test indicates the soil's strength under a static load, making it less suitable compared to Mr for evaluating materials for dynamic conditions like roads. Summarized results from various studies are provided in Table 3.

Table 3. Resilient modulus (M_r) parameter for non-stabilized and stabilized clay soil.

Parameters	M_r Values	Notes	Source
Unstabilized clay	20–60 MPa	Baseline values before stabilization	[122]
Stabilized clay (RHA + Lime)	100–200 MPa (7 days curing)	Significant improvement due to pozzolanic reactions; values depend on dosage and curing time	[123]
	150–300 MPa (28 days curing)	Long-term curing increases M_r due to continued reaction	[124]
	>300 MPa (optimized mix, extended curing)	Observed in some studies with well-optimized RHA-lime mixes	[125]

The resilient modulus of stabilized clay soils is significantly higher than non-stabilized clay due to the improved soil structure and enhanced bonding mechanisms. In non-stabilized clay, M_r values are typically low because of the soil's high plasticity, poor particle interlocking, and susceptibility to deformation under repeated loads. Stabilization using materials like RHA and LS initiates pozzolanic reactions, forming CSH, which binds soil particles together and reduces plasticity, leading to a denser, more cohesive matrix with greater resistance to deformation under cyclic loads. Studies have shown that stabilized clay can achieve M_r values two to five times higher than non-stabilized clay, with values increasing further over time as the curing process continues. This improvement makes stabilized clay more suitable for subgrade applications in road construction.

4. Cost and Sustainability Evaluation

4.1. Cost Evaluation

Several researchers have conducted cost evaluations comparing the use of RHA and LS with traditional stabilizers, like lime and OPC, for clay soil stabilization worldwide. Conducting an extensive cost analysis for the stabilization process involves several factors, including material, transportation, application, performance, and environmental and regulatory costs. RHA and LS are often byproduct materials and can be sourced at low cost in some areas, but lime and OPC are commercially produced, with generally higher raw ma-

terials and production costs. RHA and LS may require less transport cost if sourced locally from agricultural or industrial facilities, but lime and OPC often require transport from production plants, potentially increasing costs, especially for remote sites. The application process for all stabilizers is similar, involving mixing, compaction, and curing. Labor costs are unlikely to vary significantly. RHA and LS may require higher quantities compared to lime and OPC to achieve similar performance, impacting total costs. Additionally, waste material use (RHA and LS) can reduce environmental costs and long-term maintenance. Utilizing RHA and LS supports waste recycling, reduces disposal costs, and potentially qualifies for subsidies or incentives, while OPC production has a high carbon footprint, potentially incurring environmental compliance costs. Summarized cost comparison results from various studies are provided in Table 4.

Table 4. Cost evaluation for clay stabilization using RHA and LS versus traditional stabilizers.

Materials	Cost Savings	Findings	Source
RHA + Natural Lime (NL)	17% reduction in earthwork costs, 39% savings in subgrade construction costs	RHA with 2% NL effectively stabilized clay soils, offering lower costs than traditional techniques	[126]
RHA + Lime	Reduced cost compared to OPC or lime stabilization	RHA as an agricultural waste provided economic and sustainable stabilization, significantly lowering material expenses	[127]
RHA + Lime	Estimated 25% cost reduction compared to OPC	Higher performance with RHA–lime mixture, utilizing industrial waste at lower costs	[72]
RHA + Lime	Approximately 30% cheaper than using OPC	Optimal mix of 8% RHA and 5% lime reduced costs due to local availability of RHA and less lime requirement	[128]
RHA + LS	Significantly lower material costs compared to OPC or LS stabilization	RHA and LS provided sustainable alternatives with good performance characteristics at lower cost thresholds	[129]

These studies demonstrate that using RHA and LS for clay soil stabilization can be a cost-effective alternative to traditional methods, offering both economic and environmental benefits.

4.2. Sustainability Evaluation

Life cycle assessment (LCA) is a comprehensive method to evaluate the environmental impacts of all stages of a product's life and plays a vital role in assessing sustainability. Conducting a comprehensive LCA for stabilizing clay soils using RHA and LS involves evaluating environmental impacts across various stages, including material extraction, processing, transportation, application, and end-of-life scenarios. Existing studies provide insights into their environmental benefits compared to traditional stabilizers like OPC and lime. Summarized results from various studies are provided in Table 5.

Table 5. Life cycle assessment for clay stabilization using RHA and LS.

LCA Aspect	RHA + LS Stabilization	Traditional Stabilizers (Lime/OPC)	Findings	Source
Carbon Emissions	~30–50% reduction compared to OPC stabilization	High emissions from production (~800–1000 kg CO_2/ton for OPC)	RHA and LS are byproducts with negligible emissions during production, compared to OPC and lime, which involve energy-intensive processes like calcination	[72]
Energy Consumption	~60% lower than lime or OPC	High energy (~4–5 GJ/ton for OPC)	RHA and LS use energy only during minimal processing or transportation, compared to lime and OPC, which require extensive energy for raw material extraction and processing	[130]
Waste Utilization	100% reuse of agricultural (RHA) and industrial (LS) byproducts	Zero waste reuse	RHA and LS reduce waste disposal needs and landfill usage, making the stabilization process sustainable	[126]
Transportation Emissions	Low (local availability in rice/agriculture regions)	Moderate to high (dependent on production site distance)	RHA and LS sourced locally minimize transportation emissions, while OPC and lime often require transport over long distances, adding to the carbon footprint	[129]
Landfill Reduction	Significant reduction in waste sent to landfills	No landfill impact	By utilizing RHA and LS, waste that would typically go to landfills is repurposed, reducing the environmental impact of disposal and the need for landfill space	[131]
Cost of Stabilization	~25–50% lower than lime or OPC	High (cost of production and transport)	RHA and LS are low-cost or free byproducts, whereas lime and OPC involve substantial production costs that increase overall project expenses	[128]

These studies highlight the advantages of using RHA and LS for clay soil stabilization, providing specific data on material quantities, transportation distances, energy usage, and emissions factors.

To sum up the cost and sustainability evaluation, the adoption of sustainable materials such as rice husk ash and lime sludge, despite offering substantial environmental and economic benefits, is often constrained not by their quality or performance but by shortcomings in legislative frameworks at both national and EU levels. These materials are frequently classified as waste rather than valuable raw materials, subjecting them to restrictive regulations that limit their potential for reuse and valorization. Additionally, the absence of specific standards tailored to their properties and applications creates uncertainty, making it difficult for industries to incorporate them into industrial applications confidently. Lengthy and inconsistent regulatory approval processes further compound

these challenges, creating barriers to innovation and increasing adoption costs. To address these issues, transparent and harmonized end-of-waste criteria must be established, allowing rice husk ash and lime sludge to be officially recognized as resources rather than waste. Developing EU-wide standards and certification processes tailored to these materials would ensure consistent quality and streamline their integration into industrial applications. Furthermore, legislative incentives, such as subsidies, tax benefits, and grants, could encourage industries to adopt these sustainable materials, driving the transition toward a circular economy. By resolving these legislative challenges, policymakers can unlock the full potential of rice husk ash and lime sludge, reducing waste, promoting resource efficiency, and advancing sustainability goals across multiple sectors.

5. Results and Discussion

Rice husk ash and lime sludge offer unique advantages and disadvantages in clay soil stabilization. RHA, rich in amorphous silica, provides excellent pozzolanic properties, enhancing soil properties while promoting environmental sustainability by recycling agricultural waste. Similarly, LS, high in calcium hydroxide, improves soil properties and offers a cost-effective stabilization solution by repurposing industrial byproducts. However, both materials have drawbacks. RHA can release airborne silica particles, posing health risks if improperly handled, and LS may contain heavy metals or cause pH imbalances in water bodies if not managed responsibly.

This section presents the findings from the investigation into the stabilization of clay soil using RHA and LS. The results of standard Proctor compaction tests, unconfined compressive strength (UCS) tests, and California Bearing Ratio (CBR) tests are analyzed to evaluate the effects of varying proportions of RHA and LS on the clay soil characteristics. The discussion highlights the optimal proportions of RHA and LS for effective stabilization and their combined impact on improving clay soil performance.

The standard Proctor compaction test results reveal significant impacts of adding RHA and LS on the OMC and MDD of clay soils. The addition of RHA increases the OMC of the clay soil, with a notable rise when 10–20% RHA is added due to the water-absorbing capacity of RHA particles. Similarly, including LS results in increased OMC values, with optimal performance observed up to 15% LS. Beyond this threshold, the OMC declines as the clay soil matrix becomes overly rigid, reducing water retention capacity. The combined addition of RHA and LS further enhances the OMC progressively with increasing amounts of admixtures. An inverse relationship is observed between MDD and the content of RHA and LS. The reduction in MDD is linked to the lower specific gravity of the admixtures compared to natural soil, resulting in less dense compacted samples. Although the reduction in MDD could indicate decreased matrix strength, this is compensated by improved cohesion and binding effects due to RHA and LS.

The UCS tests show varied results based on the type and proportion of admixtures. Adding up to 4% LS enhances the UCS value, reflecting improved bonding between clay soil particles and lime. UCS increases with up to 10% RHA but decreases beyond this threshold. This decline is linked to a reduction in cohesion and internal friction, excess porosity, and unreactive RHA particles acting as fillers. The combination of RHA and LS has a synergistic effect, significantly improving UCS. However, the maximum UCS value is achieved with up to 6% RHA, indicating a lower optimal threshold when combined with LS. Higher LS proportions correlate with increased UCS, showcasing the stabilizing and strengthening potential of LS.

The CBR test results highlight the influence of RHA and LS on the load-bearing capacity of clay soil samples. The addition of 4% LS and RHA leads to increased CBR values, while excessive RHA (>15%) results in decreased CBR, attributed to increased

porosity and reduced cohesive strength. Combining RHA and LS significantly enhances the CBR values overall, improving clay soil load-bearing capacity and reducing plasticity. While both RHA and LS improve CBR values, excessive usage (above optimal thresholds) can have adverse effects, emphasizing the need for precise mix proportions.

The extracted results underscore the effectiveness of RHA and LS as stabilizing agents for clay soils. While each admixture has its independent impact, their combined use yields enhanced mechanical properties, including higher UCS and CBR values. However, the performance depends on maintaining optimal proportions to avoid adverse effects on clay soil strength.

Regarding cost evaluation, RHA and LS are consistently more cost-effective alternatives to OPC and lime, as they are readily available byproducts from industrial and agricultural processes. Depending on the method and application, cost savings range from 17% to 39%. Moreover, their use contributes to environmental sustainability, enhancing their overall value in various applications.

Regarding LCA analysis, RHA and LS offer notable environmental benefits by significantly reducing carbon emissions, energy consumption, and waste, aligning with sustainable practices. Their cost efficiency, driven by reduced expenses and easier environmental compliance, positions them as economically viable alternatives to OPC and lime. Additionally, their local availability, particularly in agricultural and industrial regions, enhances their practicality and supports regional development.

6. Conclusions

This comprehensive review aimed to assess the efficacy of clay soil stabilization using green materials, including RHA and LS, to determine the optimum quantity of RHA and LS. Adopting alternative green materials for clay stabilization offers a win–win solution, benefiting both the environment and the construction industry. The construction sector plays a crucial role in promoting sustainability by reducing carbon emissions, preserving natural resources, and decreasing reliance on chemical stabilizers. Based on the analyzed studies, an increase in the content of RHA and LS led to an increase in the OMC of clay soil and a corresponding reduction in its MDD. Adding RHA up to 10% improved the UCS and CBR values, after which a decline was observed. Similarly, using LS content of up to 8% for structural purposes and up to 4% for roadway and pavement purposes enhanced the UCS and CBR values. Moreover, the combined use of RHA and LS resulted in a significant increase in UCS and CBR values. For optimal stabilization, a combination of 6% RHA and 7% LS is recommended for structural purposes, while 10% RHA and 4% LS are ideal for roadway and pavement applications. Finally, future studies can focus on conducting a comprehensive review of the mechanical characteristics of various soil types treated with RHA and LS, including an in-depth analysis of stabilization effectiveness, variations in strength parameters, and the long-term durability of treated soils under diverse environmental conditions. Such research can provide valuable insights into optimizing application methods, understanding soil-behavior interactions, and expanding the practical applications of RHA and LS in sustainable geotechnical engineering.

Author Contributions: Conceptualization, H.R.M., E.P., N.C. and T.M.; methodology, H.R.M., E.P., N.C. and T.M.; formal analysis, H.R.M., E.P. and T.M.; investigation, H.R.M., E.P. and T.M.; resources, E.P., N.C. and T.M.; writing—original draft, H.R.M.; writing—review and editing, H.R.M., E.P., N.C. and T.M.; supervision, E.P., N.C. and T.M.; project administration, E.P., N.C. and T.M.; funding acquisition, E.P., N.C. and T.M. All authors have read and agreed to the published version of the manuscript.

Funding: This research was funded by the project "NGS—New Generation Storage", with reference C644936001-00000045, financed by the Recovery and Resilience Plan and the Next Generation EU European Funds.

Institutional Review Board Statement: Not applicable.

Informed Consent Statement: Not applicable.

Data Availability Statement: Not available.

Acknowledgments: The authors would like to thank the Recovery and Resilience Plan.

Conflicts of Interest: The authors declare no conflicts of interest.

References

1. Afrin, H. A Review on Different Types of Soil Stabilization Techniques. *Int. J. Transp. Eng. Technol.* **2017**, *3*, 19–24. [CrossRef]
2. Amhadi, T.S.; Assaf, G.J. Overview of Soil Stabilization Methods in Road Construction. In *Sustainable Solutions for Railways and Transportation Engineering: Proceedings of the 2nd GeoMEast International Congress and Exhibition on Sustainable Civil Infrastructures, Egypt 2018–The Official International Congress of the Soil-Structure Interaction Group in Egypt (SSIGE)*; Springer International Publishing: Cham, Switzerland, 2019; pp. 21–33.
3. Manaviparast, H.R.; Araújo, N.; Cristelo, N.; Miranda, T. Study on Guardrail Post Behavior Located on Organic Soil Using Simplified Experimental and Numerical Methods. *Soils Rocks* **2022**, *45*, e2022077921. [CrossRef]
4. Sujatha, E.R.; Saisree, S. Geotechnical Behaviour of Guar Gum-Treated Soil. *Soils Found.* **2019**, *59*, 2155–2166. [CrossRef]
5. Huang, J.; Kogbara, R.B.; Hariharan, N.; Masad, E.A.; Little, D.N. A State-of-the-Art Review of Polymers Used in Soil Stabilization. *Constr. Build. Mater.* **2021**, *305*, 124685. [CrossRef]
6. Onodagu, P.D.; Uzodinma, F.C.; Aginam, C.H. Effects of Untreated Oil-Palm Fruit Fibre Reinforcements on the Strength and Durability Properties of Non-Fired Pressed Mud Blocks. *Niger. J. Technol.* **2022**, *41*, 21–25. [CrossRef]
7. Ullah, A.; Boumezerane, D.; Ahmad, F. Subgrade Improvement with Mixed Lime and Cement as Additives. *Mater. Today Proc.* **2023**, *in press*. [CrossRef]
8. Yang, J.; Tan, F.H.; Tan, A. The Ancient Construction Materials and Methods: The Great Wall of China in Jinshanling as a Case Study. *J. Constr. Eng. Proj. Manag.* **2017**, *7*, 37–49. [CrossRef]
9. Su, Z.; Yan, Z.; Nakashima, K.; Takano, C.; Kawasaki, S. Naturally Derived Cements Learned from the Wisdom of Ancestors: A Literature Review Based on the Experiences of Ancient China, India, and Rome. *Materials* **2023**, *16*, 603. [CrossRef] [PubMed]
10. Vitti, P. Mortars and Masonry—Structural Lime and Gypsum Mortars in Antiquity and Middle Ages. *Archaeol. Anthropol. Sci.* **2021**, *13*, 164. [CrossRef]
11. Mendonça, A.; Morais, P.V.; Pires, A.C.; Chung, A.P.; Oliveira, P.V. A Review on the Importance of Microbial Biopolymers Such as Xanthan Gum to Improve Soil Properties. *Appl. Sci.* **2020**, *11*, 170. [CrossRef]
12. Jang, J. A Review of the Application of Biopolymers on Geotechnical Engineering and the Strengthening Mechanisms Between Typical Biopolymers and Soils. *Adv. Mater. Sci. Eng.* **2020**, 1465709. [CrossRef]
13. Ferreira, F.A.; Desir, J.M.; De Lima, G.E.S.; Pedroti, L.G.; De Carvalho, J.M.F.; Lotero, A.; Consoli, N.C. Evaluation of Mechanical and Microstructural Properties of Eggshell Lime/Rice Husk Ash Alkali-Activated Cement. *Constr. Build. Mater.* **2023**, *364*, 129931. [CrossRef]
14. Ikeagwuani, C.C.; Nwonu, D.C. Emerging Trends in Expansive Soil Stabilisation: A Review. *J. Rock Mech. Geotechnol. Eng.* **2019**, *11*, 423–440. [CrossRef]
15. Türköz, M.; Umu, S.U.; Öztürk, O. Effect of Silica Fume as a Waste Material for Sustainable Environment on the Stabilization and Dynamic Behavior of Dispersive Soil. *Sustainability* **2021**, *13*, 4321. [CrossRef]
16. ALERTA, A.Z.A.; BAYRAKTAR, O.Y.; Soylemez, H. Investigation of the Effects of Modified Bitumen on Asphalt Concrete Performance by Industrial Waste. *Kastamonu Univ. J. Eng. Sci.* **2019**, *5*, 93–100.
17. Kamal, I.; Bas, Y. Materials and Technologies in Road Pavements—An Overview. *Mater. Today Proc.* **2021**, *42*, 2660–2667. [CrossRef]
18. Garipov, A.; Makarov, D.; Khozin, V.; Stepanov, S.; Ayupov, D. Cement Concrete Modified by Fine-Dispersed Anionactive Bitumen Emulsion for Road Construction. *IOP Conf. Ser. Mater. Sci. Eng.* **2020**, *890*, 012107. [CrossRef]
19. Sinha, P.; Anusha Raj, K.; Kumar, S.; Singh, D. Mechanical Behavior of Geotextile and Geogrids on Soil Stabilization: A Review. In *Recent Advances in Mechanical Engineering: Select Proceedings of CAMSE 2021*; Springer: Berlin/Heidelberg, Germany, 2022; pp. 299–308.
20. Kumar, S.; Singh, S.K. Subgrade Soil Stabilization Using Geosynthetics: A Critical Review. *Mater. Today Proc.* **2023**, *in press*. [CrossRef]

21. Karami, H.; Pooni, J.; Robert, D.; Costa, S.; Li, J.; Setunge, S. Use of Secondary Additives in Fly Ash Based Soil Stabilization for Soft Subgrades. *Transp. Geotechnol.* **2021**, *29*, 100585. [CrossRef]
22. Manaviparast, H.R.; Pinheiro, J.; Najafi, E.K.; Abreu, C.; Araújo, N.; Cristelo, N.; Miranda, T. Mechanical Behavior of a Mine Tailing Stabilized with a Sustainable Binder. *Appl. Sci.* **2023**, *13*, 4103. [CrossRef]
23. Wu, J.; Deng, Y.; Zhang, G.; Zhou, A.; Tan, Y.; Xiao, H.; Zheng, Q. A Generic Framework of Unifying Industrial Byproducts for Soil Stabilization. *J. Clean. Prod.* **2021**, *321*, 128920. [CrossRef]
24. Nawaz, M.; Heitor, A.; Sivakumar, M. Geopolymers in Construction—Recent Developments. *Constr. Build. Mater.* **2020**, *260*, 120472. [CrossRef]
25. Onyelowe, K.; Van, D.B.; Igboayaka, C.; Orji, F.; Ugwuanyi, H. Rheology of Mechanical Properties of Soft Soil and Stabilization Protocols in the Developing Countries—Nigeria. *Mater. Sci. Energy Technol.* **2019**, *2*, 8–14. [CrossRef]
26. Haris, A.; Dhanya, M. A Review on the Combined Effect of Lime, Fly Ash, and Geosynthetic Reinforcement on Soil. *Appl. Sci.* **2020**.
27. Andavan, S.; Pagadala, V.K. A Study on Soil Stabilization by Addition of Fly Ash and Lime. *Mater. Today Proc.* **2020**, *22*, 1125–1129. [CrossRef]
28. Indiramma, P.; Sudharani, C.; Needhidasan, S. Utilization of Fly Ash and Lime to Stabilize the Expansive Soil and to Sustain Pollution-Free Environment—An Experimental Study. *Mater. Today Proc.* **2020**, *22*, 694–700. [CrossRef]
29. Adabi, M.; Darvishan, E.; Eyvazi, G.; Jahanbaksh Motlagh, H. Geoenvironmental Application of Novel Persian Gum Biopolymer in Sandy Soil Stabilization. *Arab. J. Sci. Eng.* **2022**, *47*, 12915–12929. [CrossRef]
30. Divya, M.J.; Bikku, M.P. Techniques of Ground Improvement and its Applications. *Dogo Rangsang Res. J.* **2022**, *12*, 7–21.
31. Jawad, Z.H.; Shakir, R.R. Behavior of Foundation Rested on Geogrid-Reinforced Soil: A Review. *IOP Conf. Ser. Mater. Sci. Eng.* **2021**, *1094*, 012110. [CrossRef]
32. Zhang, T.; Liu, S.; Zhan, H.; Ma, C.; Cai, G. Durability of Silty Soil Stabilized with Recycled Lignin for Sustainable Engineering Materials. *J. Clean. Prod.* **2020**, *248*, 119293. [CrossRef]
33. Tan, E.H.; Zahran, E.M.M.; Tan, S.J. A Review of Chemical Stabilisation in Road Construction. *IOP Conf. Ser. Mater. Sci. Eng.* **2020**, *943*, 012005. [CrossRef]
34. Phang, I.R.K.; Wong, K.S.; Chan, Y.S.; Lau, S.Y. Effect of Surcharge Load on Microbial-Induced Calcite Precipitation (MICP) Treatment of Tropical Peat. *IOP Conf. Ser. Mater. Sci. Eng.* **2019**, *495*, 012068. [CrossRef]
35. Schwerdt, S.; Mirschel, D.; Hildebrandt, T.; Wilke, M.; Schneider, P. Substitute Building Materials in Geogrid-Reinforced Soil Structures. *Sustainability* **2021**, *13*, 12519. [CrossRef]
36. Puppala, A.J.; Congress, S.S.; Banerjee, A. Research Advancements in Expansive Soil Characterization, Stabilization, and Geoinfrastructure Monitoring. In *Frontiers in Geotechnical Engineering*; Springer: Singapore, 2019; pp. 15–29.
37. Zhang, Y.; Wang, Y.; Shah, K.F.; Li, T. Moisture Stabilization of Embankment Subgrade with Capillary Barrier Cover Under Dry and Rainy Weathers. *Transp. Geotechnol.* **2023**, *42*, 101057. [CrossRef]
38. Sharonova, O.M.; Kirilets, V.M.; Yumashev, V.V.; Solovyov, L.A.; Anshits, A.G. Phase Composition of High-Strength Binding Material Based on Fine Microspherical High-Calcium Fly Ash. *Constr. Build. Mater.* **2019**, *216*, 525–530. [CrossRef]
39. Anburuvel, A. The Engineering Behind Soil Stabilization with Additives: A State-of-the-Art Review. *Geotechnol. Geol. Eng.* **2023**, *42*, 1–42. [CrossRef]
40. Chen, K.; Wu, D.; Zhang, Z.; Pan, C.; Shen, X.; Xia, L.; Zang, J. Modeling and Optimization of Fly Ash–Slag-Based Geopolymer Using Response Surface Method and Its Application in Soft Soil Stabilization. *Constr. Build. Mater.* **2022**, *315*, 125723. [CrossRef]
41. Wang, S.; Guo, S.; Gao, X.; Zhang, P.; Li, G. Effects of Cement Content and Soil Texture on Strength, Hydraulic, and Microstructural Characteristics of Cement-Stabilized Composite Soils. *Bull. Eng. Geol. Environ.* **2022**, *81*, 264. [CrossRef]
42. Qiao, G.; Hou, D.; Li, W.; Yin, B.; Zhang, Y.; Wang, P. Molecular Insights into Migration of Heavy Metal Ion in Calcium Silicate Hydrate (CSH) Surface and Intra-CSH (Ca/Si = 1.3). *Constr. Build. Mater.* **2023**, *365*, 130097. [CrossRef]
43. Baldovino, J.J.; Izzo, R.L.; Rose, J.L.; Domingos, M.D. Strength, Durability, and Microstructure of Geopolymers Based on Recycled-Glass Powder Waste and Dolomitic Lime for Soil Stabilization. *Constr. Build. Mater.* **2021**, *271*, 121874. [CrossRef]
44. Chen, R.; Zhu, Y.; Lai, H.P.; Bao, W. Stabilization of Soft Soil Using Low-Carbon Alkali-Activated Binder. *Environ. Earth Sci.* **2020**, *79*, 1–13. [CrossRef]
45. Muhammad, A.; Yusuf, A.; Umar, M. Assessment of Lateritic Soil Stabilized Using Metakaolin. *J. Geotechnol. Stud.* **2020**, *5*, 15–26.
46. Naeini, A.A.; Siddiqua, S.; Cherian, C. A Novel Stabilized Rammed Earth Using Pulp Mill Fly Ash as Alternative Low Carbon Cementing Material. *Constr. Build. Mater.* **2021**, *300*, 124003. [CrossRef]
47. Lu, J.; Jiang, S.Y.; Chen, J.; Lee, C.H.; Cai, Z.; Ruan, H.D. Fabrication of Superhydrophobic Soil Stabilizers Derived from Solid Wastes Applied for Road Construction: A Review. *Transp. Geotechnol.* **2023**, *40*, 100974. [CrossRef]
48. Chand, G.; Ram, S.; Kumar, S.; Gupta, U. Microstructural and Engineering Properties Investigation of Sustainable Hybrid Concrete Produced from Industrial Wastes. *Cleaner Eng. Technol.* **2021**, *2*, 100052. [CrossRef]

49. Sim, S.; Her, S.; Suh, H.; Cho, S.; Im, S.; Li, P.; Bae, S. Influences of Alumina Type and Sulfate Content on Hydration and Physicochemical Changes in Portland–Limestone Cement. *Constr. Build. Mater.* **2024**, *426*, 135989. [CrossRef]
50. Hossain, M.U.; Poon, C.S.; Wong, M.Y.K.; Khine, A. Techno-Environmental Feasibility of Wood Waste Derived Fuel for Cement Production. *J. Clean. Prod.* **2019**, *230*, 663–671. [CrossRef]
51. Costa, F.N.; Ribeiro, D.V. Reduction in CO_2 Emissions During Production of Cement, with Partial Replacement of Traditional Raw Materials by Civil Construction Waste (CCW). *J. Clean. Prod.* **2020**, *276*, 123302. [CrossRef]
52. Patil, M.; Boraste, S.; Minde, P. A Comprehensive Review on Emerging Trends in Smart Green Building Technologies and Sustainable Materials. *Mater. Today Proc.* **2022**, *65*, 1813–1822. [CrossRef]
53. Rosa, L.; Sanchez, D.L.; Realmonte, G.; Baldocchi, D.; D'Odorico, P. The Water Footprint of Carbon Capture and Storage Technologies. *Renew. Sustain. Energy Rev.* **2021**, *138*, 110511. [CrossRef]
54. Najafi, E.K.; Tavares, P.; Miranda, T.; Manaviparast, H.R.; Cristelo, N. Ophthalmic Glass Lens Waste as an Alternative Soluble Silica Source for Alkali-Activation Reactions. *Constr. Build. Mater.* **2023**, *392*, 131854. [CrossRef]
55. Amakye, S.Y.; Abbey, S.J.; Booth, C.A.; Mahamadu, A.M. Enhancing the Engineering Properties of Subgrade Materials Using Processed Waste: A Review. *Geotechnics* **2021**, *1*, 307–329. [CrossRef]
56. Kamseu, E.; Alzari, V.; Rosa, R.; Nuvoli, D.; Sanna, D.; Mariani, A.; Leonelli, C. Marble Wastes Recycling: Design and Synthesis of Low-Temperature Calcium Silicate Hydrate Under Various CaO Ratio and Alkalinity. *Materialia* **2021**, *20*, 101224. [CrossRef]
57. Sangmesh, B.; Patil, N.; Jaiswal, K.K.; Gowrishankar, T.P.; Selvakumar, K.K.; Jyothi, M.S.; Kumar, S. Development of Sustainable Alternative Materials for the Construction of Green Buildings Using Agricultural Residues: A Review. *Constr. Build. Mater.* **2023**, *368*, 130457.
58. Boonphayak, P.; Khansumled, S.; Yatongchai, C. Synthesis of CaO-SiO2 Catalyst from Lime Mud and Kaolin Residue for Biodiesel Production. *Mater. Lett.* **2021**, *283*, 128759. [CrossRef]
59. Sakr, M.A.; Azzam, W.R.; El-Sawwaf, M.A.; El-Disouky, E.A. Lime Columns Technique for the Improvement of Soft Clay—A Review. *J. Multidiscip. Eng. Sci. Stud.* **2021**, *7*, 3893–3897.
60. Zada, U.; Jamal, A.; Iqbal, M.; Eldin, S.M.; Almoshaogeh, M.; Bekkouche, S.R.; Almuaythir, S. Recent Advances in Expansive Soil Stabilization Using Admixtures: Current Challenges and Opportunities. *Case Stud. Constr. Mater.* **2023**, *18*, e01985. [CrossRef]
61. Rabbani, P.; Lajevardi, S.H. Laboratory Investigation of the Effect of Deep Soil Mixing Method on Engineering Properties of Soft Clay Stabilized by Slag and Lime. *Methodology* **2019**, *7*, 9.
62. Vu, H.H.T.; Khan, M.D.; Chilakala, R.; Lai, T.Q.; Thenepalli, T.; Ahn, J.W.; Kim, J. Utilization of Lime Mud Waste from Paper Mills for Efficient Phosphorus Removal. *Sustainability* **2019**, *11*, 1524. [CrossRef]
63. Eliaslankaran, Z.; Daud, N.N.N.; Yusoff, Z.M.; Rostami, V. Evaluation of the Effects of Cement and Lime with Rice Husk Ash as an Additive on Strength Behavior of Coastal Soil. *Materials* **2021**, *14*, 1140. [CrossRef] [PubMed]
64. Ferronato, N.; Torretta, V. Waste Mismanagement in Developing Countries: A Review of Global Issues. *Int. J. Environ. Res. Public Health* **2019**, *16*, 1060. [CrossRef] [PubMed]
65. Abhijith, L.; Varghese, E.M. Removal of Zinc and Copper from Contaminated Soil by Using Adsorbents and Mulches. In *AIP Conference Proceeding*; AIP Publishing LLC: Melville, NY, USA, 2021; Volume 2396, p. 030005.
66. Singh, S.; Ashesh, A.; Devi, N.L.; Yadav, I.C. A Comprehensive Review on Occurrence, Source, Effect, and Measurement Techniques of Polycyclic Aromatic Hydrocarbons in India. *Microchem. J.* **2022**, *183*, 108005. [CrossRef]
67. Jasim, N.A.; Ibrahim, J.A.K. Stabilization of Al-Rustamiya Waste Water Treatment Plant Sludge Using Lime. *J. Eng.* **2020**, *26*, 165–172. [CrossRef]
68. Elbehiry, F.; Alshaal, T.; Elhawat, N.; Elbasiouny, H. Environmental-Friendly and Cost-Effective Agricultural Wastes for Heavy Metals and Toxicants Removal from Wastewater. In *Cost-Efficient Wastewater Treatment Technologies: Natural Systems*; Springer International Publishing: Cham, Switzerland, 2021; pp. 107–127.
69. Riza, M.; Ehsan, M.N.; Pervez, M.N.; Khyum, M.M.O.; Cai, Y.; Naddeo, V. Control of Eutrophication in Aquatic Ecosystems by Sustainable Dredging: Effectiveness, Environmental Impacts, and Implications. *Case Stud. Chem. Environ. Eng.* **2023**, *7*, 100297. [CrossRef]
70. Raja, K.; Venkatachalam, S.; Vishnuvardhan, K.; Krishnan, R.S.R.; Selvan, V.T.; Vetriselvan, N. A Review on Soil Stabilization Using Rice Husk Ash and Lime Sludge. *Mater. Today Proc.* **2022**, *65*, 1205–1212. [CrossRef]
71. Vijayan, D.S.; Parthiban, D. Effect of Solid Waste-Based Stabilizing Material for Strengthening of Expansive Soil—A Review. *Environ. Technol. Innov.* **2020**, *20*, 101108. [CrossRef]
72. Pushpakumara, B.H.J.; Mendis, W.S.W. Suitability of Rice Husk Ash (RHA) with Lime as a Soil Stabilizer in Geotechnical Applications. *Int. J. Geo-Eng.* **2022**, *13*, 4. [CrossRef]
73. Das, S.K.; Adediran, A.; Kaze, C.R.; Mustakim, S.M.; Leklou, N. Production, Characteristics, and Utilization of Rice Husk Ash in Alkali-Activated Materials: An Overview of Fresh and Hardened State Properties. *Constr. Build. Mater.* **2022**, *345*, 128341.
74. Rahmat, A.; Nissa, R.C.; Nuraini, L.; Nurtanto, M.; Ramadhani, W.S. Analysis of Rice Husk Biochar Characteristics Under Different Pyrolysis Temperature. *IOP Conf. Ser. Earth Environ. Sci.* **2023**, *1201*, 012095.

75. Naveen, C.C.; Kunnoth, B.; Pilli, S.; Rao, P.V.; Surampalli, R.Y.; Zhang, T.C.; Bhunia, P. Effects of Different Parameters and Co-Digestion Options on Anaerobic Digestion of Parboiled Rice Mill Wastewater: A Review. *Bioenergy Res.* **2022**, *17*, 1191–1207. [CrossRef]
76. Liou, T.H.; Tseng, Y.K.; Zhang, T.Y.; Liu, Z.S.; Chen, J.Y. Rice Husk Char as a Sustainable Material for the Preparation of Graphene Oxide-Supported Biocarbons with Mesoporous Structure: A Characterization and Adsorption Study. *Fuel* **2023**, *344*, 128042. [CrossRef]
77. Abbass, M.; Singh, D.; Singh, G. Properties of Hybrid Geopolymer Concrete Prepared Using Rice Husk Ash, Fly Ash, and GGBS with Coconut Fiber. *Mater. Today Proc.* **2021**, *45*, 4964–4970. [CrossRef]
78. Ge, S.; Yek, P.N.Y.; Cheng, Y.W.; Xia, C.; Mahari, W.A.W.; Liew, R.K.; Lam, S.S. Progress in Microwave Pyrolysis Conversion of Agricultural Waste to Value-Added Biofuels: A Batch to Continuous Approach. *Renew. Sustain. Energy Rev.* **2021**, *135*, 110148. [CrossRef]
79. Rithuparna, R.; Jittin, V.; Bahurudeen, A. Influence of Different Processing Methods on the Recycling Potential of Agro-Waste Ashes for Sustainable Cement Production: A Review. *J. Clean. Prod.* **2021**, *316*, 128242. [CrossRef]
80. Bouzón, N.; Font, A.; Borrachero, M.V.; Soriano, L.; Monzó, J.; Tashima, M.M.; Payá, J. Evaluation of Thermo-Chemical Treatments for Rice Husk Ash Valorisation as a Source of Silica in Preparing Geopolymers. *Materials* **2023**, *16*, 4667. [CrossRef]
81. Isberto, C.D.; Labra, K.L.; Landicho, J.M.B.; De Jesus, R. Optimized Preparation of Rice Husk Ash (RHA) as a Supplementary Cementitious Material. *Geomate J.* **2019**, *16*, 56–61. [CrossRef]
82. Plando, F.R.P.; Gili, M.B.Z.; Maquiling, J.T. Microstructural Characterizations and Radiation Shielding Quantities of Rice Husk Ash-Based Self-Compacting Concrete and Its Precursors. *Radiat. Phys. Chem.* **2023**, *208*, 110916. [CrossRef]
83. Lu, S.G.; Sun, F.F.; Zong, Y.T. Effect of Rice Husk Biochar and Coal Fly Ash on Some Physical Properties of Expansive Clayey Soil (Vertisol). *Catena* **2014**, *114*, 37–44. [CrossRef]
84. Das, S.K.; Mishra, J.; Singh, S.K.; Mustakim, S.M.; Patel, A.; Das, S.K.; Behera, U. Characterization and Utilization of Rice Husk Ash (RHA) in Fly Ash–Blast Furnace Slag Based Geopolymer Concrete for Sustainable Future. *Mater. Today Proc.* **2020**, *33*, 5162–5167. [CrossRef]
85. Nazarpour-Fard, H. Rice Husk Ash: Economical and High-Quality Natural-Based Reinforcing Filler for Linear Low-Density and High-Density Polyethylene. *Polymers Renew. Resour.* **2022**, *13*, 206–222. [CrossRef]
86. Abdullah, M.N.I.; Mustapha, F.; Ahmad, K.A.; Mustapha, M.; Khan, T.; Singh, B.; Sebaey, T.A. Effect of Different Pre-Treatment on the Microstructure and Intumescent Properties of Rice Husk Ash-Based Geopolymer Hybrid Coating. *Polymers* **2022**, *14*, 2252. [CrossRef] [PubMed]
87. Sivalingam, S.; Sen, S. Rice Husk Ash Derived Nanocrystalline ZSM-5 for Highly Efficient Removal of a Toxic Textile Dye. *J. Mater. Res. Technol.* **2020**, *9*, 14853–14864. [CrossRef]
88. Nduka, D.O.; Olawuyi, B.J.; Fagbenle, O.I.; Fonteboa, B.G. Assessment of the Durability Dynamics of High-Performance Concrete Blended with a Fibrous Rice Husk Ash. *Crystals* **2022**, *12*, 75. [CrossRef]
89. Althoey, F.; Zaid, O.; de-Prado-Gil, J.; Palencia, C.; Ali, E.; Hakeem, I.; Martínez-García, R. Impact of Sulfate Activation of Rice Husk Ash on the Performance of High Strength Steel Fiber Reinforced Recycled Aggregate Concrete. *J. Build. Eng.* **2022**, *54*, 104610. [CrossRef]
90. Pham, T.M. Enhanced Properties of High-Silica Rice Husk Ash-Based Geopolymer Paste by Incorporating Basalt Fibers. *Constr. Build. Mater.* **2020**, *245*, 118422.
91. Bijalwan, A.; Mishra, A.K.; Sonowal, B. Strength, Durability, and Toxicity Characteristics of Water Treatment Sludge Based Geopolymers for Subgrade Application. *Constr. Build. Mater.* **2024**, *447*, 138162. [CrossRef]
92. Han, J.S.; Kang, D.S.; Seo, Y.B. Application of In Situ Calcium Carbonate Process for Producing Papermaking Fillers from Lime Mud. *ACS Omega* **2021**, *6*, 3884–3890. [CrossRef] [PubMed]
93. Vashistha, P.; Kumar, V.; Singh, S.K.; Dutt, D.; Tomar, G.; Yadav, P. Valorization of Paper Mill Lime Sludge via Application in Building Construction Materials: A Review. *Constr. Build. Mater.* **2019**, *211*, 371–382. [CrossRef]
94. Phanikumar, B.R.; Raju, E.R. Compaction and Strength Characteristics of an Expansive Clay Stabilized with Lime Sludge and Cement. *Soils Found.* **2020**, *60*, 129–138. [CrossRef]
95. Peter, M.A. Effects of Stone Dust on Lime Stabilized Granular Soil. *IOP Conf. Ser. Earth Environ. Sci.* **2023**, *1110*, 012024. [CrossRef]
96. Avinash, B.; Kumar, S.R. Influence of Industrial Wastes and Lime on Strength Characteristics of Clayey Soil. *Magaz. Civ. Eng.* **2023**, *120*, 12002.
97. Majumder, M.; Venkatraman, S. Utilization of Lime as Subgrade Stabilizer in the Pavement Construction. *Arab. J. Sci. Eng.* **2022**, *47*, 4929–4942. [CrossRef]
98. Guleria, A.; Thakur, S.; Gautam, C.P. *Stabilization of Mohali Soil Using RHA and Lime Sludge*; Jaypee University of Information Technology: Waknaghat, India, 2017.
99. Liu, Y.; Su, Y.; Namdar, A.; Zhou, G.; She, Y.; Yang, Q. Utilization of Cementitious Material from Residual Rice Husk Ash and Lime in Stabilization of Expansive Soil. *Adv. Civ. Eng.* **2019**. [CrossRef]

100. Muntohar, A.S.; Widianti, A.; Hartono, E.; Diana, W. Engineering Properties of Silty Soil Stabilized with Lime and Rice Husk Ash and Reinforced with Waste Plastic Fiber. *J. Mater. Civ. Eng.* **2013**, *25*, 1260–1270. [CrossRef]
101. Modarres, A.; Nosoudy, Y.M. Clay Stabilization Using Coal Waste and Lime—Technical and Environmental Impacts. *Appl. Clay Sci.* **2015**, *116*, 281–288. [CrossRef]
102. Maheswaran, S.; Kalaiselvam, S.; Karthikeyan, S.S.; Kokila, C.; Palani, G.S. β-Belite Cements (β-Dicalcium Silicate) Obtained from Calcined Lime Sludge and Silica Fume. *Cement Concr. Compos.* **2016**, *66*, 57–65. [CrossRef]
103. Kashyap, S.; Datta, D. Industrial Lime Sludge Waste–HDPE Composites: A Study of Their Mechanical, Thermal, and Morphological Properties. *J. Thermoplast. Compos. Mater.* **2018**, *31*, 1323–1340. [CrossRef]
104. Vashistha, P.; Singh, S.K.; Dutt, D.; Kumar, V. Synthesis of Nanosilica from Fly Ash and Its Utilization with Lime Sludge in Concrete: An Environmentally Friendly and Sustainable Solution. *Clean Technol. Environ. Policy* **2019**, *21*, 1841–1853. [CrossRef]
105. Prakash, J.; Kumari, K.; Kumar, V. Stabilization of Soil Using Rice Husk Ash. *Int. J. Innov. Res. Sci. Eng. Technol.* **2017**, *6*, 12997–13003.
106. Bhattacharjee, A.; Borgohain, B. Improvement of California Bearing Ratio of Laterite Soil Using Rice Husk Ash. In Proceedings of the 50th Indian Geotechnical Conference, Pune, India, 17–19 December 2015.
107. Rather, S.A.; Sharma, N.; Najar, I.A. Effects of Rice Husk Ash (RHA) and Alccofine-1101 on Stabilization of Clay Soil. *Int. Res. J. Eng. Technol.* **2019**, *6*, 474–478.
108. Chandak, N.R.; Babu, A. Effect of Lime Sludge on Strength and Compaction of Soil. *J. Civ. Eng. Res.* **2015**, *5*, 18–20.
109. Sabat, A.K. Engineering Properties of an Expansive Soil Stabilized with Rice Husk Ash and Lime Sludge. *Int. J. Eng. Technol.* **2013**, *5*, 4826–4833.
110. Burra, S.G.; Kolay, P.K.; Puri, V.K.; Kumar, S. Strength and Compressibility of Kaolinite Clay Stabilized with Lime Sludge and Fly Ash. In *Ground Improvement and Reinforced Soil Structures: Proceedings of Indian Geotechnical Conference 2020*; Springer Singapore: Singapore, 2021; Volume 2, pp. 271–281.
111. Harichane, K.; Ghrici, M.; Kenai, S.; Grine, K. Use of Natural Pozzolana and Lime for Stabilization of Cohesive Soils. *Geotechnol. Geol. Eng.* **2011**, *29*, 759–769. [CrossRef]
112. Singh, S.; Chohan, J.S.; Kumar, R. Stabilization of Kaolin via Lime and Pond Ash. *Mater. Today Proc.* **2022**, *51*, 988–992. [CrossRef]
113. Chenarboni, H.A.; Lajevardi, S.H.; Molaabasi, H.; Zeighami, E. The Effect of Zeolite and Cement Stabilization on the Mechanical Behavior of Expansive Soils. *Constr. Build. Mater.* **2021**, *272*, 121630. [CrossRef]
114. Lin, D.F.; Lin, K.L.; Hung, M.J.; Luo, H.L. Sludge Ash/Hydrated Lime on the Geotechnical Properties of Soft Soil. *J. Hazard. Mater.* **2007**, *145*, 58–64. [CrossRef] [PubMed]
115. Sabat, A.K. Utilization of Bagasse Ash and Lime Sludge for Construction of Flexible Pavements in Expansive Soil Areas. *Electron. J. Geotechnol. Eng.* **2012**, *17*, 1037–1046.
116. Hossain, K.M.A. Stabilized Soils Incorporating Combinations of Rice Husk Ash and Cement Kiln Dust. *J. Mater. Civ. Eng.* **2011**, *23*, 1320–1327. [CrossRef]
117. Sabat, A.K.; Nanda, R.P. Effect of Marble Dust on Strength and Durability of Rice Husk Ash Stabilized Expansive Soil. *Int. J. Civ. Struct. Eng.* **2011**, *1*, 939–948.
118. Jiang, X.; Huang, Z.; Ma, F.; Luo, X. Analysis of Strength Development and Soil–Water Characteristics of Rice Husk Ash–Lime Stabilized Soft Soil. *Materials* **2019**, *12*, 3873. [CrossRef] [PubMed]
119. Niyomukiza, J.B.; Wardani, S.P.R.; Setiadji, B.H. The Effect of Curing Time on the Engineering Properties of Sawdust and Lime Stabilized Expansive Soils. In *Proceedings of the 2nd International Symposium on Transportation Studies in Developing Countries (ISTSDC 2019)*; Atlantis Press: Amsterdam, The Netherlands, 2020; pp. 157–161.
120. Gunjagi, M.D.; Wadar, R.; Patil, A.; Gurme, S.; Nalang, A.; Kamble, M. To Study the Effect of Lime and Rice Husk Ash on CBR Parameters of Black Cotton Soil. *Int. Res. J. Eng. Technol.* **2019**, *6*.
121. Lakshmi, S.M.; Geetha, S.; Selvakumar, M.; Susanna, K.D. Strength Enhancement of Clayey Sand Subgrade Using Lime and Rice Husk Ash. *Mater. Today Proc.* **2021**, *46*, 7430–7435. [CrossRef]
122. Lu, C.; Chen, J.; Gu, C.; Wang, J.; Cai, Y.; Zhang, T. Resilient and permanent deformation behaviors of construction and demolition wastes in unbound pavement base and subbase applications. *Transp. Geotechnol.* **2021**, *28*, 100541. [CrossRef]
123. Anupam, A.K.; Kumar, P.; Ransingchung RN, G.D. Performance evaluation of structural properties for soil stabilised using rice husk ash. *Road Mater. Pavement Des.* **2014**, *15*, 539–553. [CrossRef]
124. Domphoeun, R.; Otaghsaraei, A.E.; Nishimura, S. Geotechnical Properties of Rice Husk Ash and Coconut Fiber Stabilized Soil and Its Performance Evaluation as Subbase Material. Ph.D. Dissertation, Thammasat University, Bangkok, Thailand, 2023.
125. Fall, M.; Sawangsuriya, A.; Benson, C.H.; Edil, T.B.; Bosscher, P.J. On the investigations of resilient modulus of residual tropical gravel lateritic soils from Senegal (West Africa). *Geotechnol. Geol. Eng.* **2008**, *26*, 13–35. [CrossRef]
126. Karatai, T.R. Technical and Economic Evaluation of Soil Stabilization Using Rice Husk Ash (RHA) and Natural Lime (NL) as an Alternative to Cutting and Filling in Road Construction. Ph.D. Dissertation, JKUAT, Juja, Thika, 2018.
127. Ganta, S. Soil Stabilization with Rice Husk Ash and Lime Sludge. *Int. J. Res.* **2017**, *4*, 1112–1119.

128. Harikumar, M.; Firozemon, N.P.; Rithika, S.; Nipin, S.; Shayifa, T.S.; Jini, K.M. Experimental Investigation on Compressed Stabilized Earth Block. *Int. J. Sci. Eng. Res.* **2016**, *7*, 76–84.
129. Chen, R.; Congress, S.S.C.; Cai, G.; Duan, W.; Liu, S. Sustainable Utilization of Biomass Waste-Rice Husk Ash as a New Solidified Material of Soil in Geotechnical Engineering: A Review. *Constr. Build. Mater.* **2021**, *292*, 123219. [CrossRef]
130. Barwar, A.; Chandrappa, A.K.; Sahoo, U.C. Laboratory Investigations on Stabilization of Weak Clay Soil Using Rice Husk Ash and Cement. *Innov. Infrastruct. Solut.* **2022**, *7*, 327. [CrossRef]
131. Asavapisit, S.; Macphee, D.E. Immobilization of Metal-Containing Waste in Alkali-Activated Lime–RHA Cementitious Matrices. *Cem. Concr. Res.* **2007**, *37*, 776–780. [CrossRef]

Disclaimer/Publisher's Note: The statements, opinions and data contained in all publications are solely those of the individual author(s) and contributor(s) and not of MDPI and/or the editor(s). MDPI and/or the editor(s) disclaim responsibility for any injury to people or property resulting from any ideas, methods, instructions or products referred to in the content.

applied sciences

MDPI

Review

A Comprehensive Review on Mine Tailings as a Raw Material in the Alkali Activation Process

Hamid Reza Manaviparast [1,*], Tiago Miranda [2], Eduardo Pereira [3] and Nuno Cristelo [4]

[1] Department of Civil Engineering, University of Minho, 4800-058 Guimarães, Portugal
[2] Institute for Sustainability and Innovation in Structural Engineering (ISISE), Associate Laboratory Advanced Production and Intelligent Systems (ARISE), Department of Civil Engineering, University of Minho, 4800-058 Guimarães, Portugal; tmiranda@civil.uminho.pt
[3] IB-S/ISISE, University of Minho, 4800-058 Guimarães, Portugal; eduardo.pereira@civil.uminho.pt
[4] School of Science and Technology, University of Trás-os-Montes e Alto Douro, 5000-801 Vila Real, Portugal; ncristel@utad.pt
* Correspondence: id8028@alunos.uminho.pt

Abstract: The mining industry generates vast quantities of mine tailings on an annual basis. However, due to their limited economic value, a significant portion of these tailings are deposited close to mining sites, often underwater. The principal environmental apprehensions associated with mine tailings revolve around their elevated levels of heavy metals and sulfidic minerals. The oxidation of these sulfidic minerals can lead to the formation of acid mine drainage, which in turn releases heavy metals into nearby water systems. The effective management of tailing dams requires substantial financial investments for their construction and meticulous control. Consequently, a pressing need exists for stable, sustainable, and economically viable management approaches. One promising method for addressing mine tailings is through alkali activation, a technique that serves as a stabilization process. This approach yields robust, concrete-like structures by utilizing raw materials abundant in aluminum and silicon, which conveniently constitute the primary components of mining residues. This comprehensive review outlines the research on utilizing alkali activation for mine tailings. It delves into the reactivity and chemical attributes of diverse minerals. Numerous mine tailings exhibit an inadequate level of reactivity under alkaline conditions, so various pre-treatment methodologies and their impacts on mineralogy are meticulously explored.

Keywords: mine tailings; sustainability; alkali activation; mechanical activation; thermal treatment; alkaline fusion

1. Introduction

Construction is indispensable for the growth, development, and well-being of societies. It shapes their physical, economic, and social landscapes, leaving a lasting impact on generations to come [1]. In recent years, there has been a growing focus on recycling and repurposing waste materials to mitigate environmental impacts and promote sustainable practices within the construction industry [2,3]. Mine tailings are the waste materials left over after valuable minerals and metals have been extracted from mined ore through various processes. These tailings are composed of finely ground rock, water, and leftover chemicals used in the extraction and processing of minerals and are typically disposed of in tailing storage facilities or tailing dams [4].

During the mining process, rocks and minerals are excavated from the Earth's crust, often containing valuable minerals and metals, such as gold, copper, silver, or iron [5]. They undergo processing to separate the valuable components from the surrounding waste rock by crushing, grinding, chemical treatments, and other methods to extract the desired minerals [6]. The leftover materials that remain after the valuable minerals have been extracted are known as mine tailings. A substantial portion of the materials (estimated to

range from 97 wt% to 99 wt%) extracted from mining operations end up as mine tailings [7]. This percentage can vary depending on the type of mining, the ore being extracted, and the efficiency of the extraction process. The mentioned estimate indicates that only a tiny fraction of the original material is converted into valuable minerals. The rest, making up the majority of the material, becomes waste in the form of tailings. The estimated annual solid mine waste production is 20–35 billion tons, which includes 7–14 billion tons of mine tailings, underscoring the scale of the waste produced by mining operations worldwide [8].

The composition of mine tailings can vary widely depending on the type of ore being mined and the extraction methods used. Tailings can contain minerals, heavy metals, and processing chemicals. The size of the particles can range from fine silt to larger gravel-sized particles [9]. The Earth's crust is primarily composed of a few abundant elements like silicon, aluminum, calcium iron, sodium, and potassium, making mine tailings theoretically suitable as a raw material for construction purposes [10].

The poor reactivity of minerals within tailings can make it difficult to extract valuable components or repurpose the tailings effectively. Mine tailings often consist of minerals undergoing extensive processing during mining operations. This processing can alter the minerals' original crystalline structures and chemical compositions, making them less reactive to traditional extraction or reprocessing methods [11]. Moreover, the valuable minerals in mine tailings are usually present in low concentrations, which further compounds the challenge. Even if the minerals are reactive, their low abundance might not make extraction or recovery economically viable [12].

The fine particle size of tailings can affect their reactivity. Smaller particles can be harder to process due to issues such as agglomeration, handling difficulties, and challenges in separating minerals from one another. Furthermore, the processing chemicals used during the initial extraction can sometimes lead to changes in the mineralogy of tailings, resulting in the formation of new minerals or mineral phases that are less amenable to extraction [13].

Many mine tailings can contain high concentrations of sulfur, heavy metals, and metalloids since the valuable metals extracted from ores are frequently found within sulfidic minerals. Sulfidic minerals are minerals that contain sulfur combined with other elements, often including valuable metals such as copper, zinc, lead, and nickel [14]. These metals are chemically bonded to the sulfur within the minerals. In addition to sulfur, mine tailings can contain elevated levels of heavy metals, such as lead, copper, zinc, and cadmium, and metalloids such as arsenic. When the tailings are exposed to the environment, these elements can leach out and contaminate soil and water, posing serious environmental and health risks [15,16]. The sulfur in sulfidic minerals becomes concentrated in the resulting mine tailings. When these tailings are exposed to air and water, sulfur-containing compounds can undergo oxidation reactions, producing sulfuric acid and contributing to acid mine drainage (AMD), which is a critical environmental issue associated with mine tailing management and poses significant challenges during the active mining phase and after a mine has been closed [17].

The presence of sulfidic minerals and high concentrations of heavy metals in mine tailings can hinder their recycling potential, and the effective safety management of hazardous mine tailings is essential. Improper handling or inadequate containment can result in safety risks to surrounding communities. Tailings dams, if not constructed and appropriately managed, can pose significant risks and can lead to catastrophic events. Researchers actively seek innovative solutions to mitigate the challenges associated with sulfidic minerals, heavy metals, and tailing management by developing materials and processes that can safely immobilize or utilize these components [18].

Mine tailings are typically stored in tailing storage facilities, which have specially designed areas to contain and manage these waste materials. Tailing dams are constructed to hold the tailings in place, and they are often built using earthen embankments and containment structures. Since certain mine tailings are not considered hazardous waste, the option of reusing or recycling them stands out as an appealing alternative to disposing

of them in landfills [19]. Using mine tailings as a component of backfilling operations is a common approach in the mining industry. Backfilling is a technique used in mining in which voids or underground spaces created by mining activities are filled with suitable materials. This serves various purposes, providing stability to underground workings and preventing subsidence [20]. Tailings, which are often already in a slurry form due to the processing methods used during mineral extraction, can be mixed with other binding materials, such as cement, to create a paste-like substance that can be used as a backfill material in underground mining operations [21]. The final properties of paste backfill material in mining operations are influenced by a combination of factors, including the physical, chemical, and mineralogical characteristics of the tailings, the properties of the co-binder, such as cement or other binding agents, and the water content [22]. The particle size distribution, particle shape, and density of the tailings play a role in determining the overall stability and strength of the paste. Moreover, the chemical composition of the tailings, especially the presence of sulfides and heavy metals, can affect the reactivity and potential environmental impacts of the paste [23]. The types of minerals present in the tailings influence the overall behavior of the paste, including its strength, reactivity, and long-term stability. Furthermore, the choice of co-binder, often cement, affects the setting and hardening of the paste, and the amount of co-binder used in the mixture influences the mechanical properties and setting time of the paste [24]. Also, the ratio of water to solid components in the paste affects its workability, setting time, and strength when aiming to achieve the desired consistency and performance [25].

Within paste backfill technology and the stabilization of mine tailings, the prevalent choice for a binding agent is Portland cement (including cement, lime, and other calcium-containing materials) [26,27]. Nevertheless, the production of Portland cement results in significant CO_2 emissions, making it suboptimal for employment in paste backfilling [28]. Furthermore, in cases in which mine tailings possess the potential to generate acid, utilizing cement-based paste backfilling is not appropriate due to the adverse impact of the resulting acid on the formed matrix. On the other hand, the utilization of pozzolanic products in paste backfill technology is a notable approach that can enhance the properties and sustainability of the backfill material. Pozzolanic materials, such as blast furnace slag or fly ash, react with calcium hydroxide in the presence of water to form cementitious compounds, adding to the strength and durability of the mixture and offering enhanced acid resistance [29].

Since cement-based stabilization may not always be the optimal approach for mine tailings, an alternative strategy for repurposing mining waste is to utilize the tailings as a raw material in alkali activation to create an environmentally friendly construction material for subsequent use [30]. Alkali activation is a stabilization method that is particularly effective with raw materials rich in silicon and aluminum and relies on the reaction between alkaline solutions (often sodium or potassium hydroxide) and source materials containing silicon and aluminum. These elements are essential for the formation of the three-dimensional network of linked mineral compounds known as geopolymers. The raw material, which is rich in silicon and aluminum, is mixed with an alkaline solution, typically containing sodium hydroxide (NaOH) or potassium hydroxide (KOH), serving as an activator for the reaction and raising the pH of the mixture, making it highly alkaline [31]. The high-pH environment triggers the dissolution of silicon (Si) and aluminum (Al) components from the raw material. These elements are released as ions into the solution, undergo a complex series of chemical reactions, and combine with hydroxide ions from the alkaline solution to form new compounds, such as aluminosilicate gel, which is the basis of the three-dimensional network structure of the geopolymer [32]. In the newly formed aluminosilicate gel, the silicon and aluminum atoms are linked together through shared oxygen atoms, similar to how cement particles in traditional concrete are connected through calcium silicate hydrate (C-S-H) bonds [33]. Materials activated through alkali processes exhibit enhanced mechanical properties, a robust level of durability, and resistance to acids and thermal fluctuations [34]. Alkali-activated material shows the ability to immobilize hazardous components such as

heavy metals within their structure, significantly contributing to environmental protection and the safe management of waste materials [35].

Mine tailings, especially those generated from the extraction of metal ores, have gained significant attention as potential precursors in alkali activation due to their abundant content of silicon and aluminum, which are essential elements for the formation of the geopolymeric structure through the alkali activation process [36–38]. One critical challenge associated with using mine tailings in alkali activation processes is the low reactivity of these materials, and it can vary depending on factors such as mineralogical composition, particle size distribution, pre-treatment, and chemical characteristics [39]. Mine tailings with poor reactivity can still be valuable as a filler material when paired with the appropriate co-binder. This approach allows for the utilization of tailings in construction applications while addressing their reactivity limitations. To deploy mine tailings as a reactive material in alkali activation, enhancing the reactivity of the minerals contained within them is essential [40]. Mechanical activation methods, such as grinding, thermal treatment (calcination), and alkaline fusion, are effective in increasing the reactivity of minerals, including those found in mine tailings [41]. These processes modify their mineral structure and composition, making them more amenable to subsequent chemical reactions, such as alkali activation or the formation of geopolymers. Within alkali activation technologies, the resulting materials have versatile applications, including use in paste backfilling, as construction materials at mining sites, or for designing dry landfill alternatives, rather than being discarded in tailing dams [42].

This paper aims to provide a comprehensive review of recent research focused on the alkali activation of mine tailings. Since mine tailings are considered waste, and waste-based materials typically face limitations in large-scale applications, it is necessary to establish laws and policies that facilitate the integration of tailings into construction industries. However, before such policies can be enacted, it is crucial to accumulate sufficient data regarding the practical utilization of mine tailings in construction.

2. Mineralogy of Mine Tailings

The mineralogy of mine tailings can vary widely depending on the type of ore being mined, the processing methods used, and the geological characteristics of the deposit [43]. The mineral phases in mine tailings can be categorized into two main groups: primary phases (reacted and unreacted) and secondary phases (precipitated and weathered). These distinctions are crucial for understanding the mineralogical evolution of mine tailings and their potential environmental impact, as shown in Figure 1. Unreacted primary phases are the mineral phases that originally existed in the ore or rock being mined [44]. These minerals remain largely unchanged during the milling and processing of the ore. Examples include quartz, feldspar, and primary sulfide minerals like pyrite, chalcopyrite, and sphalerite. Reacted primary phases are mineral phases that have undergone some degree of alteration or reaction during the mining and milling process, such as sulfide minerals that may oxidize to form secondary sulfate minerals like jarosite or goethite due to air and water exposure [45]. During precipitated secondary phases, these secondary mineral phases form after the deposition of tailings into the environment. They often result from chemical reactions between tailings, water, and other environmental factors. Examples include the precipitation of iron or aluminum hydroxides (e.g., ferrihydrite and gibbsite) due to changes in pH conditions. Furthermore, weathered secondary phases can alter tailings over time. For example, exposure to rainwater and temperature fluctuations can lead to the leaching of soluble components, the transformation of minerals, and the formation of new weathering products, like clay minerals or iron oxides.

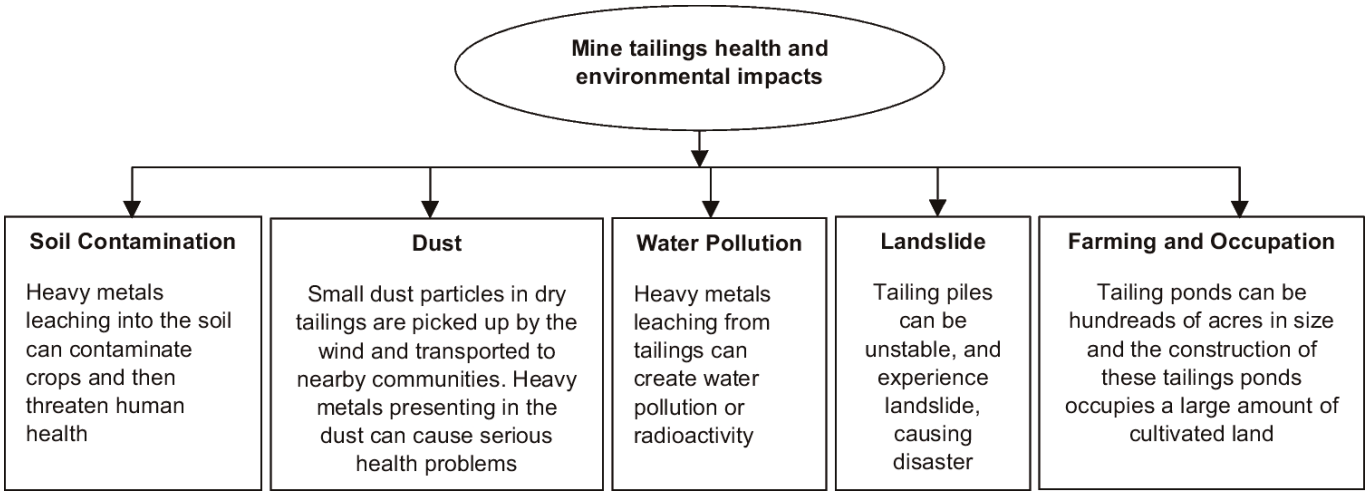


Figure 1. Health and environmental impacts of mine tailings [46].

The comprehensive characterization of fresh and weathered mine tailing materials is essential for thoroughly understanding their material properties and behavior. In order to develop an effective waste management plan, it is essential to study the mineralogy, chemical composition, and potential behavior of the tailings under various environmental conditions [47]. The chemical compositions of various mine tailings are demonstrated in Table 1.

The variability in the elemental composition of mine tailings from different mining sites presents a significant challenge for their standardized use in the construction industry. A multifaceted approach can be implemented to address this issue by focusing on characterization, classification, treatment, and regulatory guidelines. X-ray fluorescence (XRF) and X-ray diffraction (XRD) tests could be conducted to determine the exact composition of the tailings. Developing a classification system based on the chemical and physical properties of tailings can categorize them into different types, each suitable for specific construction applications. In some cases, thermal treatments can alter the physical and chemical properties of tailings, making them more suitable for use in construction. Regulatory guidelines and standards for using mine tailings in construction will help to ensure their safety and performance. By implementing these strategies, the variability in the elemental composition of mine tailings can be managed, allowing for their standardized and safe use in construction applications.

Minerals are fundamental components of the Earth's crust, and they play a vital role in geological processes, the formation of rocks, and the development of natural resources. They are naturally occurring, inorganic solids that possess specific chemical compositions and atomic arrangements, leading to unique crystal structures.

Table 1. The chemical compositions of various mine tailings.

Mine Tailings	Country	SiO_2	Fe_2O_3	Al_2O_3	CaO	MgO	Na_2O	K_2O	P_2O_5	V_2O_3	V_2O_5	SO_2	TiO_2	SO_3	ZnO	MnO	CuO	BaO	PbO	LOIa	Others	Ref.
Copper	China	58.5	10.8	13.3	5.4	1.9	2.8	4.0	-	-	-	-	-	0.6	-	-	-	-	-	-	-	[48]
	USA	55.8	3.07	14.11	2.27	1.77	3.02	3.88	0.19	-	-	2.26	0.50	-	-	0.067	-	-	-	-	-	[49]
	Africa	65.48	8.07	12.08	5.91	2.85	1.23	0.55	0.12	-	0.04	-	0.88	-	-	0.07	0.09	-	-	3.52	0.07	[50]
Gold	Africa	74.6	7.03	6.98	0.54	5.16	0.28	1.26	0.09	-	0.03	-	0.45	3.05	0.03	0.06	0.02	0.08	0.03	-	0.42	[51]
	Turkey	89.22	0.84	6.2	-	0.29	-	1.24	-	-	-	-	-	0.09	-	-	-	-	-	-	-	[52]
	Finland	49.9	9.2	10.4	11.8	6.8	-	1.2	-	-	-	-	1.2	-	-	-	-	-	-	13.6	-	[53]
Phosphate	Finland	32.98	7.98	7.08	12.92	17.28	-	5.53	0.96	-	-	-	0.27	-	-	0.12	-	-	-	14.01	0.88	[54]
	Morrocco	22.8	0.85	2.5	34.3	4.1	0.9	0.4	14.0	-	-	-	-	-	-	-	-	-	-	19	-	[55]
Iron	Brazil	40.0	48.9	8.7	-	-	-	-	-	-	-	-	-	-	-	-	-	-	-	6	1.8	[56]
	Australia	57.30	25.12	9.57	0.03	0.07	0.05	0.04	-	-	-	-	0.61	0.16	-	-	-	-	-	6.67	-	[57]
Vanadium	China	61.92	4.13	7.35	6.52	1.24	2.68	1.25	-	-	0.42	-	0.46	7.15	-	-	-	-	-	6.93	-	[58]
Kaolinite	Finland	72.55	1.90	16.44	0.05	0.83	0.08	3.06	-	-	-	-	-	-	-	-	-	-	-	4.42	0.74	[59]
Lead–zinc	China	62.09	2.73	4.35	20.45	0.56	-	0.55	-	-	-	-	0.2	3.63	-	-	-	-	-	-	-	[60]
Hematite	USA	68.77	28.13	0.87	0.28	0.74	0.03	0.04	-	-	-	-	0.05	-	-	-	0.001	0.02	-	-	0.07	[61]
Lithium	Finland	78.45	0.51	12.56	0.30	0.15	4.44	2.81	-	-	-	-	-	-	-	-	-	-	-	0.2	0.58	[56]
Bauxite	China	32.25	8.66	37.39	3.16	0.85	0.86	-	-	-	-	-	2.31	-	-	-	-	-	-	13.74	-	[62]
Quartz	China	97.48	0.30	1.11	0.17	0.22	0.04	0.02	-	-	-	-	-	-	-	-	-	-	-	-	-	[63]
Tungsten	Portugal	47.85	9.97	21.07	0.85	1.01	1.32	4.12	-	-	-	-	0.66	8.73	-	-	-	-	-	-	-	[64]
Zinc	China	38.4	11.8	12.65	29.8	-	-	1.65	0.84	-	-	-	0.59	0.52	2.96	0.62	0.21	-	0.23	-	0.12	[65]
Sphalerite	China	6.22	0.18	2.06	33.65	9.94	0.32	0.24	0.27	-	-	-	0.09	1.43	1.75	-	-	0.31	0.15	43.65	-	[65]

In the Earth's crust, minerals are classified into four major classes based on their chemical composition [66]. (1) Silicate minerals are the most abundant class of minerals in the Earth's crust and are composed primarily of silicon (Si) and oxygen (O) atoms combined with various cations (positively charged ions), such as aluminum (Al), iron (Fe), magnesium (Mg), and others. Silicate minerals include feldspars, quartz, micas, amphiboles, and pyroxenes [67]. (2) Carbonate minerals are characterized by the carbonate ion (CO_3^{2-}) as a fundamental building block. They are primarily composed of carbon, oxygen, and various cations. Common carbonate minerals include calcite and dolomite [68]. (3) Oxide minerals are primarily composed of oxygen (O) combined with metal cations. These minerals often form as a result of the weathering of other minerals. Oxide minerals include magnetite, hematite, and cassiterite. (4) Sulfide minerals are composed of sulfur (S) combined with metal cations. These minerals often form in hydrothermal environments and are associated with ore deposits [69]. Common sulfide minerals include pyrite, galena, and chalcopyrite.

Valuable metals, including gold (Au), copper (Cu), lead (Pb), and zinc (Zn), are commonly found in sulfide minerals. The mining industry extracts these valuable metals from sulfide ores, and as a result, a significant portion of mine tailings generated in mining operations are sulfur-rich [70]. However, this also poses environmental challenges. When sulfide minerals are exposed to air and water during mining operations or in tailing storage facilities, they can oxidize, producing sulfuric acid and releasing metals into the environment [71]. Pyrite, often called "fool's gold", is one of the most common sulfide minerals found on Earth and is widely distributed in various geological environments. The oxidation of pyrite (iron disulfide, FeS_2) involves the reaction of pyrite with oxygen (O_2) and water (H_2O) to produce sulfuric acid (H_2SO_4) and iron oxide (Fe_2O_3). The chemical reaction is represented by Equation (1) as follows:

$$4FeS_2 + 14O_2 + 4H_2O \rightarrow 4Fe_2(OH)_6 + 8H_2SO_4 \quad (1)$$

In this reaction, pyrite (FeS_2) reacts with oxygen (O_2) from the air and water (H_2O) and produces iron hydroxide ($Fe_2(OH)_6$) as a solid product and sulfuric acid (H_2SO_4) as a solution in water. This process produces acid mine drainage (AMD) when pyrite-containing rocks are exposed to air and water during mining operations [72].

The bioavailability of hazardous components in mine tailings is influenced by a complex interplay of factors, including the oxidation state of elements, mineralogy of tailings, grain size and surface area, morphology, chemical composition, environmental conditions, microbial activity, and hydraulic conditions [73]. When the leaching of harmful components from mine tailings surpasses the legally defined limits for waste, these tailings are classified as hazardous. When such tailings are disposed of in tailing ponds, extensive landfill spaces, along with meticulous construction and ongoing maintenance, are necessary, even after the closure of the mining operation.

Carbonates (e.g., calcite and dolomite) and silicates (e.g., feldspars and olivine) are minerals that can neutralize acidic conditions in tailing ponds and should be characterized to understand the environmental behavior of mine tailings. They are used as neutralizing agents to mitigate the effects of acid mine drainage (AMD) [74]. Calcite (calcium carbonate, $CaCO_3$) is highly effective in neutralizing acid due to its reaction with acidic water. The reaction can be represented by Equation (2) as follows:

$$CaCO_3 + H_2SO_4 \rightarrow CaSO_4 + CO_2 + H_2O \quad (2)$$

The above reaction represents the neutralization of sulfuric acid (H_2SO_4) by calcium carbonate ($CaCO_3$), resulting in the formation of gypsum ($CaSO_4$), carbon dioxide (CO_2), and water (H_2O). Dolomite (calcium magnesium carbonate, $CaMg(CO_3)_2$) is similar to calcite but contains calcium and magnesium ions, providing a buffering capacity [75].

Feldspars are aluminosilicate minerals that can react with acidic solutions. The aluminum (Al) and silicon (Si) in their structure can neutralize acidic conditions. Olivine

(magnesium iron silicate, $(Mg, Fe)_2SiO_4$) is another silicate mineral that can neutralize acid; the reaction involves the release of magnesium and iron ions, which can help buffer against acid [76].

Carbonates can provide the short-term neutralization of acidic conditions by decreasing the acidity of water by raising the pH and decreasing the concentration of hydrogen ions (H^+), while silicates are considered more long-lasting neutralization minerals [77,78]. These minerals, when present in tailings or added as amendments, can help to reduce the risk of environmental damage associated with acid mine drainage [79].

3. Alkali Activation

Alkali activation creates new construction materials from silicon- and aluminum-rich raw materials by mixing these raw materials with a highly alkaline solution. This solution, typically an alkali hydroxide or silicate, serves as an activator. It increases the pH of the mixture and facilitates the formation of a new 3D concrete-like structure. Various elements like iron (Fe), magnesium (Mg), and calcium (Ca) can also play crucial roles in the reaction. These elements contribute to the formation of calcium–(sodium) aluminosilicate hydrate (C(N)ASH), which is a complex amorphous gel-like structure with cementitious properties, similar to the products of cement hydration in ordinary Portland cement and Mg–Al-layered double hydroxide, which can contribute to the mechanical properties and stability of the resulting material. Alkali-activated mine tailing concrete and mortar show a promising level of durability against aggressive ions such as chlorides and sulfates. The durability of these materials can be influenced by the type of activator used, the mix design, and the curing conditions [80]. In terms of chloride resistance, the high alumina and silica content in mine tailings, when activated, can form a dense and chemically stable matrix, reducing the permeability of the concrete or mortar and limiting chloride ingress. The choice of activator (e.g., sodium hydroxide or sodium silicate) affects the pore structure and binding phases, producing more amorphous aluminosilicate gels that tend to enhance chloride resistance. Moreover, proper curing is crucial for developing a dense microstructure that improves chloride penetration resistance. Regarding sulfate resistance, alkali-activated materials often exhibit better levels of resistance than ordinary Portland cement (OPC) due to the absence of calcium hydroxide, which reacts with sulfates to form expansive compounds like ettringite. Meanwhile, incorporating supplementary materials, such as fly ash or slag, can further improve sulfate resistance by refining the pore structure and reducing permeability [81]. When the calcium content is low in alkali-activated materials (AAMs), they are called geopolymers. Geopolymers are a subset of AAMs with distinct characteristics and are defined as inorganic, amorphous to semi-crystalline aluminosilicate materials formed by the reaction of a source material rich in silicon and aluminum with an alkaline activator. Geopolymers, like other AAMs, form a three-dimensional structure through a process known as polycondensation. This results in a network of linked silicon and aluminum atoms [82]. The resulting 3D structure of geopolymers can vary in crystallinity. Some geopolymers may have a poorly crystalline structure, while others may exhibit more crystalline characteristics, depending on the specific raw materials and curing conditions used [83]. Geopolymers often possess excellent mechanical properties, high levels of resistance to chemical attack, and good levels of thermal stability. They also offer sustainability benefits similar to those of other AAMs, including the use of industrial by-products and waste materials, reduced carbon emissions, and lower energy consumption during production. These properties of alkali-activated materials (AAMs) position them as a more sustainable alternative to traditional construction materials like ordinary Portland cement (OPC) [84,85].

The choice of raw materials in alkali activation depends on their reactivity and composition. Among the various aluminosilicate materials suitable for alkali activation, metakaolin and blast furnace slag have received an extensive amount of attention and research [86]. The properties of the alkaline activator play a crucial role in determining the final structure and properties of alkali-activated materials (AAMs). A higher alkalinity

promotes more robust reactions and leads to the formation of a denser and stronger structure, and higher concentration can accelerate the activation process, potentially leading to faster setting times and higher early strength development [87]. The most common types of alkaline reagents used as activators in alkali activation processes are hydroxides (e.g., sodium hydroxide and potassium hydroxide) and silicates (e.g., sodium silicate). Sodium hydroxide (NaOH) is a strong alkaline compound, is highly soluble in water, and provides a significant source of hydroxide ions (OH^-) for the activation process. Potassium hydroxide (KOH) shares properties similar to NaOH, and like NaOH, KOH provides hydroxide ions to drive activation reactions. Sodium silicate (Na_2SiO_4) is an alkaline compound derived from the reaction of sodium carbonate and silica sand, providing both alkalinity and a source of reactive silicon, making it a versatile activator for alkali-activated materials [88].

Alkali-activated materials (AAMs) can immobilize harmful components like heavy metals due to their unique chemical and mechanical properties. AAMs have a robust chemical structure formed through polycondensation reactions between silicon (Si) and aluminum (Al) in the aluminosilicate raw materials. This structure is resistant to chemical breakdown, providing a stable matrix for encapsulating heavy metals [89]. The reactive sites within the AAMs' 3D structure can undergo ion exchange reactions. Heavy metal ions can bind to these sites, displacing other cations, and some heavy metals can be adsorbed onto the surfaces of AAM particles. Moreover, during the activation process, chemical reactions can lead to the formation of low-solubility phases. These phases can incorporate heavy metal ions, effectively immobilizing them within the material [90]. AAMs have good mechanical properties, so they can physically encapsulate heavy metal particles or ions within their structure, preventing their release into the surrounding environment. Finally, the chemical and physical properties of AAMs can reduce the leachability of heavy metals, which means that even under conditions in which an AAM is exposed to water, the release of heavy metals is minimized [91]. When different co-binder materials are introduced, the immobilization mechanism becomes more complex because each co-binder material may have its own chemical properties, which can lead to various interactions with heavy metals. When multiple co-binders are used together, their synergistic effects can enhance the immobilization process; the presence of multiple co-binders introduces heterogeneity to the mixture, making it more challenging to predict and analyze the immobilization process [92]. Co-binders can have different particle sizes and shapes, which affect their accessibility to heavy metals and the overall immobilization efficiency. Furthermore, the pH and redox conditions of the environment can influence how co-binders interact with heavy metals. These conditions can vary depending on factors such as local geology, water chemistry, and microbial activity [93–95]. Finally, alkali activation technology is a promising alternative to traditional Portland cement, but its practical application faces the following challenges: (1) The properties of alkali-activated materials are highly dependent on the source and composition of raw materials, such as fly ash, slag, and other industrial by-products, leading to inconsistent performance. (2) Design mixes for alkali-activated materials are challenging due to the lack of standardized guidelines and the need for the precise control of the activator concentration, water content, and curing conditions. (3) Alkali-activated materials can have excellent levels of durability, but there are concerns related to alkali–aggregate reactions, sulfate attack, and carbonation. More research is needed to fully understand and mitigate these issues. (4) Alkaline activators, such as sodium hydroxide and sodium silicate, are caustic and require careful handling. This poses safety risks and requires specific storage and handling protocols. (5) The cost and availability of suitable raw materials and activators can vary regionally. In some areas, the raw materials needed for alkali activation might not be available or could be more expensive than traditional materials. (6) Comprehensive life cycle assessments (LCAs) and long-term performance data are needed to fully understand the sustainability and durability of alkali-activated materials over extended periods.

3.1. Alkali-Activated Mine Tailings

Mine tailings are a by-product of the mining industry, and their proper handling, disposal, and reuse are essential aspects of responsible mining practices to obtain various benefits, such as those shown in Figure 2. Testing the solubility of different elements in raw materials for alkali activation is crucial to understanding their reactivity. This procedure is a common method used to assess reactivity. After the reaction period, the solution is collected and analyzed using inductively coupled plasma spectrometry (ICP), which is a highly sensitive analytical method that can determine the concentrations of various elements in a sample [96]. These data help us understand which elements are readily available for reactions and incorporation into the final alkali-activated material. Elements that exhibit a high level of solubility under alkaline conditions are considered more reactive [97].

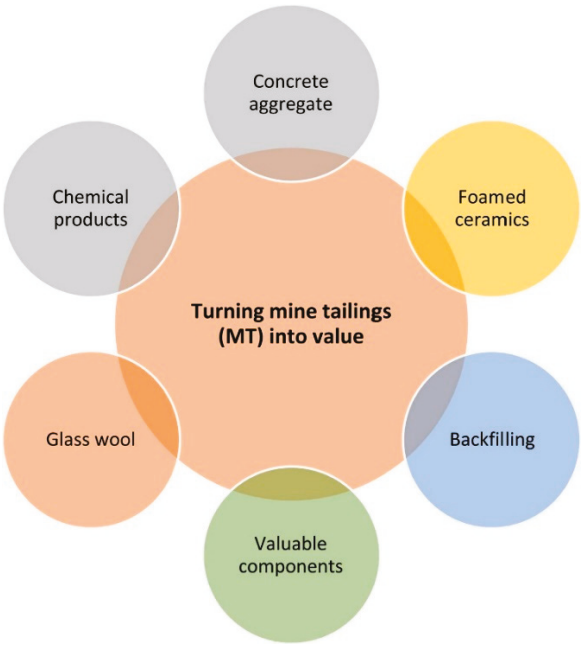


Figure 2. Benefits of recycling and reusing mine tailings [98].

Assessing the crystalline structure of a material through X-ray diffraction (XRD) and scanning electron microscopy (SEM) is another crucial method for estimating its reactivity. XRD provides information about the material's crystalline phases and their relative abundance, while SEM provides detailed images of the material's microstructure and surface morphology [99,100]. Despite the abundance of silicon and aluminum in most mine tailings, their reactivity under alkaline conditions can be limited due to the highly crystalline structure of many mine tailings. The minerals in mine tailings often have well-defined crystalline structures. This means their atoms are arranged in a repeating pattern, which can resist dissolution and chemical reactions. Moreover, in highly crystalline materials, the surface atoms may be less chemically active compared to those in amorphous or poorly crystalline phases, reducing the likelihood of reactions with the alkaline solution [101]. The capacity of highly crystalline materials for ion exchange and chemical interactions with an activator may be limited and can hinder the dissolution of essential components needed for the activation process [102]. The poor reactivity of mine tailings is a significant challenge in their utilization for alkali-activated materials. Poorly reactive mine tailings may contribute less to the strength and durability of alkali-activated materials and can limit their usefulness as a primary component in construction. The slow reactivity of highly crystalline mine tailings can result in slower activation kinetics and require longer curing times or additional processing to achieve the desired properties [103]. Additional processing steps like mechanical activation or thermal treatment may be necessary to enhance the reactivity of mine tailings, adding complexity and cost to the recycling process. One

way to enhance the reactivity of poorly reactive mine tailings is by combining them with a reactive co-binder, such as metakaolin or blast furnace slag, in an alkali activation process. This approach enhances the strengths of both materials to create a more effective and sustainable material [104]. However, the reactivity of mine tailings can be enhanced through various treatment methods aimed at modifying the physical and chemical properties of the tailings to make them more suitable for the alkali activation process. Finally, the decision to use mine tailings as a binder or inert filler should be made after carefully assessing their reactivity. This reactivity, in turn, is influenced by the mineralogical composition of the tailings and how they respond to various treatment processes.

3.2. Mine Tailings as a Filler Material in Alkali Activation

Using mine tailings as a filler material in alkali activation is a sustainable approach to repurposing mining waste. Mine tailings with low levels of reactivity can find a valuable role as inert fillers in alkali activation when combined with an appropriate co-binder material [105]. This approach helps us use tailings that might otherwise have limited levels of reactivity. Different studies demonstrate the potential of alkali activation as a stabilizing method for a range of mine tailings, including those from base metal, coal, uranium, and potash mining sites, and the crucial role of metakaolin as a co-binder [106–108]. Alkali activation, as a versatile process, not only has a great capacity to immobilize hazardous elements but also results in a final matrix with a robust mechanical performance, making alkali activation a sustainable solution for repurposing mine tailings. Analyzing the geochemistry of Kaltails tailings produced under different conditions is crucial before utilizing them in alkali-activated materials, which provides critical insights into the chemical composition, mineralogy, and potential reactivity of the tailings [109]. The material composition, rich in Si (silicon), Al (aluminum), Mg (magnesium), Fe (iron), Na (sodium), and SO_3 (sulfate), suggests a potentially reactive mixture when combined with fly ash or blast furnace slag, demonstrates excellent mechanical properties, and good levels of durability and permeability. Notably, these positive outcomes were achieved when the mixture had a low proportion of tailings (less than 70 wt%), indicating that even with a relatively low proportion of tailings, they could contribute to the desirable properties of the final material significantly, demonstrating the potential for effectively utilizing mine tailings as a valuable component in construction materials [110].

Studies provide valuable insights into the alkali activation of copper mine tailings, which consist of minerals like quartz, albite, potassium aluminum silicate, and gypsum, contributing to the reactivity of the tailings. Sodium hydroxide (NaOH) was employed as the activator to initiate the polycondensation reactions necessary for forming a 3D structure in a material [111,112]. Studies have also highlighted the essential role of a co-binder in achieving good mechanical properties and levels of durability in the final material, suggesting that the inherent reactivity of copper mine tailings alone may not be sufficient to achieve the desired properties [113]. Adding fly ash to the mixture further enhanced the final strength of the alkali-activated copper mine tailings. The successful alkali activation of copper mine tailings and the essential role of co-binders underscore the potential for repurposing mining waste in sustainable construction materials [114]. Moreover, optimizing the curing conditions can substantially impact the mechanical properties of alkali-activated materials. Specifically, a study demonstrated that better mechanical properties were achieved by carefully controlling the curing conditions. This involved either controlling the pressure or using an elevated curing temperature of 90 °C [115].

The composition of the mine tailings, including dolomite, kaolinite calcite, and quartz, from the vanadium mining site in China provides insight into the potential reactivity and properties of these materials. The tailings were used as a raw material in alkali activation, with metakaolin as a co-binder and sodium silicate as an activator [116].

Another study used metakaolin, a thermally activated form of kaolinite clay, as a co-binder for molybdenum mine tailings, with the potential for the use of mining waste. The molybdenum mining site was rich in minerals like quartz and calcite and phases containing

calcium, aluminum, and iron [117]. It was found that with a greater content of metakaolin, there was a greater amount of tetrahedral silicon (Si) coordination in the geopolymer gel, and the greater metakaolin content resulted in the final material having better mechanical properties [118]. Furthermore, gold mine tailings that were rich in dolomite, quartz, sulfur, and mullite were studied. The study highlighted the necessity of a suitable co-binder, such as blast furnace slag or metakaolin, for the alkali activation process and suggested that the gold mine tailings alone may not have been reactive enough to achieve the desired hardening. A matrix is suitable for construction material was generated by incorporating a higher co-binder content. However, employing a high concentration of NaOH (15 M) led to a notable reduction in the workability of the resulting paste, potentially exerting a substantial influence on the properties of the final material [119].

The use of alkali activation in paste backfill technology represents an intriguing avenue in sustainable construction practices. An inverse relationship is observed when employing alkali-activated blast furnace slag in conjunction with gold mine tailings containing quartz, albite, mica, sanidine, and microcline for the production of paste backfill material; as the compressive strength of the final matrix increases, the workability of the mixture decreases [120]. The superior strength exhibited by the matrix, compared to Portland-cement-based paste, under optimal curing conditions and with an ideal concentration of the alkali activator (a blend of NaOH and Na_2SiO_3), affirms the appropriateness of alkali-activated slag as a co-binder in paste backfill technology [121]. Alkali-activated fly ash can serve as a co-binder for sulfidic-rich mine waste rocks, enabling the production of paste backfill materials or construction materials. Utilizing sulfidic waste rock as the aggregate significantly reduces the acid generation potential of the waste in landfills, resulting in the production of environmentally acceptable materials. This stands as one of the foremost advantages of employing alkali activation in paste backfill technology, as opposed to ordinary Portland cement (OPC) [122].

Mine tailings, which may have a limited reactivity on their own, can contribute to the final material when used as an inert filler when suitable co-binder materials, like metakaolin or blast furnace slag, are chosen. Each type of mine tailing requires a meticulous study of mix design due to the influence of mineralogy, chemical composition, and physical properties on co-binder materials, alkali activators, and process conditions [123]. However, the accessibility of a co-binder is equally crucial, as the mining site may not always be in close proximity to the industry or manufacturing facility that produces a compatible co-binder. The summarized results of relevant studies are shown in Table 2.

Table 2. Summary of studies using various mine tailings as filler materials in alkali activation.

Mine Tailings	Procedure Parameters	Main Elements	Mineralogy	Final Properties	Ref.
Metal, coal, uranium, and potash tailings	Liquid toxic waste mixed with a geopolymer precursor; curing at 60 °C	-	-	High immobilization of heavy metals; high mechanical performance	[106–108]
Kaltails tailings	Fly ash as a co-binder	Si, Fe, Al, Ca, Mg, Na, and SO_3	-	Maximum mine tailing content of 70 wt%; stronger hardpan achieved with greater fly ash content	[109,110]
Copper tailings	Fly ash as a co-binder; curing at 90 °C; pressure used in preparation stage	-	Quartz, albite, potassium aluminum silicate, and gypsum	Improved mechanical strength with higher co-binder content and elevated curing temperature	[111–115]

Table 2. *Cont.*

Mine Tailings	Procedure Parameters	Main Elements	Mineralogy	Final Properties	Ref.
Molybdenum tailings	Metakaolin as a co-binder; curing at room temperature	-	Calcite, andradite, quartz, dolomite, and calcium aluminum silicate	The improved strength of the final material with metakaolin	[116–118]
Gold tailings	Blast furnace slag and metakaolin as co-binders; curing at room temperature	-	Dolomite, quartz, chlinoclore, muscovite, albite, and gypsum	Metakaolin used for adjusting the scarce Al content in the mixture; the effect of co-binder content on the mechanical properties of the final material	[119]
Gold tailings	Slag, gypsum, cement, lime, and silica fume as co-binders	-	Quartz, albite, mica, sanidine, and microcline	Appropriate material to utilize for paste backfill technology	[120,121]
Sulfidic mine waste rock	Fly ash as a co-binder	-	Chlorite, quartz, illite, and pyrite	Suitable to utilize sulfidic mining waste rock as aggregate in alkali activation	[122]

4. Pre-Treatment Methods

Addressing the poor reactivity of mine tailings is a crucial aspect of their utilization in alkali activation technology. Due to the observed low level of reactivity of mine tailings in alkaline conditions, various pre-treatment methods have been explored to augment the reactivity of distinct minerals. Mechanical activation, heat treatment or calcination, and alkaline fusion have been the subject of extensive research in this context. This review delves into a discussion of how each method impacts the reactivity of various minerals.

4.1. Mechanical Activation

Mechanical activation is a crucial pre-treatment step in maximizing the potential of mine tailings for use in alkali activation technology. The primary goal of mechanical activation is to enhance the reactivity of specific components within the mine tailings. This is achieved by subjecting the material to grinding or milling processes, including reducing the particle size, increasing the surface area, and disrupting crystalline structures [124]. The increased reactivity observed after milling is attributed to the higher amorphous content of the reactive elements. As the particle size of the mine tailings is reduced through milling, the total surface area of the material increases significantly since smaller particles have a more exposed surface area relative to their volume. This increased surface area means that a larger proportion of the material is now available for chemical reactions, allowing for a greater number of reactive sites to participate in the formation of the 3D structure [125]. The larger surface area facilitates faster reaction kinetics, meaning that chemical reactions can occur more quickly, leading to a more efficient alkali activation process [126].

A study focused on investigating mechanical treatments with the aim of enhancing the ultimate properties of alkali-activated mine tailings originating from a vanadium mining site that were primarily composed of quartz, feldspar, diopside, mullite, and hematite. After a 60 min grinding process, the particles exhibited a more uniform shape, and the average particle size was reduced from 31 to 2 μm, resulting in a higher mechanical strength in the final alkali-activated material [127]. Furthermore, the grinding process led to the increased solubility of silicon (Si) and aluminum (Al) in the material [128]. The ultimate alkali-activated materials were created by blending mine tailings, fly ash, and solid sodium silicate powder. This dry mixture was subsequently combined with water, exhibiting superior thermal resistance properties compared to those of composites made with Portland cement [127,129].

Copper mine tailings that were rich in quartz, albite, dolomite, and chlorite were studied. After grinding copper mine tailings for 3 h, a remarkable increase in solubility was observed. Specifically, there was a 93% higher solubility of aluminum (Al) and a 23% higher solubility of silicon (Si) compared to a mine tailing material that was not ground [130].

Antigorite ($Mg_3Si_2O_5(OH)_4$)-rich mining waste was also mechanically activated. The tailings were milled with a planetary mill (0.5–10 min). According to that study, the process of dehydroxylation was evidently linked to the generation of a greater amount of amorphous material during the milling process. Furthermore, there was a notable increase in the solubility of silicon [131].

Phyllite-rich material was studied, and its cementitious properties were demonstrated following the milling process. Phyllite is a type of metamorphic rock that forms from the metamorphism of shale or mudstone, belonging to the category of foliated metamorphic rocks, which means it has a layered or banded appearance due to the alignment of minerals under heat and pressure. The decrease in muscovite and chamosite content was noticeably evident, whereas the quantity of quartz remained unchanged, and the amorphous content increased by mechanical activation [132]. The summarized results of relevant studies are shown in Table 3.

Table 3. Summary of studies regarding mechanically activated mine tailings.

Mine Tailings	Procedure Parameters	Mineralogy	Mineralogical Changes	Ref.
Vanadium tailings	60 min grinding; 10:1 weight ratio of grinding ball to powder	Quartz, feldspar, diopside, mullite, and hematite	Decreased amount of crystalline quartz; higher mechanical strength of alkali-activated material obtained with higher leaching of Al and Si and higher amorphous content	[127]
Copper tailings	1–4 h grinding; 10:1 weight ratio of grinding ball to powder	Quartz, dolomite, chlorite, and albite	Decreased content of albite (lower crystalline silica content)	[130]
Antigorite waste	600 s grinding; 6:1 weight ratio of grinding ball to powder	Mg and Si minerals	Cementitious properties obtained in milled mine tailings	[131]
Phyllite waste	9–15 min grinding	Clay, quartz, and albite	Reduction in chamosite and muscovite; decreased albite content	[132]

4.2. Heat Treatment

Conducting a preliminary heat treatment prior to alkali activation has displayed the potential to augment the reactivity of mine tailings [133]. The heat treatment of mine tailings is a process aimed at modifying their chemical and physical properties by subjecting them to high temperatures to induce changes in their mineralogy and reactivity, improving their suitability for various applications. One specific effect of this treatment is the removal or alteration of hydroxyl groups, which are oxygen and hydrogen atom pairs (-OH) found in minerals [134]. The specific temperature range used in heat treatments can vary depending on the desired outcomes and the composition of the tailings. The high temperatures applied during heat treatment can lead to the removal of hydroxyl groups from minerals containing hydroxyl groups, such as clays and certain silicates present in the tailings, and transform them into more stable phases with altered properties for the formation of a 3D structure [135]. Moreover, elevating the temperature can facilitate the dissolution of aluminum and silicon units from the original material, heightening its reactivity in alkaline conditions. When mine tailings are subjected to high temperatures during heat treatment, the intense thermal energy causes the minerals to change, leading to the generation of amorphous phases. The higher amorphous content means that a larger portion of the material is now in a highly reactive state, crucial for subsequent processing steps, like alkali activation [136].

A pioneering investigation used a thermal pre-treatment before alkali activation to enhance the reactivity of tungsten mine tailings, which were notably abundant in quartz and muscovite. The study revealed a substantial thermal resistance in quartz,

whereas a portion of the muscovite (approximately 12%) remained unchanged even after exposure to temperatures exceeding 950 °C [137]. Subsequent research indicated that boron mine tailings, which included Ca and Mg minerals like colemanite and hydroboracite, transformed into an amorphous state at 600 °C [138]. Illite, a mineral with properties akin to those of muscovite, underwent decomposition at 800 °C, while albite decomposed only at temperatures above 900 °C [139,140].

Another study delved into the utilization of heat-treated phosphate mine tailings as a raw material in alkali activation in conjunction with fly ash and metakaolin. During alkali activation, dolomite and calcite underwent a reduction process, whereas other phases, like quartz, fluorapatite, and mullite, remained unaffected [141]. In the case of kaolinite tailings, calcination at 750 °C emerged as the most efficient approach to enhance their reactivity. This is attributed to the probable transformation of kaolinite into metakaolin during decomposition [142]. It is crucial to note that optimizing the calcination temperature is paramount, as metakaolin continues to react and produces crystalline and insoluble mullite. This transformation becomes noticeable at temperatures surpassing 800 °C [143]. Moreover, copper tailings have displayed heightened levels of reactivity following calcination at 600 °C, coinciding with the observed decomposition of crystalline chloride [144]. The summarized results of relevant studies are shown in Table 4.

Table 4. Summary of studies regarding heat-treated mine tailings.

Mine Tailings	Main Minerals	Calcination Temperatures	Mineralogy Changes	Other Comments	Ref.
Tungsten tailings	Muscovite and quartz	950 °C	High thermal resistance for muscovite	Increased amount of amorphous phase; thermal behavior similar to that of phyllosilicate minerals	[137]
Boron tailings	Colemanite ($Ca_2B_6O_{11}\cdot 5H_2O$), hydroboracite ($CaMgB_6O_8(OH)_6\cdot 3H_2O$), quartz, illite, and calcite	600, 700, and 800 °C	Colemanite and hydroboracite turned into amorphous phase at 600 °C; illite and calcite decomposed at 800 °C	Illite had similar properties to muscovite	[138]
Phosphate tailings	Quartz, calcite, fluorapatite, dolomite, mullite, and feldspar	750 °C (2 h)	Quartz, fluorapatite, and mullite remained constant; dolomite and calcite content was reduced; feldspar content was eliminated	High mechanical strength achieved with 50 wt% phosphate tailing in the mixture	[141]
Kaolinite tailings	Muscovite, kaolinite, and quartz	750°C	Kaolinite turned into amorphous metakaolin	Possible recrystallization of amorphous phase beyond optimum temperature	[142]
Copper tailings	Quartz, albite, chlorite, and dolomite	400–600 °C	Crystalline chlorite was dissolved	-	[144]

4.3. Alkaline Fusion

Alkaline fusion is a chemical process that involves heating a material, typically in the presence of an alkaline substance like sodium hydroxide (NaOH) or potassium hydroxide (KOH), to create a fusion or reaction. This process is used to alter the composition and properties of the material and increase the reactivity of the material prior to alkali activation [145]. In the context of mine tailings, alkaline fusion refers to subjecting the tailings to high temperatures in the presence of an alkaline substance. The high temperatures and alkaline environment cause chemical reactions within the tailings, leading to the transformation of the minerals into different phases or forms. The process involves elevating the temperature beyond the melting point of the alkali source present in the mixture. Following this heat treatment, the processed material is subjected to alkali activation using an alkaline solution. Alkaline fusion can facilitate the removal of impurities or unwanted components from the tailings, making them more suitable for specific applications [146].

A study investigated alkaline fusion in conjunction with poorly reactive volcanic ash. This process resulted in a greater quantity of soluble aluminosilicates due to the conversion of minerals like muscovite, anorthoclase, and diopside. Consequently, this led to an enhancement in the reactivity of the ash [147].

Alkaline fusion has been explored as a method for treating gold mine tailings. In this process, an Al_2O_3 additive was blended with the tailings at different concentrations, and NaOH pellets were introduced to the mixture. The fusion process was carried out at 550 °C for 1 h, with the temperature increasing at a rate of 10 °C per minute. Following the heating process, the mixture was combined with Na_2SiO_3. It was observed that the primary factor influencing the reactivity was the content of Al_2O_3 rather than the curing temperature [52].

A study on alkaline fusion with granite waste was also conducted, and it was found that the crucial factor influencing the reactivity of the material was the quantity of alkaline reagent applied [148]. Moreover, when alkaline fusion was employed with phosphate tailings, notable changes were observed [149]. This included the decomposition of illite, palygorskite, and dolomite phases alongside an augmentation in the content of Na-rich crystalline phases [150].

5. Conclusions

Mine tailings constitute the largest volume of solid waste generated by the mining industry. Unfortunately, due to their limited economic value, a significant portion of these tailings are typically deposited in controlled landfills submerged underwater. The landfilling of mine tailings has not always been viewed as a significant problem. However, their environmental impacts, especially incidents like tailing dam failures leading to tailing draining or flooding, have resulted in severe consequences, including a loss of life, leading to the issue gaining critical attention. Consequently, stringent legislative regulations have compelled the mining industry to explore alternative methods of disposal. The possibility of employing mine tailings as a primary material in alkali activation has garnered significant attention from researchers. Among the crucial factors for examination, the mineral composition of mine tailings takes precedence. Predominantly, these tailings exhibit low levels of reactivity under alkaline conditions based on their mineralogy. Therefore, using them as a raw material in alkali activation proves to be challenging due to this inherent low level of reactivity. Mine tailings can be effectively employed as an inert filler in alkali activation technology, especially when combined with a compatible co-binder, like metakaolin, fly ash, or blast furnace slag. Factors such as curing conditions, the duration of curing, the type and concentration of the alkali activator, and the choice of co-binder materials all exert pivotal influences on this process. Sustainable high-performance building materials can be created that leverage waste materials for environmental and economic benefits and that can be tailored to specific requirements by adjusting the mix design and using different types of aluminosilicate precursors. An alternative approach involves enhancing the reactivity of the initial material through methods like thermal treatment, mechanical activation, or alkaline fusion before subjecting it to alkali activation. Alkali-activated mine tailings hold potential applications as construction materials and as recyclable paste backfill materials. Furthermore, this method can serve as a stabilization approach before landfilling, particularly for managing hazardous mine tailings. Finally, future studies on mine tailing alkali-activated materials could focus on optimizing activation processes to enhance the mechanical and durability properties of mine tailings. Moreover, performing life cycle assessment (LCA) analyses to develop sustainable and efficient activation methods by understanding the long-term environmental impact and stability of these materials should be considered.

Author Contributions: Conceptualization, H.R.M., E.P., N.C. and T.M.; methodology, H.R.M., E.P., N.C. and T.M.; formal analysis, H.R.M., E.P. and T.M.; investigation, H.R.M., E.P. and T.M.; resources, E.P., N.C. and T.M.; writing—original draft, H.R.M.; writing—review and editing, H.R.M., E.P., N.C. and T.M.; supervision, E.P., N.C. and T.M.; project administration, E.P., N.C. and T.M.; funding acquisition, E.P., N.C. and T.M. All authors have read and agreed to the published version of the manuscript.

Funding: This research was funded by the "NGS–New Generation Storage" project (reference number C644936001-00000045), financed by the Recovery and Resilience Plan and the Next Generation EU European Funds.

Institutional Review Board Statement: Not applicable.

Informed Consent Statement: Not applicable.

Data Availability Statement: Not applicable.

Acknowledgments: The authors would like to thank the Recovery and Resilience Plan and the Next Generation EU European Funds for funding this project.

Conflicts of Interest: The authors declare no conflicts of interest.

References

1. Wu, X.; Ma, T.; Zhang, J.; Shi, B. The Role of Construction Industry and Construction Policy on Sustainable Rural Development in China. *Environ. Sci. Pollut. Res.* **2023**, *30*, 7942–7955. [CrossRef] [PubMed]
2. Najafi, E.K.; Tavares, P.; Miranda, T.; Manaviparast, H.R.; Cristelo, N. Ophthalmic Glass Lens Waste as an Alternative Soluble Silica Source for Alkali-Activation Reactions. *Constr. Build. Mater.* **2023**, *392*, 131854. [CrossRef]
3. Manaviparast, H.R.; Pinheiro, J.; Najafi, E.K.; Abreu, C.; Araújo, N.; Cristelo, N.; Miranda, T. Mechanical Behavior of a Mine Tailing Stabilized with a Sustainable Binder. *Appl. Sci.* **2023**, *13*, 4103. [CrossRef]
4. Shengo, L.M. Review of Practices in the Management of Mineral Wastes: The Case of Waste Rocks and Mine Tailings. *Water Air Soil Pollut.* **2021**, *232*, 273. [CrossRef]
5. Maijin, R. Mineral Characterization Study of Gold Deposit in Tawau, Sabah Focusing on Mineralogy and Geochemistry. Ph.D. Thesis, Universiti Sains Malaysia, Gelugor, Malaysia, 2022.
6. Yao, G.; Liu, Q.; Wang, J.; Wu, P.; Lyu, X. Effect of Mechanical Grinding on Pozzolanic Activity and Hydration Properties of Siliceous Gold Ore Tailings. *J. Clean. Prod.* **2019**, *217*, 12–21. [CrossRef]
7. Kiventerä, J.; Perumal, P.; Yliniemi, J.; Illikainen, M. Mine Tailings as a Raw Material in Alkali Activation: A Review. *Int. J. Miner. Metall. Mater.* **2020**, *27*, 1009–1020. [CrossRef]
8. Kalisz, S.; Kibort, K.; Mioduska, J.; Lieder, M.; Małachowska, A. Waste Management in the Mining Industry of Metals Ores, Coal, Oil and Natural Gas—A Review. *J. Environ. Manag.* **2022**, *304*, 114239. [CrossRef] [PubMed]
9. Barati, S.; Tabatabaie Shourijeh, P.; Samani, N.; Asadi, S. Stabilization of Iron Ore Tailings with Cement and Bentonite: A Case Study on Golgohar Mine. *Bull. Eng. Geol. Environ.* **2020**, *79*, 4151–4166. [CrossRef]
10. Shalash, I. *Introduction to Geology & Minerals*; Atlantic International University: Honolulu, HI, USA, 2019.
11. Maruthupandian, S.; Chaliasou, A.; Kanellopoulos, A. Recycling Mine Tailings as Precursors for Cementitious Binders—Methods, Challenges and Future Outlook. *Constr. Build. Mater.* **2021**, *312*, 125333. [CrossRef]
12. Park, I.; Tabelin, C.B.; Jeon, S.; Li, X.; Seno, K.; Ito, M.; Hiroyoshi, N. A Review of Recent Strategies for Acid Mine Drainage Prevention and Mine Tailings Recycling. *Chemosphere* **2019**, *219*, 588–606. [CrossRef]
13. Queiroz, H.M.; Ruiz, F.; Deng, Y.; de Souza Júnior, V.S.; Ferreira, A.D.; Otero, X.L.; Ferreira, T.O. Mine Tailings in a Redox-Active Environment: Iron Geochemistry and Potential Environmental Consequences. *Sci. Total Environ.* **2022**, *807*, 151050. [CrossRef] [PubMed]
14. Nguyen, T.H.; Won, S.; Ha, M.G.; Nguyen, D.D.; Kang, H.Y. Bioleaching for Environmental Remediation of Toxic Metals and Metalloids: A Review on Soils, Sediments, and Mine Tailings. *Chemosphere* **2021**, *282*, 131108. [CrossRef] [PubMed]
15. Kan, X.; Dong, Y.; Feng, L.; Zhou, M.; Hou, H. Contamination and Health Risk Assessment of Heavy Metals in China's Lead–Zinc Mine Tailings: A Meta–Analysis. *Chemosphere* **2021**, *267*, 128909. [CrossRef] [PubMed]
16. Manaviparast, H.R.; Araújo, N.; Cristelo, N.; Miranda, T. Study on Guardrail Post Behavior Located on Organic Soil Using Simplified Experimental and Numerical Methods. *Soils Rocks* **2022**, *45*, e2022077921. [CrossRef]
17. Mora-Sánchez, F.J.; Gómez-Álvarez, A.; Encinas-Romero, M.A.; Villalba-Atondo, A.I.; Valenzuela-García, J.L.; Jara-Marini, M.E.; Encinas-Soto, K.K. Prediction of Acid Mine Drainage Generation from Mine Waste at an Abandoned Mining Site in a Semi-arid Environment. *Water Air Soil Pollut.* **2024**, *235*, 140. [CrossRef]
18. Oboni, F.; Oboni, C. *Tailings Dam Management for the Twenty-First Century*; Springer International Publishing: Berlin/Heidelberg, Germany, 2020.
19. Yilmaz, E.; Koohestani, B.; Cao, S. Recent Practices in Mine Tailings' Recycling and Reuse. In *Managing Mining and Minerals Processing Wastes*; Elsevier: Amsterdam, The Netherlands, 2023; pp. 271–304.

20. Behera, S.K.; Mishra, D.P.; Singh, P.; Mishra, K.; Mandal, S.K.; Ghosh, C.N.; Mandal, P.K. Utilization of Mill Tailings, Fly Ash and Slag as Mine Paste Backfill Material: Review and Future Perspective. *Constr. Build. Mater.* **2021**, *309*, 125120. [CrossRef]
21. Mashifana, T.; Sithole, T. Clean Production of Sustainable Backfill Material from Waste Gold Tailings and Slag. *J. Clean. Prod.* **2021**, *308*, 127357. [CrossRef]
22. Al-Bakri, A.Y.; Ahmed, H.M.; Hefni, M.A. Eco-Sustainable Recycling of Cement Kiln Dust (CKD) and Copper Tailings (CT) in the Cemented Paste Backfill. *Sustainability* **2023**, *15*, 3229. [CrossRef]
23. Liu, L.; Xin, J.; Huan, C.; Qi, C.; Zhou, W.; Song, K.I. Pore and Strength Characteristics of Cemented Paste Backfill Using Sulphide Tailings: Effect of Sulphur Content. *Constr. Build. Mater.* **2020**, *237*, 117452. [CrossRef]
24. Samarakoon, M.H.; Ranjith, P.G.; Rathnaweera, T.D.; Perera, M.S.A. Recent Advances in Alkaline Cement Binders: A Review. *J. Clean. Prod.* **2019**, *227*, 70–87. [CrossRef]
25. Tekle, B.H.; Holschemacher, K. Alkali Activated Cement Mixture at Ambient Curing: Strength, Workability, and Setting Time. *Struct. Concr.* **2022**, *23*, 2496–2509. [CrossRef]
26. Siddique, S.; Jang, J.G. Assessment of Molybdenum Mine Tailings as Filler in Cement Mortar. *J. Build. Eng.* **2020**, *31*, 101322. [CrossRef]
27. dos Santos, C.P.; Bruschi, G.J.; Mattos, J.R.G.; Consoli, N.C. Stabilization of Gold Mining Tailings with Alkali-Activated Carbide Lime and Sugarcane Bagasse Ash. *Transp. Geotech.* **2022**, *32*, 100704. [CrossRef]
28. Zhang, Y.; Li, Z.; Gu, X.; Nehdi, M.L.; Marani, A.; Zhang, L. Utilization of Iron Ore Tailings with High Volume in Green Concrete. *J. Build. Eng.* **2023**, *72*, 106585. [CrossRef]
29. Behera, S.K.; Ghosh, C.N.; Mishra, K.; Mishra, D.P.; Singh, P.; Mandal, P.K.; Sethi, M.K. Utilization of Lead–Zinc Mill Tailings and Slag as Paste Backfill Materials. *Environ. Earth Sci.* **2020**, *79*, 389. [CrossRef]
30. Mendes, B.C.; Pedroti, L.G.; Vieira, C.M.F.; Marvila, M.; Azevedo, A.R.; de Carvalho, J.M.F.; Ribeiro, J.C.L. Application of Eco-Friendly Alternative Activators in Alkali-Activated Materials: A Review. *J. Build. Eng.* **2021**, *35*, 102010. [CrossRef]
31. Marvila, M.T.; Azevedo, A.R.G.D.; Vieira, C.M.F. Reaction Mechanisms of Alkali-Activated Materials. *Rev. IBRACON Estrut. Mater.* **2021**, *14*, e14309. [CrossRef]
32. Parthiban, D.; Vijayan, D.S.; Koda, E.; Vaverkova, M.D.; Piechowicz, K.; Osinski, P.; Van Duc, B. Role of Industrial Based Precursors in the Stabilization of Weak Soils with Geopolymer—A Review. *Case Stud. Constr. Mater.* **2022**, *16*, e00886. [CrossRef]
33. Tang, S.; Wang, Y.; Geng, Z.; Xu, X.; Yu, W.; Chen, J. Structure, Fractality, Mechanics and Durability of Calcium Silicate Hydrates. *Fract. Fract.* **2021**, *5*, 47. [CrossRef]
34. John, S.K.; Nadir, Y.; Girija, K. Effect of Source Materials, Additives on the Mechanical Properties and Durability of Fly Ash and Fly Ash-Slag Geopolymer Mortar: A Review. *Constr. Build. Mater.* **2021**, *280*, 122443. [CrossRef]
35. Chen, C.; Liu, H.; Zhang, Y.; Gu, G.; Hu, J. Micro-assessment of Heavy Metal Immobilization within Alkali-Activated Copper Tailings-Slag Geopolymer. *Cem. Concr. Compos.* **2024**, *149*, 105510. [CrossRef]
36. Liu, Q.; Li, X.; Cui, M.; Wang, J.; Lyu, X. Preparation of Eco-Friendly One-Part Geopolymers from Gold Mine Tailings by Alkaline Hydrothermal Activation. *J. Clean. Prod.* **2021**, *298*, 126806. [CrossRef]
37. Liu, Q.; Cui, M.; Li, X.; Wang, J.; Wang, Z.; Li, L.; Lyu, X. Alkali-Hydrothermal Activation of Mine Tailings to Prepare One-Part Geopolymer: Activation Mechanism, Workability, Strength, and Hydration Reaction. *Ceram. Int.* **2022**, *48*, 30407–30417. [CrossRef]
38. Mashifana, T.; Sebothoma, J.; Sithole, T. Alkaline Activation of Basic Oxygen Furnace Slag Modified Gold Mine Tailings for Building Material. *Adv. Civ. Eng.* **2021**, *2021*, 9984494. [CrossRef]
39. Obenaus-Emler, R.; Falah, M.; Illikainen, M. Assessment of Mine Tailings as Precursors for Alkali-Activated Materials for On-Site Applications. *Constr. Build. Mater.* **2020**, *246*, 118470. [CrossRef]
40. Akinyemi, B.A.; Alaba, P.A.; Rashedi, A. Selected Performance of Alkali-Activated Mine Tailings as Cementitious Composites: A Review. *J. Build. Eng.* **2022**, *50*, 104154. [CrossRef]
41. Xiaolong, Z.; Shiyu, Z.; Hui, L.; Yingliang, Z. Disposal of Mine Tailings via Geopolymerization. *J. Clean. Prod.* **2021**, *284*, 124756. [CrossRef]
42. Krishna, R.S.; Shaikh, F.; Mishra, J.; Lazorenko, G.; Kasprzhitskii, A. Mine Tailings-based Geopolymers: Properties, Applications and Industrial Prospects. *Ceram. Int.* **2021**, *47*, 17826–17843. [CrossRef]
43. Guedes, J.P.C.; Silvani, C.; Carvalho, J.V.D.A.; Wagner, A.C.; Silva, J.P.D.S.; Consoli, N.C. Mechanical Behaviour of Fibre-Reinforced Cemented Iron Ore Tailings Across the Compaction Curve. *Geotech. Geol. Eng.* **2024**, 1–12. [CrossRef]
44. Luo, X.; Zhang, Y.; Zhou, H.; He, K.; Luo, C.; Liu, Z.; Tang, X. Review on the Development and Utilization of Ionic Rare Earth Ore. *Minerals* **2022**, *12*, 554. [CrossRef]
45. Seigneur, N.; De Windt, L.; Déjeant, A.; Lagneau, V.; Descostes, M. Long-term Evolution of Uranium Mobility within Sulfated Mill Tailings in Arid Regions: A Reactive Transport Study. *Minerals* **2021**, *11*, 1201. [CrossRef]
46. Mahabub, M.S.; Alahi, F.; Al Imran, M. Unlocking the Potential of Microbes: Biocementation Technology for Mine Tailings Restoration—A Comprehensive Review. *Environ. Sci. Pollut. Res.* **2023**, *30*, 91676–91709. [CrossRef] [PubMed]
47. Silva, J.P.S.; Rissoli, A.L.C.; Cacciari, P.P.; da Fonseca, A.J.P.V.; Scheuermann Filho, H.C.; Wagner, A.C.; Consoli, N.C. Triaxial Testing Response of Compacted Iron Ore Tailings Considering a Broad Spectrum of Confining Pressures. *Soils Found.* **2024**, *64*, 101438. [CrossRef]
48. Yu, L.; Zhang, Z.; Huang, X.; Jiao, B.; Li, D. Enhancement Experiment on Cementitious Activity of Copper-Mine Tailings in a Geopolymer System. *Fibers* **2017**, *5*, 47. [CrossRef]

49. Manjarrez, L.; Nikvar-Hassani, A.; Shadnia, R.; Zhang, L. Experimental Study of Geopolymer Binder Synthesized with Copper Mine Tailings and Low-Calcium Copper Slag. *J. Mater. Civ. Eng.* **2019**, *31*, 04019156. [CrossRef]
50. Gitari, M.W.; Akinyemi, S.A.; Thobakgale, R.; Ngoejana, P.C.; Ramugondo, L.; Matidza, M.; Nemapate, N. Physico-Chemical and Mineralogical Characterization of Musina Mine Copper and New Union Gold Mine Tailings: Implications for Fabrication of Beneficial Geopolymeric Construction Materials. *J. Afr. Earth Sci.* **2018**, *137*, 218–228. [CrossRef]
51. Falayi, T. A Comparison Between Fly Ash- and Basic Oxygen Furnace Slag-Modified Gold Mine Tailings Geopolymers. *Int. J. Energy Environ. Eng.* **2020**, *11*, 207–217. [CrossRef]
52. Demir, F.; Derun, E.M. Modelling and Optimization of Gold Mine Tailings Based Geopolymer by Using Response Surface Method and Its Application in Pb2+ Removal. *J. Clean. Prod.* **2019**, *237*, 117766. [CrossRef]
53. Kiventerä, J.; Sreenivasan, H.; Cheeseman, C.; Kinnunen, P.; Illikainen, M. Immobilization of Sulfates and Heavy Metals in Gold Mine Tailings by Sodium Silicate and Hydrated Lime. *J. Environ. Chem. Eng.* **2018**, *6*, 6530–6536. [CrossRef]
54. Niu, H.; Abdulkareem, M.; Sreenivasan, H.; Kantola, A.M.; Havukainen, J.; Horttanainen, M.; Illikainen, M. Recycling Mica and Carbonate-Rich Mine Tailings in Alkali-Activated Composites: A Synergy with Metakaolin. *Miner. Eng.* **2020**, *157*, 106535. [CrossRef]
55. Park, J.; Lee, B.; Shin, W.; Jo, S.; Jun, H. Psychrophilic Methanogenesis of Food Waste in a Bio-Electrochemical Anaerobic Digester with Rotating Impeller Electrode. *J. Clean. Prod.* **2018**, *188*, 556–567. [CrossRef]
56. dos Santos, L.F.; de Carvalho, J.M.F.; Peixoto, R.A.F.; Brigolini, G.J. Iron Ore Tailing-Based Geopolymer Containing Glass Wool Residue: A Study of Mechanical and Microstructural Properties. *Constr. Build. Mater.* **2019**, *220*, 375–385.
57. Kuranchie, F.A.; Shukla, S.K.; Habibi, D. Utilization of Iron Ore Mine Tailings for the Production of Geopolymer Bricks. *Int. J. Min. Reclam. Environ.* **2016**, *30*, 92–114. [CrossRef]
58. Wei, B.; Zhang, Y.; Bao, S. Preparation of Geopolymers from Vanadium Tailings by Mechanical Activation. *Constr. Build. Mater.* **2017**, *145*, 236–242. [CrossRef]
59. Perumal, P.; Piekkari, K.; Sreenivasan, H.; Kinnunen, P.; Illikainen, M. One-Part Geopolymers from Mining Residues–Effect of Thermal Treatment on Three Different Tailings. *Miner. Eng.* **2019**, *144*, 106026. [CrossRef]
60. Zhao, S.; Xia, M.; Yu, L.; Huang, X.; Jiao, B.; Li, D. Optimization for the Preparation of Composite Geopolymer Using Response Surface Methodology and Its Application in Lead-Zinc Tailings Solidification. *Constr. Build. Mater.* **2021**, *266*, 120969. [CrossRef]
61. McDonald, J.E.D.; Roache, S.C.; Kawatra, S.K. Repurposing Mine Tailings: Cold Bonding of Siliceous Iron Ore Tailings. *Miner. Metall. Process.* **2016**, *33*, 47–52. [CrossRef]
62. Ye, J.; Zhang, W.; Shi, D. Properties of an Aged Geopolymer Synthesized from Calcined Ore-Dressing Tailing of Bauxite and Slag. *Cem. Concr. Res.* **2017**, *100*, 23–31. [CrossRef]
63. Song, M.; Jiaping, L.; Qian, J.; Jianzhong, L.; Liang, S. Experimental Study on Utilization of Quartz Mill Tailings as a Filler to Prepare Geopolymer. *Miner. Process. Extr. Metall. Rev.* **2016**, *37*, 311–322. [CrossRef]
64. Kastiukas, G.; Zhou, X.; Castro-Gomes, J. Preparation Conditions for the Synthesis of Alkali-Activated Binders Using Tungsten Mining Waste. *J. Mater. Civ. Eng.* **2017**, *29*, 04017181. [CrossRef]
65. Wan, Q.; Rao, F.; Song, S.; Leon-Patino, C.A.; Ma, Y.; Yin, W. Consolidation of Mine Tailings through Geopolymerization at Ambient Temperature. *J. Am. Ceram. Soc.* **2019**, *102*, 2451–2461. [CrossRef]
66. Povarennykh, A.S. *Crystal Chemical Classification of Minerals*; Springer: Berlin/Heidelberg, Germany, 2014.
67. Samantray, J.; Anand, A.; Dash, B.; Ghosh, M.K.; Behera, A.K. Silicate Minerals—Potential Source of Potash—A Review. *Miner. Eng.* **2022**, *179*, 107463. [CrossRef]
68. Bai, S. Wettability Alteration Mechanisms in Carbonate Rocks: An Experimental and Molecular-Scale Computational Study. Ph.D. Thesis, University of Wyoming, Laramie, Wyoming, 2020.
69. El Aref, M.; Abd El-Rahman, Y.; Zoheir, B.; Surour, A.; Helmy, H.M.; Abdelnasser, A.; El Aref, M. Mineral Resources in Egypt (I): Metallic Ores. In *The Geology of Egypt*; Springer International Publishing: Cham, Switzerland, 2019; pp. 521–587.
70. Kasap, T.; Yilmaz, E.; Sari, M. Physico-Chemical and Micro-Structural Behavior of Cemented Mine Backfill: Effect of pH in Dam Tailings. *J. Environ. Manag.* **2022**, *314*, 115034. [CrossRef]
71. Liu, Y.; Li, K.; Yin, Z.; Dong, J.; Xu, L.; Ma, R.; Li, S. Pretreatment of Refractory Gold Ore by Curing with Concentrated Sulfuric Acid. *Min. Metall. Explor.* **2024**, *41*, 1079–1087. [CrossRef]
72. Wang, S.; Zhao, Y.; Li, S. Silicic Protective Surface Films for Pyrite Oxidation Suppression to Control Acid Mine Drainage at the Source. *Environ. Sci. Pollut. Res.* **2019**, *26*, 25725–25732. [CrossRef] [PubMed]
73. Gao, Y.; Wu, P.; Jeyakumar, P.; Bolan, N.; Wang, H.; Gao, B.; Wang, B. Biochar as a Potential Strategy for Remediation of Contaminated Mining Soils: Mechanisms, Applications, and Future Perspectives. *J. Environ. Manag.* **2022**, *313*, 114973. [CrossRef]
74. Plante, B.; Schudel, G.; Benzaazoua, M. Generation of Acid Mine Drainage. In *Hard Rock Mine Reclamation: From Prediction to Management of Acid Mine Drainage*; CRC Press: Boca Raton, FL, USA, 2021; pp. 1–20.
75. Firnia, D.; Rohmawati, I. Chemical Properties of Acid Soil after Amelioration of Dolomite, Coal, and Microbes. In *IOP Conference Series: Earth and Environmental Science*; IOP Publishing: Bristol, UK, 2022; Volume 978, Issue 1; p. 012010.
76. Xiu-ting, S.; Mei-rong, L.; Jun-tao, X.; Chen-chu, L.; Guang-hui, Y.; Ying-Chang, C. The Complex Effect of Organic Acids on the Dissolution of Feldspar at High Temperature. *Environ. Earth Sci.* **2021**, *80*, 244. [CrossRef]
77. Zhou, Y.; Short, M.D.; Li, J.; Fan, R.; Qian, G. Non-carbonate Geochemical Options for Long-term Sustainable Acid and Metalliferous Drainage Control At-source. *Environ. Earth Sci.* **2019**, *78*, 157. [CrossRef]

78. Zhang, T.; Zhang, C.; Du, S.; Zhang, Z.; Lu, W.; Su, P.; Zhao, Y. A Review: The Formation, Prevention, and Remediation of Acid Mine Drainage. *Environ. Sci. Pollut. Res.* **2023**, *30*, 111871–111890. [CrossRef]
79. Rezaie, B.; Anderson, A. Sustainable Resolutions for Environmental Threat of the Acid Mine Drainage. *Sci. Total Environ.* **2020**, *717*, 137211. [CrossRef]
80. Kanagaraj, B.; Lubloy, E.; Anand, N.; Hlavicka, V.; Kiran, T. Investigation of Physical, Chemical, Mechanical, and Micro-Structural Properties of Cement-less Concrete–State-of-the-Art Review. *Constr. Build. Mater.* **2023**, *365*, 130020. [CrossRef]
81. Nodehi, M.; Taghvaee, V.M. Alkali-Activated Materials and Geopolymer: A Review of Common Precursors and Activators Addressing Circular Economy. *Circ. Econ. Sustain.* **2022**, *2*, 165–196. [CrossRef]
82. Ralli, Z.G.; Pantazopoulou, S.J. State of the Art on Geopolymer Concrete. *Int. J. Struct. Integr.* **2021**, *12*, 511–533. [CrossRef]
83. Kamseu, E.; Alzari, V.; Nuvoli, D.; Sanna, D.; Lancellotti, I.; Mariani, A.; Leonelli, C. Dependence of the Geopolymerization Process and End-products to the Nature of Solid Precursors: Challenge of the Sustainability. *J. Clean. Prod.* **2021**, *278*, 123587. [CrossRef]
84. Amran, M.; Debbarma, S.; Ozbakkaloglu, T. Fly Ash-based Eco-friendly Geopolymer Concrete: A Critical Review of the Long-term Durability Properties. *Constr. Build. Mater.* **2021**, *270*, 121857. [CrossRef]
85. Amran, M.; Al-Fakih, A.; Chu, S.H.; Fediuk, R.; Haruna, S.; Azevedo, A.; Vatin, N. Long-term Durability Properties of Geopolymer Concrete: An In-depth Review. *Case Stud. Constr. Mater.* **2021**, *15*, e00661. [CrossRef]
86. Xing, J.; Zhao, Y.; Qiu, J.; Sun, X. Microstructural and Mechanical Properties of Alkali Activated Materials from Two Types of Blast Furnace Slags. *Materials* **2019**, *12*, 2089. [CrossRef] [PubMed]
87. Portela Farenzena, H.; Bruschi, G.J.; Schmitt Medina, G.; de Sousa Silva, J.P.; Lotero, A.; Consoli, N.C. Iron Ore Tailings Stabilization with Alternative Alkali-activated Cement for Dry Stacking: Mechanical and Microstructural Insights. *Can. Geotech. J.* **2024**, *61*, 4. [CrossRef]
88. Adesanya, E.; Perumal, P.; Luukkonen, T.; Yliniemi, J.; Ohenoja, K.; Kinnunen, P.; Illikainen, M. Opportunities to Improve Sustainability of Alkali-activated Materials: A Review of Side-stream Based Activators. *J. Clean. Prod.* **2021**, *286*, 125558. [CrossRef]
89. Zhang, P.; Muhammad, F.; Yu, L.; Xia, M.; Lin, H.; Huang, X.; Li, D. Self-cementation solidification of heavy metals in lead-zinc smelting slag through alkali-activated materials. *Constr. Build. Mater.* **2020**, *249*, 118756. [CrossRef]
90. Alnahhal, M.F.; Kim, T.; Hajimohammadi, A. Waste-Derived Activators for Alkali-Activated Materials: A Review. *Cem. Concr. Compos.* **2021**, *118*, 103980. [CrossRef]
91. Pan, Z.; Zhang, C.; Li, Y.; Yang, C. Solidification/Stabilization of Gold Ore Tailings Powder Using Sustainable Waste-Based Composite Geopolymer. *Eng. Geol.* **2022**, *309*, 106793. [CrossRef]
92. Martins, N.P.; Srivastava, S.; Simão, F.V.; Niu, H.; Perumal, P.; Snellings, R.; Habert, G. Exploring the Potential for Utilization of Medium and Highly Sulfidic Mine Tailings in Construction Materials: A Review. *Sustainability* **2021**, *13*, 12150. [CrossRef]
93. Tuomivaara, S. Granulation and Alkali Activation of MSWI Bottom Ash. Master's Thesis, University of Oulu, Oulu, Finland, 2021. Available online: https://oulurepo.oulu.fi/handle/10024/18879 (accessed on 10 June 2024).
94. Zhao, X.; Liu, W.; Cai, Z.; Fu, J.; Duan, J.; Zhao, D.; Feng, Y. Reductive Immobilization of Uranium by Stabilized Zero-Valent Iron Nanoparticles: Effects of Stabilizers, Water Chemistry, and Long-Term Stability. *Colloids Surf. A Physicochem. Eng. Asp.* **2020**, *604*, 125315. [CrossRef]
95. Illikainen, M.; Kiventerä, J. Mine Tailings as Precursors for Alkali-Activated Materials and Ettringite Binders. In *Industrial Waste: Characterization, Modification and Applications of Residues*; De Gruyter: Berlin, Germany, 2021; p. 345.
96. Seney, C.S.; Kiefer, A.M.; Aljic, S. Determination of Mercury Solvation during Cyanidation of Artisanal & Small-Scale Gold Mining Tailings via Inductively Coupled Plasma Optical Emission Spectroscopy in Comparison to Direct Mercury Analysis. *Int. J. Environ. Anal. Chem.* **2021**, *101*, 2058–2068.
97. Yu, J.; Guo, Q.; Gong, Y.; Ding, L.; Wang, J.; Yu, G. A Review of the Effects of Alkali and Alkaline Earth Metal Species on Biomass Gasification. *Fuel Process. Technol.* **2021**, *214*, 106723. [CrossRef]
98. Qaidi, S.M.; Tayeh, B.A.; Zeyad, A.M.; de Azevedo, A.R.; Ahmed, H.U.; Emad, W. Recycling of Mine Tailings for Geopolymers Production: A Systematic Review. *Case Stud. Constr. Mater.* **2022**, *16*, e00933. [CrossRef]
99. Simonsen, A.M.T.; Solismaa, S.; Hansen, H.K.; Jensen, P.E. Evaluation of Mine Tailings' Potential as Supplementary Cementitious Materials Based on Chemical, Mineralogical, and Physical Characteristics. *Waste Manag.* **2020**, *102*, 710–721. [CrossRef] [PubMed]
100. Asadizadeh, M.; Clements, C.; Hedayat, A.; Tunstall, L.; Gonzalez, J.A.V.; Alvarado, J.W.V.; Neira, M.T. The Effect of Class F Fly Ash on the Geopolymerization and Compressive Strength of Lightweight Aggregates Made from Alkali-Activated Mine Tailings. *Constr. Build. Mater.* **2023**, *395*, 132275. [CrossRef]
101. Ding, H.; Liu, H.; Chu, W.; Wu, C.; Xie, Y. Structural Transformation of Heterogeneous Materials for Electrocatalytic Oxygen Evolution Reaction. *Chem. Rev.* **2021**, *121*, 13174–13212. [CrossRef]
102. Cheah, C.B.; Tan, L.E.; Ramli, M. Recent Advances in Slag-Based Binder and Chemical Activators Derived from Industrial By-Products—A Review. *Constr. Build. Mater.* **2021**, *272*, 121657. [CrossRef]
103. Ng, W.S.; Liu, Y.; Wang, Q.; Chen, M. The Fate of the Arsenic Species in the Pressure Oxidation of Refractory Gold Ores: Practical and Modelling Aspects. *Miner. Process. Extr. Metall. Rev.* **2023**, *44*, 155–187. [CrossRef]
104. Kiventerä, J.; Yliniemi, J.; Golek, L.; Deja, J.; Ferreira, V.; Illikainen, M. Utilization of Sulphidic Mine Tailings in Alkali-Activated Materials. *MATEC Web Conf.* **2019**, *274*, 01001. [CrossRef]

105. Cristelo, N.; Coelho, J.; Oliveira, M.; Cesar Consoli, N.; Palomo, Á.; Fernández-Jiménez, A. Recycling and Application of Mine Tailings in Alkali-Activated Cements and Mortars—Strength Development and Environmental Assessment. *Appl. Sci.* **2020**, *10*, 2084. [CrossRef]
106. Kehinde, O.; Hughes, D.; Amalu, E.H. Mineral Wastes. In *Green Materials in Civil Engineering*; Elsevier: Amsterdam, The Netherlands, 2024; pp. 181–199.
107. Han, R.; Guo, X.; Guan, J.; Yao, X.; Hao, Y. Activation Mechanism of Coal Gangue and Its Impact on the Properties of Geopolymers: A Review. *Polymers* **2022**, *14*, 3861. [CrossRef]
108. Tian, Q.; Bai, Y.; Pan, Y.; Chen, C.; Yao, S.; Sasaki, K.; Zhang, H. Application of Geopolymer in Stabilization/Solidification of Hazardous Pollutants: A Review. *Molecules* **2022**, *27*, 4570. [CrossRef]
109. Perumal, P.; Kiventerä, J.; Illikainen, M. Influence of Alkali Source on Properties of Alkali-Activated Silicate Tailings. *Mater. Chem. Phys.* **2021**, *271*, 124932. [CrossRef]
110. Sari, M.; Yilmaz, E.; Kasap, T. Long-term Ageing Characteristics of Cemented Paste Backfill: Usability of Sand as a Partial Substitute of Hazardous Tailings. *J. Clean. Prod.* **2023**, *401*, 136723. [CrossRef]
111. Qing, L.; Shaokang, S.; Zhen, J.; Junxiang, W.; Xianjun, L. Effect of CaO on Hydration Properties of One-Part Alkali-Activated Material Prepared from Tailings through Alkaline Hydrothermal Activation. *Constr. Build. Mater.* **2021**, *308*, 124931. [CrossRef]
112. Castillo, H.; Droguett, T.; Vesely, M.; Garrido, P.; Palma, S. Simple Compressive Strength Results of Sodium-Hydroxide-and Sodium-Silicate-Activated Copper Flotation Tailing Geopolymers. *Appl. Sci.* **2022**, *12*, 5876. [CrossRef]
113. Watari, T.; Northey, S.; Giurco, D.; Hata, S.; Yokoi, R.; Nansai, K.; Nakajima, K. Global Copper Cycles and Greenhouse Gas Emissions in a 1.5 °C World. *Resour. Conserv. Recycl.* **2022**, *179*, 106118. [CrossRef]
114. Esmaeili, J.; Aslani, H. Use of Copper Mine Tailing in Concrete: Strength Characteristics and Durability Performance. *J. Mater. Cycles Waste Manag.* **2019**, *21*, 729–741. [CrossRef]
115. Xu, W.; Li, Q.; Liu, B. Coupled Effect of Curing Temperature and Age on Compressive Behavior, Microstructure, and Ultrasonic Properties of Cemented Tailings Backfill. *Constr. Build. Mater.* **2020**, *237*, 117738. [CrossRef]
116. Sedira, N. Novel Waste-Based Alkali-Activated Binders by Combining Mining and Other Mineral Waste. Ph.D. Dissertation, Universidade da Beira Interior, Covilhã, Portugal, 2021.
117. Yang, Y.; Zhang, J.; Fu, Y.; Hou, D.; Dong, B. Alkaline Hydrothermal Activation of Molybdenum Tailings to Prepare One-Part Geopolymer: Activation Mechanism and Strength. *J. Mater. Res. Technol.* **2023**, *25*, 3789–3802. [CrossRef]
118. Tian, X.; Xu, W.; Song, S.; Rao, F.; Xia, L. Effects of Curing Temperature on the Compressive Strength and Microstructure of Copper Tailing-Based Geopolymers. *Chemosphere* **2020**, *253*, 126754. [CrossRef]
119. Helser, J.; Perumal, P.; Cappuyns, V. Valorizing (Cleaned) Sulfidic Mine Waste as a Resource for Construction Materials. *J. Environ. Manag.* **2022**, *319*, 115742. [CrossRef]
120. Jiang, H.; Qi, Z.; Yilmaz, E.; Han, J.; Qiu, J.; Dong, C. Effectiveness of Alkali-Activated Slag as Alternative Binder on Workability and Early Age Compressive Strength of Cemented Paste Backfills. *Constr. Build. Mater.* **2019**, *218*, 689–700. [CrossRef]
121. Falah, M.; Obenaus-Emler, R.; Kinnunen, P.; Illikainen, M. Effects of Activator Properties and Curing Conditions on Alkali-Activation of Low-Alumina Mine Tailings. *Waste Biomass Valorization* **2020**, *11*, 5027–5039. [CrossRef]
122. Sephton, M.G.; Webb, J.A.; McKnight, S. Applications of Portland Cement Blended with Fly Ash and Acid Mine Drainage Treatment Sludge to Control Acid Mine Drainage Generation from Waste Rocks. *Appl. Geochem.* **2019**, *103*, 1–14. [CrossRef]
123. Allah, P. Exploring the Use of Mineral Carbonation and Alkali Activation for the Valorization of Mg-rich Mine Tailings. Master's Thesis, University of Oulu, Oulu, Finland, 2022.
124. Luukkanen, S.; Tanhua, A.; Zhang, Z.; Canales, R.M.; Auranen, I. Towards Waterless Operations from Mine to Mill. *Miner. Eng.* **2022**, *187*, 107793. [CrossRef]
125. Mucsi, G. A Review on Mechanical Activation and Mechanical Alloying in Stirred Media Mill. *Chem. Eng. Res. Des.* **2019**, *148*, 460–474. [CrossRef]
126. Gao, Y.; Yue, Q.; Gao, B.; Li, A. Insight into Activated Carbon from Different Kinds of Chemical Activating Agents: A Review. *Sci. Total Environ.* **2020**, *746*, 141094. [CrossRef] [PubMed]
127. Jiao, X.; Zhang, Y.; Chen, T. Thermal Stability of a Silica-Rich Vanadium Tailing Based Geopolymer. *Constr. Build. Mater.* **2013**, *38*, 43–47. [CrossRef]
128. Abboud, J.; Mazumder, J. Developing of Nano Sized Fibrous Eutectic Silicon in Hypereutectic Al–Si Alloy by Laser Remelting. *Sci. Rep.* **2020**, *10*, 12090. [CrossRef] [PubMed]
129. El-Seidy, E.; Chougan, M.; Sambucci, M.; Al-Kheetan, M.J.; Valente, M.; Ghaffar, S.H. Lightweight Alkali-Activated Materials and Ordinary Portland Cement Composites Using Recycled Polyvinyl Chloride and Waste Glass Aggregates to Fully Replace Natural Sand. *Constr. Build. Mater.* **2023**, *368*, 130399. [CrossRef]
130. LV, C.; Ding, J.; Liu, Y.; Fu, G.Y.; Qian, P.; Ye, S.F. Characterization of a Copper Mine Tailing and Comprehensive Recovery of Cu and S from the Tailing. *J. Residuals Sci. Technol.* **2017**, *14*, 125.
131. Kalinkina, E.V.; Gurevich, B.I.; Kalinkin, A.M. Alkali-Activated Binder Based on Milled Antigorite. *Minerals* **2018**, *8*, 503. [CrossRef]
132. Adesanya, E.; Ohenoja, K.; Yliniemi, J.; Illikainen, M. Mechanical Transformation of Phyllite Mineralogy toward Its Use as Alkali-Activated Binder Precursor. *Miner. Eng.* **2020**, *145*, 106093. [CrossRef]

133. Niu, H.; Kinnunen, P.; Sreenivasan, H.; Adesanya, E.; Illikainen, M. Structural Collapse in Phlogopite Mica-Rich Mine Tailings Induced by Mechanochemical Treatment and Implications to Alkali Activation Potential. *Miner. Eng.* **2020**, *151*, 106331. [CrossRef]
134. Zhang, L.; Guo, J.; Hao, M.; Li, B.; Liu, S. Microscopic Spreading Characteristics of Non-Polar Oil Droplet on Low Rank Coal Surface: Effects of Surfactant Pre-Treatment and Oxygen-Containing Groups. *J. Mol. Liq.* **2021**, *325*, 115232. [CrossRef]
135. Hanein, T.; Thienel, K.C.; Zunino, F.; Marsh, A.T.; Maier, M.; Wang, B.; Martirena-Hernández, F. Clay Calcination Technology: State-of-the-Art Review by the RILEM TC 282-CCL. *Mater. Struct.* **2022**, *55*, 3. [CrossRef]
136. Xu, W.; Shen, K.; Cao, Z.; Liu, F.; Zhang, Y.; Zhang, T.; Ouyang, S. Crystallization and Thermal Stability Effects on Tailings Glass-Ceramics by Various Heat Treating Processes. *Mater. Chem. Phys.* **2021**, *263*, 124334. [CrossRef]
137. Fernando, P.T.; João, C.G.; Said, J. Durability and Environmental Performance of Alkali-Activated Tungsten Mine Waste Mud Mortars. *J. Mater. Civ. Eng.* **2010**, *22*, 897–904. [CrossRef]
138. Aydın, S.; Kızıltepe, C.Ç. Valorization of Boron Mine Tailings in Alkali-Activated Mortars. *J. Mater. Civ. Eng.* **2019**, *31*, 04019224. [CrossRef]
139. Ionescu, C.; Höck, V.; Simon, V. Effect of the Temperature and the Heating Time on the Composition of an Illite-Rich Clay: An XRPD Study. *Babes-Bolyai Phys* **2011**, *56*, 70.
140. Feng, D.; Provis, J.L.; van Deventer, J.S. Thermal Activation of Albite for the Synthesis of One-Part Mix Geopolymers. *J. Am. Ceram. Soc.* **2012**, *95*, 565–572. [CrossRef]
141. Haddaji, Y.; Majdoubi, H.; Mansouri, S.; Tamraoui, Y.; Manoun, B.; Oumam, M.; Hannache, H. Effect of Synthetic Fibers on the Properties of Geopolymers Based on Non-Heat Treated Phosphate Mine Tailing. *Mater. Chem. Phys.* **2021**, *260*, 124147. [CrossRef]
142. da Silva, M.R.C.; Malacarne, C.S.; Longhi, M.A.; Kirchheim, A.P. Valorization of Kaolin Mining Waste from the Amazon Region (Brazil) for Low-Carbon Cement Production. *Case Stud. Constr. Mater.* **2021**, *15*, e00756. [CrossRef]
143. Solouki, A.; Viscomi, G.; Lamperti, R.; Tataranni, P. Quarry Waste as Precursors in Geopolymers for Civil Engineering Applications: A Decade in Review. *Materials* **2020**, *13*, 3146. [CrossRef]
144. Bao, J.; Ning, P.; Wang, F.; Sun, X.; Wang, C.; Song, X.; Li, K. Thermal Modification of Copper Slag via Phase Transformation for Simultaneous Removal of SO2 and NOx from Acid-Making Tail Gas. *Chem. Eng. J.* **2021**, *425*, 131646. [CrossRef]
145. Moukannaa, S.; Nazari, A.; Bagheri, A.; Loutou, M.; Sanjayan, J.G.; Hakkou, R. Alkaline Fused Phosphate Mine Tailings for Geopolymer Mortar Synthesis: Thermal Stability, Mechanical and Microstructural Properties. *J. Non-Cryst. Solids* **2019**, *511*, 76–85. [CrossRef]
146. Ray, A.R.; Mishra, S. Hydro Metallurgical Technique as Better Option for the Recovery of Rare Earths from Mine Tailings and Industrial Wastes. *Sustain. Chem. Pharm.* **2023**, *36*, 101311. [CrossRef]
147. Kouamo, H.T.; Mbey, J.A.; Elimbi, A.; Diffo, B.K.; Njopwouo, D. Synthesis of Volcanic Ash-Based Geopolymer Mortars by Fusion Method: Effects of Adding Metakaolin to Fused Volcanic Ash. *Ceram. Int.* **2013**, *39*, 1613–1621. [CrossRef]
148. Zhu, P.; Xia, B.; Li, H.; Liu, H.; Qian, G. A Novel Approach to Recycle Waste Serpentine Tailing for Mg/Al Layered Double Hydroxide Used as Adsorption Material. *Environ. Eng. Sci.* **2021**, *38*, 99–106. [CrossRef]
149. Moukannaa, S.; Aboulayt, A.; Hakkou, R.; Benzaazoua, M.; Ohenoja, K.; Palomo, A.; Fernández-Jimenez, A. Fusion of Phosphate By-Products and Glass Waste for Preparation of Alkali-Activated Binders. *Compos. Part B Eng.* **2022**, *242*, 110044. [CrossRef]
150. Vizureanu, P.; Nergis, D.D.B.; Sandu, A.V.; Nergis, D.P.B.; Baltatu, M.S. The Physical and Mechanical Characteristics of Geopolymers Using Mine Tailings as Precursors. In *Advances in Geopolymer-Zeolite Composites-Synthesis and Characterization*; IntechOpen: London, UK, 2021.

Disclaimer/Publisher's Note: The statements, opinions and data contained in all publications are solely those of the individual author(s) and contributor(s) and not of MDPI and/or the editor(s). MDPI and/or the editor(s) disclaim responsibility for any injury to people or property resulting from any ideas, methods, instructions or products referred to in the content.

MDPI AG
Grosspeteranlage 5
4052 Basel
Switzerland
Tel.: +41 61 683 77 34

Applied Sciences Editorial Office
E-mail: applsci@mdpi.com
www.mdpi.com/journal/applsci



Disclaimer/Publisher's Note: The title and front matter of this reprint are at the discretion of the Guest Editor. The publisher is not responsible for their content or any associated concerns. The statements, opinions and data contained in all individual articles are solely those of the individual Editor and contributors and not of MDPI. MDPI disclaims responsibility for any injury to people or property resulting from any ideas, methods, instructions or products referred to in the content.





Academic Open
Access Publishing

mdpi.com

ISBN 978-3-7258-8628-9